



The Relevance of Black-Hole Kicks in Gravitational-Wave Astronomy

Von der QUEST-Leibniz-Forschungsschule
der Gottfried Wilhelm Leibniz Universität Hannover

zur Erlangung des Grades
Doktor der Naturwissenschaften
Dr. rer. nat.

genehmigte Dissertation von

M. Sc. Angela Borchers Pascual

2025

Referent:

Dr. Frank Ohme

Max-Planck-Institut für Gravitationsphysik

Korreferenten:

Prof. Guido Müller

Max-Planck-Institut für Gravitationsphysik

Prof. Mark Hannam

Cardiff University

Tag der Promotion:

September 30, 2025

*Al sillón rojo, donde descansaron
mis pensamientos y nacieron estas páginas.*

Zusammenfassung

Am 14. September 2015 machten Forscher der LIGO Kollaboration eine bahnbrechende Entdeckung: Zum ersten Mal war es gelungen, *Gravitationswellen* direkt zu detektieren. Diese winzig kleinen Wellen in Raum und Zeit selbst wurden bereits von Albert Einstein als Konsequenz seiner Allgemeinen Relativitätstheorie vorhergesagt. Obwohl prinzipiell jede beschleunigte Masse Gravitationswellen produziert, sind diese im Normalfall so schwach, dass nur die gewaltigsten Ereignisse im Kosmos messbare Wellen erzeugen.

Ein Beispiel dafür ist die *Verschmelzung von zwei Schwarzen Löchern* – extrem dichte und kompakte Objekte, die durch den Kollaps massereicher Sterne entstehen. Umkreisen sich zwei Schwarze Löcher, so entsteht dabei ein charakteristisches Gravitationswellensignal, das sich durch das Universum ausbreitet. Wenn ein solches Signal die Erde erreicht, kann es mit äußerst empfindlichen Laserinterferometern nachgewiesen werden. Seit der ersten Entdeckung hat ein stetig wachsendes Netzwerk von Detektoren viele weitere Signale von der Verschmelzung zweier kompakter Objekte gemessen. Die meisten davon, 86 an der Zahl, kamen von Binärsystemen Schwarzer Löcher.

Eine der offenen Fragen in der Gravitationswellenastronomie ist es, die Herkunft der beobachteten Schwarzen Löcher zu ermitteln. Einige könnten direkt aus dem Kernkollaps massereicher Sterne in Supernova-Explosionen entstanden sein, während andere die Überreste von vorhergehenden Verschmelzungen Schwarzer Löcher sein könnten. Ein Szenario, das als *hierarchische Verschmelzung* bekannt ist. Die Unterscheidung zwischen diesen beiden Entstehungsmöglichkeiten erfordert zwei Dinge: Präzise theoretische Modelle der Eigenschaften Schwarzer Löcher aus jedem Entstehungsszenario und genaue Messungen der Quellparameter aus Gravitationswellendaten.

Um dieser Frage nachzugehen, konzentriert sich meine Dissertation auf ein spezielles Merkmal der Verschmelzung Schwarzer Löcher: die *Rückstoßgeschwindigkeit* des übrig gebliebenen Schwarzen Loches. Wenn zwei Schwarze Löcher verschmelzen, senden sie Gravitationswellen aus, die nicht nur Energie und Drehimpuls, sondern auch einen translatorischen Impuls mit sich führen. Aufgrund der Impulserhaltung wird das resultierende Schwarze Loch mit einer Geschwindigkeit geboren, die als Rückstoß- oder Kick-Geschwindigkeit bezeichnet wird. Dieser Kick ist in den abgestrahlten Gravitationswellen kodiert und kann somit aus dem beobachteten Signal extrahiert werden. Die Stärke des Rückstoßes hängt von den Eigenschaften der ursprünglichen Schwarzen Löcher ab und kann so groß sein, dass sie die Fluchtgeschwindigkeit von kompakten Sternhaufen oder sogar ganzen Galaxien übersteigt. Daher können diese hohen Kick-Geschwindigkeiten der verschmolzenen Schwarzen Löcher, jene aus ihren Ursprungsumgebungen herausschleudern und sie daran hindern, neue Binärsysteme zu bilden und erneut zu verschmelzen.

In dieser Arbeit untersuche ich, wie der Kick uns helfen kann, aussagekräftigere Messungen der Quelleneigenschaften zu erzielen und charakteristische Merkmale von Schwarzen Löchern zu identifizieren, die durch hierarchische Verschmelzungen entstehen. Durch die Untersuchung dieses Effekts können wir die Ursprünge Schwarzer Löcher, die durch Gravitationswellen beobachtet werden, besser verstehen.

Summary

On September 14, 2015, scientists of the LIGO collaboration made a groundbreaking discovery: they directly detected *gravitational waves* for the first time. These waves, tiny ripples in the fabric of space and time, were first predicted by Albert Einstein as part of his theory of General Relativity. While any accelerated mass can create gravitational waves, the effects are usually so faint that only the most powerful cosmic events produce waves strong enough for us to detect.

One such event is the merger of two *black holes*, extremely dense and compact objects that form when massive stars collapse. When two black holes orbit around each other, they generate a distinct gravitational-wave signal that travels across the universe. When this signal reaches Earth, it may be picked up by highly sensitive laser interferometers. Since the first detection, a growing network of gravitational-wave observatories have consistently unveiled signals from compact binary mergers, primarily from black-hole binaries, recording a total of 86 such signals.

One of the open questions in gravitational-wave astronomy is whether we can determine the origin of the black holes we observe. Some may have formed directly from the core collapse of massive stars in supernova explosions, while others could be the remnants of previous black hole mergers, a scenario known as *hierarchical mergers*. Distinguishing between these formation channels requires two things: precise theoretical models of black hole properties in each scenario and accurate measurements of source parameters extracted from gravitational-wave data.

To address this question, my thesis focuses on one specific feature of black hole mergers: the remnant kick velocity. When two black holes merge, they emit gravitational waves that carry away not only energy and angular momentum, but also linear momentum. Because of conservation of momentum, the final black hole is born with a velocity, which is known as the *recoil* or *kick velocity*. This kick is encoded in the gravitational waves radiated, and therefore it can be extracted from the observed signal. The magnitude of the kick depends on the properties of the progenitor black holes and can be large enough to exceed the escape velocities of dense star clusters, or even entire galaxies. In some cases, these high kick velocities can eject remnant black holes from their host environments, preventing them from forming new binaries and merging again.

In this thesis, I explore how the kick can help us to make more meaningful measurements of the source properties and to identify distinctive features of black holes formed through hierarchical mergers. By studying this effect, we can better understand the population of black holes observed through gravitational waves.

Abstract

Gravitational-wave observations provide a unique opportunity to study black holes. With a growing catalog of binary black hole mergers, one of the main challenges is to extract as much information as possible from each detection to better understand the underlying black hole population. Spin measurements, in particular, are crucial for probing the origin of these systems. However, such measurements require accurate waveform models and are limited by the finite signal-to-noise ratio of the detections. In addition, accurate predictions of black hole properties across different formation scenarios are essential for a robust interpretation of the origin of these sources.

In this thesis, we demonstrate that one particular feature of binary black hole mergers, the recoil or "kick" velocity of the remnant, can provide valuable insight into this challenge. When two black holes merge, the anisotropic emission of gravitational waves carries away linear momentum, imparting a kick to the final black hole. This kick is imprinted in the gravitational-wave signal, particularly during the highly relativistic merger phase, where waveform models are least accurate. Because the kick is sensitive to subtle features in this regime, we show that it can be used to investigate waveform systematics across the parameter space. Furthermore, we demonstrate that the imprint of the kick gives more structure to the signal, enabling more informative parameter measurements. In particular, our study shows that kicks lead to more precise spin measurements in binary configurations that previously were thought to be uninformative.

Additionally, we explore the astrophysical role of kicks by investigating their impact on hierarchical mergers in dense star clusters. We demonstrate that black holes formed through hierarchical mergers may not necessarily have a spin of 0.7 as previously predicted. Instead, when accounting for kick velocities, the spin distribution is skewed towards higher values. We show that higher-generation black holes can have spins that span a broad range of values, $a \in (0.4, 1)$. By improving parameter measurements and refining the spin distribution of hierarchical mergers, we show that the kick velocity can help us gain deeper insight into the population of black holes.

Keywords: gravitational-wave astronomy, black-hole binaries, black-hole remnant kicks

Symbols and acronyms

Frequently used symbols:

h	gravitational-wave strain, $h = h_+ - ih_\times$
h_+, h_\times	plus and cross polarization of the gravitational wave
$h_{\ell,m}$ or $h_{\ell,m}^+$	symmetric gravitational-wave mode
$h_{\ell,m}^-$	antisymmetric gravitational-wave mode
m_1, m_2	individual masses of the black holes in the binary
M	total mass of the binary, $M = m_1 + m_2$
q	mass ratio of the binary, $q = m_1/m_2$
η	symmetric mass ratio, $\eta = m_1 m_2 / (m_1 + m_2)^2$
\vec{J}	total angular momentum of the binary
\vec{L}	orbital angular momentum of the binary
$\vec{\chi}_1, \vec{\chi}_2$	dimensionless spins of the black holes
χ_{eff}	effective spin parameter
χ_{p}	effective spin-precession parameter
a_1, a_2	spin magnitudes of the black holes
θ_1, θ_2	spin tilt angles of the black holes
φ_1, φ_2	spin azimuthal angles of the black holes
\vec{v}	kick velocity of the remnant black hole
a_f	spin magnitude of the remnant black hole
θ_{JN}	angle between the total angular momentum and the line-of-sight

Acronyms:

LIGO	Laser Interferometer Gravitational-Wave Observatory
LVK	LIGO-Virgo-KAGRA Collaborations
LISA	Laser Interferometer Space Antenna
PTA	Pulsar Timing Array
NR	numerical relativity
PN	post-Newtonian
EOB	effective-one-body
XPHM	PhenomXPHM
XO4a	PhenomXO4a
PSD	power spectral density
SNR	signal-to-noise ratio
PDF	probability density function
SMBH	supermassive black hole

Contents

1	Introduction	2
I	Introductory notions	8
2	Foundations of gravitational-wave astronomy	9
2.1	Gravitational waves	9
2.1.1	Einstein’s theory of General Relativity	9
2.1.2	Small spacetime perturbations	12
2.1.3	The source of gravitational waves	14
2.1.4	The effect of gravitational waves	17
2.2	Gravitational-wave observatories	19
2.2.1	Ground-based interferometric gravitational-wave detectors	20
2.2.2	Noise sources and detector sensitivity	22
2.3	Gravitational-wave data analysis	25
2.3.1	Searching for gravitational waves in noisy data	25
2.3.2	Inferring source properties	28
3	Binary black hole mergers	31
3.1	Techniques to predict the gravitational-wave signal	31
3.1.1	The Newtonian binary	31
3.1.2	The post-Newtonian formalism	33
3.1.3	Numerical relativity	35
3.2	Anatomy of the signal	36
3.2.1	Phases of the binary merger	36
3.2.2	Source parameters	37
3.2.3	Effect of masses on the signal	40
3.2.4	Effect of spins on the signal	41
3.3	Waveform models	42
3.3.1	Effective-one-body models	43
3.3.2	Phenomenological models	45
3.3.3	NR surrogate models	46
3.4	Waveform accuracy requirements for data analysis	46

4	Black-hole remnant kicks	49
4.1	The gravitational-wave recoil or kick	49
4.2	Astrophysical relevance	51
4.3	Extracting the kick from the signal	53
II	Original scientific results	56
5	Inconsistent black hole kick estimates from gravitational-wave models	57
6	Observability of spin precession in the presence of a black-hole remnant kick	90
7	Gravitational-wave kicks impact the spins of black holes from hierarchical mergers	115
8	Conclusions	130
8.1	Summary of results	130
8.2	Future work and outlook on key questions	134
	Acknowledgements	138
	Bibliography	142
	Curriculum Vitae	158

Chapter 1

Introduction

When two of the most compact objects in the universe collide, they generate tiny ripples in space and time, known as *gravitational waves*, that travel across the universe at the speed of light. As these waves pass through Earth, they can be detected by incredibly sensitive scientific instruments: kilometer-scale Michelson laser interferometers. Unlike optical telescopes, which observe light from specific regions of the sky, gravitational-wave detectors are sensitive to signals from nearly every direction, acting like incredibly sensitive microphones that "listen" to the vibrations of spacetime.

Ten years ago, gravitational waves were detected for the first time by the LIGO observatories [1, 2]. This historic discovery not only confirmed one of the most fascinating predictions of Einstein's theory of General Relativity, but also marked the first direct observation of black holes, specifically, *black holes in a binary*. Since then, gravitational-wave observatories, LIGO [3], Virgo [4] and KAGRA [5], have continued listening to the universe. Together, the LIGO-Virgo-KAGRA (LVK) Collaborations have confidently detected 86 binary black hole mergers to date [6–8].

Unlike electromagnetic waves, gravitational waves travel through the universe without being perturbed or dispersed by matter. As a result, the signals we receive are remarkably clean and encode valuable information about the astrophysical systems that generated them.

Identifying gravitational-wave signals within the noisy data of the detectors is a challenging task, unless we know what we search for. The most sensitive detection methods rely on theoretical predictions of the gravitational-wave signals we expect to observe. However, predicting the exact gravitational-wave signal from a binary black hole merger is difficult, as there is no exact analytic solution to the two-body problem in General Relativity. Despite this, significant progress in the gravitational-wave modelling community has resulted in the development of various semi-analytical waveform models that provide accurate representations of the astrophysical signals. One question that may arise is, *are waveform models accurate enough in all relevant regions of the parameter space? How do we assess waveform systematic errors?*

Once a signal has been detected, we can infer the properties of the binary using Bayesian inference. This statistical framework allows us to estimate the source parameters, such as the black hole masses and spins, but always with limited accuracy and precision. These limitations arise from various sources, including detector noise, imperfections in our wave-

form models, and degeneracies between different parameters. As a result, some parameters are better constrained than others. For example, the chirp mass, a specific combination of the black hole masses that strongly influences the frequency evolution of the signal, is typically well constrained. In contrast, other parameters, such as the individual black hole spins, are much harder to constrain [7, 9]. This difficulty stems mainly from parameter degeneracies. In particular, certain combinations of the spin parameters are difficult to distinguish from variations in the mass ratio, which reduces our ability to disentangle their individual contributions [10–12]. Accurately measuring the spin magnitudes and orientations of both black holes generally requires very high signal-to-noise ratios (SNRs), often on the order of 10^2 [9]. Given that most observed events have lower SNRs, these limitations lead to a natural question: *With the limited signal strength of current detections, how can we extract the most information out of these signals? Can we make more meaningful measurements of the source parameters?*

Precise measurements of source parameters are essential for several key areas of gravitational-wave astronomy: improving tests of General Relativity [13], refining measurements of the Hubble constant [14] and gaining a deeper understanding of the population properties of black holes [15]. These goals are central to advancing our knowledge of fundamental physics, cosmology, and astrophysics. This thesis focuses primarily on the third area, and in particular, on the questions: *How did the black holes we observe through gravitational waves form? Can we distinguish black holes from different formation channels?*

Current theoretical models suggest that black holes may form in a variety of astrophysical environments. Some are thought to originate through isolated binary evolution, where two massive stars evolve together, largely undisturbed by external interactions (see e.g. [16]). Others may form in dynamical environments, such as dense stellar clusters or active galactic nuclei, where interactions between multiple bodies can lead to the formation of binary black holes (see e.g. [17]). Each formation scenario is expected to produce systems with characteristic physical properties.

To infer the formation origin of black holes, it is first necessary to understand the expected distributions of the source properties, such as masses and spin, for each formation channel. These theoretical expectations can then be compared to the parameters inferred from gravitational-wave observations, allowing us to make statistical inferences about their likely origin. For this comparison to be meaningful, accurate knowledge of the expected characteristics from each channel is essential.

In particular, *spins* have long been considered a promising diagnostic for identifying black hole formation channels. Black holes formed through isolated evolution are expected to have small, aligned spins, as a result of the angular momentum transfer during stellar evolution (see e.g. [16, 18]). In contrast, black holes formed in dynamical environments are predicted to have random spin orientations, and larger spins magnitudes, typically of around 0.7 in dimensionless units [19, 20]. While spins are a key element for distinguishing different formation scenarios, as mentioned earlier, they are poorly constrained in most gravitational-wave observations. This limitation reinforces one of the central questions of this thesis, that is, whether more informative spin measurements can be achieved to better identify the origins of binary black holes. At the same time, our ability to extract reliable spin information is closely tied to the accuracy of the waveform

models used to analyse the signals (see e.g. [21]). Hence, the *three core challenges* outlined above—assessing waveform accuracy, improving parameter measurements, and understanding formation channels—are not independent, but rather deeply interconnected.

These questions represent some of the current challenges in gravitational-wave astronomy. In this thesis, we address them by focusing on a specific feature of binary black hole mergers that is intrinsically related to spin and waveform accuracy: *the remnant recoil*, or *kick velocity*. As the name suggests, the remnant black hole can acquire a non-zero velocity when gravitational waves emitted during the merger carry away linear momentum. To conserve the total linear momentum, the remnant recoils in the opposite direction of the linear momentum flux. The magnitude of this velocity depends on the mass ratio and spins of the binary, and can reach values of up to 5000 km s^{-1} for quasi-circular orbits [22–26]. In certain cases, such velocities may be sufficient to eject the remnant black hole from its host environment.

At first glance, the remnant kick may appear to be merely another parameter describing the merger remnant. However, in this thesis, we will demonstrate that it has profound astrophysical significance, with implications that span across multiple areas of gravitational-wave astronomy:

- The kick velocity is highly sensitive to the dynamics of the binary during the merger. Even small variations in the spin magnitudes or orientations at merger can lead to large differences in the resulting kick velocity (see e.g. Figure 4 in [23]). From the perspective of waveform modelling, the merger phase is the most challenging part of the gravitational-wave signal to model accurately, due to the strong, non-linear relativistic effects involved. This sensitivity of the kick to the merger dynamics is not only a curiosity, it also provides a useful opportunity to test models. Because the kick depends so strongly on the fine details of the merger, even small modelling inaccuracies in this brief but highly non-linear phase can result in significant errors in the predicted kick velocity. As a result, the kick can serve as a diagnostic tool for identifying and quantifying systematic errors in the modelling of the merger phase. In Chapter 5, we explore the use of the kick velocity to assess the accuracy of waveform models.
- As we mentioned earlier, determining the spins of black holes in gravitational-wave observations is inherently difficult. In General Relativity, binaries with spins misaligned with the orbital angular momentum of the system undergo spin precession [27], a phenomenon that introduces subtle modulations in the gravitational-wave signal. Detecting these modulations is challenging, as the imprint of precession is typically weak unless certain conditions are met: the binary has a significantly unequal mass ratio, it is inclined relative to the observer, or it has a high SNR.

However, the majority of gravitational-wave events observed to date have nearly equal masses and are oriented face-on or face-away relative to the detectors, which make precession especially difficult to identify. Consequently, without a sufficiently high SNR, extracting reliable information about spin misalignment is rarely possible. One event, however, stands out of the catalog: GW200129_065458 (hereafter GW200129). This signal provided the first clear evidence of spin precession, as

demonstrated by Hannam et al. [28]. Remarkably, GW200129 also shows evidence of a large kick velocity, as reported in [29].

This coincidence raised an intriguing question: could the presence of a large kick enhance our ability to extract spin information from gravitational-wave signals? In Chapter 6, we investigate whether events with significant kicks enable more informative measurements of source parameters, particularly the black hole spins.

- As gravitational-wave detectors continue to observe an increasing number of binary black hole mergers, we are gradually building a clearer picture of the black hole population. These observations are beginning to reveal the distributions of black hole masses, spins, and redshift, starting to offer clues about their astrophysical origins [15]. Among the various formation scenarios that have been proposed, this thesis focuses on a particular class of dynamical environments: dense star clusters. These clusters are particularly interesting because they are expected to host *hierarchical mergers*: a process in which the remnant of a binary black hole merger remains in the cluster, forms a new binary with another black hole, and merges again. This cycle can repeat multiple times, leading to the formation of black holes with distinctive properties.

However, for hierarchical mergers to occur, a key condition must be met: the kick velocity imparted to the remnant black hole must be smaller than the escape velocity of the host cluster. Only then can the remnant be *retained* in its environment and participate in future mergers. Previous studies have suggested that black holes formed through hierarchical mergers tend to acquire spin magnitudes around 0.7 [19, 20]. However, these studies did not account for the kick velocity on the retention of merger remnants. In Chapter 7, we address this gap by investigating how the inclusion of remnant kicks refines predictions for the spin distribution of black holes formed through hierarchical mergers. This analysis provides a more realistic understanding of the spins expected in hierarchical mergers.

The results of the three investigations presented in this thesis have been published in the following peer-reviewed articles:

- [30] Angela Borchers and Frank Ohme. Inconsistent black hole kick estimates from gravitational-wave models. *Class. Quant. Grav.*, 40, 095008 (2023)
- [31] Angela Borchers, Frank Ohme, Jannik Mielke, and Shrobona Ghosh. Observability of spin precession in the presence of a black-hole remnant kick. *Phys. Rev. D*, 110, 024037 (2024)
- [32] Angela Borchers, Claire S. Ye, and Maya Fishbach. Gravitational-wave kicks impact the spins of black holes from hierarchical mergers. *The Astrophysical Journal*, 987, 146 (2025)

For each of these studies, I conducted all parts of the research and was responsible for writing the full manuscript. In addition, I am a co-author in the following paper:

- [33] Jannik Mielke, Shrobana Ghosh, Angela Borchers and Frank Ohme. Revisiting the relationship of black-hole kicks and multipole asymmetries. *Phys. Rev. D*, 111, 064009 (2025)

My contribution to this work involved producing the values of the kick velocities and dominant mode asymmetries for the initial implementation of the waveform model PhenomXO4a [34]. As explained in [33], these results revealed an inconsistency with the estimates of the model NRSur7dq4 [35], which motivated a closer examination of PhenomXO4a. This led to the identification and correction of a parameter definition in its implementation, and the fix has now been incorporated into the updated model PhenomX-PNR [36].

This thesis is structured as follows: Chapter 2 provides a broad overview of the foundations of gravitational-wave astronomy. Chapter 3 then introduces the specific source studied in this thesis, binary black hole mergers, describing their dynamics, their characteristic gravitational-wave signal and the various waveform modelling approaches currently in use. Chapter 4 focuses on the key feature of binary black hole mergers that is the central theme of this thesis: the black-hole remnant kick. Following this background material, the three research papers are presented. The thesis concludes with a reflection of the most significant findings.

Part I

Introductory notions

Chapter 2

Foundations of gravitational-wave astronomy

2.1 Gravitational waves

2.1.1 Einstein's theory of General Relativity

A little over a century ago, Albert Einstein revolutionised our understanding of gravity. He redefined gravity not as an instantaneous force acting between massive bodies, but as a *geometrical effect* arising from the curvature of *spacetime* itself [37, 38]. The idea of gravity as geometry was inspired by a series of thought experiments, that culminated in the formulation of the *equivalence principle*. According to this principle, the laws of physics in a local, freely falling frame are indistinguishable from those in an inertial frame in the absence of gravity. However, two bodies that move parallel to each other in a freely falling frame might not remain parallel if they are subject to a non-uniform gravitational field. This deviation, along with the observation that all objects follow the same trajectory in a gravitational field regardless of their mass or composition, led Einstein to conclude that gravity is best described as the manifestation of curved spacetime.

In his theory of General Relativity, spacetime is described as a four-dimensional Riemannian manifold that is endowed with a *metric* tensor $g_{\alpha\beta}$, which defines distances and angles via the *line element* ds^2 :

$$ds^2 = g_{\alpha\beta} dx^\alpha dx^\beta. \quad (2.1)$$

In this expression we have introduced the Einstein summation convention, meaning repeated indices are implicitly summed over. The quantities dx^α and dx^β represent infinitesimal vector displacements along a curve. As shown in Eq. (2.1), the metric provides a notion of *length* or *distance* on a manifold. Additionally, the metric allows us to describe the intrinsic curvature of spacetime through the *Riemann curvature tensor*, defined as,

$$R^\alpha_{\beta\mu\nu} = \partial_\mu \Gamma^\alpha_{\beta\nu} - \partial_\nu \Gamma^\alpha_{\beta\mu} + \Gamma^\alpha_{\sigma\mu} \Gamma^\sigma_{\beta\nu} - \Gamma^\alpha_{\sigma\nu} \Gamma^\sigma_{\beta\mu}, \quad (2.2)$$

where the symbols $\Gamma^\alpha_{\beta\nu}$, known as *Christoffel symbols*, are functions of the metric and its first derivatives:

$$\Gamma^\alpha_{\beta\nu} = \frac{1}{2} g^{\alpha\beta} (\partial_\nu g_{\beta\mu} + \partial_\mu g_{\beta\nu} - \partial_\beta g_{\mu\nu}), \quad (2.3)$$

with partial derivatives defined as $\partial_\nu g_{\alpha\beta} = \partial g_{\alpha\beta} / \partial x^\nu$.

By analogy with Newtonian gravity, where the source of the gravitational field is the mass density ρ , and the gravitational potential Φ is related to it via

$$\Delta\Phi = 4\pi\rho, \quad (2.4)$$

in General Relativity, the source of spacetime curvature is the distribution of matter and energy. We note that in this equation and throughout this chapter, we adopt geometric units, in which the gravitational constant G and the speed of light c are set to one, $G = c = 1$, unless other units are explicitly stated. In General Relativity, the Newtonian concept of mass is generalised to the *energy-momentum tensor*, $T_{\alpha\beta}$, a covariant quantity that encodes the energy density, the momentum density, the energy flux, the momentum flux and the stress of matter. On the other hand, the left-hand side of Eq. (2.4), which involves second derivatives of the gravitational potential, is replaced by a geometric tensor that captures the curvature of spacetime through second derivatives of the metric,

$$G_{\alpha\beta} = R_{\alpha\beta} - \frac{1}{2} R g_{\alpha\beta}. \quad (2.5)$$

Here, $R_{\alpha\beta}$ is the *Ricci tensor*, obtained by contracting the Riemann curvature tensor as $R_{\alpha\beta} = R^\mu{}_{\alpha\mu\beta}$, and R is the *Ricci scalar*, defined by $R = g^{\alpha\beta} R_{\alpha\beta}$.

Guided by the equivalence principle, Einstein extended Newtonian gravity into a covariant framework, resulting in the *Einstein field equation*,

$$G_{\alpha\beta} = 8\pi T_{\alpha\beta}. \quad (2.6)$$

This equation describes how matter and energy determine the curvature of spacetime. It encodes a system of ten coupled, non-linear partial differential equations for the components of the metric $g_{\alpha\beta}$.

In the absence of matter and energy, the right-hand side of Eq. (2.6) vanishes, and the Einstein field equation reduces to $R_{\alpha\beta} = 0$. One solution to this vacuum equation is the metric from Minkowski space,

$$ds^2 = \eta_{\alpha\beta} dx^\alpha dx^\beta, \quad (2.7)$$

$$ds^2 = -dt^2 + dx^2 + dy^2 + dz^2, \quad (2.8)$$

which describes flat spacetime.

Another exact solution to Einstein's equation for vacuum is the Schwarzschild metric, which describes the geometry outside a static and spherically symmetric source [39]:

$$ds^2 = -\left(1 - \frac{2M}{R}\right) dt^2 + \left(1 - \frac{2M}{R}\right)^{-1} dr^2 + r^2(d\theta^2 + \sin^2\theta d\phi^2). \quad (2.9)$$

This solution was found by Karl Schwarzschild soon after Einstein published the theory of General Relativity and it is the only spherically symmetric vacuum solution that exists. The Schwarzschild metric describes the geometry of a black hole of mass M concentrated at $r = 0$.



Figure 2.1: Image from a physically realistic simulation of a rotating, axially symmetric black hole, produced by 59 Productions [45] in collaboration with the Tycho Brahe Planetarium in Copenhagen [46], as part of their "Cosmos" exhibition.

Although initially black holes were seen as a mathematical curiosity, in the 1960s Roger Penrose and Stephen Hawking demonstrated that they were a generic prediction of General Relativity [40–42]. Around that time, Roy Kerr found a more generic exact solution of a black hole, which described the geometry outside a rotating, axially symmetric black hole [43].

In the last decade, several observations have proved their existence, including the first detection of a black-hole binary through gravitational waves announced by the LIGO and Virgo Collaborations in 2016 [1] and the first image of a black hole published in 2017 by the Event Horizon Telescope Collaboration [44]. Figure 2.1 shows an image of a rotating black hole, simulated by 59 Productions [45] in collaboration with the Tycho Brahe Planetarium in Copenhagen [46], and illustrates the characteristic lensed accretion disk, and the lensed paths of light around the black hole happening as a consequence of the strong curvature of spacetime near the black hole.

In more general situations, however, solving Einstein's field equation analytically is highly non-trivial. One important example relevant to this thesis is the *two-body problem*. As we mentioned earlier, no exact analytical solution is known for the full evolution of the problem. To address this and similar challenges, *numerical relativity* (NR) techniques are commonly used to find approximate solutions to this equation (see e.g. [47]).

The theory of General Relativity not only redefined our understanding of gravity, it also led to groundbreaking predictions, including the existence of black holes and gravitational waves. In the following section, we explore how gravitational waves arise naturally as a prediction from this theory.

2.1.2 Small spacetime perturbations

We start by considering that spacetime is nearly flat and only includes a *small perturbation*. In this case, one can find a coordinate system in which the spacetime is described as

$$g_{\alpha\beta} = \eta_{\alpha\beta} + h_{\alpha\beta}, \quad (2.10)$$

where $h_{\alpha\beta}$ is the small perturbation and all of its components satisfy $|h_{\alpha\beta}| \ll 1$. Using this metric, we will first solve Einstein's field equation for vacuum, keeping only linear order terms. One can show that to first order, the Riemann tensor is given by

$$R^\alpha_{\beta\mu\nu} = \partial_\mu \Gamma^\alpha_{\beta\nu} - \partial_\nu \Gamma^\alpha_{\beta\mu}, \quad (2.11)$$

where the Christoffel symbol is expressed as,

$$\Gamma^\mu_{\alpha\beta} = \frac{1}{2} \eta^{\mu\nu} (\partial_\alpha h_{\nu\beta} + \partial_\beta h_{\nu\alpha} - \partial_\nu h_{\alpha\beta}). \quad (2.12)$$

Similarly, one can find that the Ricci tensor takes the form,

$$R_{\alpha\beta} = R^\mu_{\alpha\mu\beta}, \quad (2.13)$$

$$= \frac{1}{2} (-\square h_{\alpha\beta} + \partial_\alpha V_\beta + \partial_\beta V_\alpha), \quad (2.14)$$

where we have introduced the d'Alembertian operator,

$$\square = \partial^\alpha \partial_\alpha = \eta^{\alpha\beta} \partial_\alpha \partial_\beta, \quad (2.15)$$

and the new term is defined as [48],

$$V_\alpha = \partial_\beta h_\alpha^\beta - \frac{1}{2} \partial_\alpha h^\beta_\beta. \quad (2.16)$$

Given the long form of Eq. (2.13), we can try to find a *new coordinate system* for which the solution of the linearized Einstein field equation has a simpler form. We can do so by imposing some conditions on the new coordinates. When considering a coordinate transformation of the form,

$$x'^\alpha = x^\alpha + \xi^\alpha, \quad (2.17)$$

where the small transformation satisfies $|\partial_\beta \xi^\alpha| \ll 1$, the new coordinates leave $\eta_{\alpha\beta}$ unchanged, but change the functional form of $h_{\alpha\beta}$. In this new coordinate system, the metric is given by

$$g'_{\alpha\beta} \approx \eta_{\alpha\beta} + h_{\alpha\beta} - \partial_\alpha \xi_\beta - \partial_\beta \xi_\alpha, \quad (2.18)$$

meaning that the new metric perturbation is $h'_{\alpha\beta} = h_{\alpha\beta} - \partial_\alpha \xi_\beta - \partial_\beta \xi_\alpha$. We can now impose that these new coordinates satisfy $V'_\alpha = 0$. In analogy with electromagnetism, this condition is commonly denoted as the *Lorenz gauge*, but also as the *Einstein-de Donder gauge*. Hence, when transforming into a coordinate system via Eq. (2.17) that satisfies the

gauge condition, the Ricci tensor of Eq. (2.13) becomes

$$R'_{\alpha\beta} = -\frac{1}{2}\square h'_{\alpha\beta}. \quad (2.19)$$

Therefore, in linearized gravity, the Einstein field equation for vacuum, $R'_{\alpha\beta} = 0$, takes the following form:

$$\square h'_{\alpha\beta} = 0, \quad (2.20)$$

which is a wave equation for $h'_{\alpha\beta}$. From now on we will assume we are in the new coordinate system and we will drop the prime for convenience. Together with Eq. (2.20), the metric perturbation needs to satisfy the gauge condition,

$$\partial_\beta h_\alpha^\beta - \frac{1}{2}\partial_\alpha h_\beta^\beta = 0. \quad (2.21)$$

Solutions to the wave equation typically have the form

$$h_{\alpha\beta} = A_{\alpha\beta} e^{ik_\mu x^\mu}. \quad (2.22)$$

Even though this is a complex expression, we assume that $h_{\alpha\beta}$ has real valued components. When applying the field equation for vacuum to Eq. (2.22), we find that the wave vector satisfies $k_\alpha k^\alpha = 0$, which means that the wave vector is a null vector and therefore, these waves travel at the speed of light.

One can show that the Lorenz gauge allows further coordinate transformations, meaning that we have additional gauge freedom to simplify the metric perturbation further. Using this gauge freedom, it is common to set the following components to zero:

$$h_{0i} = 0, \quad (2.23)$$

$$h_\alpha^\alpha = 0. \quad (2.24)$$

The second expression together with the Lorenz gauge condition imply that

$$a_{00} = 0, \quad (2.25)$$

$$k^j a_{ij} = 0. \quad (2.26)$$

where, $i, j = 1, 2, 3$ are the spatial components. This last condition implies that these waves are transverse. In this *transverse-traceless gauge*, from the ten independent components of the perturbation $h_{\alpha\beta}$, we have fixed eight of them to zero. Hence, these waves have *two* independent components, which are called *polarizations* and are commonly referred to as h_+ and h_\times . In order to write an explicit form of the solution, we assume that these waves propagate along the z -axis. With all these choices, the metric perturbation takes the form:

$$h_{\alpha\beta} = \begin{pmatrix} 0 & 0 & 0 & 0 \\ 0 & h_+ & h_\times & 0 \\ 0 & h_\times & -h_+ & 0 \\ 0 & 0 & 0 & 0 \end{pmatrix} e^{i\omega(z-t)}, \quad (2.27)$$

and the wave vector becomes $k = (\omega, 0, 0, \omega)$.

In summary, after solving Einstein's field equation for vacuum, we have found that a small perturbation in spacetime evolves as waves that propagate at the speed of light. We call these waves *gravitational waves*. But, what causes these perturbations in the first place? In the following, we explore which processes generate gravitational waves.

2.1.3 The source of gravitational waves

To understand what causes these gravitational waves, we have to look at the full linearized Einstein field equation. We continue assuming flat spacetime with a small perturbation, as defined in Eq. (2.10), and the Lorenz gauge, Eq. (2.21). As we are considering a source, the right-hand side of the field equation is non-zero, and we cannot use the transverse-traceless gauge to set certain components to zero. Instead, we can use the *trace-reversed* perturbation tensor, defined by

$$\bar{h}_{\alpha\beta} = h_{\alpha\beta} - \frac{1}{2} \eta_{\alpha\beta} h_{\gamma}^{\gamma}. \quad (2.28)$$

With this gauge choice, we find that the field equation transforms into

$$\square \bar{h}_{\alpha\beta} = -16\pi T_{\alpha\beta}. \quad (2.29)$$

Similar to the theory of electromagnetism, this is a wave equation with a source term. The general solution to such an equation is given by the integral

$$\bar{h}_{\alpha\beta}(t, x^i) = 4 \int \frac{T_{\alpha\beta}(t - |x^i - x'^i|, x'^i)}{|x^i - x'^i|} d^3x', \quad (2.30)$$

which is evaluated at the retarded time $t' = t - |x^i - x'^i|$. One can also show that Eq. (2.30) satisfies the Lorenz gauge condition as a consequence of the conservation of energy and momentum locally. Assuming that we are far from the source, that is, $r \gg R_{\text{source}}$, where R_{source} quantifies the size of the source, and assuming that the source moves slowly, $\lambda \gg R_{\text{source}}$, where λ is the wavelength associated with the movement of the source, we can rewrite the solution to Einstein's equation as

$$\bar{h}_{\alpha\beta}(t, x^i) \approx \frac{4}{r} \int T_{\alpha\beta}(t - r, x'^i) d^3x'. \quad (2.31)$$

To simplify this expression, first, we can use the conservation of energy and momentum and express the energy-momentum tensor as,

$$T^{ij} = \frac{1}{2} \frac{\partial(x^i x^j)}{\partial x^k x^l} T^{kl}. \quad (2.32)$$

Second, we integrate by parts using Eq. (2.32), which leads to

$$h^{ij}(t, r) \approx \frac{2}{r} \frac{d^2}{dt^2} \int x'^i x'^j T^{00}(t - r, x'^i) d^3x'. \quad (2.33)$$

We can now use the definition of the quadrupole moment,

$$I^{ij} = \int x^i x^j \rho(t - r, x^i) d^3x, \quad (2.34)$$

to rewrite Eq. (2.33) as,

$$h^{ij}(t, r) \approx \frac{2}{r} \frac{d^2}{dt^2} I^{ij}(t - r). \quad (2.35)$$

This expression reveals that gravitational waves arise from systems with a time varying quadrupole moment. These are non-spherically symmetric systems with one or several bodies in accelerated motion. As indicated by the equation, the amplitude of these waves increases with the mass and acceleration of these bodies, with binary systems standing as one example. However, because the amplitude of gravitational waves is proportional to the factor $G/c^4 \approx 10^{-43} \text{ N}^{-1}$ in SI units, the amplitude of these waves is generally extremely tiny. Although any body with a time-changing quadrupole moment creates spacetime perturbations, in reality, only the most energetic processes involving strong gravitational fields generate gravitational waves that are large enough to be detectable by instruments on Earth.

We should note that strong sources, such as black-hole binaries, where the source moves at relativistic speeds and the gravitational fields become extremely large, do not satisfy the assumptions used to derive this expression. For relativistic speeds and strong gravitational fields, numerical simulations are required to determine the spacetime perturbations generated by these sources.

Gravitational-wave sources can be classified in different ways. Typically, they are divided into different categories based on the the characteristic form of the gravitational waves, or equivalently, the type of dynamical processes that generate these waves. Following this criteria it is common to classify these sources into four classes: (I) compact binaries, (II) continuous gravitational waves, (III) gravitational-wave bursts and (IV) stochastic background. Figure 2.2 illustrates these four sources and their predicted characteristic signals.

Given that *compact binaries* are the main focus of this thesis, we dedicate a full chapter, Chapter 3, to explain the most relevant concepts about these sources and the gravitational-wave signals they generate.

Continuous waves are those signals emitted over periods of time that are longer than the observation time and have a nearly constant frequency. Sources of continuous gravitational waves are primarily rotating, non-spherically symmetric bodies, where the rotational motion determines the frequencies of the gravitational waves. Rotating neutron stars with a small, non-axial distortion are one such example. Binary systems that are far from merging emit continuous gravitational waves as well. Despite significant efforts in searching for these signals, a detection of continuous gravitational-wave signals has so far remain elusive. See [49–51] on the most recent searches, leading to the most stringent upper limits of the gravitational-wave amplitude made so far. For prospects of detectability see e.g. [52, 53].

Gravitational-wave bursts are produced in violent events that are relatively short compared to the observation time. Sources of burst radiation include supernovae explosions,

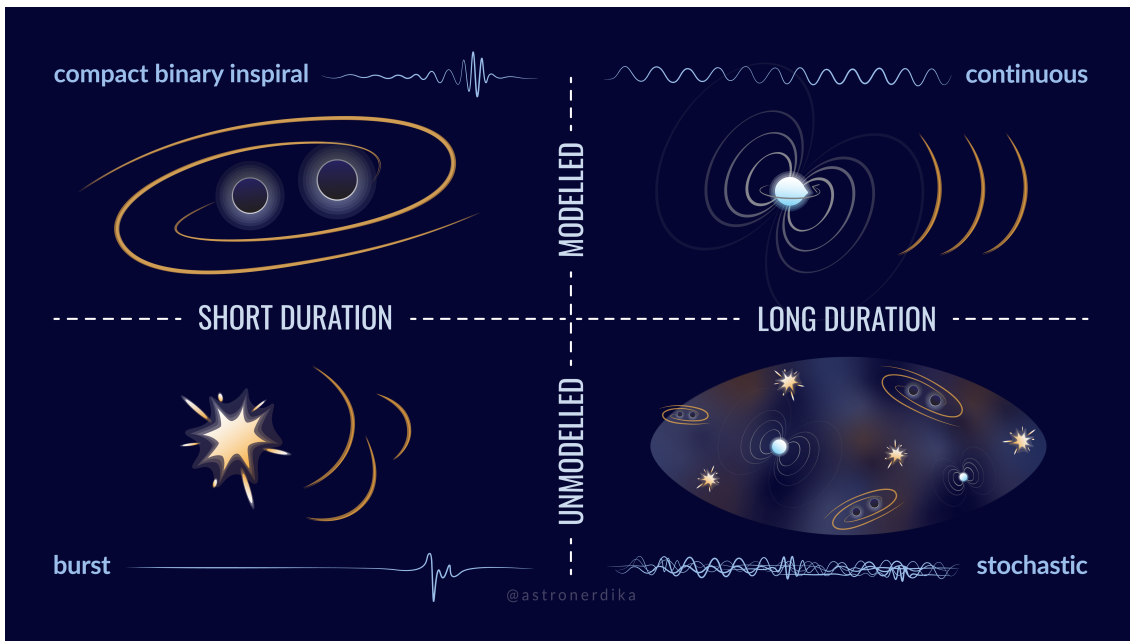


Figure 2.2: Illustration of the different sources of gravitational waves: compact binaries (top left), continuous gravitational waves (top right), bursts (bottom left) and stochastic gravitational waves (bottom right). The figure includes an illustration of the characteristic signal that is expected from each of these sources. Credit: Shanika Galaudage.

collisions of compact binaries formed by white dwarfs, neutron star or black holes, and other highly energetic events. See [54–56] for the latest searches of gravitational-wave bursts performed by the LVK Collaborations.

The *stochastic gravitational-wave background* is the superposition of signals from multiple sources in both time and frequency. When many sources contribute to the stochastic background, it may become impossible to resolve individual sources, and, as a consequence, the gravitational-wave background is regarded as radiation distributed over the sky. Several detection methods have been proposed in the last years [57,58]. Although no detection of a stochastic background has been made so far, there is evidence for a stochastic background from Pulsar Timing Array (PTA) observations [59–62]. See also [63] for the latest upper limits on the gravitational-wave strain of a persistent stochastic background.

Gravitational-wave sources can also be classified based on the frequencies of the waves they radiate. Table 2.1 provides a list of gravitational-wave sources classified according to the frequency band and the detectors operating in such frequencies.

As shown in Table 2.1, ground-based interferometers—LIGO [3], Virgo [4], KAGRA [5] and GEO [64]—operate in the *high-frequency band*, covering the range from 1 Hz to 10 kHz. The primary sources of gravitational waves in this frequency range include stellar-mass compact binaries, pulsars, supernovae and a stochastic background of binary mergers. At the time of writing, only black-hole, neutron-star and black-hole-neutron-star binaries have been detected. Since the first direct gravitational-wave detection in 2015 [1, 2, 65, 66], signals from binary mergers are now regularly observed, with detections happening on a weekly basis whenever ground-based detectors are operational [7].

This thesis focuses on gravitational-wave signals from binary black hole mergers. As these are currently detected exclusively by ground-based interferometers, we will dedicate a section (Section 2.2) to reviewing the basic principles and functioning of these instruments.

The *low frequency range* (1 mHz – 1 Hz) is expected to be populated by signals from supermassive black hole binaries with masses between $10^3 M_\odot$ and $10^9 M_\odot$, extreme mass ratio inspirals, white dwarf binaries and a stochastic background produced by the superposition of multiple signals from dwarf binaries. To access this window, two space-based detectors are planned to be operational in the 2030s: LISA [67] and DECIGO [68]. These detectors have a triangular shape with an opening angle of 60 degrees, with 2.5 Gm and 1 Mm arm lengths respectively.

PTAs are sensitive to gravitational waves in the *very low frequency range*, spanning from 1 nHz to 1 mHz. As their name suggests, PTAs rely on the precise timing of pulsars, which are rapidly rotating neutron stars that emit electromagnetic radiation along their magnetic poles. When a pulsar's beam points towards Earth, this radiation appears as regular pulses. By timing these pulses, astronomers can predict the arrival times of future pulses, enabling them to probe various aspects of fundamental physics, including tests of General Relativity.

In the case of PTAs, the goal is to detect gravitational waves by analysing pulsar timing variations. When a gravitational wave passes between a pulsar and Earth, it alters the pulsar's observed arrival times, causing pulses to arrive a little earlier or later than expected. General Relativity predicts that timing variations between different pulsars should exhibit a specific correlation pattern based on their angular separation in the sky. This pattern, known as the Hellings-Downs curve, serves as a key signature for detecting gravitational waves using PTAs [69]. Recent results from different PTA collaborations can be found in [59–62].

2.1.4 The effect of gravitational waves

Before going into the details of how gravitational-wave observatories work, we need to understand what is the effect of these waves on particles. First, we can examine whether the position of a particle located at coordinates x^α changes when a gravitational wave passes through it. In the transverse-traceless gauge, the particle is initially at rest, hence its four-velocity is

$$\frac{dx^\alpha}{d\tau} = U^\alpha = (1, 0, 0, 0), \quad (2.36)$$

where τ refers to the proper time. We now use the geodesic equation to find out what is the effect of gravitational waves on the particle:

$$\frac{d^2 x^\alpha}{d\tau^2} = -\Gamma^{\alpha}_{\mu\nu} \frac{dx^\mu}{d\tau} \frac{dx^\nu}{d\tau}, \quad (2.37)$$

$$= -\Gamma^{\alpha}_{tt}, \quad (2.38)$$

$$= -\frac{1}{2} g^{\alpha\beta} (2\partial_t g_{t\beta} - \partial_\beta g_{tt}), \quad (2.39)$$

$$= 0. \quad (2.40)$$

Band	Typical sources	Detectors
Very low frequency 1 nHz – 1 mHz	Supermassive black hole binaries ($M \sim 10^9 M_\odot$); Stochastic background (supermassive black hole binaries)	Pulsar Timing Arrays
Low frequency 1 mHz – 1 Hz	Supermassive black hole binaries ($M \sim 10^3 - 10^9 M_\odot$); Extreme mass ratio inspirals; White dwarf binaries; Stochastic background (dwarf binaries)	Space-based interferometers (LISA, DECIGO)
High frequency 1 Hz – 10 kHz	Black hole/neutron star binaries ($M \sim 1 - 10^3 M_\odot$); Pulsars; Supernovae; Stochastic background (binary mergers)	Ground-based interferometers (LIGO, Virgo, KAGRA, GEO)

Table 2.1: Main sources of gravitational waves classified in terms of the frequency band and the corresponding gravitational-wave detectors. The green color indicates which sources have already been detected by gravitational-wave observatories. Table adapted from the textbook "Gravitational-Wave Physics and Astronomy" by Creighton and Anderson [70].

Thus, the coordinate position of the particle is not affected by a gravitational wave passing through it. By looking at this result, one might think that the particle is not affected by gravitational waves at all. However, if instead, we consider two particles, we find that the proper distance between the two particles changes, even though their individual coordinate positions remain unchanged. To illustrate this, we consider two particles that are separated along the x -axis by a distance L . Assuming that a gravitational wave travels in the z -direction and has the form of Eq. (2.27), one can show that the proper distance between two particles changes according to

$$\frac{\delta L}{L} \approx \frac{h_+(t)}{2}. \quad (2.41)$$

Hence, the change of the proper distance is proportional to the amplitude of the gravitational wave. We can have a better picture of the effect of gravitational waves by considering multiple particles arranged in a circle. In a local inertial frame, the geodesic equation takes the form,

$$\frac{d^2 \xi^\alpha}{d\tau^2} = -R_{\tau\mu\tau}^\alpha \xi^\mu. \quad (2.42)$$

For a wave travelling in the z -direction, the components of the Riemann tensor are given by,

$$R_{\tau x \tau}^x = -\frac{1}{2} \frac{\partial^2 h_+}{\partial \tau^2}, \quad R_{\tau x \tau}^y = -\frac{1}{2} \frac{\partial^2 h_\times}{\partial \tau^2}, \quad R_{\tau y \tau}^y = \frac{1}{2} \frac{\partial^2 h_+}{\partial \tau^2}. \quad (2.43)$$

Therefore, for particles that are separated along the x -direction, $\xi^\alpha = (0, \xi, 0, 0)$, the geodesic equation is

$$\frac{d^2 \xi^x}{d\tau^2} = \frac{\xi}{2} \frac{\partial^2 h_+}{\partial \tau^2}, \quad \frac{d^2 \xi^y}{d\tau^2} = \frac{\xi}{2} \frac{\partial^2 h_\times}{\partial \tau^2}, \quad (2.44)$$

while for particles separated in the y -direction, $\xi^\alpha = (0, 0, \xi, 0)$, we find

$$\frac{d^2 \xi^x}{d\tau^2} = \frac{\xi}{2} \frac{\partial^2 h_\times}{\partial \tau^2}, \quad \frac{d^2 \xi^y}{d\tau^2} = -\frac{\xi}{2} \frac{\partial^2 h_+}{\partial \tau^2}. \quad (2.45)$$

Here, the separation vector quantifies the proper distance between the two particles. These expressions show that both polarizations stretch and squeeze the space between particles, and have the same effect but are rotated by 45° . Figure 2.3 illustrates these effects on a ring of particles. As shown by the figure, the subscripts of the polarizations, h_+ and h_\times , are motivated by the effect they induce on test particles.

2.2 Gravitational-wave observatories

The first attempts to detect gravitational waves began in the 1960s with Joseph Weber's development of resonant mass, or bar detectors. These detectors consisted of cylindrical bars tuned to resonate at frequencies close to those expected from gravitational-wave signals. The idea was that when a gravitational wave passed through Earth, it would cause these bars to oscillate, amplifying the effect of gravitational waves. However, these detectors were sensitive only to a narrow frequency band of around 1 kHz.

After several generations of resonant-mass detectors, a new type of instruments emerged

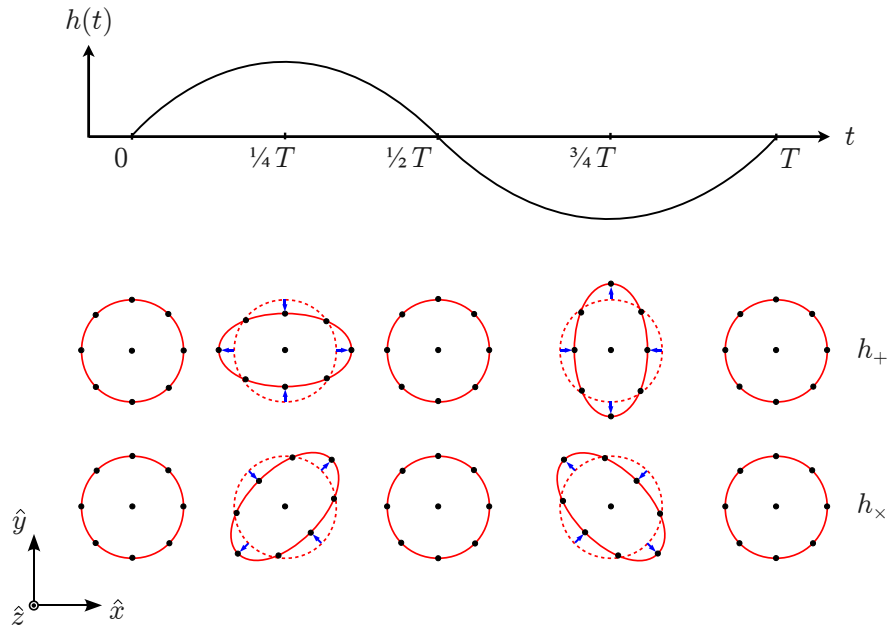


Figure 2.3: Effect of gravitational-wave polarizations of the a ring of test particles. Figure from [71].

in the late 1990s: kilometer-scale ground-based detectors that used laser interferometry. These interferometers measured tiny changes in the length of optical paths between test masses placed at the ends of the detector's arms. Unlike resonant-bar detectors, interferometric detectors covered a broader frequency band, from about 10 Hz to 1 kHz. Thanks to continuous improvements in sensitivity, these interferometers made the first direct detection of a gravitational-wave signal in 2015. Since then, they have been the only instruments that have detected astrophysical signals. In the following subsection, we will explain in more detail how these detectors work, their sensitivity, and the sources of noise that affect them.

2.2.1 Ground-based interferometric gravitational-wave detectors

Ground-based interferometric gravitational-wave detectors are designed to measure the tiny changes in distance between test masses caused by passing gravitational waves. These detectors are Michelson interferometers with two arms, each several kilometers long and arranged at a 90° angle. At the ends of these arms, there are test masses—highly reflective mirrors—suspended by multistage pendulums and placed within ultrahigh-vacuum systems. As illustrated in Figure 2.4, a laser beam entering the interferometer is split by a beam splitter into two beams, each traveling through one arm. The mirrors in each arm form a Fabry-Pérot cavity—a resonant optical cavity—that causes the laser light to be reflected multiple times between the mirrors, effectively increasing the distance the light travels and amplifying the laser power in the arms [3]. In the case of the LIGO detectors, the light makes roughly 300 roundtrips, extending the effective path length from 4 km to about 1200 km [72]. This amplification not only increases the effective arm length

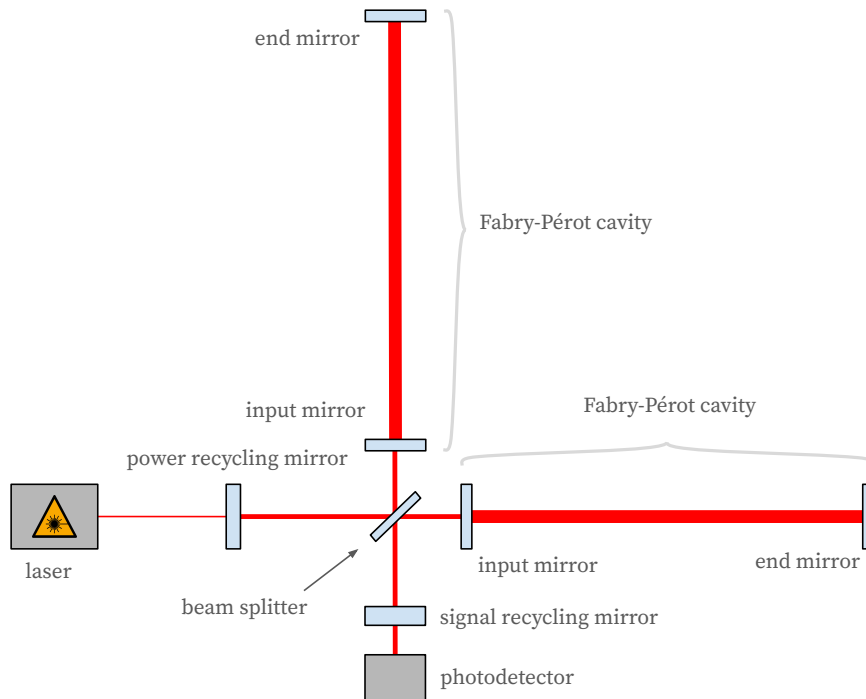


Figure 2.4: Illustration of the key optical components of an L-shaped gravitational-wave laser interferometer, such as the LIGO, Virgo, GEO or KAGRA detectors.

but also enhances the detector's sensitivity at lower frequencies.

The laser power is further amplified by a power recycling mirror that forms an additional resonant cavity with the interferometer arms. As a result, the initial laser power entering the interferometer is around 40 W, and is increased to approximately 750 kW inside the arms [3]. Furthermore, a signal recycling mirror improves the detector's response to gravitational-wave signals [3].

When a gravitational wave passes through the interferometer, it causes tiny changes in the optical length of the arms. For a wave traveling perpendicular to the detector plane, the relative change in arm length follows approximately $\delta L/L \approx h(t)/2$ (Eq. 2.41). Because a gravitational wave stretches space along one direction while squeezing it in the perpendicular direction, the laser beam will typically travel a slightly longer distance in one arm and a slightly shorter distance in the other. However, depending on the source location, both arms can sometimes be stretched or squeezed in the same manner, making it impossible to detect such signals.

These length changes induce a *phase shift* in the laser light traveling through the arms, given by $\delta\phi \approx h(t) k \delta L(t)$ at leading order, where k is the laser's wave vector. Since the phase change scales with the arm length, kilometer-scale arms are essential. For example, with a laser wavelength of 1064 nm and a gravitational-wave amplitude of $h = 10^{-23}$, the

expected phase shift is roughly $\delta\phi = 6 \times 10^{-14}$ per kilometer of arm length. This shift is far smaller than the intrinsic phase noise of even the most stable lasers in the world.

When the laser beams of the two arms are recombined at the beam splitter, the tiny phase differences caused by gravitational waves are converted into measurable amplitude modulations, which are detected as variations in light power by photodetectors. These phase shifts are also amplified by the Fabry-Pérot cavities in the arms, leading to stronger amplitude modulations and enhancing the sensitivity of the detector.

The interferometer is operated near the *dark fringe*, a condition where almost no light reaches the photodetector [3]. At this operating point, the interference between the two arms nearly cancels out the main laser field at the output, significantly reducing laser power noise and thereby improving the ability to detect weak signals.

The amplitude modulations induced by gravitational waves can be described in terms of *sidebands* using a phasor or complex vector representation. When the interferometer is tuned to the dark fringe, these gravitational-wave-induced sidebands are the only components of the optical field that appear at the photodetector. Their amplitude is directly proportional to the gravitational-wave strain, the length of the interferometer arms, and the amplitude of the electric field of the laser. Therefore, increasing the laser's field amplitude enhances the strength of the gravitational-wave sidebands, making the signal more detectable. This is why power enhancement techniques such as Fabry-Pérot cavities and power recycling are employed: they amplify the circulating laser power and, in turn, increase the amplitude of a gravitational wave measured at the photodetector.

2.2.2 Noise sources and detector sensitivity

Gravitational-wave detectors are limited in sensitivity by a variety of environmental and instrumental noise sources. These sources produce sidebands that can interfere with or even mask the gravitational-wave sidebands at the photodetector. To successfully detect astrophysical signals, the noise must remain below the amplitude of the gravitational-wave signal across the relevant frequency band.

As shown in Figure 2.5, the most significant noise sources are as follows [3]:

- **Quantum Vacuum Noise:** This fundamental noise originates from quantum fluctuations and has two main components. At high frequencies, detector sensitivity is limited by **photon shot noise**, caused by statistical fluctuations in the number of photons arriving to the photodetectors. These fluctuations manifest as power noise in the readout. Increasing the laser power can help reduce shot noise. At low frequencies, the sensitivity is limited by **radiation pressure noise**, which results from fluctuations in the number of photons in the laser beam exerting random forces on the suspended mirrors. This creates phase noise due to the mirrors' back-action. The impact of radiation pressure noise can be modulated by the frequency dependent mechanical response of the suspension system. To mitigate these quantum noise sources, quantum squeezing techniques are commonly used [74].
- **Seismic Noise:** Ground vibrations from natural and human activity, such as earthquakes, wind and ocean waves, can couple into the detector. To mitigate seismic noise, detectors are constructed in geologically quiet locations or underground and

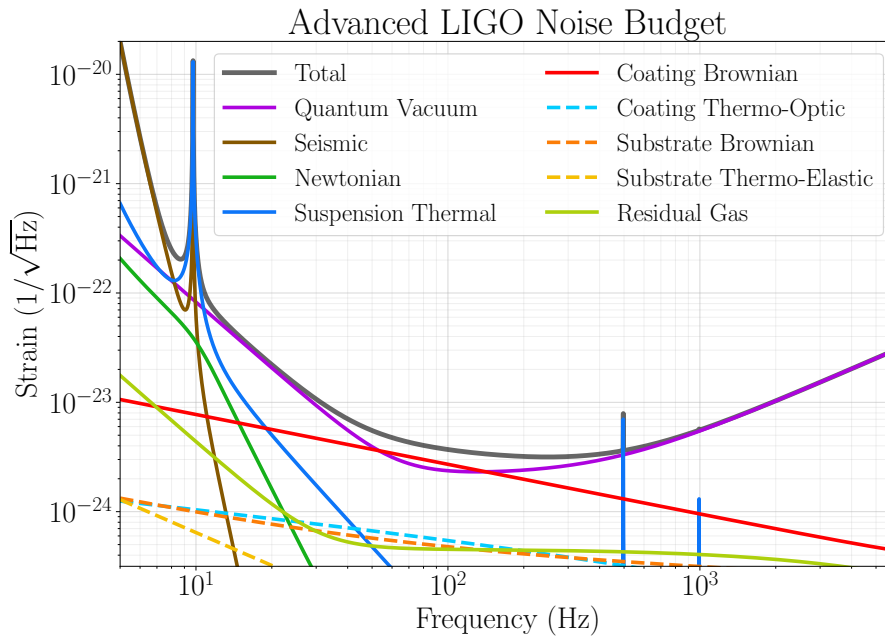


Figure 2.5: Main noise sources as a function of frequency for Advanced LIGO. The curve of each noise is computed by calculating a transfer function of noise sources. This figure was created using the `pygwinc` noise modelling package [73].

are equipped with advanced seismic isolation systems. Additionally, the mirrors are suspended in multi-stage pendulums (typically triple pendulums) to further decouple them from ground motion [3].

- **Newtonian Noise** (Gravity Gradient Noise): Seismic waves also create fluctuating mass densities in the Earth, which in turn cause time-varying gravitational fields. These low-frequency gravity perturbations cannot be shielded and affect the mirrors directly. One way to reduce their impact is to monitor and subtract the effects of these gravitational field changes from the data. Instead, future space-based detectors like LISA and DECIGO avoid both seismic and Newtonian noise by operating in a microgravity environment [67, 68].
- **Suspension Thermal Noise**: The test masses are suspended by fused silica fibres, which exhibit thermal fluctuations due to internal vibrations. These fibres have a fundamental vibrational mode at around 510 Hz, commonly known as **violin mode**, because the fibres resonate in a similar way to violin strings under tension. Additionally, they can exhibit a **vertical stretching mode**, with a resonance frequency around 9 Hz. This mode causes a sharp peak in the detector sensitivity curve. For frequencies larger than the resonance frequencies, the mirrors effectively behave as free masses, less influenced by the suspension system.
- **Coating Brownian Noise**: Thermal noise also arises from microscopic mechanical losses in the thin reflective coatings on the surfaces of the test masses. These coatings

are not perfectly elastic, and part of the mechanical energy is converted into heat, producing tiny vibrations. To reduce this noise, KAGRA operates at cryogenic temperatures, which lower the amplitude of thermal fluctuations [5]. Third-generation ground-based detectors, Cosmic Explorer and Einstein Telescope, also plan to operate at these temperatures [75,76].

The sum of all noise sources is often referred to as $S_n(f)$. As illustrated by Figure 2.5, for most frequencies, the sensitivity of gravitational-wave detectors is limited by quantum noise, which competes with the signal sidebands at the photodetector. As laser power increases, relative shot noise—which dominates at high frequencies—decreases, but radiation pressure noise—which dominates at low frequencies—increases. This trade-off defines the *standard quantum limit* of interferometry: the point where the contributions from shot noise and radiation pressure noise are equal [77]. To surpass this limit and improve sensitivity, quantum squeezing techniques are employed.

Quantum noise in laser light manifests as uncertainties in both amplitude and phase quadratures. These uncertainties are often visualized using a quadrature diagram, where the coherent amplitude is represented by an arrow, and the associated quantum uncertainties appear as a circular region centered at the tip of that arrow (see the left panel of Figure 2.6). This same representation also applies to the vacuum state, where no photons are present. In both vacuum and coherent states, the quantum noise is symmetrically distributed between the amplitude and phase quadratures.

The *Heisenberg Uncertainty Principle* constrains the product of these uncertainties: the standard deviations of two non-commuting quadratures cannot be simultaneously reduced below a certain limit. However, this principle does not require the uncertainties to be equal. The noise distribution can be unevenly redistributed, forming an ellipse instead of a circle in the quadrature diagram (see Figure 2.6). These quantum states are known as *squeezed states*, and they allow one quadrature’s uncertainty to be reduced below the vacuum noise level, at the expense of increasing uncertainty in the other [78].

By choosing which quadrature is squeezed, different parts of the quantum noise spectrum can be suppressed. To reduce shot noise at high frequencies, phase-quadrature-squeezed light is injected into the interferometer. Conversely, to suppress radiation pressure noise at low frequencies, amplitude-quadrature-squeezed light is needed. Recent advancements in frequency-dependent squeezing have enabled simultaneous reduction of both noise components [79,80]. This groundbreaking technique is now being used in both LIGO and Virgo for their fourth-observing run (O4) [81,82].

As previously mentioned, we now have a global network of ground-based gravitational-wave observatories formed by the two LIGO detectors in the US, VIRGO in Italy, GEO600 in Germany and KAGRA in Japan. Having this network is essential for distinguishing astrophysical signals from environmental noise. Occasionally, noise alone can mimic the signature of a gravitational-wave event. However, if it were a true gravitational-wave signal, it would be observed by all detectors in the network, albeit with slight differences in arrival time due to the finite speed at which gravitational waves travel between locations.

It is extremely unlikely for random noise to produce a noise pattern similar to an astrophysical signal in multiple detectors at the same time, especially if the detectors are located in different parts of the planet. Hence, by comparing data from different detec-

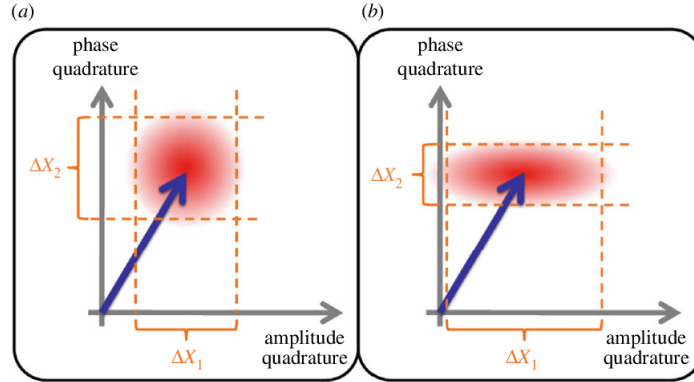


Figure 2.6: Amplitude and phase quadratures illustrating the uncertainty in these two quantities for (a) a coherent state and (b) a squeezed state. Figure from [74].

tors and checking for coincident signals within a time difference of a few milliseconds, we can reliably identify true gravitational-wave signals. For example, the two LIGO interferometers, separated by approximately 3000 km, can measure a maximum arrival time difference of about 10 milliseconds.

Furthermore, the time delays between detectors are key to localise the source of the gravitational-wave signal in the sky. The more detectors involved, and the greater the distances between them, the more precisely we can localise the source. This was crucial in the detection of the binary neutron star merger GW170817. The participation of VIRGO alongside the two LIGO detectors significantly improved the source localization, enabling astronomers to observe the event across multiple wavelengths of the electromagnetic spectrum [83].

2.3 Gravitational-wave data analysis

2.3.1 Searching for gravitational waves in noisy data

We now wish to find gravitational-wave signals in a noisy data stream. When both the exact form of the signal and the statistical properties of the noise are known, it is possible to construct an *optimal detection statistic* that quantifies the probability that a signal is present in the data. We will explain the basic principles following the derivation presented in [70].

Let us consider a data stream $d(t)$ recorded by an interferometer. This stream includes noise $n(t)$, and it may include a gravitational-wave signal $h(t)$ of known form. We aim to test the following two hypotheses:

$$\text{Null Hypothesis } \mathcal{H}_0 : d(t) = n(t) \quad (2.46)$$

$$\text{Alternative Hypothesis } \mathcal{H}_1 : d(t) = n(t) + h(t) \quad (2.47)$$

To assess which hypothesis is more likely, we consider the *odds ratio*,

$$\mathcal{O}(\mathcal{H}_1|d) = \frac{\mathcal{P}(\mathcal{H}_1|d)}{\mathcal{P}(\mathcal{H}_0|d)}, \quad (2.48)$$

which compares the probabilities of the two hypotheses given the data $d(t)$. This ratio can be calculated using *Bayes' theorem* [84, 85], which determines the probability of a hypothesis \mathcal{B} given \mathcal{A} through the following expression,

$$\mathcal{P}(\mathcal{B}|\mathcal{A}) = \frac{\mathcal{P}(\mathcal{B})\mathcal{P}(\mathcal{A}|\mathcal{B})}{\mathcal{P}(\mathcal{A})}, \quad (2.49)$$

where:

- $\mathcal{P}(\mathcal{B})$ is the *prior* probability of \mathcal{B} being true,
- $\mathcal{P}(\mathcal{A}|\mathcal{B})$ is the *likelihood*, i.e. the probability of \mathcal{A} being true given \mathcal{B} ,
- $\mathcal{P}(\mathcal{A})$ is the *evidence* and is the marginal probability of \mathcal{A} .

The quantity $\mathcal{P}(\mathcal{B}|\mathcal{A})$ is called the *posterior probability*, and is the probability that \mathcal{B} is true given \mathcal{A} . We can rewrite Bayes' theorem in a more convenient form using the completeness relationship, $\mathcal{P}(\mathcal{A}) = \mathcal{P}(\mathcal{A}|\mathcal{B})\mathcal{P}(\mathcal{B}) + \mathcal{P}(\mathcal{A}|\bar{\mathcal{B}})\mathcal{P}(\bar{\mathcal{B}})$, where $\bar{\mathcal{B}}$ denotes the negation of \mathcal{B} , and $\mathcal{P}(\bar{\mathcal{B}}) = 1 - \mathcal{P}(\mathcal{B})$. Substituting this into Equation (2.49) yields

$$\mathcal{P}(\mathcal{B}|\mathcal{A}) = \frac{\mathcal{P}(\mathcal{B})\mathcal{P}(\mathcal{A}|\mathcal{B})}{\mathcal{P}(\mathcal{A}|\mathcal{B})\mathcal{P}(\mathcal{B}) + \mathcal{P}(\mathcal{A}|\bar{\mathcal{B}})\mathcal{P}(\bar{\mathcal{B}})}, \quad (2.50)$$

$$= \frac{\Lambda(\mathcal{B}|\mathcal{A})}{\Lambda(\mathcal{B}|\mathcal{A}) + \mathcal{P}(\bar{\mathcal{B}})/\mathcal{P}(\mathcal{B})}, \quad (2.51)$$

where $\Lambda(\mathcal{B}|\mathcal{A})$ is the *likelihood ratio*,

$$\Lambda(\mathcal{B}|\mathcal{A}) = \frac{\mathcal{P}(\mathcal{A}|\mathcal{B})}{\mathcal{P}(\mathcal{A}|\bar{\mathcal{B}})}. \quad (2.52)$$

Finally, the odds ratio can be rewritten as a product of the prior odds and the likelihood ratio,

$$\mathcal{O}(\mathcal{B}|\mathcal{A}) = \mathcal{O}(\mathcal{B})\Lambda(\mathcal{B}|\mathcal{A}), \quad (2.53)$$

where $\mathcal{O}(\mathcal{B}) = \mathcal{P}(\mathcal{B})/\mathcal{P}(\bar{\mathcal{B}})$ is the prior odds.

To distinguish between the two hypotheses, \mathcal{H}_0 and \mathcal{H}_1 , we need to compute the odds ratio for the alternative hypothesis given the data: $\mathcal{O}(\mathcal{H}_1|d)$. As shown in Equation (2.53), the odds ratio is proportional to the likelihood ratio, defined as

$$\Lambda(\mathcal{H}_1|d) = \frac{\mathcal{P}(d|\mathcal{H}_1)}{\mathcal{P}(d|\mathcal{H}_0)}. \quad (2.54)$$

Switching from probabilities to probability densities, we can write

$$\Lambda(\mathcal{H}_1|d) = \frac{p(d|\mathcal{H}_1)}{p(d|\mathcal{H}_0)}. \quad (2.55)$$

Assuming the noise is Gaussian, the probability density of the null hypothesis \mathcal{H}_0 can be written as

$$p(d|\mathcal{H}_0) = p_n[d(t)] \propto e^{-(d|d)/2}, \quad (2.56)$$

where we have used $n(t) = d(t)$. Here, $\langle a|b \rangle$ denotes a *noise-weighted inner product* in the frequency domain, defined as

$$\langle a|b \rangle = 4\Re \int_0^\infty \frac{\tilde{a}(f) \tilde{b}^*(f)}{S_n(f)} df, \quad (2.57)$$

with $\tilde{a}(f)$ and $\tilde{b}(f)$ denoting the Fourier transforms of $a(t)$ and $b(t)$, respectively, and $S_n(f)$ the one-sided power spectral density of the noise.

For the alternative hypothesis \mathcal{H}_1 , the data consists of noise plus a known signal, so the probability density becomes

$$p(d|\mathcal{H}_1) = p_n[d(t) - h(t)] \propto e^{-\langle d-h|d-h \rangle/2}. \quad (2.58)$$

Hence, the likelihood ratio simplifies to

$$\Lambda(\mathcal{H}_1|d) = \frac{e^{-\langle d-h|d-h \rangle/2}}{e^{-\langle d|d \rangle/2}}, \quad (2.59)$$

$$= e^{\langle d|h \rangle} e^{-\langle h|h \rangle/2}. \quad (2.60)$$

The only term in this expression that depends on the observed data is the inner product between the data and the signal, which is given explicitly by

$$\langle d|h \rangle = 4\Re \int_0^\infty \frac{\tilde{d}(f) \tilde{h}^*(f)}{S_n(f)} df. \quad (2.61)$$

Since the likelihood ratio is a monotonically increasing function of the inner product $\langle d|h \rangle$, any threshold imposed on the odds ratio for accepting the alternative hypothesis \mathcal{H}_1 can equivalently be expressed as a threshold on this inner product. Therefore, the optimal detection statistic is $\langle d|h \rangle$, known as the *matched filter* [86]. This statistic quantifies the correlation between the data and the expected gravitational-wave signal.

In practice, the data is compared to a catalog of theoretically predicted signals. As we will explain in Chapter 3, in the case of binary black hole mergers, we do not have exact predictions of the signals. Instead, we rely on approximate waveform models with limited accuracy. These predicted waveforms are defined by a variety of binary parameters, such as component masses and spins, and form a *template bank*, a discrete set of waveforms that samples the relevant parameter space. Each waveform in the bank is called a *template* and we will refer to it by h_m to indicate that it represents a modelled signal.

Search algorithms correlate the data with each template of the template bank. According to Equation (2.61), the maximum likelihood ratio is maximised when the template closely matches the actual signal present in the data.

As we just mentioned, gravitational-wave signals from binary black holes are characterised by a set of parameters θ_i , $i = 1, \dots, N$. Since these parameters are generally unknown, the likelihood must be marginalised over these. The likelihood ratio for a particular signal with parameters $\vec{\theta}$ is given by

$$\Lambda(\mathcal{H}_{\vec{\theta}}|d) = \frac{p(d|\mathcal{H}_{\vec{\theta}})}{p(d|\mathcal{H}_0)}. \quad (2.62)$$

The *marginalised likelihood ratio* is then

$$\Lambda(\mathcal{H}_1|d) = \frac{\int p(d|\mathcal{H}_{\vec{\theta}}) p(\mathcal{H}_{\vec{\theta}}) d\vec{\theta}}{p(d|\mathcal{H}_0)} \quad (2.63)$$

$$= \int \Lambda(\mathcal{H}_{\vec{\theta}}|d) p(\mathcal{H}_{\vec{\theta}}) d\vec{\theta}, \quad (2.64)$$

where $p(\mathcal{H}_{\vec{\theta}})$ is a prior probability distribution of the parameters, representing our expectation for which parameter values are more likely.

Assuming Gaussian noise, the logarithm of the likelihood ratio for a particular template becomes

$$\ln \Lambda(\mathcal{H}_{\vec{\theta}}|d) = \langle d|h_m(\vec{\theta}) \rangle - \frac{1}{2} \langle h_m(\vec{\theta})|h_m(\vec{\theta}) \rangle, \quad (2.65)$$

which can also be rewritten as

$$\ln \Lambda(\mathcal{H}_{\vec{\theta}}|d) = \langle h_0|h_m(\vec{\theta}) \rangle - \frac{1}{2} \langle h_m(\vec{\theta})|h_m(\vec{\theta}) \rangle, \quad (2.66)$$

where h_0 is the astrophysical signal and $h_m(\vec{\theta})$ is the template used in the matched filtering.

According to the Neyman-Pearson criterion, a detection can only be declared when the likelihood ratio Λ exceeds a predefined threshold. This threshold is typically chosen based on the *false alarm probability*, which quantifies the probability that a detection is declared when a signal is not present in the data. Alternatively, the threshold can be expressed in terms of the *SNR*, defined as the inner product between the astrophysical signal h_0 and a template $h_m(\vec{\theta})$, normalised by the norm of the template:

$$\rho(\vec{\theta}) = \frac{\langle h_0|h_m(\vec{\theta}) \rangle}{\|h_m(\vec{\theta})\|}, \quad (2.67)$$

where the norm is given by $\|h_m(\vec{\theta})\| = \sqrt{\langle h_m(\vec{\theta})|h_m(\vec{\theta}) \rangle}$. The *maximum likelihood detection statistic* is then defined as the maximum SNR over the template parameter space: $\max_{\vec{\theta}} \rho(\vec{\theta})$.

A commonly cited quantity is the *optimal SNR*, which corresponds to the case where the template exactly matches the astrophysical signal, i.e. $h_m(\vec{\theta}) = h_0$. In this case, the SNR reduces to

$$\rho_{\text{opt}} = \|h_0\|. \quad (2.68)$$

In practice, a detection threshold of $\rho \approx 8$ is typically used to control the false alarm rate while maintaining a high detection efficiency (see, e.g. [1, 87]).

2.3.2 Inferring source properties

Once a signal has been detected, the next goal is to extract as much information as possible about its source. In the case of binary black hole mergers, the signal is described by a set of parameters characterising the system. Bayesian inference offers a powerful and well-established framework for performing this task (see e.g. [2, 88]).

Within this framework, our goal is to compute the marginalised posterior probability density functions (PDFs) of the source parameters, $p(\theta|d)$. As introduced in the previous subsection, the posterior probability of a signal with parameters $\vec{\theta}$ is given by Bayes' theorem (Equation (2.49)), which in this context takes the form,

$$p(\vec{\theta}|d, h_m) = \frac{\pi(\vec{\theta}|h_m) \mathcal{L}(d|\vec{\theta}, h_m)}{p(d|h_m)}. \quad (2.69)$$

This equation shows that the posterior is proportional to the product of the *prior* $\pi(\vec{\theta}|h_m)$, which encodes our assumptions about the parameters before observing the data and assuming a signal model h_m , and the *likelihood* of the data given the parameters and a signal model $\mathcal{L}(d|\vec{\theta}, h_m)$, which is proportional to

$$\mathcal{L}(d|\vec{\theta}, h_m) \propto \exp[-\langle d - h_m | d - h_m \rangle / 2]. \quad (2.70)$$

The denominator $p(d|h_m)$, known as the *evidence*, serves as a normalisation constant. It is computed by marginalising the likelihood over all parameters of the model h_m , weighted by the prior,

$$p(d|h_m) = \int d\theta_1 \dots d\theta_N \mathcal{L}(d|\vec{\theta}, h_m) p(\vec{\theta}|h_m). \quad (2.71)$$

To obtain the posterior probability of a specific parameter we marginalise the full posterior over the remaining parameters:

$$p(\theta_1|d, h_m) = \int d\theta_2 \dots d\theta_N p(\vec{\theta}|d, h_m). \quad (2.72)$$

Obtaining these marginalised distributions requires evaluating multidimensional integrals. In the case of binary black hole mergers, the posterior distribution spans fifteen dimensions. Due to this high dimensionality and the complexity of the signal models, computing posterior probabilities becomes a significant computational challenge. One effective way to solve this problem is to use *stochastic sampling algorithms*. These methods generate a set of samples from the posterior distribution such that the number of samples within an interval $(\theta, \theta + \Delta\theta)$ is proportional to the posterior probability density $p(\theta)$ [88]. Two of the stochastic sampling methods most widely used in the parameters estimation of binary black hole signals are:

- **Markov chain Monte Carlo (MCMC)** [89, 90]: MCMC methods are designed to stochastically navigate through the parameter space, by proposing new points $\vec{\theta}'$ based on the current position $\vec{\theta}$ using a transition function. Each proposed point is accepted or rejected based on a criterion involving the posterior probability. Through many iterations, this process produces a sequence of accepted samples that statistically represent the target posterior distribution.
- **Nested sampling** [91]: This technique is designed to compute the Bayesian evidence while simultaneously generating posterior samples. It begins by populating the parameter space with a set of points called "live points", which are drawn from the prior distribution. At each iteration, the point with the lowest likelihood is removed

and replaced with a new point drawn from the prior that has a higher likelihood than the removed one. This drives the sampling algorithm toward regions of higher likelihood. The evidence is computed by assigning prior volumes to each point and multiplying them by their likelihoods. The process stops when the evidence is above a predefined threshold [92].

These stochastic sampling techniques are implemented in several software packages tailored for Bayesian parameter estimation of compact binary signals. Commonly used tools are LALInference [88] written in C and Bilby [93], a Python-based package. In my second project (Chapter 6), we use Bilby to simulate and infer the properties of gravitational-wave signals from black-hole binaries.

These parameter estimation codes calculate the posterior probability functions of all the parameters that characterise a black-hole binary. While the individual masses and spins are of primary astrophysical interest, the parameters most accurately measured by gravitational-wave detectors are specific combinations of them. As we will explain in Chapter 3, the amplitude and phase evolution of a gravitational-wave signal are governed by these parameter combinations, for instance, the chirp mass, defined as $\mathcal{M} = (m_1 m_2)^{3/5} / (m_1 + m_2)^{1/5}$. Variations in the chirp mass have a more pronounced effect on the waveform than changes in the individual component masses. As a result, detectors are more sensitive to these parameters and are measured with higher precision than the parameters describing the individual black holes.

Chapter 3

Binary black hole mergers

Among all the fascinating sources that generate gravitational waves, compact binary mergers stand out as exceptional candidates. These objects are incredibly compact, allowing them to orbit one around the other for many cycles before they merge, reaching orbital velocities close to the speed of light. Compact binaries are formed by white dwarfs, neutron stars or black holes. In this thesis, we will focus on a specific type of compact binaries: *black-hole binaries*, which radiate a distinct gravitational-wave signal. In this section, we examine the characteristics of this signal and discuss various signal modelling techniques, following closely the recent review by Chatziioannou et al. [94].

3.1 Techniques to predict the gravitational-wave signal

3.1.1 The Newtonian binary

Building on the expression we derived for the gravitational-wave emission in terms of the mass quadrupole moment (see Eq. (2.35)), we will now calculate the radiation emitted by a binary system. We consider a binary that moves in circular orbits. We assume that the binary orbits in the x - y plane, with rest masses $m_1 \geq m_2$, separated by a distance so large that the sizes of the two objects can be ignored. In the coordinate system of the center-of-mass, the position of each object can be expressed as

$$x_1^i = \frac{m_2 r}{M} (\cos(\omega t), \sin(\omega t), 0), \quad x_2^i = -\frac{m_1}{m_2} x_1^i, \quad (3.1)$$

where r is the separation between the two bodies, ω is the orbital frequency and M is the total mass. Using these expressions, we can then calculate the mass quadrupole moment. In this idealised scenario, the gravitational-wave tensor of the binary takes the form

$$h_{ij}(t, d) = -\frac{4M\omega^2 r^2 \eta}{d} \begin{pmatrix} \cos(2\omega t') & \sin(2\omega t') & 0 \\ \sin(2\omega t') & -\cos(2\omega t') & 0 \\ 0 & 0 & 0 \end{pmatrix}, \quad (3.2)$$

where η is the *symmetric mass ratio* defined as

$$\eta = \frac{m_1 m_2}{(m_1 + m_2)^2}, \quad (3.3)$$

and t' refers to the retarded time $t' = t - d$. This means that the gravitational waves radiated by a binary are proportional to the total mass, the orbital frequency of the system, and are inversely proportional to the distance from the source to the observer. Additionally, this expression indicates that these gravitational waves oscillate at a frequency that is twice the orbital motion of the binary, $f_{\text{GW}} = 2f_{\text{orbital}} = \omega/\pi$.

In reality, the observer might not be exactly positioned along the z -axis. In such cases, the gravitational-wave strain can be determined by projecting h_{ij} into the subspace that is perpendicular to the direction of propagation, which allows us to remain in the transverse-traceless gauge. Mathematically, this can be expressed as

$$h'_{kl} = P_k^i P_l^j h_{ij} - \frac{1}{2} P_{kl} P^{ij} h_{ij}, \quad (3.4)$$

where P_{kl} is the projection operator and is defined by

$$P_{kl} = \mathbb{I}_{kl} - \hat{N}_k \hat{N}_l. \quad (3.5)$$

In this context, \mathbb{I} represents the three-dimensional identity matrix, and \hat{N} is the unit vector pointing from the source to the detector.

As gravitational waves carry away energy from the system, the binary orbit will shrink and will not remain circular. We call these quasi-circular orbits. The energy carried away by gravitational waves can be quantified by the luminosity, which is derived from the gravitational-wave flux averaged over one orbit and integrated over a sphere of radius d . One can show that the luminosity of compact binaries takes the form

$$\mathcal{L} = \frac{32}{5} \eta^2 v^{10}, \quad (3.6)$$

where v is the relative velocity defined as $v = \omega r$. We can derive how this velocity changes over time from the energy balance. We know that gravitational waves carry away energy from the system, meaning that:

$$\frac{dE(t)}{dt} = -\mathcal{L}(t). \quad (3.7)$$

The orbital energy of the binary is given by

$$E = -\frac{M\eta}{2} v^2. \quad (3.8)$$

Assuming the mass of the objects remains constant, we can rewrite Eq. (3.7) as

$$\frac{dv(t)}{dt} = -\frac{\mathcal{L}(t)}{dE(v)/dv}, \quad (3.9)$$

$$= \frac{32}{5M} \eta v^9(t), \quad (3.10)$$

which means that the velocity changes according to

$$v(t) = \frac{1}{2} \sqrt[8]{\frac{5M}{\eta(t_c - t)}}. \quad (3.11)$$

This expression shows that the velocity appears to diverge at the coalescence time t_c . The separation between the two objects r is related to the velocity and total mass through Kepler's third law:

$$r = \frac{M}{v^2}. \quad (3.12)$$

Knowing how the relative velocity changes over time, we can determine how the separation decreases with time:

$$r(t) = 4M \sqrt[4]{\frac{\eta(t_c - t)}{5M}}. \quad (3.13)$$

On the other hand, the orbital frequency changes according to

$$\omega(t) = \frac{v^3(t)}{M} = \frac{1}{8\mathcal{M}^{5/8}} \left(\frac{5}{t_c - t} \right)^{3/8}, \quad (3.14)$$

where we have introduced a mass parameter called the *chirp mass*, defined as

$$\mathcal{M} = M \eta^{3/5} = \frac{(m_1 m_2)^{3/5}}{(m_1 + m_2)^{1/5}}. \quad (3.15)$$

From the orbital frequency we can derive the time dependence of the orbital phase:

$$\phi(t) = \int \omega(t) dt = \phi_c - \left(\frac{t_c - t}{5\mathcal{M}} \right)^{5/8}, \quad (3.16)$$

where ϕ_c is the phase at the coalescence time t_c . These expressions show that the emission of gravitational waves primarily depends on one parameter: the chirp mass. Additionally, we find that the total mass acts as a scaling factor in describing the dynamics of the binary: $v(t)$, $r(t)$ and $\omega(t)$. Figure 3.1 illustrates these functions for a binary that moves in quasi-circular orbits. The figure also shows the gravitational waves radiated during the *inspiral*, the period when the two bodies are still far apart.

As the two bodies move closer together, the relative velocities increase drastically and relativistic effects become important. In this regime, the assumptions we made earlier break down and the Newtonian description becomes unsuitable. Although we cannot employ the Newtonian framework for the merger of the two bodies, it is worth noting that its predictions are remarkably accurate during the early stages of the inspiral.

3.1.2 The post-Newtonian formalism

The procedure outlined above can be generalized to include non-linear effects by expanding the physical quantities that describe the binary in terms of v/c , assuming that the relative velocity v is small compared to the speed of light [95]. In this *post-Newtonian* (PN) framework, the energy and the luminosity are expressed in terms of the velocity v

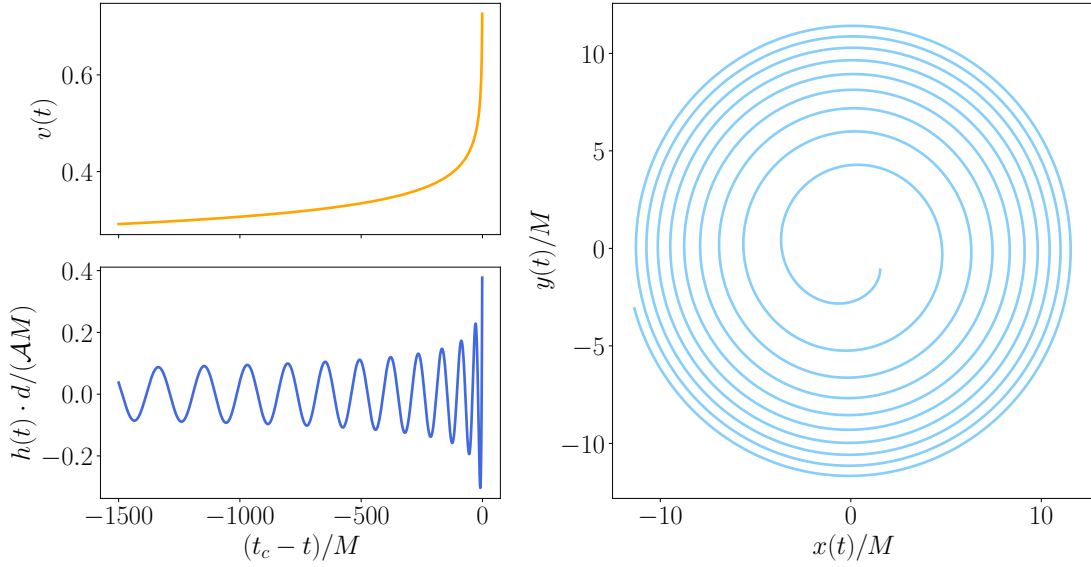


Figure 3.1: Time evolution of the relative velocity (top left), the scaled gravitational-wave signal (bottom left) and the separation vector (right) for a Newtonian binary with equal masses. Adapted from [94].

and the source parameters $\vec{\theta} = \{M, \eta, \dots\}$ as

$$E(v, \vec{\theta}) \approx -\frac{M\eta}{2}v^2 \left(1 + \sum_{k=2}^n E_k(\vec{\theta})v^k + \ln v \sum_{k=8}^n E_k^{(l)}(\vec{\theta})v^k \right), \quad (3.17)$$

$$\mathcal{L}(v, \vec{\theta}) \approx \frac{32}{5}\eta^2v^{10} \left(1 + \sum_{k=2}^n \mathcal{L}_k(\vec{\theta})v^k + \ln v \sum_{k=6}^n \mathcal{L}_k^{(l)}(\vec{\theta})v^k \right). \quad (3.18)$$

We note that since we are using geometrized units where $c = 1$, the expansion parameter is v . In this expressions, we can see that the Newtonian term has additional corrections of the order k . These higher-order contributions are commonly denoted as $k/2$ PN order terms and they account for specific physical effects. Notably, in General Relativity, the $k = 1$ term vanishes. For a more comprehensive review, see e.g. [96].

The expressions of the energy and luminosity can then be used to calculate the signal from the inspiral phase of a compact binary. The gravitational wave strain h can be generalised into the form

$$h(t, \vec{\theta}) = \mathcal{A} \frac{4Mv(t)^2\eta}{d} \cos[\phi_{\text{GW}}(t) + \phi_0], \quad (3.19)$$

where \mathcal{A} is an amplitude factor, and ϕ_0 is a phase offset that depends on the properties of the source and the detector. The gravitational-wave phase ϕ_{GW} is twice the orbital phase and can be computed from the orbital frequency $\omega(t)$.

$$\frac{d\phi}{dt}(t) = \omega(t). \quad (3.20)$$

Meanwhile, the relative velocity v is determined by

$$\frac{dv}{dt}(t) = -\frac{\mathcal{L}(t)}{dE(v)/dv}. \quad (3.21)$$

As previously mentioned, the energy E and the luminosity \mathcal{L} are now expressed as a series expansion in the velocity up to a specific PN order. There are various strategies one can follow to solve Eqs. (3.20) and (3.21) to obtain the gravitational-wave signal from a compact binary. These different approaches are referred to as PN approximants. Some well-known signal models include: **TaylorT1**, **TaylorT2**, **TaylorT3**, **TaylorT4** in the time domain, and **TaylorF2** in the frequency domain. These approximants differ in the PN order in which they express the physical quantities and in how Eqs. (3.20) and (3.21) are re-expanded and solved. For a detailed overview and comparison of various analytical approximants, we refer to Buonanno et al. [97].

In addition to the PN framework, other approaches exist to analytically model the inspiral phase of a binary coalescence. One example is the **effective-one-body** (EOB) formalism [98–100], which essentially maps the two-body problem into a one-body problem in an effective spacetime. We will explain this approach in more detail in Sec. 3.3.1.

3.1.3 Numerical relativity

As two black holes orbit each other, their separation decreases over time until they eventually merge. As they draw closer, their velocities become relativistic and gravity becomes significantly stronger. In this merger regime, analytical techniques such as the PN expansion or the EOB framework are no longer applicable, as they are valid only in the limits of weak gravity and low velocities. Instead, the highly non-linear merger phase can only be accessed through full *numerical relativity* (NR) simulations, which solve Einstein’s equation numerically. These simulations track the evolution of the binary system over time, requiring the resolution of both the small scales of the black holes and their dynamics, as well as the extraction of gravitational waves far away from the binary. To address these challenges, fixed or adaptive mesh refinement methods are employed.

For many years, simulating binary black hole mergers with NR was a major challenge. However, following key breakthroughs by several groups in 2005 [47, 101, 102], NR simulations have become routine, leading to the development of extensive publicly available catalogs. The **SXS** (Simulating eXtreme Spacetimes) catalog [103] contains 3756 binary black hole simulations with mass ratios between 1 and 20. The **RIT** (Rochester Institute of Technology) catalog [104] includes 1881 simulations with mass ratios between 1 and 128. The **Georgia Tech** group has produced a catalog with 452 simulations with mass ratios up to 15. Finally, a catalog comprising 80 simulations has been generated using the **BAM** code [105].

NR simulations produce highly accurate gravitational-wave signals, commonly referred to as *waveforms*. Yet, these simulations are computationally very expensive. One single simulation can take up to several months on a supercomputer, depending on the properties of the binary. The computational cost increases with more unequal mass ratios and higher spin magnitudes, limiting the number of simulations that can be performed

and their duration. As we showed in Chapter 2, detecting and analysing signals from binary mergers in gravitational-wave observatories requires theoretical predictions of signals from binaries with "all" possible binary configurations. With the current NR techniques, however, it is not feasible to produce such a large number of waveforms exclusively using NR simulations. This limitation has led to the development of semi-analytical waveform models that combine data from NR simulations with the PN or the EOB formalisms to describe the complete signal. We will delve into more details in Section 3.3.

In summary, in this section, we have introduced various techniques commonly used to describe the dynamics of black-hole binaries and predict their characteristic gravitational-wave signals. We presented these methods in chronological order, reflecting the timeline of their development. PN and EOB studies of these binaries emerged in the late 1990s, while the first NR simulations were achieved a few years after. It was only with the advent of NR simulations that it became possible to generate the gravitational-wave signal through the merger and ringdown phases for the first time.

So, what does the complete signal look like? In the next section, we will examine its key features and discuss the physical properties of the source.

3.2 Anatomy of the signal

3.2.1 Phases of the binary merger

A binary merger is usually divided into three phases according to its dynamics. We now summarise each of these phases and indicate which modelling techniques are appropriate in each case:

- In the *inspiral*, the black holes are far away from each other and the orbital velocities are small compared to the speed of light, $v \ll c$. In this case, the process can be well described by PN or EOB theories, which provide analytical expressions of the waveform.
- When the two black holes come closer to each other, the velocities increase up to $v \simeq 0.5c$ and relativistic effects become non-negligible. In this *merger* phase, only NR simulations can determine the radiated gravitational-wave signal and describe the dynamics. The EOB approach can also be applied in the merger regime, but its accuracy decreases significantly compared to the inspiral.
- The merger of two black holes produces a highly perturbed black hole, which settles down into a spinning, spherically symmetric black hole by emitting gravitational-wave radiation [106]. This radiation is characterised by a spectrum of exponentially decaying modes, typically called quasinormal modes. This phase is called the *ringdown* and can be well described by black-hole perturbation theory [107, 108].

Figure 3.2 illustrates these phases, together with the signal expected during this process.

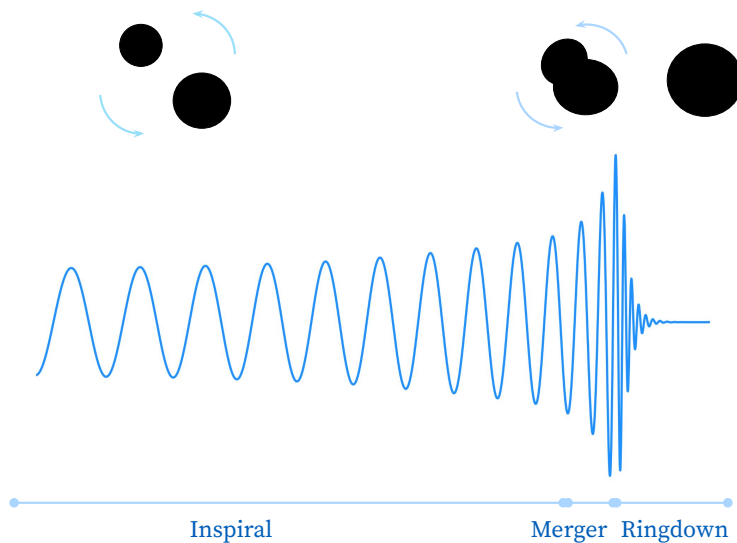


Figure 3.2: Phases of a binary black hole merger together with the typical gravitational-wave signal they radiate: inspiral, merger and ringdown. The small drawings in the top illustrate the dynamics of the binary in each phase.

3.2.2 Source parameters

The exact form of the signal depends on the properties of the binary. A black-hole binary in quasi-circular orbits can be characterized by the masses m_i , and the spin vectors or angular momenta \vec{S}_i of each black hole. We refer to these parameters as *intrinsic parameters*.

We showed earlier that the mass of the system can also be parametrized by the total mass M , the chirp mass \mathcal{M} , the mass ratio q or the symmetric mass ratio η . We will often refer to the more massive black hole as the primary and to the less massive as secondary. When the binary has unequal masses, the spin of the primary has a larger impact than the secondary on the waveform.

Regarding the spin, since the maximum spin that a Kerr black hole can have is $|\vec{S}_{\max}| = Gm^2/c$ [43], it is common to use the dimensionless spin $\vec{\chi}_i = c\vec{S}_i/(Gm_i^2)$. This means that, $\chi_i \in [0, 1]$, $\chi_i = 1$ representing maximum spin. The dimensionless spins are usually decomposed into the spin vectors parallel and orthogonal to the orbital angular momentum \vec{L} by projecting the spin vectors onto the unit vector \hat{L} . This allows to distinguish between binaries with spins aligned with the orbital angular momentum, and binaries with misaligned spins. Additionally, the dimensionless spin can be described in terms of the spin magnitudes a_i , the spin tilts θ_i and the spin azimuthal angles ϕ_i , as illustrated in Figure 3.3. The total angular momentum of the system \vec{J} is then the sum of the individual and orbital angular momenta: $\vec{J} = \vec{L} + \vec{S}_1 + \vec{S}_2$. In general, this quantity is not conserved, although it is approximately conserved throughout the inspiral.

When looking at PN theory, one finds that in binaries with aligned spins the individual spins have only a weak effect in the waveform. What we best measure is the sum of the spins. This quantity is referred to as the *effective spin* and was introduced by Ajith et al.

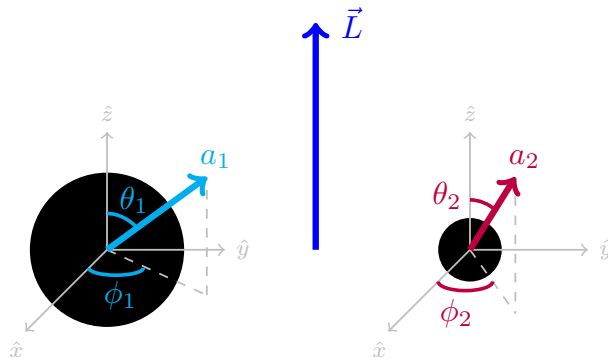


Figure 3.3: Spin parameters of the primary and secondary black holes. In gravitational-wave data analysis, spins are usually parametrized with the spin magnitudes a_i , the spin tilts θ_i and the spin azimuthal angles ϕ_i .

[109, 110]:

$$\chi_{\text{eff}} = \frac{m_1 \chi_1 \cos \theta_1 + m_2 \chi_2 \cos \theta_2}{m_1 + m_2}. \quad (3.22)$$

When the spins are misaligned with the orbital angular momentum of the system, the spins and the orbital plane precess around the total angular momentum \vec{J} due to spin-orbit and spin-spin couplings [27, 111]. This is a purely relativistic effect. The dominant effect of misaligned spins in the waveform can be quantified by the *effective spin-precession* parameter, introduced by Schmidt et al. [112]:

$$\chi_p = \max \left(\chi_{\perp}^1, \kappa \chi_{\perp}^2 \right), \quad (3.23)$$

where $\kappa = q(4q+3)/(4+3q)$ and $S_{i\perp} = |\hat{L} \times (\vec{S}_i \times \hat{L})|$, and χ_i^\perp refers to the magnitude of the in-plane spins. The effective precession parameter represents the average of the in-plane spins over a number of precession cycles. Alternative parametrizations of precession have also been proposed in the literature [113, 114].

Astrophysical studies suggest that not all binary black hole mergers might move in quasi-circular orbits. For instance, one might find binary black holes with eccentric orbits in dense star clusters (see e.g. [115]). Describing elliptic orbits requires two additional intrinsic parameters, namely, the eccentricity e and the argument of the periapsis Ω .

Apart from the intrinsic parameters, there are seven additional parameters, called *extrinsic parameters*, which describe the location of the source relative to the observer. These are the luminosity distance d_L , the time t_c and the phase ϕ_c at coalescence, the polarization angle ψ , and the orbital inclination angle θ_{JN} . It is also common to use the angle ι , the angle between the orbital angular momentum \vec{L} and the line-of-sight \hat{N} to define the inclination angle. Additionally, the right ascension α and declination δ define the sky localization.

The sky position $\{\alpha, \delta\}$ together with the polarization angle ψ define the location of the source relative to the frame of a ground-based gravitational-wave detector. In particular, the signal recorded by the detectors is a weighted linear combination of the gravitational-

wave polarizations, defined as,

$$h = F_+(\alpha, \delta, \psi) h_+ + F_\times(\alpha, \delta, \psi) h_\times, \quad (3.24)$$

where F_+ and F_\times are the antenna pattern functions. For an L-shaped detector like current ground-based detectors, these functions take the form

$$F_+(\alpha, \delta, \psi) = \frac{1}{2}(1 + \cos^2 \alpha) \cos(2\delta) \cos(2\psi) - \cos \alpha \sin(2\delta) \sin(2\psi), \quad (3.25)$$

$$F_\times(\alpha, \delta, \psi) = -\frac{1}{2}(1 + \cos^2 \alpha) \cos(2\delta) \sin(2\psi) - \cos \alpha \sin(2\delta) \cos(2\psi). \quad (3.26)$$

In a frame that is far a way from the source, typically called wave frame, it is common to expand the complex combination of the gravitational-wave polarizations on a basis of spin-weighted spherical harmonics, with spin weight $s = -2$,

$$h_+ - ih_\times = \sum_{\ell=2}^{\infty} \sum_{m=-\ell}^{\ell} h_{\ell,m}(t) {}^{-2}Y_{\ell,m}(\theta, \varphi), \quad (3.27)$$

where $h_{\ell,m}(t)$ are the gravitational-wave *multipoles*, *modes* or *harmonics*, and ${}^{-2}Y_{\ell,m}(\theta, \varphi)$ are the spin-weighted spherical harmonic functions. Given the geometry of gravitational waves, this basis represents the most convenient choice [116]. This expansion allows to separate the dependence of the intrinsic and extrinsic parameters. Specifically, the $h_{\ell,m}(t)$ modes include the dependency on the intrinsic properties, while the spherical harmonic functions depend on the extrinsic parameters θ and φ , which define the orientation of the orbital plane relative to the observer. The inclination angles ι or θ_{JN} constitute the tilt angle θ , while the coalescence phase ϕ_c takes the place of the azimuthal angle φ .

When the black hole spins are aligned with the angular momentum of the system, the orbital plane remains fixed and as a result, the gravitational-wave emission is *symmetric* over the orbital plane. Mathematically, this symmetry is expressed as

$$h_{\ell,m}(t) = (-1)^\ell h_{\ell,-m}^*(t), \quad (3.28)$$

where $*$ stands for complex conjugate. This relation does not hold in binaries where the spins are misaligned with the orbital angular momentum (i.e. precessing binaries). Instead, the gravitational-wave emission contains *mode asymmetries* (see e.g. [117]). In such cases, it is common to describe the signal as a combination of a symmetric ($h_{\ell,m}^+$) and an antisymmetric ($h_{\ell,m}^-$) part, which are typically defined as [31, 33, 118]

$$h_{\ell,m}^\pm(t) = \frac{h_{\ell,m}(t) \pm (-1)^\ell h_{\ell,-m}^*(t)}{2}. \quad (3.29)$$

This expression is valid in a non-inertial reference frame that rotates with the binary, tracking the motion of the orbital plane. In this *co-precessing frame*, the z -axis is aligned with the orbital angular momentum of the system \vec{L} and the orbital plane is fixed. A key advantage of this frame is that, while the signal from a precessing binary exhibits amplitude modulations in an inertial frame, these modulations largely disappear when switching

to the co-processing frame [119, 120]. The co-processing modes $h_{\ell,m}^{\text{CP}}$ can be obtained by rotating the inertial $h_{\ell,m}$ modes via

$$h_{\ell,m}^{\text{CP}}(t) = e^{im\alpha(t)} \sum_{\ell=2}^{\ell_{\text{max}}} \sum_{m'=-\ell}^{\ell} e^{im'\gamma(t)} d_{m',m}^{\ell}(-\beta(t)) h_{\ell,m'}(t), \quad (3.30)$$

where $d_{m',m}^{\ell}$ are the Wigner d-matrices. The Euler angles $\alpha(t), \beta(t), \gamma(t)$ define the evolution of the orbital angular momentum \vec{L} in an inertial frame, where the z -axis is aligned with the total angular momentum \vec{J} .

The gravitational-wave signal with only the dominant $(\ell, m) = (2, \pm 2)$ mode is given by

$$h(t, \theta, \varphi) = h_{2,2}(t) {}^{-2}Y_{2,2}(\theta, \varphi) + h_{2,-2}(t) {}^{-2}Y_{2,-2}(\theta, \varphi), \quad (3.31)$$

where the spherical harmonic function is defined as

$${}^{-2}Y_{2,\pm 2}(\theta, \varphi) = \sqrt{\frac{5}{64\pi}} (1 \pm \cos \theta)^2 e^{\pm 2i\varphi}, \quad (3.32)$$

and the dominant mode is expressed as $h_{2,2}(t) = A_{2,2}(t) e^{-i\phi_{\text{GW}}(t)}$. Assuming the system is a nonprecessing binary, we have $h_{2,-2} = h_{2,2}^*$, and we can rewrite the previous expression as

$$h(t, \theta, \varphi) = \sqrt{\frac{5}{4\pi}} A_{2,2}(t) \left[\frac{1 + \cos^2 \theta}{2} \cos(\phi_{\text{GW}}(t) - 2\varphi) - i \cos \theta \sin(\phi_{\text{GW}}(t) - 2\varphi) \right]. \quad (3.33)$$

The dominant mode has its maximum emission along the poles, as described by the spherical harmonic functions. When the binary is face-on ($\theta_{\text{JN}} = 0$) or face-off ($\theta_{\text{JN}} = \pi$), the signal is proportional to

$$h \propto A_{2,2}(t) [\cos(\phi_{\text{GW}}(t) - 2\varphi) - i \sin(\phi_{\text{GW}}(t) - 2\varphi)]. \quad (3.34)$$

Instead, if the binary is edge-on ($\theta_{\text{JN}} = \pi/2$), the signal received by the detectors is weaker:

$$h \propto \frac{A_{2,2}(t)}{2} \cos(\phi_{\text{GW}}(t) - 2\varphi). \quad (3.35)$$

Figure 3.4 illustrates this effect for an equal-mass binary with spins $\vec{\chi}_1 = \vec{\chi}_2 = (0, 0, 0.5)$. As noted in the figure, the x -axis, which represents the time evolution of the binary, has units of total mass in geometric units.

Similarly, in the following subsections, we discuss the effect of the intrinsic parameters on the gravitational-wave signal.

3.2.3 Effect of masses on the signal

In vacuum spacetimes, such as those describing black-hole binaries, the total mass M , along with the distance and time, act as a scaling factor due to the scale-free nature of Einstein's equation for vacuum. As a result, changing M while keeping all other parameters fixed shifts the frequency of the binary's orbital evolution and, consequently,

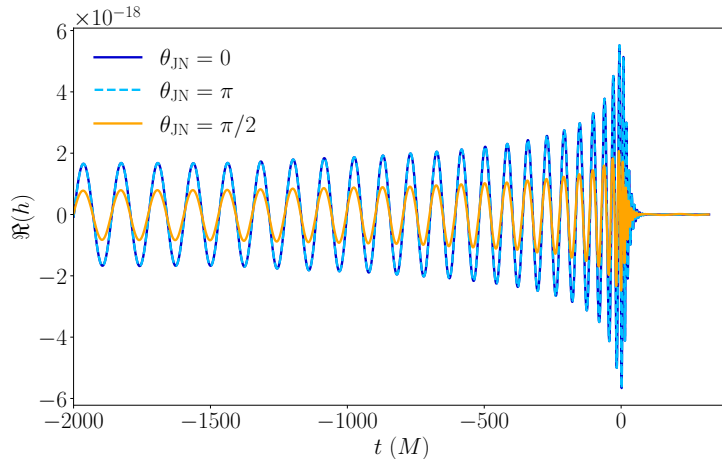


Figure 3.4: Impact of the inclination angle on the gravitational-wave signal emitted by a nonprecessing black-hole binary, oriented face-on ($\theta_{\text{JN}} = 0$) in dark blue, face-off ($\theta_{\text{JN}} = \pi$) in light blue, and edge-on ($\theta_{\text{JN}} = \pi/2$) in orange. The binary has a mass ratio of $q = 1$, and spins $\vec{\chi}_1 = \vec{\chi}_2 = (0, 0, 0.5)$ defined at a reference frequency of 20 Hz for a total mass of $70 M_{\odot}$. The signals have been generated with the waveform model IMRPhenomXHM [121].

the frequencies of the emitted gravitational waves. The product Mf remains invariant, meaning that lower-mass binaries merge at higher frequencies, while higher-mass binaries merge at lower frequencies. In time domain, the total mass determines the number of gravitational-wave cycles observable within the detector’s sensitive frequency band, as illustrated in Figure 3.5. Additionally, more massive binaries generate signals with larger amplitudes.

On the other hand, varying the mass ratio from equal masses to more asymmetric configurations, while fixing the total mass, increases the time it takes for the binary to merge. This leads to a greater number of gravitational-wave cycles in the signal. The extended merger time is governed by the leading-order (0 PN) phase term, which is inversely proportional to the symmetric mass ratio η .

Finally, increasing the chirp mass enhances the signal amplitude, scaling as $\propto \mathcal{M}^{5/6}$, and reduces the number of gravitational-wave cycles up to merger due to the inverse proportionality of the 0 PN phase on the chirp mass.

3.2.4 Effect of spins on the signal

A key difference between Newtonian dynamics and General Relativity is that, in the relativistic regime, the spins of the black holes influence their orbital motion and therefore, the gravitational-wave signal. For nonprecessing binaries with spins aligned with the orbital angular momentum (positive χ_i^z), increasing the spin magnitude delays the merger time, leading to more binary orbits and a greater number of gravitational-wave cycles. As a consequence, the binary radiates more energy and angular momentum during the binary evolution. In contrast, binaries with spins antialigned with the orbital angular momentum (negative χ_i^z) undergo fewer orbits before merging compared to nonspinning or aligned-spin binaries. This phenomenon is known as the orbital hang-up effect [122] and

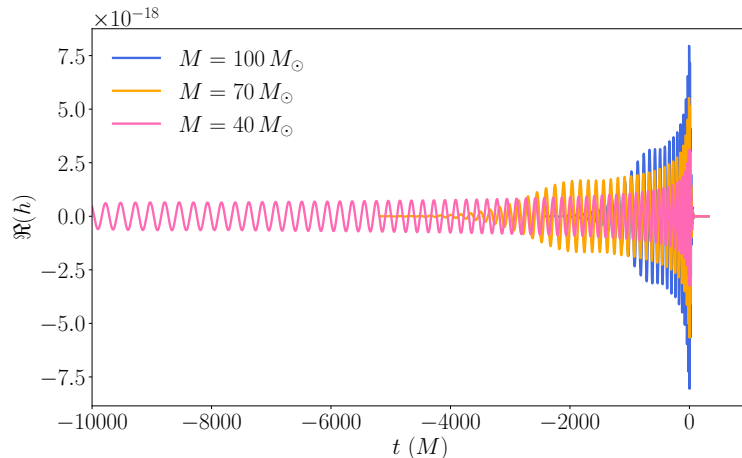


Figure 3.5: Impact of the total mass on the gravitational-wave signal emitted by a non-precessing black-hole binary, with total mass values of $100 M_{\odot}$ (blue), $70 M_{\odot}$ (orange) and $40 M_{\odot}$ (pink). The binary has a mass ratio of $q = 1$, and spins $\vec{\chi}_1 = \vec{\chi}_2 = (0, 0, 0.5)$ defined at a reference frequency of 20 Hz. The signals have been generated with the waveform model IMRPhenomXHM [121], and have been aligned such that the maximum amplitude of the signal occurs at $t = 0$.

is illustrated in Figure 3.6.

Binaries with misaligned spins undergo orbital precession, which can induce large amplitude modulations in the gravitational-wave signal. Figure 3.7 illustrates this effect by showing two different modes for a binary with symmetric mass ratio $\eta = 0.16$ and spins $\vec{\chi}_1 = (-0.6, 0.2, 0.2)$ and $\vec{\chi}_2 = (0.3, 0.6, -0.2)$ observed with an inclination angle of $\theta_{JN} = \pi/2$ at a reference frequency of 20 Hz. The waveform in blue includes only the dominant $(\ell, m) = (2, \pm 2)$ modes, while the waveform in orange includes only the subdominant $(\ell, m) = (2, \pm 1)$ modes. In both cases, the amplitude modulations characteristic of precessing binaries are clearly visible. However, such modulations might not always be apparent. In systems with nearly equal masses, or with orientations close to face-on or face-away relative to the detectors, the imprint of spin precession can become very subtle. The lack of a clear signature can hinder the detectability of spin precession in gravitational-wave data (see, e.g., [123]). The observability of precession is the main topic of my second research project and will be discussed in detail in Chapter 6.

3.3 Waveform models

As mentioned earlier, gravitational-wave data analysis requires knowledge of the signal for not just one, but millions of different binary configurations. Currently, NR simulations are far too computationally expensive to generate such a large amount of waveforms. To address this challenge, various research groups have developed *approximate waveform models* that combine different analytical and numerical techniques to describe all three phases of the gravitational-wave signal. These techniques can be combined in different ways, and as a result, three main modeling frameworks have emerged: the **effective-one-body**

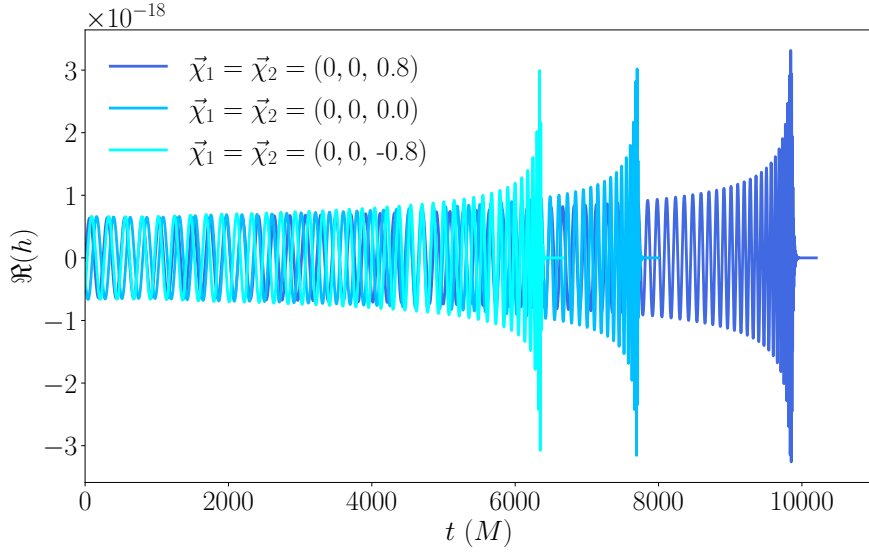


Figure 3.6: Impact of the spin magnitude on the gravitational-wave signal emitted by a nonprecessing black-hole binary, with spin aligned spins (dark blue), zero spins (medium blue) and antialigned spins (light blue). The binary has a mass ratio of $q = 1$, and a total mass of $40 M_{\odot}$. The spins were defined at a reference frequency of 20 Hz. The signals have been generated with the waveform model IMRPhenomXHM [121].

(EOB), phenomenological (Phenom) and NR surrogate (NRSur) approaches.

3.3.1 Effective-one-body models

As the name suggests, EOB models are based on the *effective-one-body* (EOB) framework, which reformulates the two-body problem as a one-body problem in an effective space-time. In this formulation, a test particle with mass $\mu = \eta M$ moves along the geodesic of a static, spherically symmetric metric $g_{\text{eff}}^{\mu\nu}$. The particle's motion during the inspiral is governed by a set of Hamiltonian equations, expressed in terms of its position and conjugate momentum (q, p) :

$$\frac{dr}{d\hat{t}} = \frac{\partial \hat{H}}{\partial p_r}, \quad (3.36)$$

$$\frac{d\varphi}{d\hat{t}} = \frac{\partial \hat{H}}{\partial p_\varphi}, \quad (3.37)$$

$$\frac{dp_r}{d\hat{t}} = -\frac{\partial \hat{H}}{\partial r}, \quad (3.38)$$

$$\frac{dp_\varphi}{d\hat{t}} = \hat{\mathcal{F}}_\varphi(r, p_r, p_\varphi), \quad (3.39)$$

where $\hat{\mathcal{F}}_\varphi$ represents the radiation reaction force responsible for the gravitational-wave emission. These equations describe the motion of the particle up to the plunge, which is the brief time interval at which the black holes have reached the innermost stable circular orbit, lose dynamical stability and undergo a rapid collision, leading to the merger phase.

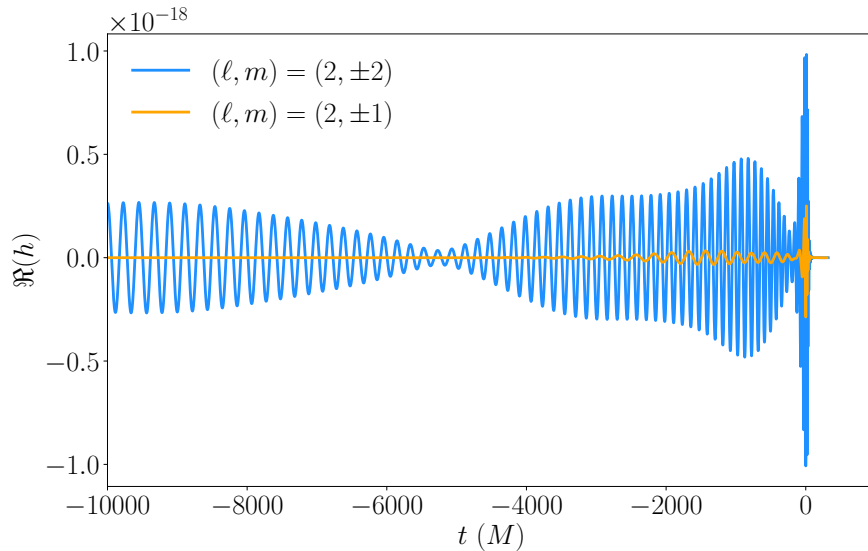


Figure 3.7: Impact of misaligned spins on the gravitational-wave signal. The waveform in blue includes the $(\ell, m) = (2, \pm 2)$ modes, while the waveform in orange includes the $(\ell, m) = (2, \pm 1)$ modes. The binary has a mass ratio of $\eta = 0.16$, a total mass of $40 M_{\odot}$, with spins $\vec{\chi}_1 = (-0.6, 0.2, 0.2)$ and $\vec{\chi}_2 = (0.3, 0.6, -0.2)$ defined at a reference frequency of 20 Hz, and an inclination angle of $\theta_{JN} = \pi/2$. The signals have been generated with the waveform model IMRPhenomXPHM [124].

These equations are typically solved numerically, and determine the inspiral and plunge phases of the waveform via the quadrupole formula. To improve its accuracy, unknown higher-order PN terms are usually incorporated into the Hamiltonian, which are then calibrated to NR waveforms. Because the Hamiltonian is invariant under time translations and rotations, the energy and the angular momentum of the system are conserved.

The ringdown phase is modeled using black hole perturbation theory, describing the quasinormal modes as a superposition of damped sinusoidal oscillations. This part of the signal is attached to the inspiral-plunge waveform near the peak amplitude, resulting in a complete waveform. It is worth noting that EOB models are developed in the time domain.

Currently, two main EOB model families are widely used in gravitational-wave data analysis:

- **SEOBNR:** This family includes models that account for the dominant gravitational-wave mode [125], higher-order harmonics [126], aligned spins [126–128], spin precession [129, 130], mode asymmetries [131], orbital eccentricity [132, 133] and tidal effects [134, 135]. While SEOBNR models are faster to evaluate than NR simulations, they remain computationally expensive for efficient parameter estimation. To mitigate this, *reduced-order-modelling* (ROM) techniques have been applied to produce SEOBNR-ROM models [136], which are simplified Fourier-domain versions of the more sophisticated time-domain models and are significantly faster to evaluate.
- **TEOBResum:** This family also incorporates various physical effects, including spin

precession [137, 138], eccentricity [138, 139] and tidal interactions [138, 140].

3.3.2 Phenomenological models

The phenomenological approach to waveform modelling differs from the EOB framework in several aspects. This subsection follows the reviews in Refs. [94, 141].

The construction of phenomenological models begins with the generation of *hybrid waveforms*, which combine a PN or an uncalibrated-EOB approximant for the inspiral phase with NR waveforms covering the late inspiral, merger, and ringdown. This hybridization can be performed in either the time or frequency domain, by aligning the two waveform segments at a specific time or over an overlapping interval to ensure optimal continuity and phase coherence.

Once hybrid waveforms are constructed across a range of binary configurations, the next step is to perform a *multi-parameter fit* to these waveforms. This involves introducing a number of fitting parameters, which should be smooth functions of the physical parameters of the binary, namely the mass ratio and the spins. This dependence enables interpolating the fit across the (physical) parameter space, and allows the resulting model to generate signals for any binary configuration within the range of calibration. The form of the fit is guided by PN or EOB descriptions for the inspiral phase, and by the known structure of quasinormal modes for the ringdown. The final result is a set of closed-form expressions that describe the complete gravitational-wave signal and are computationally efficient to evaluate, making phenomenological models particularly well-suited for gravitational-wave data analysis.

Since gravitational-wave data analysis is conducted in the *frequency domain*, phenomenological models have traditionally been constructed in this domain. Similar to EOB models, these models have evolved to incorporate a wide range of physical effects. The very first models include **PhenomA**, for non-spinning binaries [142, 143], **PhenomB** and **PhenomC** for aligned-spin binaries [144, 145]. As the number of NR simulations has increased, more accurate and sophisticated models have been developed. A second generation of models started with **PhenomD** [146, 147], an improved model for aligned-spin binaries, and subsequent variants included higher modes [148] and spin precession [149–151]. The third and current generation, based on **PhenomX** models [152], includes spin precession [34, 36, 124, 153], higher modes [121] and mode asymmetries [34, 36, 117]. These models are calibrated against a larger set of NR simulations and therefore have higher accuracy than earlier generation models.

In addition to frequency-domain models, *time-domain* phenomenological models have also been developed, as the time domain provides a more intuitive and natural framework to capture certain aspects of the waveform. These are the **PhenomT** models [154], which include spin precession [155] and higher modes [156]. More recently, the first phenomenological model for eccentric, aligned-spin black-hole binaries was developed in the time domain [157].

As waveform models expand to include more physical effects, the dimensionality of the parameter space increases, making the fitting procedure more challenging. This complexity is the primary reason why a model that simultaneously includes both eccentricity and spin precession has not yet been developed. Additionally, model evaluation becomes

more computationally demanding in higher dimensions. To address this, *speed-up techniques* such as multibanding [158] are employed in the latest generation of models to reduce computational cost without sacrificing accuracy.

3.3.3 NR surrogate models

While the EOB and Phenom models use physical motivations to describe the signal phenomenology, NR surrogates are *data-driven models*. The goal of these models is to "substitute" a set of NR waveforms that have fixed parameters $\{\vec{\theta}_i\}$ with a model that can produce a waveform for any set of parameters desired. For this subsection, we follow Refs. [35, 159].

The first step in building an NR surrogate model is the postprocessing of the NR data. All waveforms are aligned such that the peak of the waveform occurs at $t = 0$. Subsequently, the waveform modes are rotated to a co-orbital frame at a specific reference time. The co-orbital frame co-precesses with the binary, in the same way as the co-precessing frame, but, additionally, the \hat{x} axis is nearly along the line of separation from the lighter to the heavier black hole. In other words, the co-orbital frame is the same as the co-precessing frame, but rotated around the \hat{z} axis. Similar to the coprecessing frame, the waveform has a simpler form in the co-orbital frame, which facilitates its modelling. The functions are then downsampled into a set of time values t_i^{coorb} that are approximately uniformly spaced in the orbital phase.

NR surrogates model (ℓ, m) modes in the co-orbital frame. In the same way as with the EOB and phenomenological models, the strain is decomposed into the amplitude and the phase, as it is easier to build a model of these functions rather than that of oscillatory ones. Since it is not feasible to directly interpolate NR waveform modes in parameter space due to its high dimensionality, the waveform is split into many data pieces $f(t; \vec{\theta})$, which are later recombined. For each data piece, one builds a linear basis using singular value decomposition [160].

Then, one reduces the dimensionality of the problem by selecting a set of time nodes, one per basis vector. These time nodes are chosen differently for different waveform data pieces. For each time node, one constructs a *parametric fit* of the waveform data piece. This fit is a function of the intrinsic properties of the binary (i.e. the mass ratio and the spins).

Currently, several NR surrogate models are available including higher modes and precession [35, 159, 161–163], as well as eccentricity [164]. In this thesis, we use **NRHyb-Sur3dq8** [161] and **NRSur7dq4** [35], which, at the time of conducting the research, were the state-of-the-art NR surrogate models for nonprecessing and precessing quasi-circular binaries respectively.

3.4 Waveform accuracy requirements for data analysis

Waveform models provide approximate representations of the true gravitational-wave signals predicted by General Relativity. Since the techniques used to construct these models are not infinitely accurate, they inevitably introduce systematic errors. To evaluate the

accuracy of a model, it is standard practice to compute *matches* against a set of NR simulations, which currently offer the most precise waveform predictions available.

Yet, what does it mean for a waveform model to be "accurate enough"? In gravitational-wave data analysis, waveform models must be sufficiently accurate that their errors do not affect detection or parameter estimation. In this section, we derive quantitative accuracy requirements following the work of Lindblom et al. [165] and Baird et al. [12]. Waveform accuracy is also the central focus of my first paper (see Chapter 5), which motivates a dedicated discussion here.

The central question we aim to address is: *How similar must two waveforms be for them to be indistinguishable by a given detector?* More specifically, we seek to determine how accurate a waveform model h_m must be to ensure it is indistinguishable from the true astrophysical waveform h_0 . We will derive an expression that relates the waveform *mismatch* to the minimum SNR of a detector. Since gravitational-wave data analysis is typically performed in the frequency domain, we use this domain in our derivation. We begin by considering a one-parameter family of waveforms that interpolates between the true signal and the model:

$$h(\lambda, f) = (1 - \lambda) h_0(f) + \lambda h_m(f), \quad (3.40)$$

$$= h_0(f) + \lambda \delta h(f), \quad (3.41)$$

where λ takes values from 0 to 1 and the waveform difference is defined as $\delta h(f) = \|h_0(f) - h_m(f)\|$. We now ask: *How accurately can a detector measure the parameter λ ?* The precision of this measurement can be quantified by the variance of λ , which is related to the Fisher information matrix Γ_{ij} . As shown by Cutler and Flanagan [10], the variance of any parameter θ satisfies:

$$\sigma_\theta^2 = \Gamma_{ij}^{-1}. \quad (3.42)$$

The Fisher matrix is defined as:

$$\Gamma_{ij} = \left\langle \frac{\partial h}{\partial \theta^i} \middle| \frac{\partial h}{\partial \theta^j} \right\rangle, \quad (3.43)$$

where the inner product is computed in the usual noise-weighted sense. Hence, for the parameter λ , the variance of its measurement is given by

$$\sigma_\lambda^{-2} = \left\langle \frac{\partial h}{\partial \lambda} \middle| \frac{\partial h}{\partial \lambda} \right\rangle = \langle \delta h | \delta h \rangle. \quad (3.44)$$

In the second equality, we have used the definition of $h(\lambda, f)$ from Eq. (3.40). Intuitively, if the standard deviation σ_λ is greater than one, i.e., if $\langle \delta h | \delta h \rangle < 1$, then the two waveforms h_0 and h_m are indistinguishable by a given detector. This provides a general criterion: every modelled waveform is indistinguishable from the true astrophysical signal if (and only if) the noise-weighted norm of their difference satisfies

$$\langle \delta h | \delta h \rangle < 1. \quad (3.45)$$

In the context of signal detection, a more practical (and slightly more conservative) cri-

terion was derived by Lindblom et al. [165]. They showed that a sufficient condition for indistinguishability is

$$\langle \delta h | \delta h \rangle < 2\rho^2 \mathbf{m}_{\max} \quad (3.46)$$

where ρ is the optimal SNR, defined as $\rho = \langle h_0 | h_0 \rangle^{1/2}$, and \mathbf{m}_{\max} is the maximum mismatch that allows a signal to remain detectable. Combining these results, we find that

$$1 < 2\rho^2 \mathbf{m}_{\max}, \quad (3.47)$$

or, equivalently,

$$\rho^2 > \frac{1}{2\mathbf{m}_{\max}}. \quad (3.48)$$

This expression tells us the minimum SNR required for a detector to distinguish the model and the true signal:

$$\rho_{\min} = \frac{1}{\sqrt{2\mathbf{m}_{\max}}}. \quad (3.49)$$

A commonly used criterion in LVK searches is to set $\mathbf{m}_{\max} = 0.03$ [166,167], which ensures that the maximum loss in SNR due to the discreteness of the template bank is less than 3%.

In the context of parameter estimation, the indistinguishability requirement can be made more precise by specifying a desired credible level p . As shown by Baird et al. [12], the mismatch between two waveforms must satisfy:

$$\mathbf{m} < \frac{\chi_k^2(p)}{2\rho^2}, \quad (3.50)$$

where k is the number of parameters in the waveform model (i.e., the dimension of parameter space), and $\chi_k^2(p)$ is the chi-square value corresponding to a confidence level p . For instance, in a 13-dimensional parameter space:

- At an SNR of 8, the mismatch must be smaller than approximately 0.16 for two waveforms to be indistinguishable at the 90% credible level.
- At an SNR of 25, the mismatch must be smaller than about 0.016 to meet the same criterion.

These results emphasize the need for increasingly accurate waveform models as detector sensitivity (and therefore SNR) improves.

Chapter 4

Black-hole remnant kicks

In Chapter 1, we introduced gravitational waves, discussing their origin as a consequence of Einstein's theory of General Relativity, how they are generated, and the variety of astrophysical systems that can produce them. Among these sources, this thesis focuses on binary black hole mergers, whose dynamics and characteristic gravitational-wave signal were explored in detail in Chapter 2.

We now turn to a specific feature of these systems: the *remnant recoil*, or *kick velocity*. In this chapter, we will explain the nature of this effect, its astrophysical significance, and how it can be measured from gravitational-wave observations.

4.1 The gravitational-wave recoil or kick

Asymmetric binaries emit gravitational waves anisotropically, carrying away *linear momentum flux* during the merger. As a result, the center-of-mass of the binary is not stationary, but moves as the two black holes orbit around each other (see Figure 4.1). Because the linear momentum of the system needs to be conserved, the orbiting black holes impart a kick to the remnant. In other words, the final black hole is born with a velocity, which is commonly referred to as the recoil or kick velocity [168–170].

Since the majority of the linear momentum flux is radiated in the last one or two orbits before the merger, the kick velocity builds up rapidly during this short period [171] (see Figure 4.2). After the merger, the remnant may experience a brief deceleration, often referred to as "anti-kick". NR studies suggest that this deceleration originates from the emission of quasi-normal modes during the ringdown phase. Specifically, the deceleration occurs when the strongest post-merger gravitational-wave emission is directed along the same axis as the remnant's motion, effectively reducing its net velocity [172–175].

Because gravitational waves are emitted anisotropically, the amplitude of the observed signal depends on the direction of the kick relative to the observer. Specifically, if the remnant black hole is recoiling toward the observer, the signal appears weaker than if it were recoiling away. This effect is illustrated in Figure 4.3.

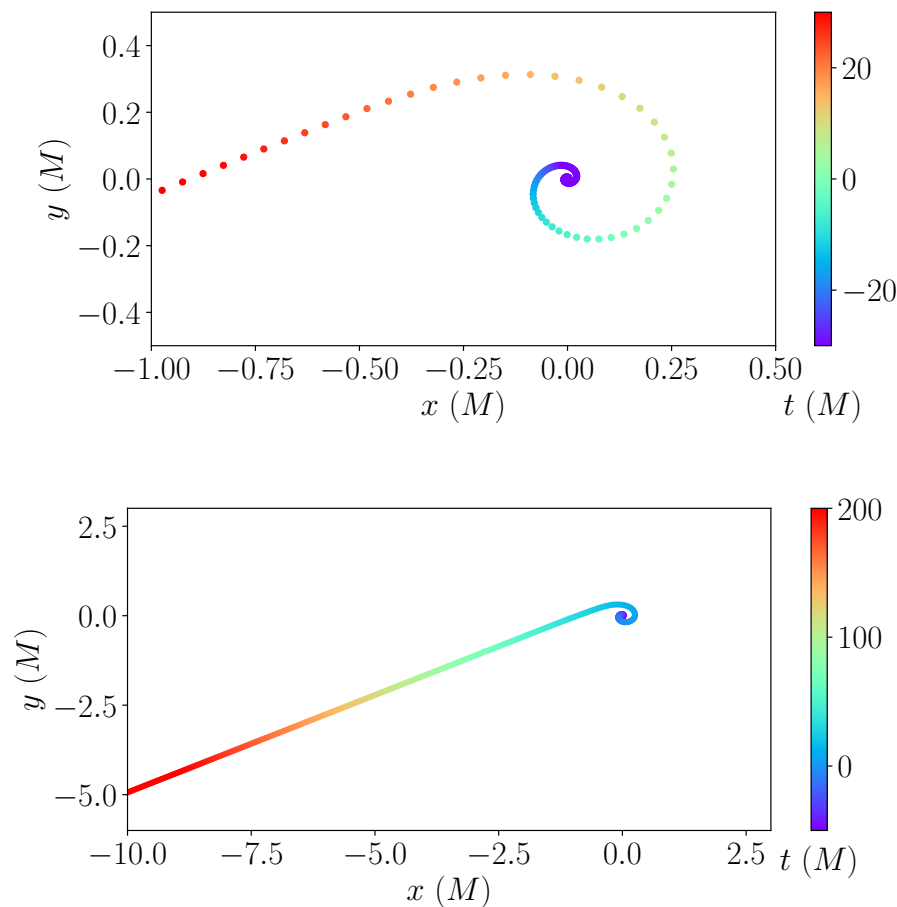


Figure 4.1: Trajectory of the center of mass for a nonprecessing binary with mass ratio $\eta = 0.188$ and individual spins $\vec{\chi}_1 = \vec{\chi}_2 = (0, 0, -0.5)$. The coordinate system is chosen such that the z -axis is aligned with the orbital angular momentum of the binary, and the x and y axes define the orbital plane and are orthogonal to each other and to z . Since nonprecessing binaries produce kick velocities parallel to the orbital plane, we only show the evolution of the center of mass in the x - y plane. The colormap represents the time evolution, with $t = 0$ defined as the moment when the amplitude of the gravitational-wave signal is maximum, corresponding to the time of merger. Both panels display the same trajectory: the bottom panel shows the full view, while the top panel provides a zoomed-in view close to the merger time.

The magnitude of this velocity is determined by the properties of the parent black holes, namely, by the asymmetry in the masses, quantified by the mass ratio, and the individual spins. The direction of the kick is determined by the spin orientations of the orbiting black holes at the time of merger. In particular, for nonprecessing binaries, kick velocities can reach up to approximately 500 km s^{-1} [177, 178] and due to symmetry, the kick lies within the orbital plane of the binary. For precessing binaries, the kick velocities can be significantly larger, reaching values of up to 5000 km s^{-1} in finely tuned configurations [22–26]. Additionally, recent studies suggest that orbital eccentricity can enhance the kick velocity further by 25% [179, 180].

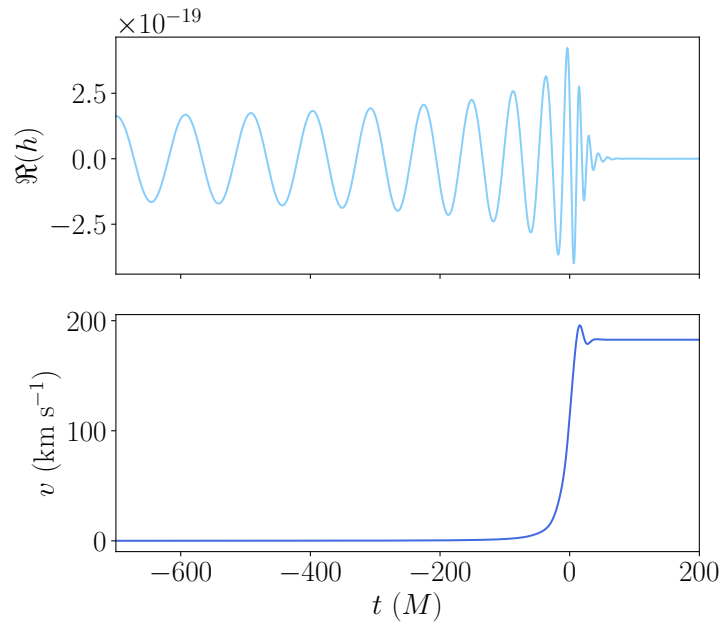


Figure 4.2: The top panel shows the gravitational-wave signal for a binary with mass ratio $\eta = 0.188$ and individual spins $\vec{\chi}_1 = \vec{\chi}_2 = (0, 0, -0.5)$. The bottom panel displays the time evolution of the velocity of the center of mass. This figure shows how the velocity builds up only one or mostly two cycles before the merger.

The first kick estimates were obtained using PN theory, and were based in calculating the linear momentum flux radiated only during the inspiral phase (see e.g. [111,170,181]). As the majority of linear momentum is emitted during the merger, a regime beyond the reach of PN approximations, accurate kick estimates only became possible following the breakthroughs in NR simulations of binary black hole mergers. Early NR results revealed that kicks could reach velocities of the order of 10^2 to 10^3 km s^{-1} (see e.g. [22,24,25,171]), significantly larger than previously expected. These findings highlighted the astrophysical importance of the kick, prompting widespread interest in its potential implications for black hole populations and galaxy evolution.

In the following section, we summarize the astrophysical relevance of black-hole kicks.

4.2 Astrophysical relevance

Supermassive black holes (SMBHs) are believed to reside at the centers of most galaxies and play a crucial role in maintaining the structure of the galaxy. When two such black holes form a binary and merge, they can produce a remnant with a significant kick velocity, which may displace the SMBH from the galactic center or even eject it entirely from its host galaxy [182]. Such an ejection can significantly affect the galaxy's structure and long-term evolution by, for example, disrupting central star formation, altering stellar dynamics, or halting the growth of the central black hole itself (see e.g. [183] for a review). Additionally, remnant kicks can impact the merger rates of massive black holes, which

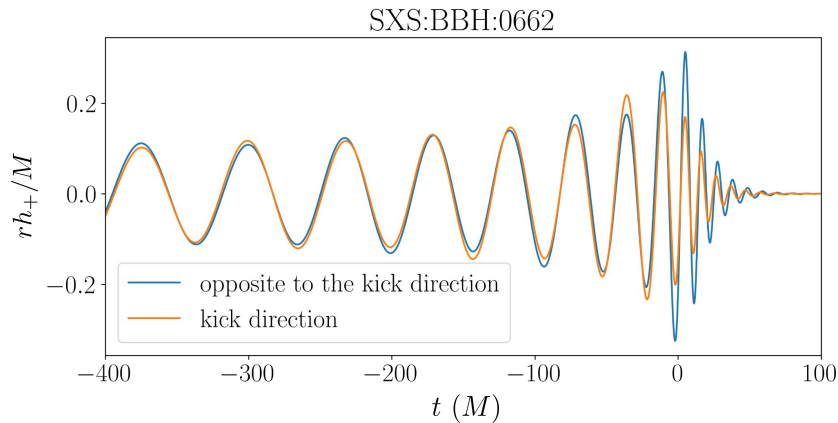


Figure 4.3: Imprint of the kick on the gravitational-wave signal. The orange curve shows the signal received when observing at the binary in the kick direction, with the remnant moving toward the observer, while the blue curve shows the signal received opposite to the kick direction. The waveform shown in this figure belongs to the SXS Catalog [176].

are relevant for future gravitational-wave detections with LISA [184].

Several candidate recoiling SMBHs have been identified through electromagnetic signatures, including spatial offsets from the host galaxy’s center and Doppler shifts in broad emission lines. The most compelling observational evidence comes from the quasar 3C 186, whose central black hole appears spatially offset from the quasar itself [185]. Other potential candidates include the SMBHs in quasars SDSSJ092712.65 + 294344.0 [186], E1821+643 [187] and CID-42 [188]. For a comprehensive overview of such candidates, we refer the reader to Komossa’s review [183].

Kick velocities are also important for understanding the merger rates of stellar-mass black-hole binaries in dense star clusters, such as nuclear star clusters or globular clusters. These environments are expected to host *hierarchical mergers*, repeated mergers where one or both black holes in the binary originate from a previous merger instead of from stellar collapse (see e.g. [17]). However, for such scenarios to occur, the merger remnants must be retained within the cluster. High kick velocities can eject these remnants from their host environments, thus suppressing the likelihood of hierarchical mergers and impacting the overall black-hole merger rate [189–192]. In my third paper, we explore how kick velocities influence the properties of black holes formed from hierarchical mergers, an essential step toward interpreting future gravitational-wave observations and understanding the astrophysical black hole population.

For stellar-mass black holes, detecting kicks through electromagnetic signals is far more challenging. Fortunately, stellar-mass black holes are now routinely observed with gravitational waves. This raises an important question: Can we measure kick velocities directly from gravitational-wave signals? And if so, have we identified any stellar-mass black holes with a large kick? The answer to both questions is yes.

The idea of measuring black-hole kicks from gravitational-wave observations was first proposed by Gerosa et al. [193], and later explored through two distinct methods for in-

ferring the kick velocity [194,195]. To date, the most compelling candidate is the remnant of the gravitational-wave event GW200129, for which the inferred recoil velocity is approximately 1500 km s^{-1} [29]. With this velocity, the remnant would have been capable of escaping not only any dense star cluster, but also entire galaxies, including the Milky Way.

But how exactly can we determine the kick velocity from a gravitational-wave signal? The next section explains the methodology used to infer this fascinating and astrophysically important parameter.

4.3 Extracting the kick from the signal

The remnant black hole is born with a momentum equal in magnitude but opposite in direction to the linear momentum carried away by the gravitational waves during the binary merger. This momentum is determined by integrating the squared time derivative of the gravitational-wave strain over the entire sphere at radius r , and over the full time evolution of the system:

$$P_i = - \lim_{r \rightarrow \infty} \frac{r^2}{16\pi} \int_{-\infty}^{\infty} dt \oint d\Omega \hat{x}_i(\theta, \varphi) |\dot{h}(t)|^2, \quad (4.1)$$

where \hat{x} is the unit radial vector in flat space,

$$\hat{x} = (\sin \theta \cos \varphi, \sin \theta \sin \varphi, \cos \theta). \quad (4.2)$$

We choose a coordinate system where the z -axis is aligned with the total angular momentum of the binary, and where the x and y axes define the orbital plane and are orthogonal to each other and to z . To calculate the integral over the sphere, the components of the unit vector can be expressed in terms of scalar spherical harmonics as [196]

$$x_x = \sin \theta \cos \varphi = \sqrt{\frac{2\pi}{3}} [Y^{1,-1} - Y^{1,1}], \quad (4.3)$$

$$x_y = \sin \theta \sin \varphi = i \sqrt{\frac{2\pi}{3}} [Y^{1,-1} + Y^{1,1}], \quad (4.4)$$

$$x_z = \cos \theta = 2 \sqrt{\frac{\pi}{3}} Y^{1,0}. \quad (4.5)$$

Instead of calculating P_x and P_y , it becomes easier to work with the complex combination $P_+ = P_x + iP_y$. By doing so, we can find the following expressions for the linear momentum of the remnant [196]:

$$P_+ = -\frac{1}{8\pi} \int_{-\infty}^{\infty} dt \sum_{\ell,m} \dot{h}_{\ell,m} \left(a_{\ell,m} \dot{h}_{\ell,m+1}^* + b_{\ell,-m} \dot{h}_{\ell-1,m+1}^* - b_{\ell+1,m+1} \dot{h}_{\ell+1,m+1}^* \right), \quad (4.6)$$

$$P_z = -\frac{1}{16\pi} \int_{-\infty}^{\infty} dt \sum_{\ell,m} \dot{h}_{\ell,m} \left(c_{\ell,m} \dot{h}_{\ell,m}^* + d_{\ell,m} \dot{h}_{\ell-1,m}^* + d_{\ell+1,m} \dot{h}_{\ell+1,m}^* \right), \quad (4.7)$$

where the coefficients $a_{\ell,m}$, $b_{\ell,m}$, $c_{\ell,m}$ and $d_{\ell,m}$ are defined as,

$$a_{\ell,m} = \frac{\sqrt{(\ell-m)(\ell+m+1)}}{\ell(\ell+1)}, \quad (4.8)$$

$$b_{\ell,m} = \frac{1}{2\ell} \sqrt{\frac{(\ell-2)(\ell+2)(\ell+m)(\ell+m-1)}{(2\ell-1)(2\ell+1)}}, \quad (4.9)$$

$$c_{\ell,m} = \frac{2m}{\ell(\ell+1)}, \quad (4.10)$$

$$d_{\ell,m} = \frac{1}{\ell} \sqrt{\frac{(\ell-2)(\ell+2)(\ell-m)(\ell+m)}{(2\ell-1)(2\ell+1)}}. \quad (4.11)$$

The velocity of the remnant is then given by

$$v = \frac{\sqrt{P_x^2 + P_y^2 + P_z^2}}{\gamma m_f}, \quad (4.12)$$

where m_f is the mass of the remnant black hole and γ is the relativistic factor, also known as Lorentz factor, $\gamma = (1 - v^2/c^2)^{-1/2}$. Given that remnant kicks take values up to ~ 5000 km s⁻¹ for quasi-circular binaries, relativistic corrections are negligible, and therefore, the γ factor is often neglected in this expression.

Hence, the kick velocity of a specific gravitational-wave signal is determined by computing the quantities P_+ and P_z . For nonprecessing binaries, symmetry in the gravitational-wave emission across the orbital plane causes the z -component P_z to cancel out. For precessing binaries, however, this symmetry is broken, and generally P_z does not vanish.

To estimate the kick velocity from a gravitational-wave event, one can generate a waveform for each posterior sample of the binary parameters and compute the corresponding kick using Equation (4.12). This approach requires selecting a specific waveform model to generate gravitational-wave signals. In Chapter 6 we compare the kick posteriors obtained using two different waveform models, PhenomXPHM and PhenomXO4a, and demonstrate the importance of including mode asymmetries in a model to accurately measure the kick velocity in gravitational-wave events.

Alternatively, several models of the remnant properties exist, which directly predict the kick velocity from the initial properties of the binary. These include precession [197], `surrkick` [198], `surf inBH3dq8` [199] and `NRSur7dq4Remnant` [35]. All models are implemented in Python and differ mainly in the number of NR simulations used for development, leading to differences in the accuracy of their kick predictions. Among these, `NRSur7dq4Remnant` is currently the most accurate, as demonstrated by Figure 7 of Varma et al. [35]. This is the model we use in Chapter 7 to estimate the kicks of hierarchical mergers.

Part II

Original scientific results

Chapter 5

Inconsistent black hole kick estimates from gravitational-wave models

In this chapter, we include a reprint of the following article:

[30] Angela Borchers and Frank Ohme. Inconsistent black hole kick estimates from gravitational-wave models. *Class. Quant. Grav.* 40, 095008 (2023)

Inconsistent black hole kick estimates from gravitational-wave models

Angela Borchers^{1,2,*}  and Frank Ohme^{1,2} 

¹ Max Planck Institute for Gravitational Physics (Albert Einstein Institute),
Callinstraße 38, D-30167 Hannover, Germany

² Leibniz Universität Hannover, 30167 Hannover, Germany

E-mail: angela.borchers.pascual@aei.mpg.de

Received 24 October 2022; revised 3 March 2023

Accepted for publication 20 March 2023

Published 4 April 2023



CrossMark

Abstract

The accuracy of gravitational-wave (GW) models of compact binaries has traditionally been addressed by the mismatch between the model and numerical-relativity (NR) simulations. This is a measure of the overall agreement between the two waveforms. However, the largest modelling error typically appears in the strong-field merger regime and may affect subdominant signal harmonics more strongly. These inaccuracies are often not well characterised by the mismatch. We explore the use of a complementary, physically motivated tool to investigate the accuracy of GW harmonics in waveform models: the remnant's recoil, or kick velocity. Asymmetric binary mergers produce remnants with significant recoil, encoded by subtle imprints in the GW signal. The kick estimate is highly sensitive to the intrinsic inaccuracies of the modelled GW harmonics during the strongly relativistic merger regime. Here we investigate the accuracy of the higher harmonics in four state-of-the-art waveform models of binary black holes. We find that the SEOBNRv4HM_ROM, IMRPhenomHM, IMRPhenomXHM and NRHybSur3dq8 models are not consistent in their kick predictions. Our results enable us to identify regions in the parameter space where the models require further improvement and support the use of the kick estimate to investigate waveform systematics. We discuss how NR kick estimates could be used to calibrate waveform models further, proposing the first steps towards kick-based gravitational-wave tuning.

* Author to whom any correspondence should be addressed.



Original Content from this work may be used under the terms of the [Creative Commons Attribution 4.0 licence](https://creativecommons.org/licenses/by/4.0/). Any further distribution of this work must maintain attribution to the author(s) and the title of the work, journal citation and DOI.

Keywords: gravitational waveform models, waveform systematics, black-hole remnant kicks

(Some figures may appear in colour only in the online journal)

1. Introduction

Every gravitational-wave (GW) transient detection reported by the LIGO, Virgo and KAGRA (LVK) Collaborations to date is consistent with the expected signal radiated by merging compact binaries [1–4]. In order to extract the properties imprinted in the detected GW signals, Bayesian parameter estimation studies rely on the use of gravitational waveform models [5, 6]. These models need to be sufficiently accurate such that they do not cause any systematic biases when analysing the observed data. Systematic uncertainties of currently available models are in most cases below the statistical errors of the Advanced LIGO [7] and Advanced Virgo [8] detectors [9]. However, in light of the enhancement in the sensitivity of the current and next generation of GW detectors, the systematic errors of the models will have to be further reduced so that they are consistently below the instrumental ones. In particular, for the third-generation detector network, the mismatch errors of semi-analytical waveform models will need to be reduced by at least three orders of magnitude [10].

Having an accurate description of the GW higher harmonics (also named modes or multipoles) is relevant for several reasons. The inclusion of subdominant harmonics significantly improves the description of the signal, in particular, when characterising asymmetric binary systems. Indeed, the omission of higher harmonics in a waveform model can influence the search and interpretation of particular GW signals when the binary is oriented in specific configurations and can lead to systematic biases in the estimation of the source parameters [11–15]. The development of waveform models which include higher harmonics and the regular detection of GWs have recently allowed performing such analyses with observed GW signals of binary black holes (BBHs). The two events GW190412 [16] and GW190814 [17] observed by the LIGO and Virgo detectors, have provided strong evidence for the measurement of gravitational higher harmonics in the observed signals. Besides, as studied in [18], the inclusion of subdominant harmonics can reduce the uncertainty of parameter estimation results and can even shift posterior samples, as shown in the re-analysis of GW170729 [19] with the latest generation of phenomenological waveform models [20–26].

As detectors become more sensitive, GW observations will become more frequent and will include higher signal-to-noise ratios. If the waveform models employed in the analysis of such events are not reliable enough, we might mischaracterise the sources of these signals. Conversely, the existence of ‘louder’ GW events will allow us to observe more subtle physical effects in the signals, such as the remnant’s kick. Asymmetric compact binaries radiate linear momentum through GWs causing, in turn, the recoil of the remnant object. This process is left imprinted in the emitted GW signal. Because of its astrophysically important consequences (see [27] for a review), there is a strong interest in inferring the remnant’s kick velocity directly from GW signals. Several methods have been proposed to discuss the detectability of kicks in GW events [28–30]. Among the current GW observations, GW190814 shows the most informative kick estimate from the events of the second GW transient catalog (GWTC-2) [31], while GW200129_06 5458 shows support for a large kick velocity [32]. However, the kick’s subtle signatures have not been precisely measured so far. If we want to observe these in the signal, we need waveform models that accurately capture such traces.

The accuracy of waveform models has traditionally been quantified by comparing the waveform model to numerical relativity (NR) or hybrid waveforms (see e.g. [33]). NR simulations

yield the most accurate description of the GW signal and they are the only way to access the highly dynamic merger regime from first principles. The standard method of comparison is based on calculating a match between the model and an NR or hybrid waveform, based on a Wiener inner product. This is the same inner product that is used to assess the likelihood of whether the GW data contain a signal, by comparing the agreement between observational data and waveform templates. The match represents a notion of the angle between two signals (related to a distance between them) and is a standard quantity used in the waveform modelling community to test the quality of a model (see e.g. [34]).

A complementary tool to standard match calculations has recently been suggested in [35]. The authors propose an infinite set of constraints on compact binary coalescence waveforms, predicted by full, non-linear general relativity (GR). The set of constraints are the Bondi-van der Burg–Metzner–Sachs (BMS) balance laws, which are induced by the infinite-dimensional group of supertranslations [36], the natural extension of the four-dimensional group of translations defined at null infinity. The theory provides the opportunity to test waveform systematic errors in a new way. The balance laws can be particularly useful for regions of the parameter space where performing NR simulations might be more challenging or where these simulations are not abundant enough for the subsequent calibration of the approximate waveform models. Because these constraints come from exact GR, the balance laws are also attractive to quantify the accuracy of NR waveforms, which are often considered as a proxy of the exact waveform predicted by GR. The set of balance laws have already been applied to currently available waveform models to test their accuracy based on their angular momentum [37] and the gravitational memory estimates [38]. Besides, the Simulating eXtreme Spacetimes (SXS) Collaboration has recently employed the BMS balance laws to correct the extracted SXS waveforms by incorporating gravitational memory effects [39]. Apart from imposing accuracy requirements, the theory presented in [35] represents new tests of GR.

Although the expression of the radiated three-momentum flux by itself does not represent a BMS balance law, the calculation of the linear momentum flux (or the kick velocity) has recently been used to test the accuracy of the relative phase shifts between the GW harmonics of the state-of-the-art phenomenological waveform models [21, 25]. These studies have focused on the dependency of the kick magnitude on the symmetric mass ratio of the binary.

Using the recoil prediction to assess the waveform accuracy is attractive for three main reasons: (1) The kick estimate is a highly sensitive quantity [40–42]. The presence of small time and phase deviations that appear from incorrect modelling can result in significantly different kick predictions. (2) The kick builds up in the merger, the highly dynamic region that is most complex to model. Therefore, a correct kick estimate requires an accurate description of the merger. (3) The asymmetries of the system that lead to the kick are most completely characterised when using the dominant and higher harmonics. Thus, an accurate description of the subdominant harmonics is essential for a correct prediction of the kick velocity.

In this paper, we explore the use of the kick velocity as a diagnostic test for waveform models, by analysing the waveform estimates of the magnitude and orientation of the kick velocity over the parameter space. Precessing binaries lead to the largest recoil velocities [43] and are therefore observationally easier to access. However, only one of the available precessing waveform models includes the mode asymmetries that generate out-of-plane kicks for precessing binaries: the NR Surrogate (NR Sur) model. This model only covers part of the parameter space relevant for LVK data analysis. Kicks in nonprecessing binaries, on the other hand, can be predicted by any of the nonprecessing models. For this reason, in this work, we focus on nonprecessing systems as a first step to understanding the accuracy of GW harmonics through remnant kicks.

We evaluate the accuracy of four waveform models which are used in current GW data analysis studies. We also analyse the performance of the NR Sur fit [44], recently used to make the first measurement of a large kick velocity in an observed GW signal [32]. By exploiting the features of the kick, we create a set of diagnostic tests that can be applied to any waveform model to identify modelling inaccuracies over the parameter space.

After a description of the methodology of our work in section 2, we use the kick velocity to evaluate the accuracy of several gravitational waveforms and analyse their harmonic contributions to the kick in section 3. In section 4 we further explore the applications of the kick in the context of waveform modelling by addressing the first steps towards kick-based GW tuning. Finally, we summarise our results in section 5.

2. Method

2.1. Waveform models

The GW signal radiated by a BBH coalescence is uniquely determined by a number of physical parameters that characterise the binary. Astrophysical quasi-circular BBHs are described by the two individual masses m_i and the individual spin vectors. It is common to use the dimensionless spin parameter $\vec{\chi}_i = \vec{S}_i/m_i^2$ for the spin components. BBHs on quasi-circular orbits are thus characterised by eight intrinsic parameters:

$$\lambda = \{m_1, m_2, \vec{\chi}_1, \vec{\chi}_2\}. \quad (1)$$

The total mass of the binary is $M = m_1 + m_2$ and the symmetric mass ratio is defined as $\eta = m_1 m_2 / M^2$. Throughout this work we use geometric units, $G = c = 1$. Apart from the intrinsic parameters, there are seven extrinsic parameters: the spherical angles $\{\theta, \varphi\}$, which describe the orientation of the binary, the luminosity distance d_L , the coalescence time t_c , the declination and right ascension $\{\vartheta, \phi\}$, and the polarization angle ψ .

In NR, it is common to use the Newman–Penrose scalar, Ψ_4 , which is derived from the Weyl tensor and encodes the outgoing gravitational radiation as $\Psi_4 = -\dot{h}$, where $h := h_+ - ih_\times$. The behaviour of a quantity under rotations is expressed by the spin weight. Because the Weyl tensor component has spin weight $s = -2$, the GW strain can be expanded in a basis of spin-weighted spherical harmonics (SWSH) [45],

$$\lim_{r \rightarrow \infty} rh = \sum_{\ell=2}^{\infty} \sum_{m=-\ell}^{\ell} h_{\ell,m}(t, \lambda) {}^{-2}Y_{\ell,m}(\theta, \varphi). \quad (2)$$

Here $h_{\ell,m}(t, \lambda)$ are the GW spherical harmonics associated to the multipole moments. The (2,2) spherical harmonic is the quadrupolar term, while those associated with higher multipole moments are referred to as higher harmonics. The $h_{\ell,m}(t, \vec{\lambda})$ depend on the time and the intrinsic physical properties of the source, $\vec{\lambda}$. The orientation of the source with respect to the observer is encoded in the spherical harmonic basis functions of spin weight -2 , ${}^{-2}Y_{\ell,m}(\theta, \varphi)$. The coalescence phase φ_c is sometimes included as an extrinsic parameter of the binary, and is degenerate with the azimuthal angle φ in nonprecessing systems.

In a nonprecessing binary, the spins of the individual black holes are parallel to the direction of the orbital angular momentum, and the evolution of the binary takes place in the

Table 1. Gravitational waveform models used in our study. The second column indicates the higher harmonics included in each of the models.

Waveform model	Multipoles (ℓ, m)
IMRPhenomHM	$(2, 2), (2, 1), (3, 3), (3, 2), (4, 4), (4, 3)$
IMRPhenomXHM	$(2, 2), (2, 1), (3, 3), (3, 2), (4, 4)$
SEOBNRv4HM_ROM	$(2, 2), (2, 1), (3, 3), (4, 4), (5, 5)$
NRHybSur3dq8	$\ell \leq 4, (5, 5)$ but not $(4, 0), (4, 1)$

plane perpendicular to the orbital angular momentum. In such case, there exists an equatorial symmetry between the (ℓ, m) and $(\ell, -m)$ modes, given by the relation:

$$h_{\ell, m}(t) = (-1)^\ell h_{\ell, -m}^*(t), \quad (3)$$

where $*$ refers to the complex conjugation.

Although NR simulations determine the closest description of the real set of $h_{\ell, m}$ harmonics, for GW data analysis purposes, waveforms need to be fast to evaluate, and NR simulations are in this context computationally excessively expensive. For this reason, different modelling strategies have been developed, leading to the establishment of three main waveform families: the NR calibrated effective-one-body (EOBNR) [46–51], the phenomenological (Phenom) [20, 24, 52–59] and the NR Sur description [60–62]. These models characterise the full inspiral-merger-ringdown signal over the parameter space, and their development has been based on combining analytic and numerical methods appropriate for each of the different phases of the binary’s evolution.

The inspiral and merger phases can be partly described by the EOB formalism, which maps the two-body problem to that of a test particle in an effective metric (see [63] for a review) and free coefficients are calibrated to NR data. On the other hand, Phenom models are based on employing hybrid waveforms that connect an analytical inspiral description with NR data for the late inspiral, merger and ringdown, which are then described by a phenomenological fit. The ringdown phase of the remnant black hole is characterised by the emission of quasinormal modes [64], mathematically described in terms of exponentially damped oscillations. In contrast, the NR Sur family is based on a reduced order method interpolation of the NR simulations over the parameter space, built to cover a larger region of the parameter space than that covered by the NR waveforms.

In our work, we analyse the kick predictions of four nonprecessing waveform models that include higher harmonics: SEOBNRv4HM_ROM [65], two phenomenological models, namely, IMRPhenomHM [57] and the more recent IMRPhenomXHM [21, 22], and NRHybSur3dq8 [61]. Table 1 indicates which gravitational multipoles are included in each waveform model.

2.2. Linear momentum flux

Because asymmetric BBHs radiate linear momentum through GWs, the remnant black hole acquires a kick velocity. This can be mathematically described from the linear momentum flux radiated by the binary. Since the linear momentum of the system is initially zero, the momentum of the remnant is equal to the opposite of the three-momentum flux carried by the radiated GWs, and is given by:

$$P_i = - \lim_{r \rightarrow \infty} \frac{r^2}{16\pi} \int_{-\infty}^{\infty} dt \oint d\Omega \hat{x}_i(\theta, \varphi) |\dot{h}|^2, \quad (4)$$

where $d\Omega = \sin\theta d\theta d\varphi$ and $\hat{x}_i = (\sin\theta \cos\varphi, \sin\theta \sin\varphi, \cos\theta)$ is the unit vector expressed in the spherical harmonic basis. Because the asymmetries that cause the kick are encoded in the GW signal, the momentum of the remnant black hole is entirely determined by the waveform h . In asymmetric BBH systems, gravitational higher harmonics are particularly loud during merger. For this reason, we express the radiated momentum in terms of the dominant and higher multipoles by decomposing the gravitational radiation on a basis of SWSH.

We choose the z axis along the orbital angular momentum of the binary. In a nonprecessing system, the binary orbits in a fixed plane, that we choose as the x - y plane. In this case, the z -component of the momentum vanishes and the kick takes place in the orbital plane. The momentum can then be expressed as a combination of the two planar coordinates, $\vec{P} := P_x + iP_y$. After expressing the unit-vector in terms of the SWSH and integrating over the 2-sphere, one can show that the components of the momentum are given by [66]:

$$\vec{P} = -\frac{1}{8\pi} \int_{-\infty}^{\infty} dt \sum_{\ell=2}^{\infty} \sum_{m=-\ell}^{\ell} \dot{h}_{\ell,m} (a_{\ell,m} \dot{h}_{\ell,m+1}^* + b_{\ell,-m} \dot{h}_{\ell-1,m+1}^* - b_{\ell+1,m+1} \dot{h}_{\ell+1,m+1}^*), \quad (5)$$

where the coefficients $a_{\ell,m}$ and $b_{\ell,m}$ read:

$$a_{\ell,m} = \frac{\sqrt{(\ell-m)(\ell+m+1)}}{\ell(\ell+1)}, \quad (6)$$

$$b_{\ell,m} = \frac{1}{2\ell} \sqrt{\frac{(\ell-2)(\ell+2)(\ell+m)(\ell+m-1)}{(2\ell-1)(2\ell+1)}}. \quad (7)$$

The kick velocity will then be given by $\vec{v}_f = -\vec{P}/M_f$, where M_f is the mass of the remnant black hole.

2.3. Implementation

We have implemented the expression of the momentum (5) for the mentioned gravitational waveform models. We use the LIGO Algorithm Library (LALSuite) software [67] to obtain individual higher harmonics of the GW signal. It is physically meaningful to compute the momentum flux in the time domain. However, for data analysis purposes the SEOBNRv4HM_ROM and Phenom models that we employ in our study have been developed in the frequency domain. For this reason, we inverse Fourier transform the GW signal after obtaining the individual spherical harmonics in the frequency domain. We use $f_{\min} = 10$ Hz for the lower frequency cut-off and because the kick velocity does not depend on the total mass of the binary, we fix the total mass to $M = 50M_{\odot}$. For a nonspinning equal-mass binary this corresponds to 63 orbits before merger. To calculate the remnant's final mass, we use waveform specific fitting functions which are available in LALSuite³. The final mass is internally computed from the radiated energy and is scaled by the original total mass. For details on how the radiated energy is calculated we refer the reader to the paper references.

We compare the kick estimates with the predictions of a set of NR waveforms. We have used SXS waveforms [68] from the LVCNR Waveform Catalog [69] with the highest resolution available. These include all subdominant harmonics up to $\ell = 8$, with $|m| \leq \ell$. The NR

³ In particular, we use `SimPhenomUtilsIMRPhenomDFinalMass` [55, 56] for PhenomHM, `SimIMRPhenomXFinalMass2017` [20] for PhenomXHM, `SimIMREOBFinalMassSpinPrec` [65] for SEOBNRv4HM_ROM and `NRSur3dq8Remnant` [44] for NRHybSur3dq8.

data come with a metadata file which includes a *coordinate* recoil velocity estimation that is calculated based on the trajectory $\vec{x}(t)$ of the coordinate centre of the apparent horizon of the remnant. Although this value is close to the one computed from the momentum flux integral, they might not be necessarily the same [68]. For this reason, we calculate the recoil velocity from the full waveform by using the momentum flux integral. For the final mass estimate, we use the value indicated at the metadata file.

Finally, we also employ the NR Sur fit [44], which estimates the final properties of the remnant black hole $\{m_f, \vec{\chi}_f, \vec{v}_f\}$ from the initial intrinsic properties of the binary $\{m_1, m_2, \vec{\chi}_1, \vec{\chi}_2\}$. The surrogate model is trained on quasicircular NR simulations using Gaussian process regression. The NR Sur fit includes two surrogate models: the NRSur7dq4Remnant fit, trained on precessing systems with $q \leq 4$ and $|\vec{\chi}_1| = 0.8$, $|\vec{\chi}_2| = 0.8$, and the NRSur3dq8Remnant fit, trained on nonprecessing systems with $q \leq 8$ and $|\vec{\chi}_1| = 0.8$, $|\vec{\chi}_2| = 0.8$.

The kick prediction is in general limited by two aspects. First, waveform models only include a finite number of harmonics. Phenom models include a subset of the spherical harmonics with $\ell \leq 4$, while SEOBNRv4HM_ROM and the NRHybSur3dq8 include a subset of the harmonics up to $\ell \leq 5$ (see table 1). What we use as the gravitational strain is given by:

$$\lim_{r \rightarrow \infty} rh = \sum_{\ell=2}^{\ell_{\max}} \sum_{m=-\ell}^{\ell} h_{\ell,m}(t, \lambda) {}^{-2}Y_{\ell,m}(\theta, \varphi). \quad (8)$$

However, the radiated momentum flux is related to the sum over an infinite number of subdominant harmonics. The omission of specific harmonics can influence the final kick velocity value.

Second, since waveforms are only available for a limited time range, the time integration of equation (5) is truncated to a finite time. Because the GW amplitude decreases exponentially in the ringdown, having a finite upper limit does not influence the final velocity value. The lower bound limits the amount of early inspiral phase included in the waveform. Based on PN calculations, there exist expressions of the net linear momentum radiated during the early inspiral phase [70–72]. The contribution of the inspiral phase to the total linear momentum is significantly smaller than the merger contribution. For a non-spinning binary with symmetric mass ratio 0.2 and total mass $50M_{\odot}$, the radiated linear momentum up to 10 Hz is less than 0.05 km s^{-1} . In our calculations we neglect the linear momentum radiated up to 10 Hz.

We apply the methods discussed to calculate the estimates of the kick velocity from the previously specified waveform models over the parameter space. We divide our results into three parts. We first make model-model comparisons of the magnitude and orientation of the kick velocity. Then, we quantify where exactly in the parameter space models show disagreements by analysing the dependence of the kick estimates on the mass ratio and the individual spin components. We then compare the harmonic contributions of the kick velocity estimated by the models.

Even though NR simulations provide the closest description of the true waveform, only a limited set of NR waveforms is available. In the region where binaries have highly asymmetric masses, simulations are particularly sparse. Therefore, studying the agreement with respect to a particular model allows us to make a more exhaustive analysis of the differences between model estimates over the parameter space. For this reason, we have analysed model-model agreement by choosing a reference model and calculating the relative difference with respect to its estimates.

Because the NRHybSur3dq8 model includes a larger set of subdominant harmonics, we are able to compare all the harmonic contributions predicted by the models (each model has a particular set of harmonic contributions, different from the other models) to the NR Sur model

estimates. The NR Sur is slightly more accurate than the Phenom and SEOBNR models. These models, on the other hand, cover a wider range of the parameter space than the NR Sur, relevant for LVK data analysis purposes.

However, since the true waveform is unknown, the actual value of the kick velocity is also unknown. By comparing the predictions of two different models, it is difficult to tell which of the two estimates is more accurate. However, disagreements between models are a reflection of systematic errors in either or both waveform models.

The direction of the kick velocity is subject to the orientation of the binary at the initial reference frame. In order to compare the estimates of the direction of the kick velocity from different models, we need to make sure that all waveforms are initially aligned in phase the same way. We first align the waveforms in time, setting $t=0$ at the maximum amplitude of the (2,2) spherical harmonic. We then apply a phase shift to each (ℓ, m) harmonic equal to $\Delta\phi_{\ell,m} = m/2 \times \phi_{2,2}$, where $\phi_{2,2}$ is the optimal phase shift of the (2,2) spherical harmonic, obtained from the match calculation between the model of interest and the reference model. The match is expressed in terms of the Wiener inner product, defined as:

$$\langle h_1, h_2 \rangle = 4 \Re \int_{f_{\min}}^{f_{\max}} \frac{\tilde{h}_1(f) \tilde{h}_2^*(f)}{S_n(f)} df, \quad (9)$$

where \tilde{h} indicates the Fourier transform of h and $S_n(f)$ is the one-sided power spectral density of a GW detector. When aligning two waveforms in phase, we consider a flat noise sensitivity $S_n = 1$. The match \mathcal{M} is defined as the normalized inner product maximized over relative time and phase shifts between the two waveforms, i.e.:

$$\mathcal{M}(h_1, h_2) = \max_{t_0, \varphi_0} \frac{\langle h_1, h_2 \rangle}{\|h_1\| \|h_2\|}. \quad (10)$$

The mismatch \mathcal{MM} is then defined as:

$$\mathcal{MM}(h_1, h_2) = 1 - \mathcal{M}(h_1, h_2). \quad (11)$$

3. Results

3.1. Model-model comparisons

We calculate the estimates of the kick velocity from the indicated waveform models for discrete points in the parameter space. The spin components are uniformly distributed by selecting points in the interval $\chi_{1,2}^z = [-0.8, 0.8]$ with step size $\Delta\chi_{1,2}^z = 0.1$. We consider masses m_1 and m_2 subject to the symmetric mass ratio and total mass values. Because the estimate of the kick velocity does not depend on the total mass, we only sample over the symmetric mass ratio. The symmetric mass ratio is sampled uniformly by choosing 31 points in the interval $\eta = [0.10, 0.25]$ with step size $\Delta\eta = 0.005$, giving a total number of 8959 points in the parameter space. The region of the parameter space that we choose to analyse is limited by the region to which the NRHybSur3dq8 model is calibrated.

In figure 1 we show the differences of the kick magnitude predicted by the PhenomHM, PhenomXHM and SEOBNRv4HM_ROM waveform models compared to the NRHybSur3dq8 model. We observe that the differences of PhenomXHM and SEOBNRv4HM_ROM have comparable values, with SEOBNRv4HM_ROM showing better agreement with the NRHybSur3dq8 model. The distribution of PhenomXHM has a mean value of $\Delta v \sim 9 \text{ km s}^{-1}$ and a standard deviation (std) of $\sigma \sim 19 \text{ km s}^{-1}$. For SEOBNRv4HM_ROM, the mean value lies at $\Delta v \sim -0.4 \text{ km s}^{-1}$ and the std $\sigma \sim 19 \text{ km s}^{-1}$. On the other hand, the PhenomHM model

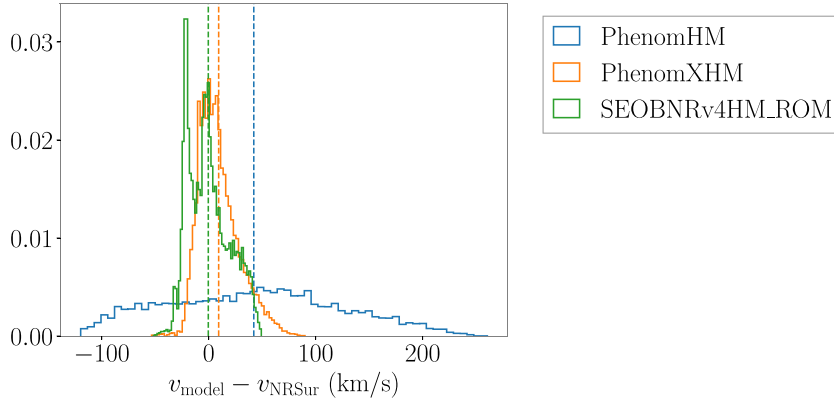


Figure 1. Distribution of the differences on the estimates of the kick magnitude between the waveform models indicated at the panel and the NRHybSur3dq8 model. We have considered nonprecessing black-hole binary configurations with $0.1 < \eta < 0.25$ and $-0.8 < \chi_{1,2}^z < 0.8$. Dashed vertical lines indicate the mean value of each normalised distribution.

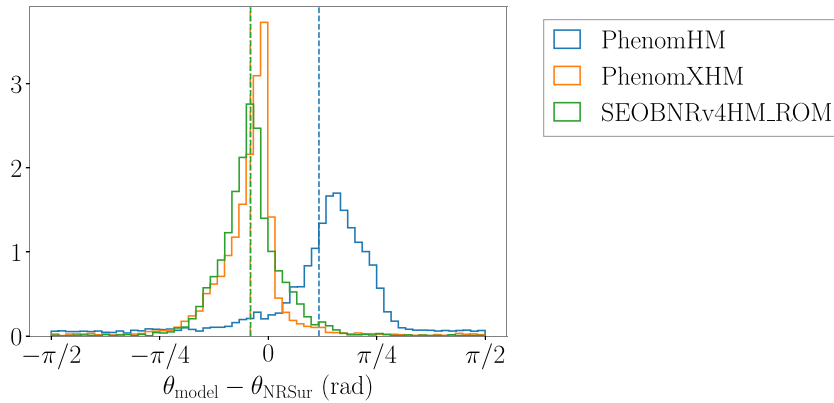


Figure 2. Distribution of the differences on the estimates of the kick orientation between the waveform models indicated at the panel and the NRHybSur3dq8 model. We have considered nonprecessing black-hole binary configurations with $0.1 < \eta < 0.25$ and $-0.8 < \chi_{1,2}^z < 0.8$. Dashed vertical lines indicate the mean value of each normalised distribution.

largely over- and underestimates the kick velocity, with a mean value of $\Delta v \sim 42 \text{ km s}^{-1}$ and a standard deviation of $\sigma \sim 81 \text{ km s}^{-1}$. Figure 1 shows that PhenomHM has been superseded in accuracy by its respective newer version, PhenomXHM.

We now discuss the distributions of the differences on the direction of the kick velocity, shown in figure 2. In this case we observe good agreement between PhenomXHM and SEOBNRv4HM_ROM with the NRHybSur3dq8 model in the kick orientation, with the mean value at $\Delta\theta \sim -0.13 \text{ rad}$ and $\Delta\theta \sim -0.13 \text{ rad}$ respectively. For PhenomHM, the distribution appears shifted by $\Delta\theta \sim 0.4 \text{ rad}$, meaning that the orientation estimates are inconsistent with the three other waveform models.

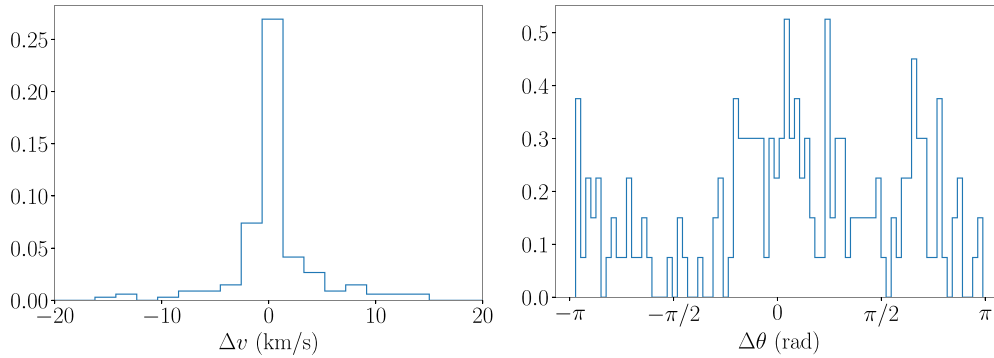


Figure 3. Error estimate of the kick magnitude (left) and orientation (right) for 173 nonprecessing SXS waveforms coming from the NR resolution error.

The NRHybSur3dq8 model is trained against 104 hybridized nonprecessing NR waveforms [61] and inherits the accuracy limitations of the hybrid waveforms. We now investigate the uncertainty of the kick estimate in NR simulations. These waveforms contain two primary sources of error: numerical resolution and extrapolation errors. In the case of SXS waveforms, the uncertainty involved in the extrapolation procedure is, on average, significantly smaller than the resolution error [68]. For this reason, here we focus on understanding the influence of the resolution error in our kick estimates. We estimate the kick uncertainty by comparing the kick values of the highest two resolutions. In particular, we have used 173 nonprecessing NR waveforms from the SXS Collaboration, which include at least two resolutions. The set of waveforms we employ cover a larger region of the parameter space than the set used to calibrate the NRHybSur3dq8, with $q \leq 10$ and $\chi_{1,2}^2 \leq 0.994$. We provide a list of the waveforms employed in appendix B. The error estimates of the kick magnitude and orientation are shown in figure 3.

The distribution of the kick-magnitude uncertainty has a std of $\sim 10 \text{ km s}^{-1}$. While the errors of waveform models have values between $(-\pi/2, \pi/2)$, the orientation errors of the NR waveforms lie between $(-\pi, \pi)$. The maximum value is set by our methodology and is different in each case. In the case of waveform models, we align the spherical harmonics with a phase shift $\Delta\phi_{\ell,m} = m/2 \times \phi_{2,2}$. Here, the phase of the $(2, 2)$ harmonic is degenerate:

$$\phi_{2,2} = \phi_{2,2}^{\text{opt}} + 2\pi n, n \in \mathbb{Z}, \quad (12)$$

where $\phi_{2,2}^{\text{opt}}$ is the optimal phase shift of the $(2, 2)$ spherical harmonic. This means that the phase shift is also degenerate:

$$\Delta\phi_{\ell,m} = m/2 \times \phi_{2,2}^{\text{opt}} + \pi n, n \in \mathbb{Z}. \quad (13)$$

Applying a phase shift $\Delta\varphi$ to a waveform translates as rotating the kick orientation by $\Delta\varphi$. Therefore, when applying $\Delta\phi_{\ell,m}$ to each spherical harmonic, the kick orientation acquires a πn degeneracy. For this reason, the orientation estimates of the waveform models take values in the range $\theta \in (-\pi/2, \pi/2)$ and thus, the orientation differences also lie between $(-\pi/2, \pi/2)$. With NR waveforms, however, there is no such degeneracy and the orientation differences lie between $(-\pi, \pi)$.

What is important here is that both waveform models and NR simulations have orientation errors that extend to the maximum values. In the case of NR waveforms, we measure a standard

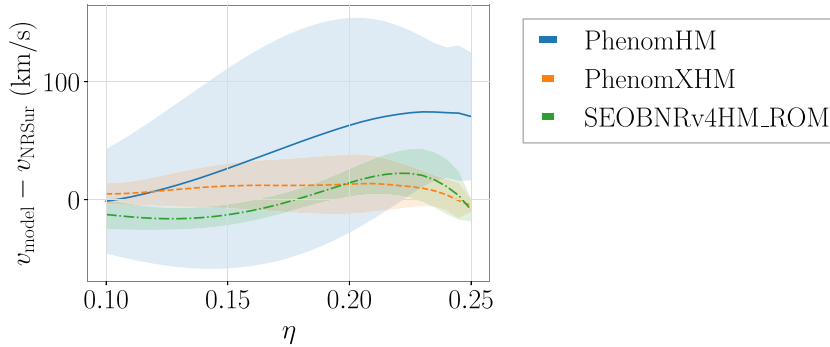


Figure 4. Comparison of the differences on the estimates of the kick magnitude between the models indicated at the panel and the NRHybSur3dq8 model. The shaded region represents the std of such distribution at each symmetric-mass-ratio value, while the curves represent the mean value of the distributions.

deviation of ~ 0.8 rad. The large uncertainty of the kick orientation is mostly related to the fact that, for each waveform resolution, the dominant harmonic contribution, which comes from the $(2, \pm 1)(2, \pm 2)$ pair of harmonics, has a significantly different kick orientation in each case.

3.2. Symmetric-mass-ratio dependency

We now proceed to find the regions in parameter space where the models show larger disagreement, reflecting the existence of waveform modelling inaccuracies in one or both of the models. We use the same data as in section 3.1 and study the dependency on the symmetric mass ratio. Figure 4 shows the differences on the magnitude of the kick velocity as a function of the symmetric mass ratio, while figure 5 shows the differences on the kick orientation. The curves represent the mean value of the distributions at each symmetric-mass-ratio value, while the shaded region represents the std in each case.

Similar to figure 1, in figure 4 we observe that the distributions of PhenomXHM and SEOBNRv4HM_ROM have comparable values for the kick magnitude. They both show the larger differences in the region between $\eta \in [0.20, 0.25]$. We observe that the differences between PhenomHM and NRHybSur3dq8 are significantly larger than for PhenomXHM and SEOBNRv4HM_ROM. In particular, the estimates of PhenomHM deteriorate in accuracy with increasing symmetric-mass-ratio values, showing the largest inconsistencies close to the equal-mass case.

Regarding the estimates of the kick orientation, in figure 5 we observe a constant close-to-zero mean and std for SEOBNRv4HM_ROM. Although the estimates of PhenomXHM are comparable to those of SEOBNRv4HM_ROM, they show a slightly more complicated correlation with the symmetric mass ratio, with small changes in the width of the distributions. Similar to the figure 2, the estimates of PhenomHM appear to be shifted by $\sim \pi/8$ rad in the region $\eta \in [0.10, 0.20]$, and show the largest std from the NRHybSur3dq8 values. The estimates converge to zero towards the equal-mass case.

In appendix A, we show the harmonic contributions of the kick velocity as a function of the symmetric mass ratio, which help to understand the origin of the broad distributions observed for PhenomHM. We also include the symmetric-mass-ratio dependency of the NR errors in appendix C.

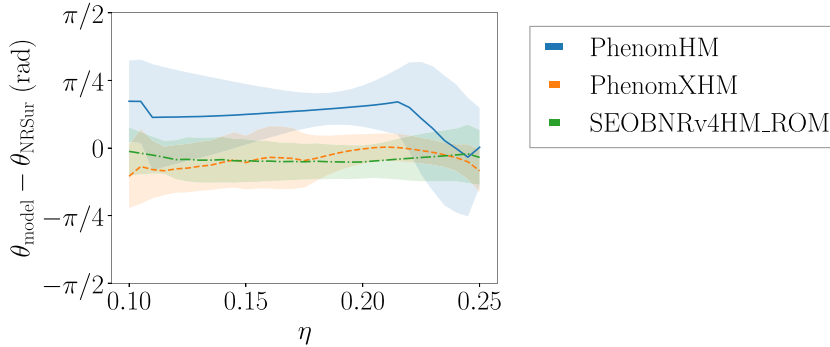


Figure 5. Comparison of the differences on the estimates of the kick orientation between the models indicated at the panel and the NRHybSur3dq8 model. The shaded region represents the std of such distribution at each symmetric-mass-ratio value, while the curves represent the mean value of the distributions.

In figure 6, we show the kick magnitude as a function of the symmetric mass ratio for two fixed spin configurations: nonspinning (left column) and positively highly spinning (right column). We analyse the kick estimates of the four waveform models for such configurations. In addition, we include the estimates of the two NR Sur fits, namely NRSur7dq4Remnant and NRSur3dq8Remnant and the estimates of a set of SXS waveforms.

In the case of nonspinning binaries (left column), we observe good agreement between the SXS waveforms and the NR Sur models. The estimates of the Phenom and SEOBNRv4HM_ROM models show disagreement in the region $\eta \in [0.15, 0.24]$. The highly spinning configurations (right column) show larger relative errors between models. In particular, we observe a secondary maximum in the estimates of PhenomXHM and SEOBNRv4HM_ROM, located in the region $\eta \in [0.05, 0.15]$. Even if the true values are not known, it is highly probable that PhenomHM largely overestimates the value of the kick velocity, since the higher harmonics that induce the kick are not calibrated to NR in this model.

We now illustrate how sensitive the kick estimate is compared to the mismatch uncertainty between the models and the NR waveforms. We choose the BBH configuration $\{\eta = 0.22, \chi_1^z = 0.0, \chi_2^z = 0.0\}$. Such binary lies within the region where the models studied here have been calibrated to NR simulations. For this reason, we expect the mismatch errors with respect to the NR waveform to be small. We have calculated the mismatch for the plus (h_+) and cross (h_\times) polarizations between the waveform models and the SXS waveform, SXS:BBH:0169, for three inclination values: 0, $\pi/3$ and $\pi/2$ (rad). We have considered the Advanced-LIGO design sensitivity curve [73] with a lower cutoff of $f_{\text{min}} = 10$ Hz. When computing the mismatch we maximise the overlap over the relative time. Here we do not optimise this quantity over the relative phase, since these waveforms include higher harmonics and for such waveforms, a relative phase shift does not leave the waveform invariant.

Table 2 displays the mismatch values and kick differences of the models with the SXS waveform. From the mismatch values we are tempted to conclude that the waveform models are highly accurate for such particular binary configuration. However, the large disagreement in the kick estimates indicates the existence of modelling errors in the description of the GW harmonics during the merger phase. These results reflect the sensitivity of the kick velocity to waveform systematic errors.

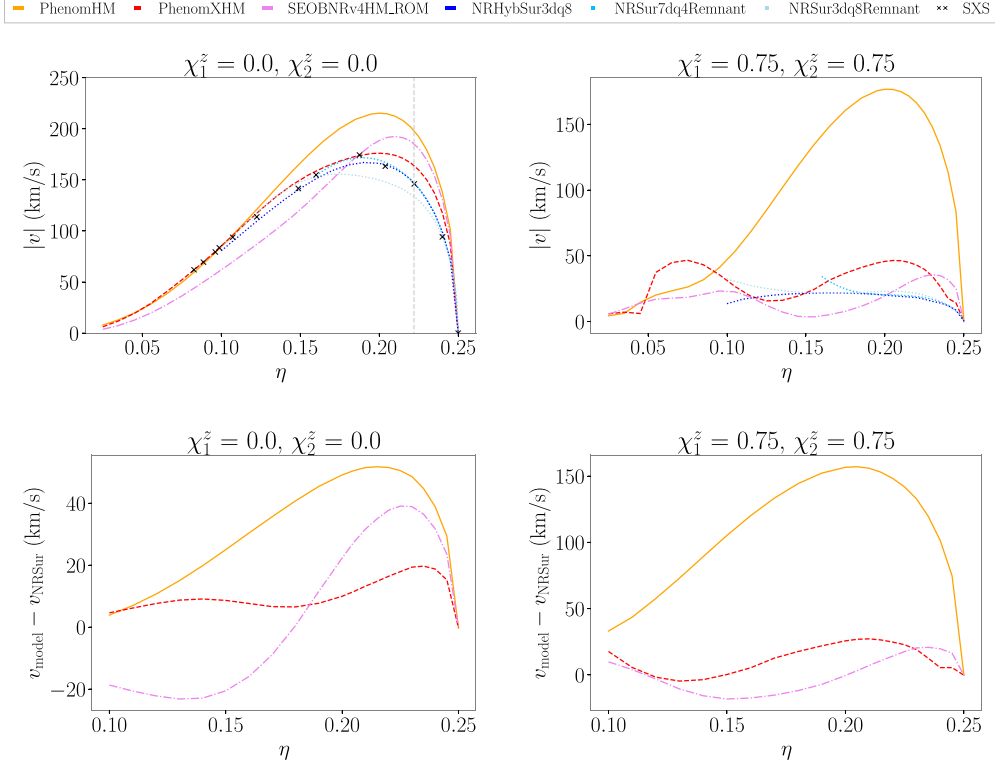


Figure 6. The top figures show the magnitude of the kick velocity as a function of the symmetric mass ratio estimated by PhenomHM (orange), PhenomXHM (red), SEOBNRv4HM_ROM (pink), NRHybSur3dq8 (dark blue), NRSur7dq4Remnant (skyblue) and NRSur3dq8Remnant (light blue), for two specific binary configurations. At each panel, the individual dimensionless spin components have a fixed value, specified on the top of each plot. The bottom panels show the difference of the kick magnitude between the indicated waveform model and the NRHybSur3dq8 model, for the same binary configurations of the corresponding top panels.

Table 2. Mismatch values and kick differences of the waveform models with SXS:BBH:0169, which has the intrinsic properties $\{\eta = 0.22, \chi_1^z = 0.0, \chi_2^z = 0.0\}$. We have computed mismatches for three different inclination angles. Here we show the minimum and maximum mismatch values obtained.

Waveform model	\mathcal{MM}	Δv (km s ⁻¹)
SEOBNRv4HM_ROM	(0.002, 0.047)	42
PhenomXHM	(0.005, 0.008)	20
PhenomHM	(0.008, 0.045)	55
NRHybSur3dq8	(0.007, 0.011)	4
NRSur3dq8Remnant	—	10
NRSur7dq4Remnant	—	4

3.3. Spin dependency

After analysing the mass ratio dependency, we now study whether there is any correlation between the waveform predictions and the spin components of the binary. Using the same data, we compute the differences with the NRHybSur3dq8 model as a functions of the individual spins and calculate the distributions' mean value. Our results are shown in figure 7. The left column shows the differences of the kick magnitude for PhenomHM (first row), PhenomXHM (second row) and SEOBNRv4HM_ROM (third row) with NRHybSur3dq8. The right column displays the differences of the estimates on the kick orientation for the same models. In addition, we include the spin dependency of the NR errors in appendix C.

We observe discrepancies between all models in the magnitude, direction and overall dependency concerning the spin components. Regarding the differences with the NRHybSur3dq8 model on the kick magnitude (left column), in the case of PhenomHM, we observe a correlation with the spin component of the more massive object. The larger the absolute magnitude of the primary spin component is, the larger the difference appears to become. PhenomXHM shows larger disagreement with the NRHybSur3dq8 model in the regions where both individual objects have the largest positive and negative spin magnitudes. In particular, we observe significantly larger relative errors in the region where both objects have negative spin components. As expected, we observe that the newer model is superior to the previous Phenom model. We observe that from the three models, it is SEOBNRv4HM_ROM the model with the closest predictions to those of NRHybSur3dq8. The largest disagreement between SEOBNRv4HM_ROM and NRHybSur3dq8 appear in the region where both spin components have large positive values and where the spin component of the more massive object has the largest negative values.

The right column in figure 7 displays the differences of the orientation estimates. In the case of the PhenomHM model, we observe discrepancies larger than $\pi/8$ rad with NRHybSur3dq8 for binaries with primary spin values of $\chi_1^z \in [-0.8, 0.4]$. For configurations with primary spin values of $\chi_1^z \in [0.4, 0.8]$, it shows good agreement with NRHybSur3dq8. PhenomXHM and SEOBNRv4HM_ROM show similar correlation with the primary spin component. The larger the magnitude of the primary spin component is, the larger inconsistencies we observe. This is more strongly reflected for the SEOBNRv4HM_ROM model, where those binaries with $\chi_1^z \in [0.4, 0.8]$ and $\chi_2^z \in [-0.8, 0.0]$ show a disagreement of $\Delta\theta \sim \pi/16$ rad with the NRHybSur3dq8 model. In the case of the PhenomXHM, such correlation appears to be more subtle. The regions where the differences are around $\Delta\theta \sim \pi/16$ rad are significantly smaller, with an outlier at $\{\chi_1^z = 0.7, \chi_2^z = -0.3\}$.

3.4. Harmonic decomposition of the kick velocity

The kick velocity results from the sum of the contributions coming from pairs of GW harmonics. We decompose the kick velocity into its harmonic contributions, which allows us to look in more detail into the GW spherical harmonics included in the waveform models. Looking at the individual harmonic contributions allows us to understand which harmonics show more significant disagreements and, in turn, indicate the presence of waveform systematics on a more detailed level.

Equation (5) relates two GW harmonics with different (ℓ, m) numbers. Besides, the contributions of the pairs $(\ell_1, m_1)(\ell_2, m_2)$ and $(\ell_2, -m_2)(\ell_1, -m_1)$ have the same magnitude and direction. The dominant contribution always comes from the $(2, 1)(2, 2)$ and $(2, -2)(2, -1)$ pairs, and we refer to them jointly as $(2, \pm 1)(2, \pm 2)$. Besides, the number of GW harmonic

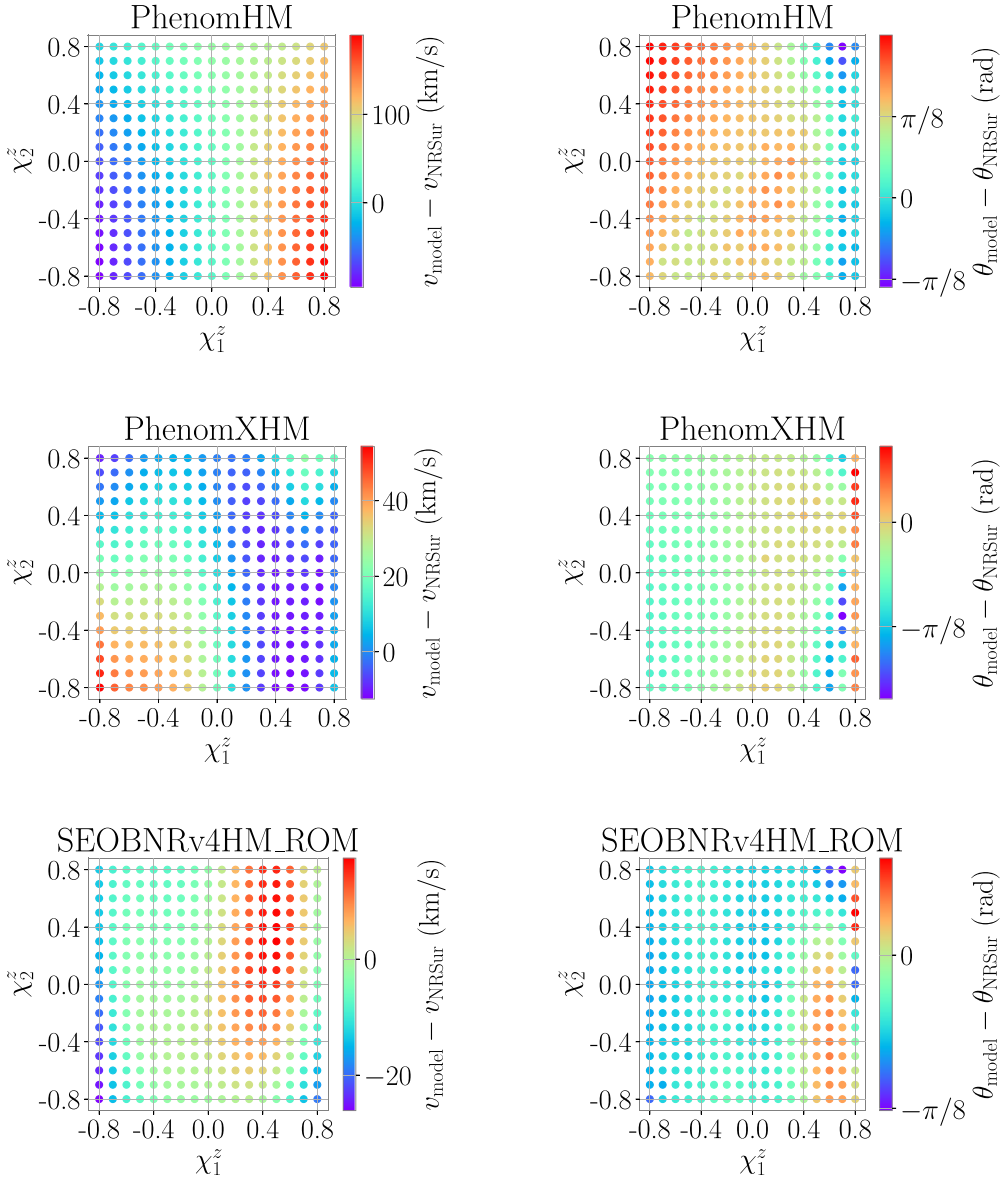


Figure 7. Comparison of the differences on the kick magnitude (left column) and orientation (right column) between PhenomHM (first row), PhenomXHM (second row), SEOBNRv4HM_ROM (third row) and the NRHybSur3dq8 model. Here we plot our results in terms of the individual spins. Each point of the plot is the mean value of a distribution of kick differences, where the spins have a fixed value and the mass ratio has values which have been sampled uniformly. We note that each panel has a different colormap scale.

contributions to the kick velocity will vary from one waveform model to another, depending on the number of spherical harmonics included in each model. We have calculated the harmonic contributions individually and compared the estimates to those of the NRHybSur3dq8

model for the same set of points as in the previous section, which are uniformly sampled in the parameter space.

Figure 8 shows the differences in the kick magnitude of four harmonic contributions. The pairs of spherical harmonics are indicated at the top of each plot. SEOBNRv4HM_ROM and PhenomXHM show comparable differences to the NRHybSur3dq8 estimates, while PhenomHM largely under- and overestimates the magnitude of the kick velocity. The largest differences appear for contributions where an $(\ell, \pm(\ell - 1))$ harmonic is involved. PhenomXHM is in good agreement with NRHybSur3dq8, particularly for the $(3, \pm 2)(3, \pm 3)$ and $(3, \pm 3)(4, \pm 4)$ contributions. We should note that the SEOBNRv4HM_ROM model does not include the $(3, 2)$ harmonic, and thus, it has no contribution coming from the $(3, \pm 2)(3, \pm 3)$ pair. In the case of SEOBNRv4HM_ROM, we observe good agreement with the NRHybSur3dq8, particularly for the $(2, \pm 1)(2, \pm 2)$ and $(2, \pm 2)(3, \pm 3)$ contributions.

Figure 9 displays the distribution of the differences in the orientation of the kick velocity. Here we observe a similar pattern to the one displayed in figure 2. The distributions of the differences are centered around zero for SEOBNRv4HM_ROM with $\sigma \sim 0.3$ rad, showing good agreement with the NRHybSur3dq8 model. In the case of the PhenomXHM estimates, we observe good agreement with NRHybSur3dq8, with $\sigma \sim 0.4$ rad, except for the $(3, \pm 2)(3, \pm 3)$ harmonic contribution, where the distribution has a significantly larger std, $\sigma \sim 0.6$ rad. The distributions of PhenomHM appear shifted at every contribution, with $\sigma \sim 0.8$ rad. In particular, the $(3, \pm 2)(3, \pm 3)$ and $(3, \pm 3)(4, \pm 4)$ contributions, show a significantly larger disagreement with the NRHybSur3dq8 model.

4. Towards kick-based GW tuning

Because the kick estimate is a highly sensitive quantity, here we investigate whether we can use the kick prediction of NR simulations to add additional information in the calibration of the EOBNR and Phenom waveform models. These models calibrate unknown coefficients to NR simulations for the merger and ringdown. Unlike the inspiral region, where the amplitude and phase of the signal are well known from PN or EOB theory, modelling inaccuracies might build up in the merger region. In the following, we propose the first steps towards incorporating the kick prediction in the calibration of a waveform model.

Ideally, one could try to improve the description of the radiated linear momentum together with the energy and angular momentum by tuning these three quantities together. However, this would significantly increase the complexity of the problem. The energy and angular momentum are dominated by the $(2, \pm 2)$ modes, while the linear momentum is dominated by the interplay of the $(2, \pm 2)$ with other higher harmonics. The EOBNR and Phenom waveform families started with models for the dominant mode, which over the years have been improved by increasing the number of NR waveforms used for the calibration. For this reason, we expect the energy and angular momentum to be better modeled than the kick velocity, which has a more subtle imprint in the waveform. As a first step, one would then focus on the kick description, making sure that the radiated energy and angular momentum are not modified dramatically. Expressions for the energy and angular momentum in terms of the radiated harmonics can be found in [66].

As indicated before, the prediction of the kick orientation in currently available NR waveforms has a large uncertainty ($\sigma \sim 0.8$ rad). For this reason, it might be difficult to significantly improve the performance of waveform models with current NR waveforms. Here we discuss how we could use information from the kick estimate once we have more accurate NR waveforms, and in turn, more precise kick estimates. By comparing the kick predictions of a

waveform model with those predicted by NR, we analyse whether it is possible to carefully tune the individual harmonic contributions and, in turn, improve the accuracy of the modelled gravitational signal. We discuss the requirements that must be fulfilled and describe the complexity of addressing such a problem.

When analysing GW data, small phase variations are much better measured compared to amplitude variations. Hence, most of the information that is inferred from the waveform comes from the phase. The first question we want to answer is, whether it is possible to calibrate the GW phase based on the kick contributions.

We tune the harmonics contributions applying a phase shift $\alpha_{\ell,m}$ to the GW harmonic $h_{\ell,m}$, such that $h_{\ell,m} = A_{\ell,m}(t) e^{-i\phi_{\ell,m}(t)}$ transforms into:

$$\bar{h}_{\ell,m} = A_{\ell,m}(t) e^{-i\bar{\phi}_{\ell,m}(t)}, \quad (14)$$

where $\bar{\phi}_{\ell,m}(t) = \phi_{\ell,m}(t) + \alpha_{\ell,m}(t, \lambda)$ is the tuned phase function. As specified, in principle, $\alpha_{\ell,m}(t, \lambda)$ can be a function of the time evolution and the intrinsic parameters of the binary. We can also write the waveform simply as:

$$\bar{h}_{\ell,m} = h_{\ell,m}(t) e^{-i\alpha_{\ell,m}(t, \lambda)}. \quad (15)$$

In reality, we are interested in the kick prediction, which involves the first time derivative of the gravitational strain:

$$\dot{h}_{\ell,m} = \dot{A}_{\ell,m}(t) e^{-i\phi_{\ell,m}(t)} - i h_{\ell,m} \dot{\phi}_{\ell,m}(t). \quad (16)$$

The time derivative of the transformed waveform is on the other hand,

$$\dot{\bar{h}}_{\ell,m} = \left(\dot{h}_{\ell,m}(t) - i h_{\ell,m}(t) \dot{\alpha}_{\ell,m}(t, \lambda) \right) e^{-i\alpha_{\ell,m}(t, \lambda)}. \quad (17)$$

4.1. Applying a constant phase shift

In the simple case where the applied phase shift is slowly varying, such that its time derivative can be neglected, the first derivative of the spherical harmonic reduces to:

$$\dot{\bar{h}}_{\ell,m} = \dot{h}_{\ell,m}(t) e^{-i\alpha_{\ell,m}}. \quad (18)$$

We now look at the the kick formula and compute the kick contribution of the pair of harmonics (ℓ, m) and $(\ell, m+1)$, each with a constant phase shift $\alpha_{\ell,m}$ and $\alpha_{\ell,m+1}$ respectively. We have:

$$\bar{v}_{(\ell,m)(\ell,m+1)} = -\frac{1}{8\pi M_f} \int_{-\infty}^{\infty} dt \left(\dot{h}_{\ell,m}(t) e^{-i\alpha_{\ell,m}} \right) a_{\ell,m} \left(\dot{h}_{\ell,m+1}(t) e^{-i\alpha_{\ell,m+1}} \right)^*. \quad (19)$$

Since the phase shift is simply a constant, the exponential term can be taken out of the integral. We can see that the transformed kick contribution is rotated by the difference of the constant phase shifts:

$$\bar{v}_{(\ell,m)(\ell,m+1)} = v_{(\ell,m)(\ell,m+1)} e^{-i(\alpha_{\ell,m} - \alpha_{\ell,m+1})}. \quad (20)$$

This means, a constant phase shift allows us to perfectly correct the orientation of the contributions, and keep the amplitude unchanged at the same time. In general, we consider two (ℓ_1, m_1) and (ℓ_2, m_2) harmonics, with a phase shift α_{ℓ_1, m_1} and α_{ℓ_2, m_2} , respectively. Their kick contribution will be shifted by:

$$\Delta\theta_{\text{kick}} = \alpha_{\ell_2, m_2} - \alpha_{\ell_1, m_1}. \quad (21)$$

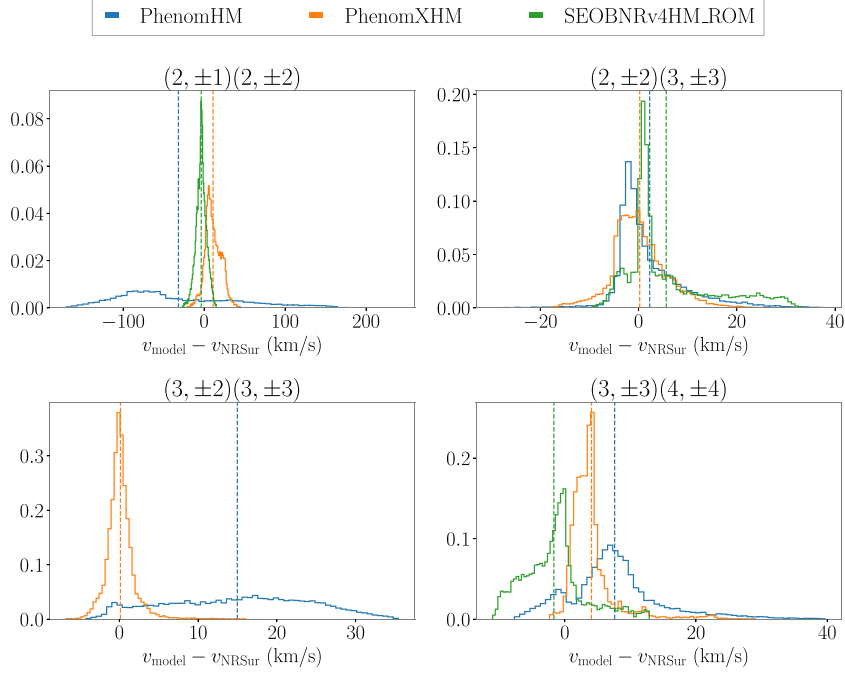


Figure 8. Harmonic contributions of the kick magnitude. We show results for PhenomHM (blue), PhenomXHM (orange) and SEOBNRv4HM_ROM (green) compared to NRHybSur3dq8. The pairs of GW harmonics are specified at the top of each panel. Dashed vertical lines indicate the mean value of each normalised distribution.

Now, the contributions from the two pairs $(\ell_1, m_1)(\ell_2, m_2)$ and $(\ell_2, -m_2)(\ell_1, -m_1)$ have the same magnitude and orientation. So, in the same way, we have:

$$\Delta\theta_{\text{kick}} = \alpha_{\ell_1, -m_1} - \alpha_{\ell_2, -m_2}. \quad (22)$$

Therefore, if the calibration phase shift of a particular harmonic $\alpha_{\ell, m}$ is known, the phase shift of the $(\ell, -m)$ harmonic will be directly determined. Thus, we only need to find the required phase shift for half of the harmonics included in the model. In the following, we use PhenomHM as the base model that we want to recalibrate. However, the procedure described next can be generalised to any waveform model. The reason why we choose PhenomHM is simply that accuracy improvements might be easier to appreciate. Looking at figures 8 and 9, we observe that the $m = \ell - 1$ harmonics, namely the $(2, 1)$, $(3, 2)$ and $(4, 3)$, are the least accurately modelled for PhenomHM. These are the harmonics we might want to tune.

In the case of PhenomHM, there are 7 kick contributions that we want to correct. The model includes 6 (positive m) harmonics. In addition, there is one extra degree of freedom that is the reference orbital phase, which is fixed in each SXS waveforms, but not for the Phenom models. The set of unknown phase shifts can be determined by solving a linear system of equations for the positive (or negative) m harmonics.

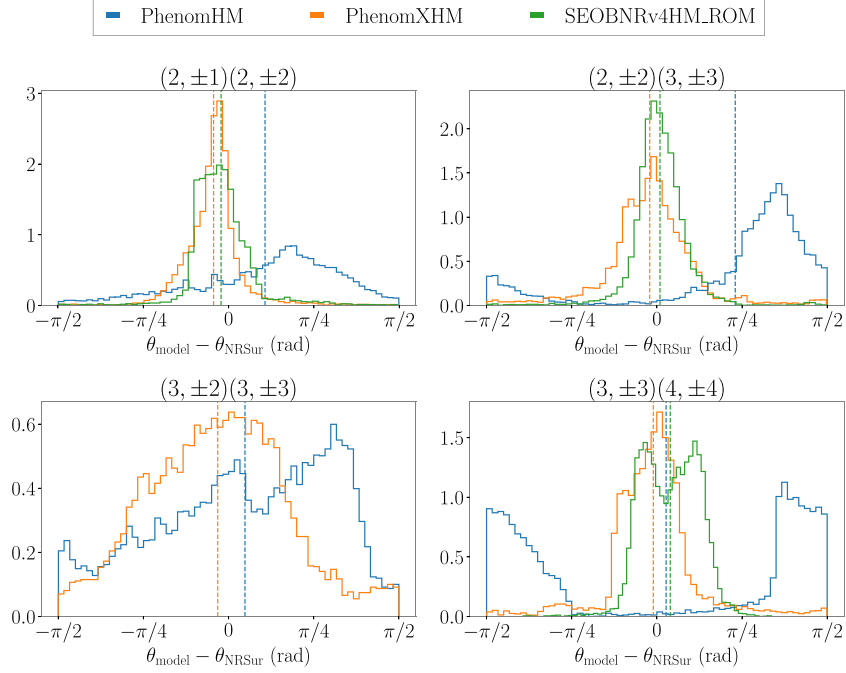


Figure 9. Harmonic contributions of the kick orientation. We show results for PhenomHM (blue), PhenomXHM (orange) and SEOBNRv4HM_ROM (green) compared to NRHybSur3dq8. The pairs of GW harmonics are specified at the top of each panel. Dashed vertical lines indicate the mean value of each normalised distribution.

The linear system of equations, $Ax = b$, is given by:

$$A = \begin{pmatrix} 1 & 1 & 0 & 0 & -1 & 0 & 0 \\ 1 & -1 & 1 & 0 & 0 & 0 & 0 \\ 1 & 0 & -1 & 1 & 0 & 0 & 0 \\ 1 & 0 & 1 & 0 & 0 & -1 & 0 \\ 1 & 0 & 0 & 1 & 0 & 0 & -1 \\ 1 & 0 & 0 & 0 & -1 & 1 & 0 \\ 1 & 0 & 0 & 0 & 0 & -1 & 1 \end{pmatrix}, \quad (23)$$

$$x = (\alpha_{ref}, \alpha_{(2,2)}, \alpha_{(3,3)}, \alpha_{(4,4)}, \alpha_{(2,1)}, \alpha_{(3,2)}, \alpha_{(4,3)}), \quad (24)$$

$$b = (\theta_{(2,1)(2,2)}, \theta_{(2,2)(3,3)}, \theta_{(3,3)(4,4)}, \theta_{(3,2)(3,3)}, \theta_{(4,3)(4,4)}, \theta_{(2,1)(3,2)}, \theta_{(3,2)(4,3)}). \quad (25)$$

$\theta_{(2,1)(2,2)}$ refers to the orientation difference between the SXS and PhenomHM (2,1)(2,2) contribution,

$$\theta_{(2,1)(2,2)} = v_{(2,1)(2,2)}^{SXS} - v_{(2,1)(2,2)}^{PhHM}. \quad (26)$$

The solution to such a system will rotate the kick contributions of the waveform model and perfectly match those predicted by the NR waveform. The next question we want to answer is whether these shifts make the waveform model more accurate. In reality, applying a constant phase shift to the waveform would change the phase of the inspiral part, which is well modelled

based on PN and EOB theory. Thus, applying a constant shift would instead make our waveforms inconsistent with the PN predictions of the early inspiral. If we want to address possible systematic errors in the waveform, we must keep the original inspiral phase and correct the merger-ringdown phase with a time-dependent phase shift.

4.2. Applying a time-dependent phase shift around the merger

We now want to leave the inspiral phase unchanged and apply a phase shift that is non-zero during the merger. The late-ringdown phase is determined by solving equation (23) for the fully integrated kick velocity. Ideally, one should find the phase shift $\alpha_{\ell,m}(\lambda, t)$ as a function of the intrinsic parameters for each harmonic, such that the time profile of the individual kick contributions predicted by a model is calibrated to the NR estimates. Thus, we are looking for a phase correction that is zero in the inspiral part, builds up around the merger and has a constant value in the late-ringdown.

We consider a phase shift that is time-dependent, and at least once differentiable. In this case, the time derivative of the tuned waveform involves an additional term:

$$\dot{\tilde{h}}_{\ell,m} = \left(\dot{h}_{\ell,m} - i h_{\ell,m} \dot{\alpha}_{\ell,m}(t) \right) e^{-i\alpha_{\ell,m}(t)}. \quad (27)$$

The tuned kick contribution of a pair of harmonics (ℓ, m) and $(\ell, m+1)$, each with a time-varying phase shift $\alpha_{\ell,m}$ and $\alpha_{\ell,m+1}$ respectively, is then given by:

$$\begin{aligned} \bar{v}_{(\ell,m)(\ell,m+1)} = & -\frac{1}{8\pi M_f} \int_{-\infty}^{\infty} dt \left[\dot{h}_{\ell,m}(t) \dot{h}_{\ell,m}^*(t) + i \dot{h}_{\ell,m}(t) h_{\ell,m+1}^* \dot{\alpha}_{\ell,m+1}^*(t) - i \dot{h}_{\ell,m+1}^*(t) h_{\ell,m} \dot{\alpha}_{\ell,m}(t) \right. \\ & \left. + h_{\ell,m} h_{\ell,m+1}^* \dot{\alpha}_{\ell,m}(t) \dot{\alpha}_{\ell,m+1}^*(t) \right] a_{\ell,m} e^{-i(\alpha_{\ell,m}(t) - \alpha_{\ell,m+1}(t))}. \end{aligned} \quad (28)$$

We observe that for a phase-shift function that necessarily changes its value over time, it is not possible to recover the expression (20), where the tuned contribution is precisely rotated by the difference of the individual phase shifts. Therefore, when using a time-dependent function, we can only aim to tune the kick contributions as *close* to the NR predictions as possible.

The rest of the subsection aims to study more deeply how well we can correct the harmonic contributions. We start with a simple function with the following characteristics: it is zero for the inspiral part, builds up around the merger following a Gaussian distribution, and has a constant value in the late-ringdown. The Gaussian distribution is centred at $t/M = 0$ and has a maximum value equal to the late-ringdown phase shift. We leave the width of the distribution as a free parameter and study how the tuned kick velocity (integrated over the whole evolution) depends on its value. Figure 10 displays the function we first try, with different values of the std of the Gaussian distribution. As a first step, we should mention that one could choose a different type of distribution, centre it at a different point in time, and would still come to the same conclusions.

Next, we want to address whether a more convenient width can be chosen for all harmonics. We compute the dependency of the kick on the width for three different configurations as shown in figure 11.

Because we are only trying to correct the orientation of the contributions, it might be that even though the direction of the kick is close to the NR prediction, the individual magnitudes differ significantly from the NR estimates. A better approach should consider both amplitude and phase corrections at the same time. Besides, one should study the dependency individually for each harmonic. We observe that the value of the distribution width might change for different binary configurations. Thus, the width should not only vary for each harmonic, but one should also find dependency on the intrinsic parameters of the binary.

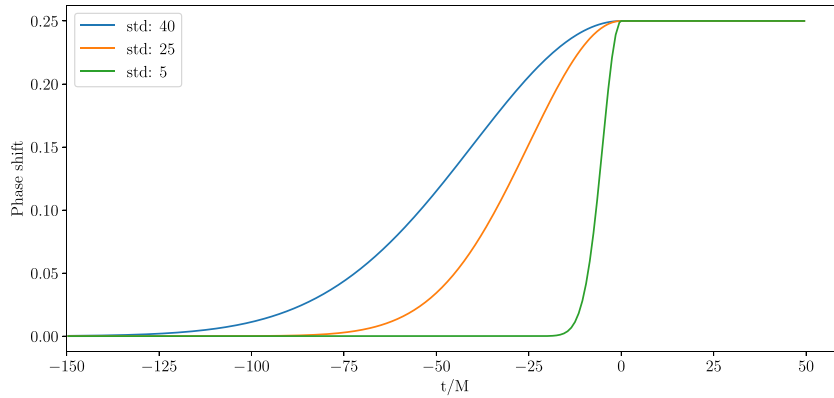


Figure 10. We consider a time-dependent phase shift that builds up in the merger following a gaussian distribution centred at $t/M = 0$. Initially, the width of the distributions is left free and can take different values, as shown in the figure.

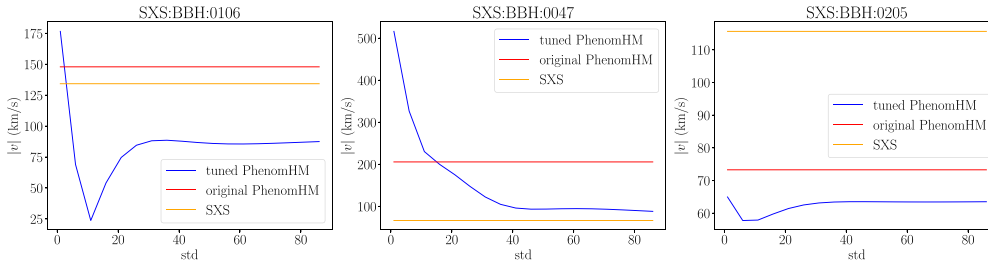


Figure 11. The dependency of the kick velocity on the value of the std of the Gaussian distribution is shown for three different configurations. The horizontal lines indicate the kick velocity estimate of the SXS waveform (orange) and that of the original PhenomHM waveform (red). The kick estimate of the transformed PhenomHM waveform with a phase shift with a specific standard deviation value is shown in blue.

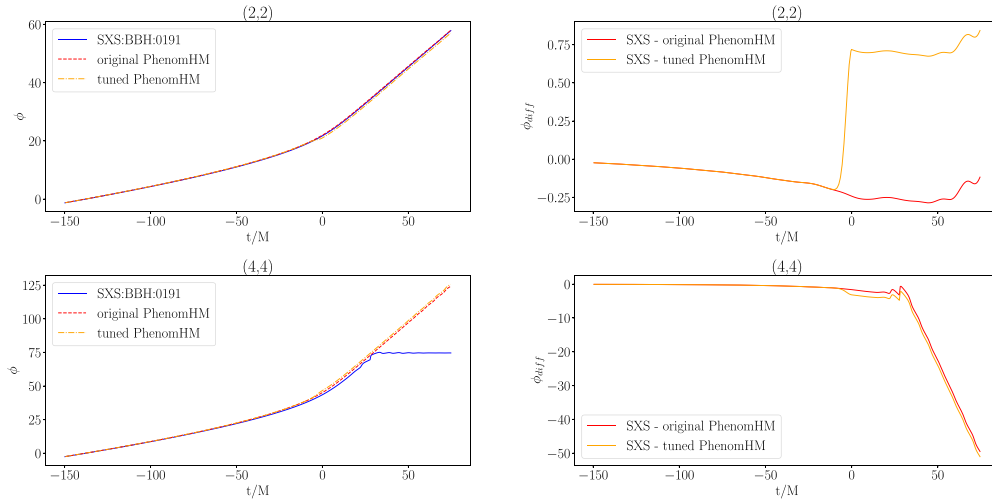
Although our current approach can be improved in many ways, we want to know whether our simple model can still improve in the phase of the modelled GW harmonic. We use 9 SXS waveforms of different configurations as indicated in table 3 and apply the following algorithm:

- Find the value of the std of the distribution that leads to a total kick value that matches the SXS prediction.
- Find the required late-ringdown phase shifts for each harmonic by solving the linear system of equations for the fully integrated kick contributions.
- Apply the tuning phase shift to each harmonic.

To analyse how the phase shift modifies the original PhenomHM harmonics, we plot the original and tuned waveform, its phase and the phase difference between the SXS and the PhenomHM waveforms. We include the results of one of the configurations in figures 12 and 13, where we show how the phase shifts modify the phase and in turn the waveform for the (2,2) and (4,4) harmonics. In all 9 studied cases, we find that the simple phase-shift function does not improve the accuracy of the modelled waveform. Just as for the constant phase shift, it is

Table 3. SXS waveforms used in our study to calibrate the kick contributions of PhenomHM.

Waveform ID	η	χ_1^z	χ_2^z
SXS:BBH:0046	0.188	-0.5	-0.5
SXS:BBH:0047	0.188	0.5	0.5
SXS:BBH:0106	0.139	0.0	0.0
SXS:BBH:0186	0.096	0.0	0.0
SXS:BBH:0191	0.204	0.0	0.0
SXS:BBH:0199	0.092	0.0	0.0
SXS:BBH:0205	0.109	-0.4	0.0
SXS:BBH:0222	0.250	-0.3	0.0
SXS:BBH:0289	0.187	0.6	0.0

**Figure 12.** The left column displays the original and tuned PhenomHM phase compared to the SXS waveform phase, while the right column shows the phase differences between the SXS and the original (tuned) PhenomHM phase in red (orange) for the binary $\{\eta = 0.204, \chi_1 = 0.0, \chi_2 = 0.0\}$. On the top row we show the (2,2) harmonic, and on the bottom the (4,4) harmonic.

not straightforward that tuning the kick contributions necessarily implies an improvement of the waveform.

From the plots of the waveform phases, we find support, once again, to use a different phase function for each harmonic. We observe that the relative error in the phase does not have a simple structure which could be corrected using a phase shift that builds up following a smooth distribution. Besides, it could be that the relative errors are randomly distributed during the merger time and even over the parameter space. These two aspects reinforce our view of how complex kick-based tuning is. The main question we want to address is still how to optimally reduce the relative errors using the information contained in the kick. As mentioned earlier, the amplitude and the phase of the kick contributions should be corrected simultaneously. A time-dependent phase shift does not only change the orientation but also the magnitude of the kick contributions, as indicated by equation (28). In our research, we have only considered the change in the orientation of the kick. One could try to analyse the

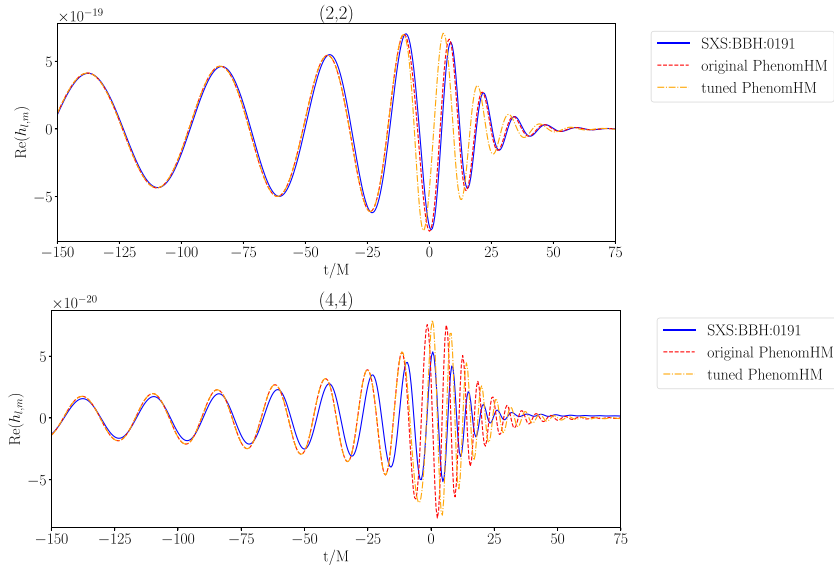


Figure 13. We show the (2,2) and (4,4) harmonics of the original (red) and tuned (orange) PhenomHM waveform together with the SXS waveform (blue) for $\{\eta = 0.204, \chi_1 = 0.0, \chi_2 = 0.0\}$.

expression (28) in more detail and study whether it is possible to tune the amplitude and phase simply with a phase-shift function.

So far, we have only calibrated the kick contributions of the late-ringdown by comparison to the fully integrated kick values. The time evolution⁴ of the individual contributions could be used instead, which would allow finding the required phase shifts at several points in time, not only at the late-ringdown. One could choose a set of collocation points and solve the set of equations of the individual phases and possibly the amplitudes at each point. Besides, in our study we have explored the use of phase shifts to calibrate our estimates. However, the kick prediction is also sensitive to time shifts, which could complement the use of phase shifts. One should take care that in the waveform calibration process, the properties of the binary system are not changed. Similar to the radiated linear momentum, the energy and the angular momentum (see [37]) would have to be corrected in the models.

5. Discussion

In this paper, we show that current waveform models, NRHybSur3dq8, SEOB-NRv4HM_ROM, PhenomHM and PhenomXHM, are not consistent with each other in their kick estimates over the parameter space. Waveform systematic deviations that occur during the merger phase can strongly impact the kick estimate. Because the kick prediction is highly sensitive to waveform inaccuracies, disagreements between models indicate where in the parameter space are waveform systematics more significant. We have studied the dependency of the kick magnitude and orientation on the symmetric mass ratio and the individual spin components of the binary. Analysing model-model agreement, we find that overall,

⁴ The time evolution of the kick velocity describes how the velocity of the system's center-of-mass increases with the binary evolution.

PhenomXHM and SEOBNRv4HM_ROM show comparable differences compared to NRHybSur3dq8. We observe large discrepancies between the predictions of PhenomHM relative to NRHybSur3dq8. Our results show that PhenomHM has been superseded in accuracy by its newer version, PhenomXHM. Such improvement is probably related to the NR calibration of the subdominant spherical harmonics in the latest model. We observe the largest discrepancies in regions of the parameter space where the spin magnitude of the more massive black hole has high absolute values. Besides, the largest uncertainties appear in the region where the symmetric mass ratio takes values between $\eta = [0.20, 0.25]$.

Since the estimate of the kick velocity involves the description of the higher harmonics during the merger phase, we are able to study the individual contributions of the kick velocity coming from different spherical harmonics. We analyse model-model agreement and find similar results as for the total kick velocity. Both PhenomXHM and SEOBNRv4HM_ROM show considerably smaller differences to NRHybSur3dq8 than PhenomHM. In particular, we observe extremely good agreement between the PhenomXHM and NRHybSur3dq8 in the magnitude of the $(3, \pm 2)(3, \pm 3)$ and $(3, \pm 3)(4, \pm 4)$ contributions. At the same time, we find large disagreement between PhenomXHM and PhenomHM with NRHybSur3dq8 on the orientation of the $(3, \pm 2)(3, \pm 3)$ and $(3, \pm 3)(4, \pm 4)$ contribution. Our results support the use of the kick estimate as a complementary tool to the mismatch uncertainty to evaluate the performance of gravitational waveform models.

We further study whether calibrating the individual kick contributions to the NR predictions can, in turn, imply an improvement in the accuracy of a waveform model. We focus on tuning the orientations of the kick contributions, and we use PhenomHM as our base model for the study. Although applying a constant phase shift would allow us to calibrate the orientation of the individual contributions, the shift would change the well modelled inspiral phase. Instead, we need a time-dependent phase shift that builds up around the merger. However, finding the appropriate time-dependent function that corrects the waveform amplitude and phase errors is highly complex. We find that a different phase-shift function is probably needed for each harmonic, which might depend on the binary's intrinsic properties. Besides, one should treat both the magnitude and orientation of the individual kick contributions simultaneously. Once there are more accurate NR predictions of the kick orientation available, this calibration framework could help improve the modelling of the kick imprint in waveform models.

Data availability statement

The data cannot be made publicly available upon publication because the cost of preparing, depositing and hosting the data would be prohibitive within the terms of this research project. The data that support the findings of this study are available upon reasonable request from the authors.

Acknowledgments

The authors are grateful to Neev Khera, Abhay Ashtekar, Badri Krishnan and Cecilio García-Quirós for useful discussions. We thank Marta Colleoni for sharing the details of the kick calculations performed in [21], which we used for comparison. We thank Vijay Varma and Sascha Husa for comments on the manuscript. We are grateful to the members of the 'Binary Merger Observations and Numerical Relativity' group for useful feedback, and we thank Max Melching for sharing his code to easily display large data sets. This work was supported by the Max Planck Society's Independent Research Group program. Computations were carried out on the Holodeck cluster of the Max Planck Institute for Gravitational Physics in Hannover.

Appendix A. Harmonic contributions as a function of the symmetric mass ratio

We further investigate our results from section 3.1 by studying the harmonic contributions of each model as a function of the symmetric-mass-ratio. Our results are displayed in figures A1 and A2, where we show the harmonic contributions of the kick magnitude and orientation respectively.

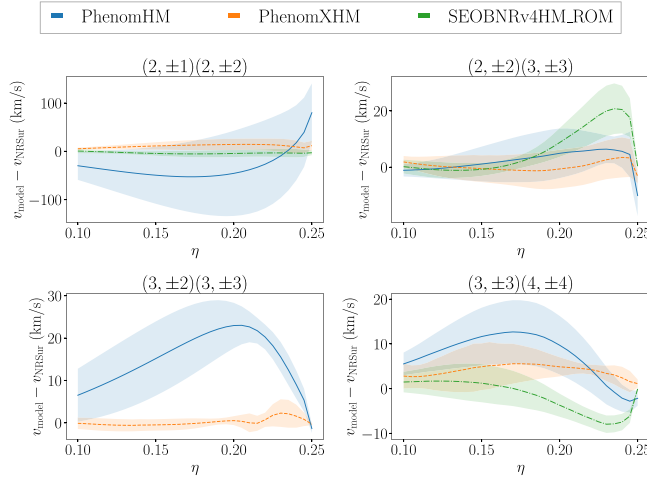


Figure A1. Harmonic contributions of the kick magnitude as a function of the symmetric mass ratio. We show results for the PhenomHM (blue), PhenomXHM (orange) and SEOBNRv4HM_ROM (green) models. The shaded region represents the std of such distribution at each symmetric-mass-ratio value, while the curves represent the mean value of the distributions.

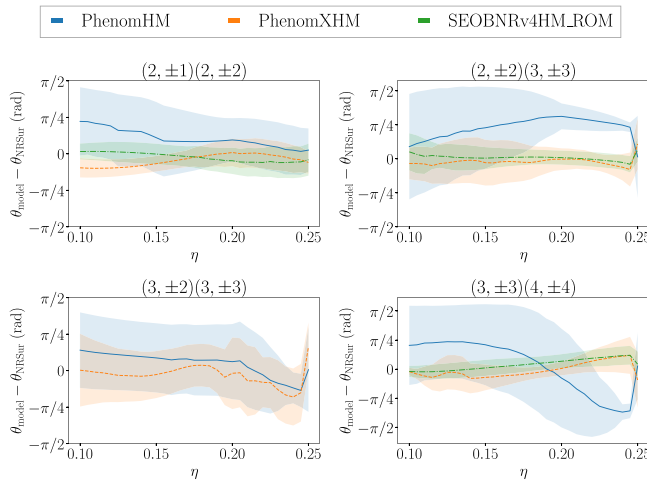


Figure A2. Harmonic contributions of the kick orientation as a function of the symmetric mass ratio. We show results for the PhenomHM (blue), PhenomXHM (orange) and SEOBNRv4HM_ROM (green) models. The shaded region represents the std of such distribution at each symmetric-mass-ratio value, while the curves represent the mean value of the distributions.

Appendix B. Table of SXS waveforms employed to estimate the kick error

In table B1, we display the list of 173 nonprecessing SXS waveforms we have used to get an estimate of the kick error in NR waveforms coming from the NR resolution uncertainty. For each simulation we include the intrinsic parameters of the BBH, and the error estimate of the kick magnitude (Δv) and direction ($\Delta\theta$).

Table B1. Error estimates of the kick magnitude (Δv) and orientation ($\Delta\theta$) for the set of SXS waveforms indicated in the first column. For each waveform, we include the intrinsic parameters of the binary.

Waveform ID	η	χ_1	χ_2	Δv	$\Delta\theta$
SXS:BBH:0002	0.09	(0.0, 0.0, 0.0)	(0.0, 0.0, 0.0)	0.005	-2.578
SXS:BBH:0004	0.086	(0.0, 0.0, 0.0)	(0.0, 0.0, 0.0)	3.529	-4.912
SXS:BBH:0005	0.083	(0.0, 0.0, 0.0)	(0.0, 0.0, 0.0)	2.049	3.23
SXS:BBH:0007	0.248	(0.0, 0.0, 0.33)	(0.0, 0.0, -0.44)	-10.064	0.368
SXS:BBH:0008	0.245	(0.0, 0.0, 0.962)	(0.0, 0.0, -0.9)	7.329	0.307
SXS:BBH:0012	0.247	(0.0, 0.0, 0.32)	(0.0, 0.0, -0.58)	0.175	0.522
SXS:BBH:0014	0.178	(0.0, 0.0, 0.523)	(0.0, 0.0, -0.448)	6.122	-0.341
SXS:BBH:0016	0.248	(0.0, 0.0, 0.33)	(0.0, 0.0, -0.44)	4.559	0.505
SXS:BBH:0019	0.248	(0.0, 0.0, 0.33)	(0.0, 0.0, -0.44)	-3.279	-0.448
SXS:BBH:0025	0.248	(0.0, 0.0, 0.33)	(0.0, 0.0, -0.44)	-82.629	0.868
SXS:BBH:0030	0.25	(0.0, 0.0, 0.0)	(0.0, 0.0, 0.0)	4.26	-0.237
SXS:BBH:0031	0.25	(0.0, 0.0, -0.5)	(0.0, 0.0, 0.0)	0.608	2.066
SXS:BBH:0036	0.25	(0.0, 0.0, 0.5)	(0.0, 0.0, 0.0)	-6.433	2.768
SXS:BBH:0054	0.24	(0.0, 0.0, 0.0)	(0.0, 0.0, 0.0)	12.079	0.27
SXS:BBH:0056	0.24	(0.0, 0.0, 0.0)	(0.0, 0.0, 0.0)	-2.289	-0.646
SXS:BBH:0063	0.24	(0.0, 0.0, -0.5)	(0.0, 0.0, 0.0)	-1.28	-0.381
SXS:BBH:0064	0.24	(0.0, 0.0, -0.5)	(0.0, 0.0, 0.0)	3.182	2.706
SXS:BBH:0065	0.24	(0.0, 0.0, -0.5)	(0.0, 0.0, 0.0)	7.317	0.575
SXS:BBH:0106	0.24	(0.0, 0.0, -0.5)	(0.0, 0.0, 0.5)	7.219	2.232
SXS:BBH:0107	0.24	(0.0, 0.0, 0.5)	(0.0, 0.0, -0.5)	2.358	-0.283
SXS:BBH:0113	0.188	(0.0, 0.0, 0.0)	(0.0, 0.0, 0.0)	12.53	1.939
SXS:BBH:0148	0.187	(0.0, 0.0, 0.5)	(0.0, 0.0, 0.0)	0.0	-2.893
SXS:BBH:0149	0.187	(0.0, 0.0, -0.5)	(0.0, 0.0, 0.0)	0.0	0.738
SXS:BBH:0150	0.139	(0.0, 0.0, 0.0)	(0.0, 0.0, 0.0)	0.002	2.724
SXS:BBH:0151	0.139	(0.0, 0.0, 0.0)	(0.0, 0.0, 0.0)	-0.0	-2.739
SXS:BBH:0152	0.099	(0.0, 0.0, 0.0)	(0.0, 0.0, 0.0)	-0.001	3.106
SXS:BBH:0154	0.099	(0.0, 0.0, -0.5)	(0.0, 0.0, 0.0)	-0.0	3.613
SXS:BBH:0155	0.099	(0.0, 0.0, 0.5)	(0.0, 0.0, 0.0)	0.002	3.025
SXS:BBH:0157	0.139	(0.0, 0.0, 0.0)	(0.0, 0.0, 0.0)	0.048	-2.979
SXS:BBH:0158	0.139	(0.0, 0.0, 0.0)	(0.0, 0.0, 0.0)	-0.388	-0.24
SXS:BBH:0159	0.139	(0.0, 0.0, 0.0)	(0.0, 0.0, 0.0)	0.006	0.284
SXS:BBH:0160	0.25	(0.0, 0.0, -0.438)	(0.0, 0.0, -0.438)	-0.001	3.523
SXS:BBH:0162	0.25	(0.0, 0.0, -0.2)	(0.0, 0.0, -0.2)	5.424	-2.418
SXS:BBH:0167	0.25	(0.0, 0.0, 0.2)	(0.0, 0.0, 0.2)	-1.817	1.264
SXS:BBH:0168	0.25	(0.0, 0.0, -0.6)	(0.0, 0.0, -0.6)	-1.819	-0.388
SXS:BBH:0169	0.25	(0.0, 0.0, 0.6)	(0.0, 0.0, 0.6)	-0.82	-0.5
SXS:BBH:0172	0.25	(0.0, 0.0, -0.8)	(0.0, 0.0, -0.8)	0.696	-0.51

(Continued.)

Table B1. (Continued.)

SXS:BBH:0174	0.25	(0.0, 0.0, 0.8)	(0.0, 0.0, 0.8)	73.582	2.475
SXS:BBH:0175	0.25	(0.0, 0.0, 0.95)	(0.0, 0.0, 0.95)	0.205	3.437
SXS:BBH:0176	0.25	(0.0, 0.0, 0.97)	(0.0, 0.0, 0.97)	-0.231	2.029
SXS:BBH:0177	0.25	(0.0, 0.0, -0.9)	(0.0, 0.0, -0.9)	-0.223	-0.693
SXS:BBH:0178	0.25	(0.0, 0.0, 0.9)	(0.0, 0.0, 0.9)	0.002	-0.292
SXS:BBH:0180	0.222	(0.0, 0.0, 0.6)	(0.0, 0.0, 0.0)	-0.003	-1.383
SXS:BBH:0181	0.16	(0.0, 0.0, 0.0)	(0.0, 0.0, 0.0)	-0.051	0.738
SXS:BBH:0182	0.188	(0.0, 0.0, 0.0)	(0.0, 0.0, 0.0)	-1.326	-2.451
SXS:BBH:0183	0.222	(0.0, 0.0, 0.0)	(0.0, 0.0, 0.0)	0.972	-2.693
SXS:BBH:0184	0.25	(0.0, 0.0, 0.98)	(0.0, 0.0, 0.98)	-0.787	-4.076
SXS:BBH:0185	0.187	(0.0, 0.0, 0.5)	(0.0, 0.0, 0.0)	0.85	-2.776
SXS:BBH:0186	0.25	(0.0, 0.0, 0.75)	(0.0, 0.0, 0.75)	-0.111	0.164
SXS:BBH:0187	0.25	(0.0, 0.0, 0.96)	(0.0, 0.0, 0.96)	-0.747	2.225
SXS:BBH:0188	0.25	(0.0, 0.0, 0.99)	(0.0, 0.0, 0.99)	-0.207	-0.125
SXS:BBH:0189	0.25	(0.0, 0.0, 0.995)	(0.0, 0.0, 0.995)	0.182	-0.543
SXS:BBH:0190	0.25	(0.0, 0.0, 0.0)	(0.0, 0.0, 0.0)	0.025	1.255
SXS:BBH:0191	0.122	(0.0, 0.0, 0.0)	(0.0, 0.0, 0.0)	0.181	0.879
SXS:BBH:0192	0.16	(0.0, 0.0, 0.0)	(0.0, 0.0, 0.0)	-0.182	0.756
SXS:BBH:0193	0.187	(0.0, 0.0, 0.0)	(0.0, 0.0, 0.0)	1.29	0.255
SXS:BBH:0194	0.222	(0.0, 0.0, 0.0)	(0.0, 0.0, 0.0)	-5.356	-0.596
SXS:BBH:0195	0.083	(0.0, 0.0, 0.0)	(0.0, 0.0, 0.0)	0.432	-4.796
SXS:BBH:0196	0.096	(0.0, 0.0, 0.0)	(0.0, 0.0, 0.0)	-0.001	0.732
SXS:BBH:0197	0.138	(0.0, 0.0, 0.0)	(0.0, 0.0, 0.0)	-0.34	0.903
SXS:BBH:0198	0.107	(0.0, 0.0, 0.0)	(0.0, 0.0, 0.0)	-3.207	-5.422
SXS:BBH:0199	0.089	(0.0, 0.0, 0.0)	(0.0, 0.0, 0.0)	-0.221	0.768
SXS:BBH:0200	0.149	(0.0, 0.0, 0.0)	(0.0, 0.0, 0.0)	3.95	0.894
SXS:BBH:0201	0.204	(0.0, 0.0, 0.0)	(0.0, 0.0, 0.0)	3.176	1.896
SXS:BBH:0202	0.115	(0.0, 0.0, 0.0)	(0.0, 0.0, 0.0)	-0.921	0.461
SXS:BBH:0203	0.173	(0.0, 0.0, 0.0)	(0.0, 0.0, 0.0)	-1.535	1.219
SXS:BBH:0204	0.239	(0.0, 0.0, 0.0)	(0.0, 0.0, 0.0)	-1.119	1.145
SXS:BBH:0205	0.101	(0.0, 0.0, 0.0)	(0.0, 0.0, 0.0)	0.589	0.745
SXS:BBH:0206	0.085	(0.0, 0.0, 0.0)	(0.0, 0.0, 0.0)	-1.417	2.264
SXS:BBH:0207	0.13	(0.0, 0.0, 0.0)	(0.0, 0.0, 0.0)	-0.51	1.02
SXS:BBH:0208	0.248	(0.0, 0.0, 0.0)	(0.0, 0.0, 0.0)	-0.041	-4.178
SXS:BBH:0209	0.092	(0.0, 0.0, 0.0)	(0.0, 0.0, 0.0)	0.195	-0.661
SXS:BBH:0210	0.179	(0.0, 0.0, 0.0)	(0.0, 0.0, 0.0)	0.054	-1.457
SXS:BBH:0211	0.211	(0.0, 0.0, 0.0)	(0.0, 0.0, 0.0)	0.506	-4.73
SXS:BBH:0212	0.109	(0.0, 0.0, 0.6)	(0.0, 0.0, 0.0)	0.04	-3.718
SXS:BBH:0213	0.109	(0.0, 0.0, 0.4)	(0.0, 0.0, 0.0)	0.116	-0.039
SXS:BBH:0214	0.109	(0.0, 0.0, 0.4)	(0.0, 0.0, 0.0)	0.413	0.105
SXS:BBH:0215	0.109	(0.0, 0.0, -0.4)	(0.0, 0.0, 0.0)	0.05	2.065
SXS:BBH:0216	0.109	(0.0, 0.0, -0.4)	(0.0, 0.0, 0.0)	0.189	0.109
SXS:BBH:0217	0.109	(0.0, 0.0, -0.6)	(0.0, 0.0, 0.0)	0.349	-0.04
SXS:BBH:0218	0.139	(0.0, 0.0, -0.9)	(0.0, 0.0, 0.0)	4.693	-2.211
SXS:BBH:0219	0.25	(0.0, 0.0, -0.9)	(0.0, 0.0, -0.5)	1.193	1.982
SXS:BBH:0220	0.25	(0.0, 0.0, -0.9)	(0.0, 0.0, 0.0)	-0.071	0.152
SXS:BBH:0221	0.25	(0.0, 0.0, -0.9)	(0.0, 0.0, 0.9)	1.534	-0.432
SXS:BBH:0222	0.25	(0.0, 0.0, -0.8)	(0.0, 0.0, -0.8)	-0.661	0.691
SXS:BBH:0223	0.25	(0.0, 0.0, -0.8)	(0.0, 0.0, 0.8)	2.164	2.203

(Continued.)

Table B1. (Continued.)

Waveform ID	η	χ_1	χ_2	Δv	$\Delta\theta$
SXS:BBH:0224	0.25	(0.0, 0.0, -0.625)	(0.0, 0.0, -0.25)	0.351	-0.409
SXS:BBH:0225	0.25	(0.0, 0.0, -0.6)	(0.0, 0.0, -0.6)	0.323	-0.597
SXS:BBH:0226	0.25	(0.0, 0.0, -0.6)	(0.0, 0.0, 0.0)	0.344	0.083
SXS:BBH:0227	0.25	(0.0, 0.0, -0.6)	(0.0, 0.0, 0.6)	0.352	-0.531
SXS:BBH:0228	0.25	(0.0, 0.0, -0.5)	(0.0, 0.0, 0.5)	0.034	1.084
SXS:BBH:0229	0.25	(0.0, 0.0, -0.5)	(0.0, 0.0, 0.9)	0.298	-0.545
SXS:BBH:0230	0.25	(0.0, 0.0, -0.4)	(0.0, 0.0, -0.8)	0.111	-0.624
SXS:BBH:0231	0.25	(0.0, 0.0, -0.4)	(0.0, 0.0, 0.8)	1.494	1.56
SXS:BBH:0232	0.25	(0.0, 0.0, -0.3)	(0.0, 0.0, 0.0)	1.849	1.817
SXS:BBH:0233	0.25	(0.0, 0.0, 0.3)	(0.0, 0.0, 0.0)	-0.449	1.556
SXS:BBH:0234	0.25	(0.0, 0.0, 0.4)	(0.0, 0.0, -0.8)	-0.784	3.297
SXS:BBH:0235	0.25	(0.0, 0.0, 0.4)	(0.0, 0.0, 0.8)	1.262	-1.979
SXS:BBH:0236	0.25	(0.0, 0.0, 0.5)	(0.0, 0.0, -0.9)	-1.284	-1.948
SXS:BBH:0237	0.25	(0.0, 0.0, 0.6)	(0.0, 0.0, 0.0)	0.294	2.663
SXS:BBH:0238	0.25	(0.0, 0.0, 0.6)	(0.0, 0.0, 0.6)	-4.591	2.405
SXS:BBH:0239	0.25	(0.0, 0.0, 0.65)	(0.0, 0.0, 0.25)	-0.344	-0.832
SXS:BBH:0240	0.25	(0.0, 0.0, 0.8)	(0.0, 0.0, 0.8)	33.268	0.223
SXS:BBH:0241	0.25	(0.0, 0.0, 0.9)	(0.0, 0.0, 0.0)	9.188	0.164
SXS:BBH:0242	0.25	(0.0, 0.0, 0.9)	(0.0, 0.0, 0.5)	30.183	0.36
SXS:BBH:0243	0.222	(0.0, 0.0, -0.871)	(0.0, 0.0, 0.85)	0.93	2.039
SXS:BBH:0244	0.222	(0.0, 0.0, -0.85)	(0.0, 0.0, -0.85)	0.759	2.489
SXS:BBH:0245	0.222	(0.0, 0.0, -0.6)	(0.0, 0.0, -0.6)	21.9	0.48
SXS:BBH:0246	0.222	(0.0, 0.0, -0.6)	(0.0, 0.0, 0.0)	3.116	0.946
SXS:BBH:0247	0.222	(0.0, 0.0, -0.6)	(0.0, 0.0, 0.6)	-1.425	-4.179
SXS:BBH:0248	0.222	(0.0, 0.0, -0.5)	(0.0, 0.0, -0.5)	4.404	-2.246
SXS:BBH:0249	0.222	(0.0, 0.0, -0.371)	(0.0, 0.0, 0.85)	-15.913	-5.173
SXS:BBH:0250	0.222	(0.0, 0.0, -0.3)	(0.0, 0.0, -0.3)	-6.795	-5.292
SXS:BBH:0251	0.222	(0.0, 0.0, -0.3)	(0.0, 0.0, 0.0)	-13.571	0.98
SXS:BBH:0252	0.222	(0.0, 0.0, -0.3)	(0.0, 0.0, 0.3)	0.442	0.045
SXS:BBH:0253	0.222	(0.0, 0.0, -0.129)	(0.0, 0.0, -0.85)	-0.564	1.978
SXS:BBH:0254	0.222	(0.0, 0.0, 0.0)	(0.0, 0.0, -0.6)	-1.315	-2.272
SXS:BBH:0255	0.222	(0.0, 0.0, 0.0)	(0.0, 0.0, -0.3)	-1.016	2.421
SXS:BBH:0256	0.222	(0.0, 0.0, 0.0)	(0.0, 0.0, 0.3)	-1.275	1.997
SXS:BBH:0257	0.222	(0.0, 0.0, 0.0)	(0.0, 0.0, 0.6)	-4.439	-2.458
SXS:BBH:0258	0.222	(0.0, 0.0, 0.129)	(0.0, 0.0, 0.85)	0.101	-3.043
SXS:BBH:0259	0.222	(0.0, 0.0, 0.3)	(0.0, 0.0, -0.3)	-7.843	2.171
SXS:BBH:0260	0.222	(0.0, 0.0, 0.3)	(0.0, 0.0, 0.0)	0.889	4.094
SXS:BBH:0261	0.222	(0.0, 0.0, 0.3)	(0.0, 0.0, 0.3)	-0.433	3.291
SXS:BBH:0262	0.222	(0.0, 0.0, 0.371)	(0.0, 0.0, -0.85)	-0.219	2.466
SXS:BBH:0263	0.222	(0.0, 0.0, 0.5)	(0.0, 0.0, 0.5)	1.253	-3.211
SXS:BBH:0264	0.222	(0.0, 0.0, 0.6)	(0.0, 0.0, -0.6)	0.459	-2.289
SXS:BBH:0265	0.222	(0.0, 0.0, 0.6)	(0.0, 0.0, 0.0)	0.215	0.47
SXS:BBH:0266	0.222	(0.0, 0.0, 0.6)	(0.0, 0.0, 0.6)	0.501	-1.989
SXS:BBH:0267	0.222	(0.0, 0.0, 0.85)	(0.0, 0.0, 0.85)	1.319	0.058
SXS:BBH:0268	0.222	(0.0, 0.0, 0.871)	(0.0, 0.0, -0.85)	0.541	-0.085
SXS:BBH:0269	0.204	(0.0, 0.0, 0.0)	(0.0, 0.0, 0.0)	0.286	-1.487
SXS:BBH:0270	0.188	(0.0, 0.0, -0.85)	(0.0, 0.0, -0.85)	-7.625	0.114
SXS:BBH:0271	0.188	(0.0, 0.0, -0.731)	(0.0, 0.0, 0.85)	-13.344	0.157
SXS:BBH:0272	0.187	(0.0, 0.0, -0.6)	(0.0, 0.0, 0.0)	-4.21	0.256

(Continued.)

Table B1. (Continued.)

SXS:BBH:0273	0.188	(0.0, 0.0, -0.6)	(0.0, 0.0, 0.6)	0.387	5.454
SXS:BBH:0274	0.188	(0.0, 0.0, -0.6)	(0.0, 0.0, -0.6)	1.144	0.382
SXS:BBH:0275	0.187	(0.0, 0.0, -0.6)	(0.0, 0.0, -0.4)	-0.136	2.122
SXS:BBH:0276	0.187	(0.0, 0.0, -0.6)	(0.0, 0.0, 0.4)	-2.085	-0.567
SXS:BBH:0277	0.188	(0.0, 0.0, -0.5)	(0.0, 0.0, -0.5)	14.362	-0.212
SXS:BBH:0278	0.188	(0.0, 0.0, -0.4)	(0.0, 0.0, -0.6)	-0.491	5.994
SXS:BBH:0279	0.188	(0.0, 0.0, -0.4)	(0.0, 0.0, 0.6)	-0.438	-0.182
SXS:BBH:0280	0.188	(0.0, 0.0, -0.3)	(0.0, 0.0, -0.3)	-0.486	-1.179
SXS:BBH:0281	0.187	(0.0, 0.0, -0.3)	(0.0, 0.0, 0.0)	1.006	0.269
SXS:BBH:0282	0.188	(0.0, 0.0, -0.3)	(0.0, 0.0, 0.3)	1.365	0.283
SXS:BBH:0283	0.188	(0.0, 0.0, -0.269)	(0.0, 0.0, -0.85)	13.888	0.239
SXS:BBH:0284	0.188	(0.0, 0.0, -0.231)	(0.0, 0.0, 0.85)	0.396	4.617
SXS:BBH:0285	0.188	(0.0, 0.0, 0.0)	(0.0, 0.0, -0.6)	0.152	2.157
SXS:BBH:0286	0.188	(0.0, 0.0, 0.0)	(0.0, 0.0, -0.3)	-0.202	0.795
SXS:BBH:0287	0.188	(0.0, 0.0, 0.0)	(0.0, 0.0, 0.3)	-0.19	-0.91
SXS:BBH:0288	0.188	(0.0, 0.0, 0.0)	(0.0, 0.0, 0.6)	-0.318	2.466
SXS:BBH:0289	0.188	(0.0, 0.0, 0.231)	(0.0, 0.0, -0.85)	-1.702	1.61
SXS:BBH:0290	0.188	(0.0, 0.0, 0.269)	(0.0, 0.0, 0.85)	-0.745	-0.958
SXS:BBH:0291	0.188	(0.0, 0.0, 0.3)	(0.0, 0.0, -0.3)	-1.241	0.467
SXS:BBH:0292	0.187	(0.0, 0.0, 0.3)	(0.0, 0.0, 0.0)	-1.491	-2.115
SXS:BBH:0293	0.188	(0.0, 0.0, 0.3)	(0.0, 0.0, 0.3)	1.642	-0.474
SXS:BBH:0294	0.188	(0.0, 0.0, 0.4)	(0.0, 0.0, -0.6)	2.581	1.489
SXS:BBH:0295	0.188	(0.0, 0.0, 0.4)	(0.0, 0.0, 0.6)	10.325	-0.021
SXS:BBH:0296	0.188	(0.0, 0.0, 0.5)	(0.0, 0.0, 0.5)	-0.552	0.965
SXS:BBH:0297	0.188	(0.0, 0.0, 0.6)	(0.0, 0.0, -0.6)	3.966	-4.49
SXS:BBH:0298	0.188	(0.0, 0.0, 0.6)	(0.0, 0.0, -0.4)	8.637	1.334
SXS:BBH:0299	0.188	(0.0, 0.0, 0.6)	(0.0, 0.0, 0.0)	3.36	-0.215
SXS:BBH:0300	0.188	(0.0, 0.0, 0.6)	(0.0, 0.0, 0.4)	7.92	-4.126
SXS:BBH:0301	0.187	(0.0, 0.0, 0.6)	(0.0, 0.0, 0.6)	4.708	1.765
SXS:BBH:0302	0.188	(0.0, 0.0, 0.731)	(0.0, 0.0, -0.85)	2.827	1.355
SXS:BBH:0303	0.188	(0.0, 0.0, 0.85)	(0.0, 0.0, 0.85)	7.128	-0.872
SXS:BBH:0305	0.173	(0.0, 0.0, 0.0)	(0.0, 0.0, 0.0)	0.305	0.054
SXS:BBH:0306	0.149	(0.0, 0.0, 0.0)	(0.0, 0.0, 0.0)	2.69	-2.853
SXS:BBH:0307	0.130	(0.0, 0.0, 0.0)	(0.0, 0.0, 0.0)	-0.3	2.773
SXS:BBH:0317	0.116	(0.0, 0.0, 0.0)	(0.0, 0.0, 0.0)	-3.448	1.909
SXS:BBH:0318	0.109	(0.0, 0.0, 0.0)	(0.0, 0.0, 0.0)	1.134	-0.07
SXS:BBH:0319	0.104	(0.0, 0.0, 0.0)	(0.0, 0.0, 0.0)	-0.186	-0.109
SXS:BBH:0320	0.094	(0.0, 0.0, 0.0)	(0.0, 0.0, 0.0)	-1.866	-2.913

Appendix C. NR error estimates as a function of the intrinsic parameters

We estimate the kick error in NR waveforms using SXS simulations which include at least two resolutions. Figures C1 and C2 show the errors as a function of the symmetric mass ratio and the spin components of the binary.

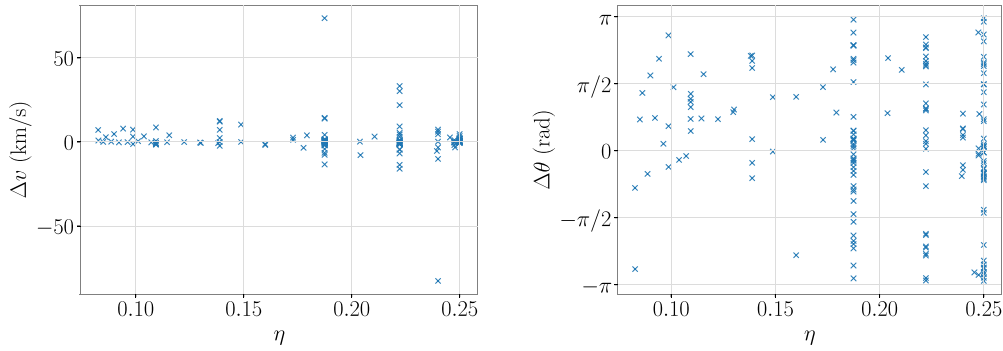


Figure C1. NR error estimates of the kick magnitude (left) and orientation (right) as a function of the symmetric mass ratio.

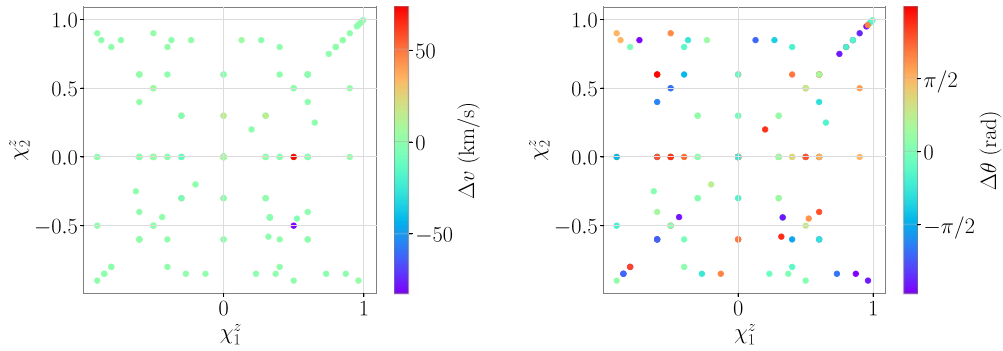


Figure C2. NR error estimates of the kick magnitude (left) and orientation (right) as a function of the individual spins.

ORCID iDs

Angela Borchers  <https://orcid.org/0000-0002-2184-7388>

Frank Ohme  <https://orcid.org/0000-0003-0493-5607>

References

- [1] Abbott B P *et al* (LIGO Scientific and Virgo) 2016 *Phys. Rev. Lett.* **116** 061102
- [2] Abbott B P *et al* (LIGO Scientific and Virgo) 2019 *Phys. Rev. X* **9** 031040
- [3] Abbott R *et al* (LIGO Scientific and Virgo) 2021 *Phys. Rev. X* **11** 021053
- [4] Abbott R *et al* (LIGO Scientific, VIRGO and KAGRA) 2021 arXiv:2111.03606
- [5] Veitch J *et al* 2015 *Phys. Rev. D* **91** 042003
- [6] Ashton G *et al* 2019 *Astrophys. J. Suppl. Ser.* **241** 27
- [7] Aasi J *et al* (LIGO Scientific) 2015 *Class. Quantum Grav.* **32** 074001
- [8] Acernese F *et al* (VIRGO) 2015 *Class. Quantum Grav.* **32** 024001
- [9] Abbott B P *et al* 2017 *Class. Quantum Grav.* **34** 104002
- [10] Pürrer M and Haster C J 2020 *Phys. Rev. Res.* **2** 023151
- [11] Varma V, Ajith P, Husa S, Bustillo J C, Hannam M and Pürrer M 2014 *Phys. Rev. D* **90** 124004
- [12] Varma V and Ajith P 2017 *Phys. Rev. D* **96** 124024
- [13] Shaik F H, Lange J, Field S E, O'Shaughnessy R, Varma V, Kidder L E, Pfeiffer H P and Wysocki D 2020 *Phys. Rev. D* **101** 124054

- [14] Kalaghatgi C, Hannam M and Raymond V 2020 *Phys. Rev. D* **101** 103004
- [15] Krishnendu N V and Ohme F 2022 *Phys. Rev. D* **105** 064012
- [16] Abbott R *et al* (LIGO Scientific and Virgo) 2020 *Phys. Rev. D* **102** 043015
- [17] Abbott R *et al* (LIGO Scientific and Virgo) 2020 *Astrophys. J. Lett.* **896** L44
- [18] Mateu-Lucena M, Husa S, Colleoni M, Estellés H, García-Quirós C, Keitel D, Planas M d L and Ramos-Buades A 2021 arXiv:2105.05960
- [19] Chatziioannou K *et al* 2019 *Phys. Rev. D* **100** 104015
- [20] Pratten G, Husa S, García-Quirós C, Colleoni M, Ramos-Buades A, Estellés H and Jaume R 2020 *Phys. Rev. D* **102** 064001
- [21] García-Quirós C, Colleoni M, Husa S, Estellés H, Pratten G, Ramos-Buades A, Mateu-Lucena M and Jaume R 2020 *Phys. Rev. D* **102** 064002
- [22] García-Quirós C, Husa S, Mateu-Lucena M and Borchers A 2021 *Class. Quantum Grav.* **38** 015006
- [23] Pratten G *et al* 2021 *Phys. Rev. D* **103** 104056
- [24] Estellés H, Ramos-Buades A, Husa S, García-Quirós C, Colleoni M, Haegel L and Jaume R 2021 *Phys. Rev. D* **103** 124060
- [25] Estellés H, Husa S, Colleoni M, Keitel D, Mateu-Lucena M, García-Quirós C, Ramos-Buades A and Borchers A 2020 arXiv:2012.11923
- [26] Estellés H, Colleoni M, García-Quirós C, Husa S, Keitel D, Mateu-Lucena M, Planas M d L and Ramos-Buades A 2021 arXiv:2105.05872
- [27] Komossa S 2012 *Adv. Astron.* **2012** 1–8
- [28] Lousto C O and Healy J 2019 *Phys. Rev. D* **100** 104039
- [29] Calderón Bustillo J, Clark J A, Laguna P and Shoemaker D 2018 *Phys. Rev. Lett.* **121** 191102
- [30] Varma V, Isi M and Biscoveanu S 2020 *Phys. Rev. Lett.* **124** 101104
- [31] Mahapatra P, Gupta A, Favata M, Arun K G and Sathyaprakash B S 2021 *Astrophys. J. Lett.* **918** L31
- [32] Varma V, Biscoveanu S, Islam T, Shaik F H, Haster C J, Isi M, Farr W M, Field S E and Vitale S 2022 arXiv:2201.01302
- [33] Lindblom L, Owen B J and Brown D A 2008 *Phys. Rev. D* **78** 124020
- [34] Kumar P, Chu T, Fong H, Pfeiffer H P, Boyle M, Hemberger D A, Kidder L E, Scheel M A and Szilagyi B 2016 *Phys. Rev. D* **93** 104050
- [35] Ashtekar A, De Lorenzo T and Khera N 2020 *Gen. Relativ. Gravit.* **52** 107
- [36] Ashtekar A and Streubel M 1981 *Proc. R. Soc. A* **376** 585–607
- [37] Khera N, Ashtekar A and Krishnan B 2021 *Phys. Rev. D* **104** 124071
- [38] Khera N, Krishnan B, Ashtekar A and De Lorenzo T 2021 *Phys. Rev. D* **103** 044012
- [39] Mitman K *et al* 2021 *Phys. Rev. D* **103** 024031
- [40] Campanelli M, Lousto C O, Zlochower Y and Merritt D 2007 *Phys. Rev. Lett.* **98** 231102
- [41] Gonzalez J A, Sperhake U, Brüggmann B, Hannam M and Husa S 2007 *Phys. Rev. Lett.* **98** 091101
- [42] Pollney D *et al* 2007 *Phys. Rev. D* **76** 124002
- [43] Brüggmann B, Gonzalez J A, Hannam M, Husa S and Sperhake U 2008 *Phys. Rev. D* **77** 124047
- [44] Varma V, Gerosa D, Stein L C, Hébert F M C and Zhang H 2019 *Phys. Rev. Lett.* **122** 011101
- [45] Newman E T and Penrose R 1966 *J. Math. Phys.* **7** 863–70
- [46] Bohé A *et al* 2017 *Phys. Rev. D* **95** 044028
- [47] Cotesta R, Buonanno A, Bohé A, Taracchini A, Hinder I and Ossokine S 2018 *Phys. Rev. D* **98** 084028
- [48] Ossokine S *et al* 2020 *Phys. Rev. D* **102** 044055
- [49] Nagar A and Rettengo P 2019 *Phys. Rev. D* **99** 021501
- [50] Nagar A *et al* 2018 *Phys. Rev. D* **98** 104052
- [51] Nagar A, Riemenschneider G, Pratten G, Rettengo P and Messina F 2020 *Phys. Rev. D* **102** 024077
- [52] Ajith P *et al* 2011 *Phys. Rev. Lett.* **106** 241101
- [53] Santamaria L *et al* 2010 *Phys. Rev. D* **82** 064016
- [54] Hannam M, Schmidt P, Bohé A, Haegel L, Husa S, Ohme F, Pratten G and Pürrer M 2014 *Phys. Rev. Lett.* **113** 151101
- [55] Husa S, Khan S, Hannam M, Pürrer M, Ohme F, Forteza X J and Bohé A 2016 *Phys. Rev. D* **93** 044006
- [56] Khan S, Husa S, Hannam M, Ohme F, Pürrer M, Forteza X J and Bohé A 2016 *Phys. Rev. D* **93** 044007
- [57] London L, Khan S, Fauchon-Jones E, García C, Hannam M, Husa S, Jiménez-Forteza X, Kalaghatgi C, Ohme F and Pannarale F 2018 *Phys. Rev. Lett.* **120** 161102
- [58] Khan S, Chatziioannou K, Hannam M and Ohme F 2019 *Phys. Rev. D* **100** 024059

- [59] Hamilton E, London L, Thompson J E, Fauchon-Jones E, Hannam M, Kalaghatgi C, Khan S, Panarale F and Vano-Vinuales A 2021 *Phys. Rev. D* **104** 124027
- [60] Blackman J, Field S E, Scheel M A, Galley C R, Hemberger D A, Schmidt P and Smith R 2017 *Phys. Rev. D* **95** 104023
- [61] Varma V, Field S E, Scheel M A, Blackman J, Kidder L E and Pfeiffer H P 2019 *Phys. Rev. D* **99** 064045
- [62] Blackman J, Field S E, Scheel M A, Galley C R, Ott C D, Boyle M, Kidder L E, Pfeiffer H P and Szilágyi B 2017 *Phys. Rev. D* **96** 024058
- [63] Damour T and Nagar A 2016 *Astrophysical Black Holes (Lecture Notes in Physics vol 905)* pp 273–312
- [64] Kokkotas K D and Schmidt B G 1999 *Living Rev. Relativ.* **2** 2
- [65] Cotesta R, Marsat S and Pürrer M 2020 *Phys. Rev. D* **101** 124040
- [66] Ruiz M, Alcubierre M, Núñez D and Takahashi R 2008 *Gen. Relativ. Gravit.* **40** 2467
- [67] LIGO Scientific Collaboration 2018 LIGO algorithm library—lalsuite free software (GPL) (<https://doi.org/10.7935/GT1W-FZ16>)
- [68] Boyle M *et al* 2019 *Class. Quantum Grav.* **36** 195006
- [69] Schmidt P, Harry I W and Pfeiffer H P 2017 arXiv:1703.01076
- [70] Fitchett M J 1983 *Mon. Not. R. Astron. Soc.* **203** 1049–62
- [71] Kidder L E 1995 *Phys. Rev. D* **52** 821–47
- [72] Blanchet L, Qusailah M S S and Will C M 2005 *Astrophys. J.* **635** 508–15
- [73] Aasi J *et al* (LIGO Scientific and VIRGO) 2015 *Class. Quantum Grav.* **32** 115012

Chapter 6

Observability of spin precession in the presence of a black-hole remnant kick

In this chapter, we include a reprint of the following article:

[31] Angela Borchers, Frank Ohme, Jannik Mielke, and Shrobana Ghosh. Observability of spin precession in the presence of a black-hole remnant kick. *Phys. Rev. D* 110, 024037 (2024)

Observability of spin precession in the presence of a black-hole remnant kickAngela Borchers¹,* Frank Ohme², Jannik Mielke², and Shrobona Ghosh²*Max-Planck-Institut für Gravitationsphysik, Albert-Einstein-Institut,
Callinstraße 38, D-30167 Hannover, Germany
and Leibniz Universität Hannover, D-30167 Hannover, Germany*

(Received 15 May 2024; accepted 17 June 2024; published 16 July 2024)

Remnants of binary black-hole mergers can gain significant recoil or kick velocities when the binaries are asymmetric. The kick is the consequence of the anisotropic emission of gravitational waves, which may leave a characteristic imprint in the observed signal. So far, only one gravitational-wave event supports a nonzero kick velocity: GW200129_065458. This signal is also the first to show evidence for spin precession. For most other gravitational-wave observations, spin orientations are poorly constrained as this would require large signal-to-noise ratios, unequal mass ratios, or inclined systems. Here we investigate whether the imprint of the kick can help to extract more information about the spins. We perform an injection and recovery study comparing binary black-hole signals with significantly different kick magnitudes, but the same spin magnitudes and spin tilts. To exclude the impact of higher signal harmonics in parameter estimation, we focus on equal-mass binaries that are oriented face-on. This is also motivated by the fact that equal-mass binaries produce the largest kicks and many observed gravitational-wave events are expected to be close to this configuration. We generate signals with IMRPhenomXO4a, which includes mode asymmetries. These asymmetries are the main cause for the kick in precessing binaries. For comparison with an equivalent model without asymmetries, we repeat the same injections with IMRPhenomXPHM. We find that signals with large kicks necessarily include large asymmetries, and these give more structure to the signal, leading to more informative measurements of the spins and mass ratio. Our results also complement previous findings that argued precession in equal-mass, face-on, or face-away binaries is nearly impossible to identify. In contrast, we find that in the presence of a remnant kick, even those signals become more informative and allow determining precession with signal-to-noise ratios observable already by current gravitational-wave detectors.

DOI: 10.1103/PhysRevD.110.024037

I. INTRODUCTION

Mergers of black-hole binaries can produce remnants with significant recoil or kick velocities. This kick is due to asymmetric emission of linear momentum through gravitational waves (GWs). In turn, this process leaves subtle imprints in the GW signal [1–3].

When the initial spins are not aligned with the orbital angular momentum, the orbital plane and the individual spins precess, and the kick magnitudes can reach up to 5000 km/s for specific configurations [4–9]. Nonprecessing binaries, on the other hand, can produce kicks with values up to ~500 km/s [10,11]. These velocities can become larger

than the escape velocities of the remnants' host environments, which impacts the evolution of gravitationally bound environments, such as stellar clusters and galaxies [12–15]. In the case of stellar black-hole binaries, remnant kicks can restrict the possibility of having multiple generation mergers in certain environments (e.g., globular clusters) and can influence the binary black-hole merger rate [16–20].

GW astronomy provides a new way of directly investigating black-hole kicks, complementing the knowledge gained through electromagnetic observations. Several methods have been proposed to extract the kick velocity from GW events, based on the calculation of the linear momentum radiated away by the binary [21,22]. For most of the GW candidates presented by the LIGO-Virgo-KAGRA (LVK) collaborations [23–27], the inferred kick posteriors appear to be uninformative. This is because the kick velocity is strongly dependent on the black-hole spin orientations, which are poorly constrained with current signal-to-noise ratios (SNRs) [27,28]. The uncertainty in our inference of the spin orientations propagates into the kick posterior. Unless the spins are well determined, it is generally difficult to make meaningful kick measurements.

*Contact author: angela.borchers.pascual@aei.mpg.de

Published by the American Physical Society under the terms of the [Creative Commons Attribution 4.0 International license](https://creativecommons.org/licenses/by/4.0/). Further distribution of this work must maintain attribution to the author(s) and the published article's title, journal citation, and DOI. Open access publication funded by the Max Planck Society.

However, there is a GW candidate with indications of a nonzero kick velocity [29]. GW200129_065458, which we will refer to as GW200129, shows support for a large kick velocity, $v = 1542_{-1098}^{+747}$ km/s. Interestingly, this event also shows evidence for the first clear measurement of spin precession in a GW event [30]. Though it is claimed that the imprint of precession could be mimicked by the presence of an instrumental artifact happening at the LIGO Livingston interferometer [31,32], further glitch-mitigation studies support the evidence of precession in this event [33]. GW200129 is special as it allows to infer meaningful information about the primary spin: the spin tilt angle [30] and the spin azimuthal angle [29]. The authors of Ref. [29] then estimated a kick posterior by using a map from the binary's mass ratio and the spin orientations to the kick velocity. If the intrinsic properties are known, one knows the kick velocity from numerical simulations of similar binaries. Spin precession, on the other hand, is generally challenging to measure as it requires unequal mass ratios, inclined systems, and large SNRs (see, e.g., [34–38]).

In this paper, we study whether the imprint of the kick can help inferring information about the spins. To do so, we investigate spin and kick measurements of simulated binary black-hole signals. We study whether, in the presence of a large kick, one can extract more information about the source parameters from the signal, with a particular focus on the spin measurements. We perform an injection and recovery study where we compare signals with similar spins but significantly different kick magnitudes.

As mentioned above, remnant kicks are caused by anisotropic emission of linear momentum, which is induced by asymmetries happening in the system. This means that there is a preferred direction at merger along which GWs are radiated more strongly. In the case of a remnant that is kicked in the direction of the line of sight towards the observer, one would receive a weaker signal than if the remnant moved away from the observer.

The geometry of the GW emission can be well described by expanding the GW signal into spin-weighted spherical harmonics, also referred to as GW modes,

$$h_+ - ih_\times = \sum_{\ell \geq 2} \sum_{m=-\ell}^{\ell} h_{\ell,m} {}^{-2}Y_{\ell,m}(\theta, \phi). \quad (1)$$

Here, h_+ and h_\times are the GW polarizations that are functions of the time or frequency and depend on all source and orientation parameters. In a spherical coordinate system, the dependence on the polar angle θ and azimuthal angle ϕ can be factored out by expanding in the spin-weight -2 spherical harmonic functions ${}^{-2}Y_{\ell,m}$. The complex functions $h_{\ell,m}$ are the GW harmonics.

In the case of precessing binaries, the largest kicks are predominantly caused by asymmetries between the (ℓ, m) and $(\ell, -m)$ GW harmonics, which are referred to as mode

asymmetries. Earlier studies have indicated that neglecting such asymmetries could lead to biased measurements of the source properties [39–41]. However, the exact relation between mode asymmetries and the kick velocity is not well understood. Here, we investigate their relation.

Our study complements Refs. [39–41], as we focus on understanding the impact of the kick. We study equal-mass systems that are oriented face-on to the observer to exclude the impact of higher harmonics on parameter measurements. The emission of equal-mass binary black holes is dominated by the quadrupolar radiation, which has its maximum face-on or face-away to the detectors and its minimum edge-on. Since the emission decreases with the inclination angle, given a false-alarm-rate threshold and assuming the sources are isotropically distributed, face-on (-away) binaries are expected to be observed more regularly than other orientations. Even though those signals might be generated by precessing binaries, measuring precession in these signals is difficult in the absence of higher harmonics (see, e.g., [35,36]). In particular, the authors of Ref. [42] concluded that it is impossible to distinguish between a precessing and nonprecessing binary when equal-mass binaries are oriented face-on or face-away from the detectors.

Besides, the largest kick velocities are produced in equal-mass binaries that undergo spin precession (see, e.g., [5]). In addition, many GW events are expected to be nearly equal mass binaries [27,43], as there are several astrophysical mechanisms that lead to the formation of equal-mass black-hole binaries [44–46]. As equal-mass systems are frequently detected, we might expect some of these signals to include a significant kick.

To generate signals that accurately include the imprint of the kick, it is fundamental to include mode asymmetries in the waveform model. An accurate description of the symmetric waveform is also vital, as inaccuracies in the symmetric waveform can lead to inconsistent kick estimates [47]. Both aspects are key to describe the imprint of the kick in the GW signal. Here, we use the model IMRPhenomXPHM [48–51] and compare it to its enhanced version, IMRPhenomXO4a [52–55], which has a more accurate description of the merger and, contrary to its underlying model, it includes the asymmetry in the dominant mode. This means that IMRPhenomXPHM cannot accurately predict kicks in precessing binaries. Having these models is useful, as we can simulate the same binary with and without a kick by simply using a different waveform model.

Based on our study, we find that the conclusion from [42] is only valid for systems without significant mode asymmetries. In the presence of a significant kick, one can actually measure precession even for equal mass, face-on, and face-away systems. We also find that the two-harmonic formalism presented in [36] does not apply in the case of equal-mass, face-on binaries when using waveform models that include mode asymmetries.

In addition, we study how well we can recover the kick velocity in our injections with IMRPhenomXO4a. The measurability of the kick has already been studied with the models NRSur7dq4 [56] and NRSur7dq4Remnant [57]. These models have the advantage of having a similar accuracy to NR simulations, but they can only be used in a limited region of the parameter space: $M \geq 65M_\odot$, $q \leq 4$, $|\vec{\chi}_i| \leq 0.8$. Here we use IMRPhenomXO4a, which is calibrated to a larger volume of the parameter space, $q \leq 8$, $\chi_1 \leq 0.8$, and it can be used to generate waveforms for arbitrarily low total masses. This allows us to investigate precessing kicks with a model that can analyze every binary black-hole event observed by the LIGO and Virgo detectors.

II. METHOD

A. Parameter estimation

To investigate the inference of binary black-hole parameters in signals with remnant kicks, we perform a Bayesian parameter estimation analysis, the standard method for parameter inference of GW signals. Within the Bayesian framework, the state of knowledge of a specific parameter is described as a probability distribution and is calculated using Bayes' theorem. The posterior probability of a parameter θ given the data d and a hypothesis \mathcal{H} can be calculated using the following expression:

$$p(\theta|d, \mathcal{H}) = \frac{\pi(\theta|\mathcal{H})\mathcal{L}(d|\theta, \mathcal{H})}{\mathcal{Z}_{\mathcal{H}}}. \quad (2)$$

Here, $\pi(\theta|H)$ is the prior probability distribution, $\mathcal{L}(d|\theta, H)$ is the likelihood of the data given θ , and $\mathcal{Z}_{\mathcal{H}}$ is the signal evidence assuming the hypothesis \mathcal{H} is the model for the data. In GW data analysis, one typically assumes stationary Gaussian noise. In such case, one can argue that the likelihood function can be written in terms of the data and a waveform template of the observable signal $h(\theta)$ parametrized by the source parameters θ , and is given by [58,59]

$$\mathcal{L} \propto \exp\left(\langle d|h(\theta) \rangle - \frac{1}{2}\langle h(\theta)|h(\theta) \rangle\right), \quad (3)$$

where we have introduced the inner product between two signals defined as

$$\langle h(\theta)|h(\theta_0) \rangle = 4\Re \int_0^\infty \frac{\tilde{h}(f, \theta)\tilde{h}^*(f, \theta_0)}{S_n(f)} df. \quad (4)$$

Here, \tilde{h} is the signal in Fourier domain, $*$ denotes complex conjugation, and S_n is the noise spectral density of the instrument. In reality, we generate waveform templates of finite length, with a lower frequency limit of $f_{\min} = 20$ Hz and an upper frequency limit of $f_{\max} = 2048$ Hz.

Quasicircular binary black holes are characterized by 15 parameters: eight intrinsic parameters, namely, the individual masses m_i and the spins $\vec{\chi}_i = \vec{S}_i/m_i^2$, and seven extrinsic parameters, the luminosity distance to the source d_L , the inclination ι , that is, the angle between the orbital angular momentum and the line of sight, the polarization angle ψ , the right ascension α and declination δ of the source, an arbitrary reference time t_c , such as the time of coalescence, and the orbital phase ϕ at the reference time t_c .

The component masses can also be parametrized by the mass ratio $q = m_1/m_2$, the total mass $M = m_1 + m_2$, or the chirp mass $\mathcal{M} = (m_1 m_2)^{3/5}/(m_1 + m_2)^{1/5}$. Here we use the convention $m_1 \geq m_2$. Two quantities can describe the dominant spin effects of a binary in the radiated GW signal. The effective spin parameter [60–62], χ_{eff} , is defined as

$$\chi_{\text{eff}} = \frac{m_1 \chi_1 + m_2 \chi_2}{m_1 + m_2}. \quad (5)$$

χ_{eff} quantifies the dominant spin effect in nonprecessing binaries, where the black-hole spins are aligned with the orbital angular momentum. The second parameter is the effective spin-precession parameter [63,64], χ_p , which parametrizes the dominant spin-precession effects in a binary and is defined as

$$\chi_p = \frac{1}{A_1 m_1^2} \max(A_1 S_{1\perp}, A_2 S_{2\perp}), \quad (6)$$

where $A_1 = (2 + 3q/2)$ and $A_2 = (2 + 3/2q)$ are functions of the initial masses and $S_{i\perp} = |\hat{L} \times (\vec{S}_i \times \hat{L})|$ are the in-plane spin components. Its value is bounded between $0 \leq \chi_p \leq 1$, where larger values represent stronger precession.

B. Waveform models

In our study we use two different waveform models: IMRPhenomXPHM and IMRPhenomXO4a. They are both frequency-domain inspiral-merger-ringdown models that belong to the phenomenological family, which is based on combining analytical expressions for the early inspiral phase with numerical relativity (NR) data for the merger and ringdown. Hybrid waveforms are produced to later perform phenomenological fits, which are interpolated over the parameter space. Both models include the same set of GW higher harmonics and model precession effects.

IMRPhenomXPHM is designed to model the expected GW signals from precessing binaries. The model includes higher harmonics and is calibrated to an extended set of NR simulations, which gives it a high degree of accuracy. In addition, it incorporates multibanding techniques to accelerate the evaluation of waveforms. Because of its good performance, it has routinely been used by the LIGO collaboration to analyze events from GWTC-3.

IMRPhenomXO4a is a new model that adds several improvements to IMRPhenomXPHM: (i) the NR calibration of the $(\ell, m) = (2, \pm 2)$ coprecessing mode, that is, the mode as measured in a noninertial frame that tracks the precession of the orbital plane; (ii) the NR calibration of the precession angles; (iii) the use of an effective ringdown frequency, and (iv) the modeling of the dominant mode asymmetry between the $(\ell, m) = (2, 2)$ and $(\ell, m) = (2, -2)$ coprecessing modes.

The orbit of aligned-spin binaries is symmetric under reflection over the orbital plane, which means that the GW harmonics satisfy a particular symmetry relation,

$$h_{\ell, -m}^* = (-1)^\ell h_{\ell, m}. \quad (7)$$

Such symmetry does not hold in precessing binaries. Instead, there is an asymmetry in the contribution from $+m$ and $-m$ modes to the waveform. On a basis of spin-weighted spherical harmonics, the symmetric ($h_{\ell, m}^+$) and antisymmetric ($h_{\ell, m}^-$) parts of the waveform can be written as

$$h_{\ell, m}^\pm(t) = \frac{h_{\ell, m}(t) \pm (-1)^\ell h_{\ell, -m}^*(t)}{2}. \quad (8)$$

The antisymmetric waveform quantifies the mode asymmetry and is responsible for generating out-of-plane kicks in precessing binaries, as we will show in the following subsection. Out-of-plane kicks can be significantly larger than the in-plane kick produced by the excitation of higher modes of the signal. For this reason, including the antisymmetric part is essential to predict precessing kicks accurately. From the currently existing waveform models, the NRSurrogates and IMRPhenomXO4a are the only models that include this effect.

C. The remnant kick velocity

To infer the remnant kick velocity of each signal, we compute the radiated momentum flux over the binary evolution, which can be expressed as

$$P_i = -\lim_{r \rightarrow \infty} \frac{r^2}{16\pi} \int_{-\infty}^{\infty} dt \oint d\Omega \hat{x}_i(\theta, \varphi) |\dot{h}(t)|^2, \quad (9)$$

where $\hat{x}_i = (\sin \theta \cos \varphi, \sin \theta \sin \varphi, \cos \theta)$ is the unit vector expressed in the spherical harmonic basis and h is the GW strain as defined in Eq. (1). We choose a coordinate system where the orbital plane is in the x - y plane, and the z axis is aligned with the orbital angular momentum at a reference frequency. We decompose the GW strain into spin-weighted spherical harmonics, and by integrating over the two-sphere, one can show that the components of the remnant's momentum are given by [65]

$$P_z = -\frac{1}{16\pi} \int_{-\infty}^{\infty} dt \sum_{\ell, m} \dot{h}_{\ell, m} (c_{\ell, m} \dot{h}_{\ell, m}^* + d_{\ell, m} \dot{h}_{\ell-1, m}^* + d_{\ell+1, m} \dot{h}_{\ell+1, m}^*), \quad (10)$$

and

$$P_\perp = -\frac{1}{8\pi} \int_{-\infty}^{\infty} dt \sum_{\ell, m} \dot{h}_{\ell, m} (a_{\ell, m} \dot{h}_{\ell, m+1}^* + b_{\ell, -m} \dot{h}_{\ell-1, m+1}^* - b_{\ell+1, m+1} \dot{h}_{\ell+1, m+1}^*), \quad (11)$$

where the coefficients $a_{\ell, m}$, $b_{\ell, m}$, $c_{\ell, m}$, and $d_{\ell, m}$ read

$$\begin{aligned} a_{\ell, m} &= \frac{\sqrt{(\ell - m)(\ell + m + 1)}}{\ell(\ell + 1)}, \\ b_{\ell, m} &= \frac{1}{2\ell} \sqrt{\frac{(\ell - 2)(\ell + 2)(\ell + m)(\ell + m - 1)}{(2\ell - 1)(2\ell + 1)}}, \\ c_{\ell, m} &= \frac{2m}{\ell(\ell + 1)}, \\ d_{\ell, m} &= \frac{1}{\ell} \sqrt{\frac{(\ell - 2)(\ell + 2)(\ell - m)(\ell + m)}{(2\ell - 1)(2\ell + 1)}}. \end{aligned} \quad (12)$$

These are the components parallel and perpendicular to the direction of the orbital angular momentum at the reference frequency. The perpendicular component is a combination of the two planar coordinates, $P_\perp := P_x + iP_y$.

The asymmetries between the positive- and negative- m inertial harmonics are responsible for the net emission of the linear momentum in the z direction, while the interplay of harmonics with different m number is responsible for the in-plane component of the emission of linear momentum. One can compute the kick velocity by dividing the linear momentum by the mass of the remnant black hole.

We generate individual $h_{\ell, m}$ harmonic modes through LALSuite, the LIGO Scientific Collaboration Algorithm Library [66,67], and integrate these to compute the kick velocity using the package SCRI [68–71], where Eqs. (10) and (11) have been implemented.

Alternatively, one could use existing fits for the kick velocity, e.g., NRSur7dq4Remnant, where the remnant kick is computed from the binary's initial masses and spins. However, using these fits on posterior samples obtained with IMRPhenomXPHM or IMRPhenomXO4a can introduce additional systematic errors. We found a disagreement between the kick posteriors estimated from applying NRSur7dq4Remnant on Phenom posterior samples and the kick posterior estimated from integrating the waveform of each sample. Based on this observation, we decided to use the same waveform model for the Bayesian analysis and estimating of the kick posterior. Hence, to infer the kick posterior, we generate a waveform for each posterior sample and compute the remnant's kick

TABLE I. Details of the first set of injections performed. We include the spin magnitudes a_1 and a_2 , the tilt angles θ_1 and θ_2 , the angle between the two spin azimuthal angles ϕ_{12} (defined at 30 Hz), the effective spin-precession parameter χ_p , the ratio between the maximum amplitude of the antisymmetric and symmetric waveforms with IMRPhenomXO4a, $\max(|h_{2,2}^-|/|h_{2,2}^+|)$, the kick magnitude estimated for these specific spin configurations with the two waveform models, $|v|_{\text{XO4a}}$ and $|v|_{\text{XPHM}}$, and the maximum opening angle β_{max} , the maximum value of the angle between the orbital angular momentum and the total angular momentum.

Injection name	a_1	a_2	θ_1	θ_2	ϕ_{12}	χ_p	$\max(h_{2,2}^- / h_{2,2}^+)$	$ v _{\text{XO4a}}$ (km/s)	$ v _{\text{XPHM}}$ (km/s)	β_{max} (rad)
A	0.748	0.748	1.007	1.007	2.789	0.63	0.39	3983	0.16	0.06
B	0.748	0.748	1.007	1.007	0.145	0.63	0.03	188	0.16	0.34
C	0.748	0.748	1.007	1.300	3.251	0.72	0.43	3474	63	0.30
D	0.748	0.748	1.007	1.300	0.053	0.72	0.03	180	33	0.37
E	0.748	0.748	1.007	0.973	3.254	0.63	0.39	203	0.19	0.03

velocity by integrating these waveforms as expressed in Eqs. (10) and (11).

The injected kick magnitudes are included in Table I. As expected from the lack or inclusion of mode asymmetries, respectively, IMRPhenomXPHM and IMRPhenomXO4a have different kick estimates for the same configurations. We infer the kick prior by applying the same procedure to samples of the source properties (e.g., the individual masses and spins) drawn from their respective priors, which we define in Sec. II E. For consistency, we generate waveforms with the same model used for the parameter estimation analysis. As the mapping from binary properties to the final kick differs between waveform models, we find that the kick prior distributions are also different for each model. The prior computed with IMRPhenomXPHM only reaches kick values of ~ 400 km/s, while the prior of IMRPhenomXO4a takes values up to ~ 4000 km/s.

In the following, we will use the wording *large kick* to refer to $v \geq 1000$ km/s. These are kicks that can only be produced in precessing binaries. Similarly, we use the term *small kick* for $v \leq 500$ km/s, the range of values produced in nonprecessing and some precessing binaries. We perform two injections with large kicks and two with low kicks. As we fix to equal-mass, face-on binaries, with kick magnitudes in the lower or upper end of the range of possible kick velocity values, these are not random points in the parameter space, but selected points that are representatives of the possible kick magnitudes and their effect on parameter estimation. Any other equal-mass binary can be understood by the cases studied here.

D. Interplay between mode asymmetries and the kick velocity

We now discuss how the amplitude of the dominant antisymmetric contribution, $|h_{2,2}^-|$, is related to the kick velocity. We compute both quantities for a set of equal-mass binaries with different spin configurations using IMRPhenomXO4a. We keep one spin vector and the magnitude of the second spin fixed while sampling over the second spin tilt, $\theta_2 \in [0, \pi]$, and azimuthal angle, $\phi_2 \in [0, 2\pi]$. We generate the antisymmetric waveform with the function

SimIMRPhenomX_PNR_GenerateAntisymmetricWaveform available in LALSuite, which we inverse Fourier transform to the time domain. For a more intuitive understanding of the antisymmetric amplitude, we use the ratio between the maximum amplitudes of the antisymmetric and symmetric mode contributions.

In Fig. 1 we show the relation between the kick velocity and the ratio between the antisymmetric and symmetric waveforms as a function of the secondary spin azimuthal angle, as indicated by the colormap. Here, we fixed the primary spin to $\vec{\chi}_1 = (0.2, -0.6, 0.4)$, and the secondary spin magnitude to $a_2 = 0.748$. What is interesting for our study is that small asymmetries are only compatible with small kicks, while large asymmetries do not necessarily mean large kicks. Signals with the same antisymmetric amplitude might have significantly different kick velocities, depending on the relative phase between the symmetric and antisymmetric waveforms. An intuitive way of understanding the impact of this phase difference on the kick is described in [72]. Yet, large kicks are only generated by large asymmetries. We find that these statements remain valid when changing the binary's mass ratio. Further investigations on the relation between kicks and mode asymmetries will be presented in a forthcoming publication.

E. Injections

We perform an injection and recovery study with equal-mass configurations. To understand whether the presence of a kick can have any impact on the estimation of source parameters, we compare binary black-hole signals with significantly different kick velocities but with spin orientations that are as similar as possible. In particular, we want these binaries to have the same precession parameter χ_p , which is defined in terms of the spin magnitudes and the spin tilts, and is independent of the spin azimuthal angle.

As shown in Fig. 1, the kick velocity is highly sensitive to the spin orientations, in particular, to the spin azimuthal angles. By modifying the angle between the two spin azimuthal angles, ϕ_{12} , and keeping the remaining parameters fixed, we can find binaries with significantly different

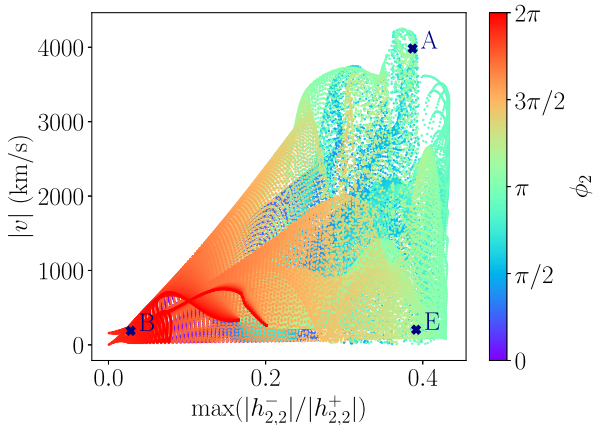


FIG. 1. Relation between the kick magnitude and the antisymmetric waveform with IMRPhenomXO4a. The colormap indicates the dependency of these two quantities on the secondary spin azimuthal angle, ϕ_2 . To produce this figure, we fixed the mass ratio $q = 1$, the primary spin vector $\vec{\chi}_1 = (0.2, -0.6, 0.4)$, the secondary spin magnitude $a_2 = 0.748$, and sampled over the secondary spin tilt and azimuthal angles. The dependency on the secondary azimuthal angle ϕ_2 can also be seen as a change in ϕ_{12} . The crosses indicate the parameters of three different binaries used in the Bayesian analysis: injection A (top cross), injection B (lower left cross), and injection E (lower right cross).

kick velocities, but with the same χ_p value. Therefore, we compare signals from binaries with the same spin magnitudes and spin tilts, but with different spin azimuthal angles.

To investigate the impact of the kick, we compare the parameter inference of a signal with a large kick with that of an equivalent signal with a small kick. As listed in Table I, we have two comparisons: injection A (large kick) with injection B (small kick), and injection C (large kick) with injection D (small kick). Most of the discussion will be focused on our findings for injections A (large kick) and B (small kick), and the purpose of performing injections C and D is to confirm the findings observed for injections A and B. In addition, we perform injection E with the goal of understanding the impact of the anti-symmetric amplitude relative to the magnitude of the kick velocity. We include the relevant parameters of our injections in Table I.

We define the black-hole spin orientations at a reference frequency of $f_{\min} = 30$ Hz. Motivated by GW200129, the first binary with support for a nonzero kick velocity and spin precession, we fix the detector frame total mass value to match the most likely value inferred for this event: $M = 70M_\odot$. We later repeat the same injections with $M = 45M_\odot$ and $M = 25M_\odot$. We choose three different SNR values: $\text{SNR} = 26.8$ (same as GW200129), 40, and 60. The luminosity distance is fixed such that the SNR has these values.

Most of the discussion is focused on the parameter inference of the face-on case, this is $\theta_{JN} = 0$. This is the angle between the total angular momentum and the line of sight of the observer. We later repeat the same injections with the angles $\theta_{JN} = \pi/4$ and $\theta_{JN} = \pi/2$.

Besides, in Table I we include the maximum value of the angle between the orbital angular momentum and the total angular momentum, commonly known as the opening angle β , which quantifies the amount of precession in the binary. When the opening angle is zero, there is no precession in the system. As we increase the opening angle, we allow the orbital plane to precess, and this causes mixing of various coprecessing GW harmonics to be present in the GW signal.

It is known that the presence of higher harmonics with different opening angles increases the measurability of precession [36]. To investigate the impact of the kick on parameter measurements and distinguish it from the impact of higher harmonics, we choose systems that suppress higher modes because of their orientation and mass symmetry. The latter suppresses all modes with odd m . Therefore, even when the orbital plane is precessing, the dominant $(\ell, m) = (2, 2)$ mode will not contain significant contributions from the corotating $(2, 1)$ mode. In contrast, for edge-on orientations, $\theta_{JN} = \pi/2$, several higher harmonics are expected to be more present in the signal. We later compare face-on to edge-on injections to understand the impact of kicks relative to that of higher harmonics.

We repeat each injection with IMRPhenomXPHM and IMRPhenomXO4a, to simulate the same binary with and without a kick. We use the same waveform model for injection and recovery to avoid introducing systematic errors arising from modeling differences between the injection and recovery models. This means the parameter biases that may arise in the Bayesian analysis can only be caused by waveform degeneracies and prior-induced constraints. These injections help us investigate the limitations of Bayesian parameter estimation when including or excluding certain physical effects in both the injected signal and the recovery model.

We use uniform priors in the masses distributed over $m_i = [1, 1000]M_\odot$. Spin magnitudes are uniformly distributed between $|\vec{\chi}_i| = [0, 0.99]$ and the spin orientations are isotropically distributed. The prior in the luminosity distance is uniform in $[10, 10000]$ Mpc. All of our injections use a zero-noise realization while assuming a three-detector network formed by the two LIGO and the Virgo detectors at their design sensitivities [24,25].

To inject signals and estimate the marginalized posterior probabilities of the black-hole parameters, we employ Bilby [73], a Python-based GW-inference library, with the nested-sampling algorithm DYNesty [74]. For the postprocessing of the posterior samples we use PESummary [75].

III. INFERENCE OF SOURCE PARAMETERS IN THE PRESENCE OF A REMNANT KICK

A. Effective precession parameter

We now compare the recoveries of the large-kick and small-kick injections. First, we look at the posterior distributions of the effective spin-precession parameter, χ_p .

Figure 2 shows the posterior distributions of χ_p for injections A and B, which we refer to as “large kick” and “small kick” injections in the figure. These binaries are only different in their kick magnitude and their spin azimuthal angle ϕ_{12} , and therefore have the same χ_p value.

When injecting and recovering the signals with IMRPhenomXO4a, we observe that the signal with a large kick has a more accurate recovery than the signal with a small kick. We find the same behavior with injections C and D. This suggests that the presence of a kick helps to extract more information from the signal. To test whether this is really true, we repeat the same injections simulating the signal with a model that does not include a kick or mode asymmetries.

When repeating the injections with IMRPhenomXPHM, without a kick and mode asymmetries in the signal, the Bayesian analysis infers that it is more likely that the source is an aligned spin system. For equal-mass face-on binaries, the signal looks very similar to that of a nonprecessing binary, and these results suggest that the signal does not include enough information for the analysis to determine precession. As IMRPhenomXPHM predicts a zero kick for both binaries, the only difference between injections A and B is ϕ_{12} , which does not influence the χ_p value, and as expected, the χ_p recovery looks the same in both cases.

These results suggest that if the source experiences a kick, the GW signal is more informative and the Bayesian analysis is able to extract more information from the signal.

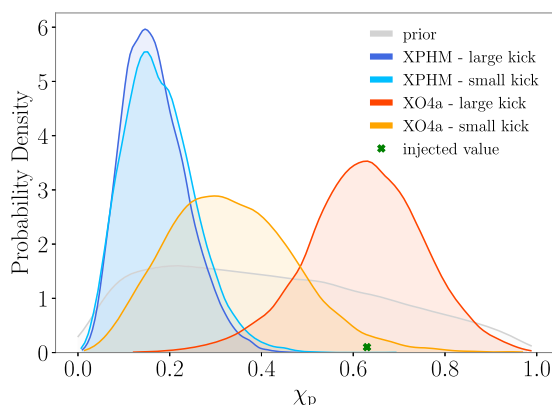


FIG. 2. Posterior probability distribution of χ_p for the injections A and B, which we refer to as the large kick and small kick injections, respectively. IMRPhenomXPHM posteriors are shown in blue, while IMRPhenomXO4a posteriors are shown in orange colors. The green cross indicates the injected value, and the prior distribution is shown in gray.

We observe that one can actually identify precession for equal-mass, face-on binaries through the improved measurement of the mass ratio and the spin tilt angles (see the following sections).

There are a few subtleties which make precession challenging to measure. Assuming a uniform prior in masses and spin magnitudes means that the prior in χ_p is not uniform (see Fig. 2). Therefore, all χ_p posteriors will exclude zero, and thus, every χ_p posterior could be considered as a measure of precession. In this line of thought, it is hard to know if the χ_p posterior represents a meaningful measurement of precession.

Since it is not always clear whether χ_p measurements represent meaningful precession measurements, a new parameter was proposed, which captures the observability of precession in a signal. This parameter is the precession SNR, ρ_p , and is based on the two-harmonic approximation proposed in [35,36]. It is defined as the SNR in the second most significant GW harmonic. A value of $\rho_p > 3$ represents a 1% false rate and is considered as strong evidence for the observability of precession.

We use the precession SNR to quantify the observability of precession in our injections. To compute this quantity we have used PESummary. For consistency with the parameter estimation analysis, we have used the same waveform models employed in parameter estimation and in the calculation of the precession SNR. We find that the posterior distributions are below the observability threshold in all face-on injections.

For the chosen equal-mass, face-on configurations, one can find that the two loudest harmonics are the $(\ell, m) = (2, \pm 2)$ coprecessing modes which get mixed into the $(2, 2)$ inertial mode (see Sec. III F for more details). PESummary does not consider the asymmetries between the $(2, 2)$ and $(2, -2)$ coprecessing modes included in IMRPhenomXO4a and identifies any subdominant harmonic except the $(2, \pm 2)$ as the second loudest harmonic. In most regions of the parameter space, such an assumption will not lead to significant bias. However, for large-kick face-on binaries, the mode asymmetries are non-negligible in the waveform and one should include them in the calculation of the precession SNR. As we incline the binary from face-on to edge-on, higher harmonics become louder and, thus, more relevant in the ρ_p calculation. In fact, we find the PESummary calculations to be meaningful in the case of the edge-on injections.

Here, we want to use the same criterion to assess the parameter recoveries of all injections. Since neither χ_p nor ρ_p might be meaningful parameters to quantify precession for the chosen binaries and waveform models, we prefer to look at the spin and mass ratio measurements directly.

B. Spin tilt angle measurements

In the following, we look at the posteriors of the spin tilt angles whose priors are uncorrelated with other

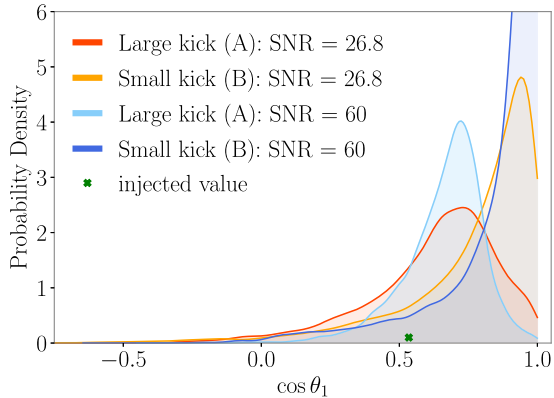


FIG. 3. Influence of the SNR on the posterior distributions of the tilt angles for the large-kick (A) and small-kick (B) injections with IMRPhenomXO4a. Orange colors represent posteriors with SNR = 26.8, while blue colors represent posteriors with SNR = 60. The injected value is shown with the green cross.

parameters. We mostly focus on the parameter recovery of IMRPhenomXO4a, as we can compare precessing binaries with significantly different kick magnitudes.

We observe that the tilt angles θ_1 and θ_2 are more accurately recovered in injections with a large kick than in the recovery of small-kick injections. All of the injections show the same trend. As an example, we include Fig. 3, which displays the posterior distributions of the primary tilt angle for two binaries that are only different in their kick magnitude. Instead of looking at θ_i , we look at the cosine of the tilt angles $\cos \theta_i$, as the prior in θ_i is not uniform, while the prior in $\cos \theta_i$ is. Having a uniform (and uncorrelated) prior means that the posterior unambiguously represents the information extracted from the data.

Figure 3 shows that the primary spin tilt angle is more accurately recovered when there is a large kick. As we increase the SNR of the injected signal, the impact of the kick becomes significantly more visible. Figure 3 compares the recovery of the primary tilt for injections A (large kick) and B (small kick), for SNR = 26.8 (orange colors) and SNR = 60 (blue colors). We observe that the distinction between the large-kick and small-kick recoveries amplifies with the increase in SNR, which supports our hypothesis that the existence of a remnant kick leads to more precise spin measurements. In the following, we investigate whether the improvement in the accuracy of the measurements is truly correlated with the existence of a remnant kick in the signal.

1. Importance of the observability of the merger

If the presence of a kick has any influence on the parameter recovery, then it is its imprint on the waveform that causes such differences in the measurements. As mentioned, the kick velocity is determined by the linear momentum that is radiated away as the two objects come

closer together. Since most of the momentum is emitted in the last few orbits before the merger, the kick builds up during the merger, and leaves a non-negligible imprint on the merger phase of the waveform. To test the influence of the kick, we reduce its observable imprint by reducing the merger phase observable by the detector network.

We can reduce the observed merger phase by changing the total mass of the injected binary. This is because GW detectors are not equally sensitive in all frequency bins. The total mass of the binary determines the frequency range of the signal, and therefore which signal parts are observed by the detector. High-mass systems merge at low frequencies and have few cycles in band, while low-mass systems merge at high frequencies and have many more cycles in band. The most sensitive region of the LIGO and Virgo detectors is located between 100 and 400 Hz.

If the last few orbits of the merger occur in a frequency where the data is dominated by the detector noise, the SNR of the signal in the merger will be smaller than the SNR of the inspiral. Effectively, this could be thought of as calculating the linear momentum radiated away with a reduced final frequency that excludes the merger. Reducing the number of cycles of the merger observable by the detector network would reduce the linear momentum radiated away by the binary, and so the kick magnitude. We can call the kick velocity observable by the detectors as the *effective kick velocity*, v_{eff} .

By diminishing the kick imprint on the injected signal we expect to decrease the effect of the kick on the spin recovery. If our hypothesis is true, we expect the decrease in total mass to increase the bias on the recovery of the spin posteriors. In binaries with no significant kick, decreasing the total mass will not change the kick imprint, as it is already small, so we expect the spin posteriors to remain unchanged. The injections we have performed, which are included in Table I, have a total mass of $M = 70M_{\odot}$. With such value, the merger phase occurs between 100 to 300 Hz, which is exactly the frequency range where the detectors are the most sensitive. We repeat the same injections with total mass values of $M = 25M_{\odot}$ and $M = 45M_{\odot}$, for which the merger occurs at higher frequencies where the detectors are not as sensitive. For the injections with $M = 25M_{\odot}$, the merger occurs at around 10^3 Hz, while for the injections with $M = 45M_{\odot}$, at around 500 Hz.

We find that in the presence of a large kick, decreasing the total mass leads to increased bias, as the posteriors shift away from the injected value. In Fig. 4 we show the posterior distributions of the spin tilt for the large-kick (A) and small-kick (B) injections with different total mass values. With the decrease in total mass, the posteriors shift towards aligned-spin configurations and align with the posterior of the small-kick injection (B). When the binary has a small kick, we observe that changes in the total mass do not impact significantly the spin posteriors. We find the

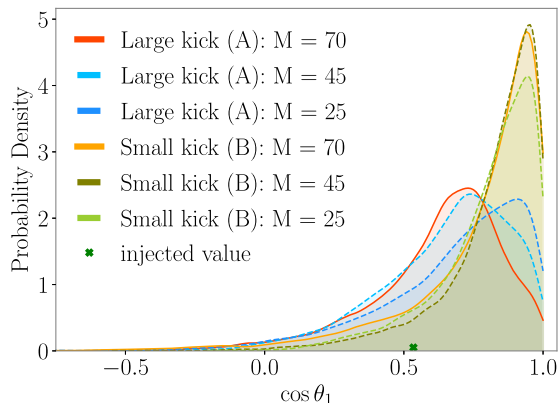


FIG. 4. Influence of the total mass on the posterior distributions of the tilt angles for the large-kick (A) and small-kick (B) injections with IMRPhenomXO4a. We test three different total mass values: $M = 25, 45$ and $70M_{\odot}$. The injected value is indicated with the green cross.

same behavior for both primary and secondary spin tilt angles.

Our results confirm that observing the merger phase is key to making more accurate measurements, only in the presence of a significant kick. We know the kick is described by the symmetric and antisymmetric parts of the waveform, and in the next two subsections we investigate how each of these play a role in the parameter inference.

2. Impact of the mode asymmetries

The authors of Ref. [41] already quantified the impact of including mode asymmetries when inferring in-plane spins for binaries with $q = 2$ and $\text{SNR} = 100$. By looking at binaries with the same antisymmetric amplitude, but different kick magnitudes, they found that it is only the asymmetry content what causes the improved recoveries. Here, we rediscuss this matter for the case of equal-mass binaries with $\text{SNR} = 26.8$.

Based on the relation between kick magnitudes and the antisymmetric waveform (see Fig. 1), we find that there are three possible cases: (i) large kicks with large asymmetries, (ii) small kicks with small asymmetries, and (iii) small kicks with large asymmetries. Injections A, B, and E represent these three cases, respectively. Regarding the spin parameters, these injections have the same spin magnitude and tilt angles and are only different in their ϕ_{12} value (see Table I).

Figure 5 compares the spin posteriors of these three injections. When we compare the injections with the same kick magnitude but different antisymmetric amplitude, B against E, we observe that the magnitude of the asymmetries has a small impact on the spin recovery. In the same way, when we compare the injections with the same antisymmetric amplitude but different kick magnitude,

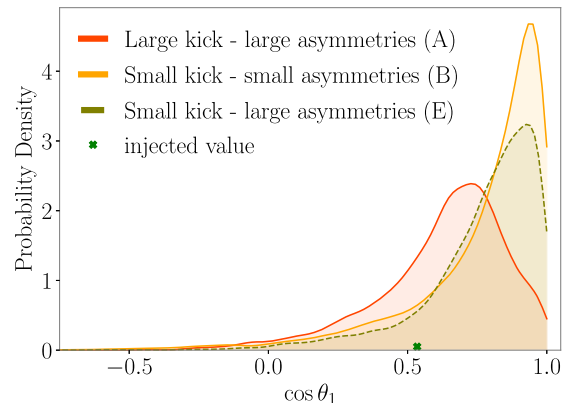


FIG. 5. This figure compares the posteriors of the primary spin tilt of injections A (a binary with a large kick and large asymmetries), B (a binary with a small kick and small asymmetries), and E (a binary with a small kick and large asymmetries), injected and analyzed with IMRPhenomXO4a. This plot shows the impact of the kick magnitude relative to the impact the antisymmetric amplitude on the spin measurements.

A against E, a large kick magnitude leads to more accurate posteriors. In summary, we find that it is the combination of a large antisymmetric amplitude with a large kick magnitude in the GW signal which helps make more accurate measurements.

In addition, we investigate the impact of including mode asymmetries when analyzing a signal with a large kick. To do so, we repeat the analysis using the full IMRPhenomXO4a (including asymmetries) for the injection, and recovering the signal with a version of IMRPhenomXO4a that excludes the asymmetries. As displayed in Fig. 6, we observe that the posteriors obtained excluding mode asymmetries in the model are slightly less precise, but generally very similar to the posteriors obtained when including them. We observe the same behavior for the secondary spin tilt.

These results suggest that it is mostly the additional structure in the observed signal that is responsible for an improved spin measurement, even if the model used for the recovery does not include the mode asymmetries. The additional phase information from the asymmetries in the injected signal helps the analysis to disfavor small spin tilts. As we increase the SNR to 60, the analysis that excludes mode asymmetries has significantly more biased posteriors. This observation is in agreement with Ref. [41], where the SNR was fixed to 100 such that the parameter biases were visible.

We now deactivate the mode asymmetries in the injected signal and test whether the asymmetries are fully responsible for the improved recoveries or not. We repeat these injections with IMRPhenomXO4a, excluding the mode asymmetries both in the injection and recovery models. We compare the posteriors with those of IMRPhenomXPHM, since IMRPhenomXPHM also excludes mode asymmetries, but has a

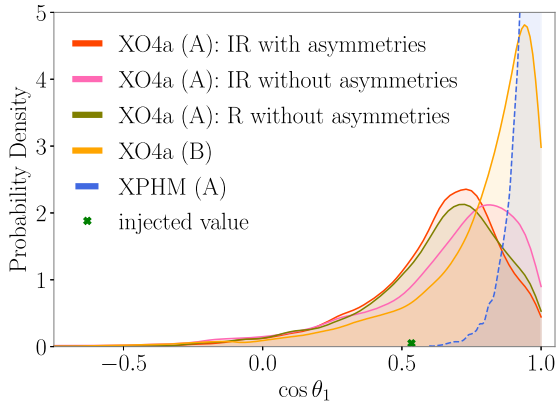


FIG. 6. This figure shows the posterior distributions of the primary spin tilt angle of injection A analyzed with IMRPhenomXO4a in red and with a version of IMRPhenomXO4a that excludes mode asymmetries in the injection and recovery models in pink. The acronyms of the legend “I” and “R” stand for injection and recovery, respectively. In brown, we show the posterior of injection A, where the injected signal includes asymmetries, and the recovery model excludes them. In blue, we show the posterior of injection A injecting and recovering the signal with IMRPhenomXPHM. The figure also includes the posterior of the primary spin tilt angle of the small-kick injection B (orange) analyzed with IMRPhenomXO4a.

slightly less accurate description of the merger and ring-down phases.

Figure 6 shows that the posterior of IMRPhenomXO4a without mode asymmetries (pink) is less accurate than the analysis with the full IMRPhenomXO4a model (red). However, the IMRPhenomXO4a posterior obtained without asymmetries is still more accurate than the low-kick injection analyzed with the full IMRPhenomXO4a. It is also significantly more accurate than the IMRPhenomXPHM posterior. This suggests that the modeling of the (symmetric) merger-ringdown phase plays a role in describing the imprint of the kick and impacts the parameter recoveries. We find that it is the combination of the inclusion of the mode asymmetries and the more accurate modeling of the merger-ringdown phases which ultimately lead to the observed spin measurements of IMRPhenomXO4a.

C. Spin magnitude measurements

We now look at the measurements of the spin magnitudes, a_1 and a_2 . In the same way as for the spin tilt angles, we observe that the recovery in injections with large kicks is in general more accurate than in injections with small kicks.

Figure 7 includes the posterior distributions of the two spin magnitudes and compares the posteriors obtained for injections A (large kick) with B (small kick). In general, we find that a_2 is poorly constrained for both large-kick and small-kick injections, with the large-kick recovery being slightly more accurate. In the case of a_1 , however, we

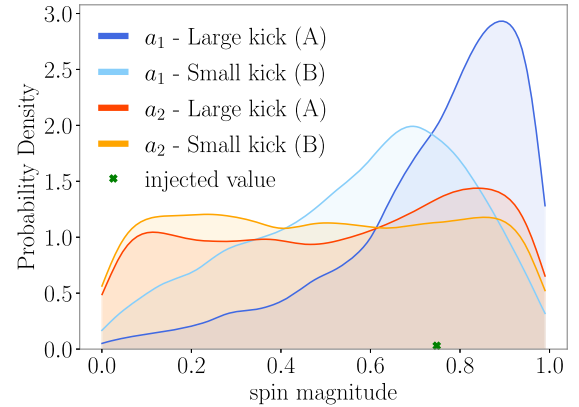


FIG. 7. Posterior distributions of the spin magnitudes a_1 (blue colors) and a_2 (orange colors) for the large-kick (A) and small-kick (B) injections with IMRPhenomXO4a.

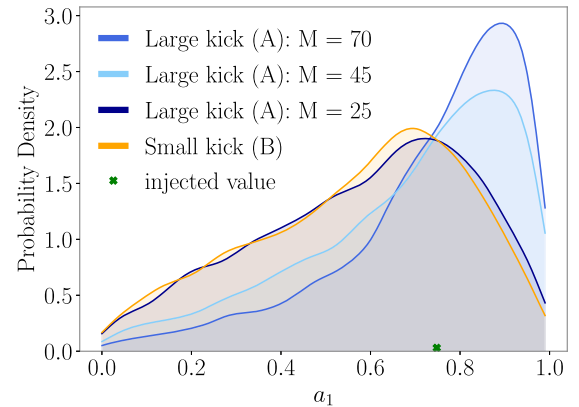


FIG. 8. Posterior distributions of the primary spin magnitude for the large-kick injection A (blue) and the small-kick injection B (orange) with IMRPhenomXO4a. The plot shows the influence of reducing the total mass on the primary spin magnitude.

observe significantly different posterior distributions for the large-kick and small-kick injections.

We investigate whether the fact that the recovery of the primary spin magnitude is more accurate in the large-kick cases is correlated with the kick magnitude. In the same way as for the spin tilts, we reduce the total mass of the binary to reduce the kick imprint observable by the detectors. When reducing the total mass, the recovery of the primary spin magnitude spreads out and becomes less precise than the original posterior with $M = 70M_\odot$. See Fig. 8 for the case of injection A. This supports our idea of the imprint of the kick leading to more accurate measurements of the spins.

D. Spin azimuthal angle measurements

Figure 9 shows the posterior distributions of the spin azimuthal angle ϕ_{12} of injections A and B. For $\text{SNR} = 26.8$, both posteriors appear flat and uninformative.

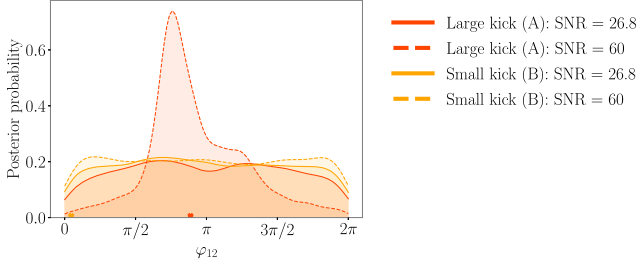


FIG. 9. Posterior distributions of the spin azimuthal angle ϕ_{12} of the large-kick injection A (red) and the small-kick injection B (orange) with IMRPhenomXO4a. The injected values are different in each injection and are indicated in the plot with colored crosses. Solid lines indicate the posteriors with SNR = 26.8, while the dashed lines indicate the posteriors with SNR = 60.

However, as we increase the SNR to 60, we observe that the posterior of the large-kick injection is peaked and centered around the injected value at $\phi_{12} \sim \pi$. On the other hand, the small-kick injection remains uninformative even when increasing the SNR to 60. This suggests once again that a source that experiences a remnant kick radiates a signal that is more informative than if the source experienced no remnant kick.

E. Mass ratio measurements

We have seen that having a significant kick leads to more accurate measurements of the effective spin-precession parameter χ_p , the spin magnitude, tilt, and azimuthal angles. Apart from the individual spins, the effective spin-precession parameter χ_p also depends on the mass ratio [see Eq. (6)]. Here we investigate whether the kick has an impact on the mass ratio measurement.

In the same way as for the spins, we find that large-kick injections have more accurate recoveries of the mass ratio than small-kick ones. Figure 10 shows the posterior distributions of the mass ratio for injections A (large kick) and B (small kick) with SNR = 26.8.

As shown in Fig. 10, when decreasing the observed strength of the merger by decreasing the injected total mass, the uncertainty in the mass ratio posteriors increases for the large kick injections. This points to the importance of observing the merger, which contains the imprint of the kick.

F. Discussion

Our results support that the imprint of the kick leads to more precise measurements of the intrinsic properties. We believe that this observation is connected to the measurability of the mode asymmetries. In our case, since we are using the model IMRPhenomXO4a, these are restricted to the dominant mode asymmetry.

When equal-mass binaries are oriented face-on to the detectors, all subdominant inertial harmonics are suppressed

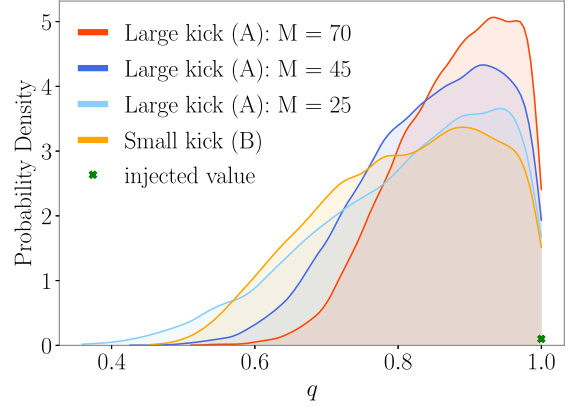


FIG. 10. Posterior distributions of the mass ratio for the large-kick (A) and small-kick (B) injections with IMRPhenomXO4a. The figure also shows the influence of the total mass on the mass ratio posterior of injection A, as we test three different total mass values: $M = 25, 45$ and $70M_\odot$. The injected value is indicated with the green cross.

in the signal, which means that only the $(\ell, m) = (2, 2)$ inertial harmonic can be measured. The dominant inertial harmonic can be expressed in terms of the coprecessing harmonics based on a frame rotation [63],

$$h_{2,2} = \sum_{m' \in \pm\{1,2\}} h_{2,m'}^{\text{CP}} e^{i2\alpha} d_{m',2}^2(-\beta) e^{-im'\epsilon}, \quad (13)$$

where $d_{m',m}^\ell$ is the Wigner matrix that depends on the opening angle β between the total and orbital angular momentum, and α and ϵ are the remaining two angles that are required to describe the instantaneous orientation of the orbital plane. The leading-order amplitude of the $h_{2,1}^{\text{CP}}$ harmonic is proportional to the mass difference between the two objects. So for equal-mass binaries, this harmonic is suppressed. The dominant inertial harmonic is thus a combination of the $(\ell, m) = (2, \pm 2)$ coprecessing harmonics:

$$h_{2,2} = h_{2,2}^{\text{CP}} e^{i2\alpha} d_{2,2}^2(-\beta) e^{-i2\epsilon} + h_{2,-2}^{\text{CP}} e^{i2\alpha} d_{-2,2}^2(-\beta) e^{i2\epsilon}. \quad (14)$$

According to the two-harmonic approximation, two harmonics with different β dependencies need to be observed to unambiguously measure precession [35]. These can be two harmonics in the inertial frame, or two harmonics in the coprecessing frame that mix into one inertial harmonic, as it was later shown in [42]. When using a waveform model that assumes the symmetry relation $h_{2,2}^{\text{CP}} = h_{2,-2}^{\text{CP}}$, then the inertial harmonic $h_{2,2}$ is the combination of the coprecessing $h_{2,2}^{\text{CP}}$ harmonic with its complex conjugate. This means we cannot measure two harmonics with different β dependencies and, therefore, precession is not measurable. This is the case

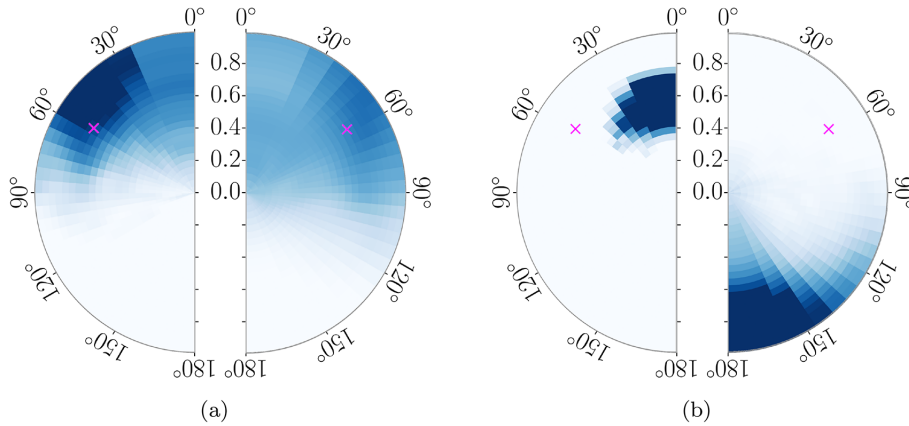


FIG. 11. Two-dimensional spin posterior distributions of the large-kick injection A with IMRPhenomXO4a (a) and IMRPhenomXPHM (b) for $\text{SNR} = 26.8$. In each case, the panel on the left shows the posterior distribution of the primary spin, while the panel on the right shows the posterior of the secondary spin. Each panel displays the posterior of the spin magnitude and the spin tilt. Injected values are indicated with pink crosses in the plots.

for all SEOBNR and Phenom waveform models, except IMRPhenomXO4a.

However, if the waveform model includes the asymmetry between the $h_{2,2}^{\text{CP}}$ and $h_{2,-2}^{\text{CP}}$ harmonics, then the inertial harmonic $h_{2,2}$ is indeed a combination of two coprecessing harmonics with different β dependencies. Therefore, precession will be observable if the two dominant coprecessing harmonics are sufficiently strong in the signal, or equivalently, the antisymmetric part of the waveform is observable. A GW signal with a significant kick necessarily includes large mode asymmetries and, therefore, based on the previous argument, we can expect to measure precession more accurately than when the mode asymmetries are small or actually neglected.

Since IMRPhenomXPHM assumes the symmetry relation between the negative- and positive- m coprecessing harmonics, effectively, the radiated signal only contains one harmonic, and the signal appears to be similar to that of a nonprecessing binary. Therefore, we do not expect precession to be measurable with IMRPhenomXPHM for face-on, equal-mass binaries.

As expected from the previous argument, the parameter recovery of IMRPhenomXPHM appears to be biased in several parameters: χ_p as shown in Fig. 2, and the spin tilt angles as shown in Fig. 11. IMRPhenomXPHM shows support for the primary spin being aligned with the orbital angular momentum and the secondary being antialigned with the orbital angular momentum. The results are consistent with the expectation of the two-harmonic approximation: face-on, equal-mass precessing waveforms appear as nonprecessing waveforms. In the case of IMRPhenomXPHM, the sampler chooses points in the parameter space that are consistent with aligned-spin configurations.

The bias in the spin orientations appears to be compensated with unequal mass ratios, as shown in Fig. 12. While the posterior distributions of IMRPhenomXO4a shift toward

the injected value as we increase the signal SNR to 60, we find that the IMRPhenomXPHM posteriors do not become more accurate. The mass ratio estimates remain biased.

Such bias is not unexpected. The face-on precessing signal mimics the signal of a nonprecessing binary. However, the phase evolution is not the same as the one from a fiducial binary where the in-plane spin components have simply been set to zero. Precession adds a secular phase drift of twice the precession phase (i.e., the accumulated phase of the orbital angular momentum around the total angular momentum) [35,76]. This missing phase can be compensated by modifying the intrinsic parameters, most notably the mass ratio in the IMRPhenomXPHM analysis. The IMRPhenomXO4a analysis does not suffer from this bias as the signal contains more structure due to mode asymmetries and an updated ringdown description. Those

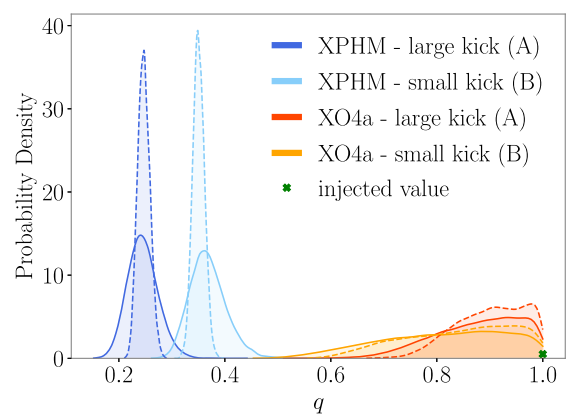


FIG. 12. Posterior distributions of the mass ratio for injections A (large kick) and B (small kick) with IMRPhenomXPHM (blue colors) and IMRPhenomXO4a (orange colors). Solid lines indicate the posteriors of the injections with $\text{SNR} = 26.8$, and dashed lines indicate the posteriors of the injections with $\text{SNR} = 60$.

additional effects can only be mimicked by actually converging towards the correct properties of a precessing binary.

We further observe that the measurement of the mass ratio influences the χ_p posterior of IMRPhenomXPHM. By using an analytical expression of the χ_p prior (see Sec. IV B in [42]), we can find how the prior distribution changes when fixing the mass ratio. We use the median value of the mass ratio posterior of A, $q = 0.24$, and we find that the new χ_p prior distribution has a peak around $\chi_p \approx 0.15$, which is exactly where the median of the A IMRPhenomXPHM distribution lies.

As we inject and recover with the same signal model, and use a zero noise realization, one might still expect the analysis to converge on the injected parameters. After all, the point of highest likelihood is, by construction, where the injected parameters are. However, the Bayesian analysis converges on the highest posterior density, which is determined by both the prior volume and the likelihood. If the prior density is small for our injection (i.e., we have chosen a special point in the parameter space) and the likelihood remains high across a significant parameter-space volume for nonprecessing binaries, the interpretation as a nonprecessing binary will be favored unless the SNR is extremely high. Here we do not explore very high SNRs, so we remain in the biased regime. For further comparisons between the two analyses, we include corner plots with posteriors of the most important injections in the Appendix.

G. Impact of the inclination angle

As we incline a binary from face-on to edge-on orientations, we expect to observe multiple GW harmonics, which generally help determine the source properties more accurately. When discussing the observability of precession in the case of large-kick injections, we also need to consider the impact of the inclination angle on the observability of the mode asymmetries, namely, the dominant-mode asymmetries as included in IMRPhenomXO4a. In the same way as the (2, 2) mode, the amplitude of the antisymmetric waveform reaches its maximum face-on and it decreases as we incline the system to edge-on [53].

When injecting and recovering signals with IMRPhenomXPHM, the posteriors shift towards the injected value as we incline the system, and as expected from [42], the model recovers the parameter best for edge-on inclinations (see Fig. 13). In the case of IMRPhenomXO4a, however, we observe that when the binary has a large kick and in turn large asymmetries, the χ_p recovery becomes less accurate as we incline the system. For an inclination of $\theta_{JN} = \pi/4$, the posterior looks similar to the face-on case. For $\theta_{JN} = \pi/2$, we observe that the χ_p recovery becomes less accurate than for $\theta_{JN} = 0$ and $\theta_{JN} = \pi/4$ inclinations and is similar to the IMRPhenomXPHM recovery. As the amplitude of the asymmetries decreases with the inclination and it vanishes for edge-on inclinations, these results show that it is the observability of the asymmetries which helps

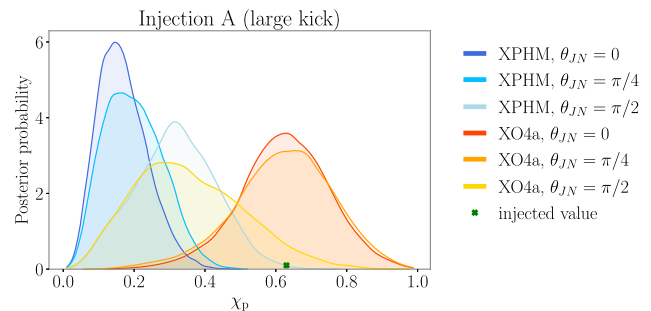


FIG. 13. Posterior probability distribution of χ_p for the injection A (large kick) with an inclination angle of $\theta_{JN} = 0, \pi/4$ and $\pi/2$ (rad). IMRPhenomXPHM posteriors are shown in blue, while IMRPhenomXO4a posteriors are shown in orange colors. The green cross indicated the injected value.

determine precession in the case of the $\theta_{JN} = 0$ and $\theta_{JN} = \pi/4$ injections. In the case of small kick injections and small mode asymmetries, IMRPhenomXO4a recovers precession more accurately when increasing the inclination angle, in the same way as with IMRPhenomXPHM.

H. The case of GW200129

The source of GW200129 is thought to be a binary black hole with a mass ratio of $q = 0.6_{-0.2}^{+0.4}$, an inclination of $\theta_{JN} = 0.5_{-0.3}^{+0.3}$ [30], and a remnant kick velocity of $v \sim 1542_{-1098}^{+747}$ km/s [29]. In both studies the signal was analyzed with the waveform model NRSur7dq4, which incorporates mode asymmetries. We have shown in Sec. IID that the presence of a large kick necessarily implies the existence of mode asymmetries in the signal, independent of the mass ratio. Indeed, Ref. [41] showed how considering mode asymmetries in the inference of the source properties was essential in finding precession in the system. In addition, we have shown that the GW imprint of the kick can help to extract more meaningful information about the spins in equal-mass binaries. With the inferred mass ratio and inclination values of GW200129, the signal probably contains higher harmonics, which help identify precession. Based on our study we find it is plausible that the presence of a kick, and therefore mode asymmetries, helped determine precession in the signal.

IV. KICK MEASUREMENTS

We infer the kick posterior of each injection using the posteriors of the source properties, and we investigate whether one can distinguish a signal with a large kick from a signal with a low kick. We should note that our findings on the imprint of the kick leading to more accurate measurements are independent of our ability to constrain the kick velocity from the signal. We might not be able to constrain a kick as for GW200129, but the presence of a kick would still have an impact on parameter estimation.

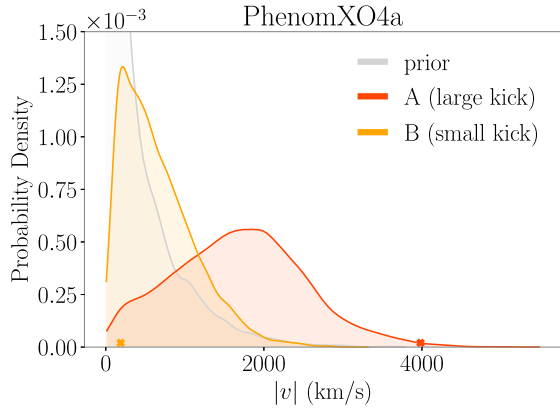


FIG. 14. Posterior distributions of the kick magnitude for the injections A (large kick) and B (small kick) computed with IMRPhenomXO4a . The prior distribution is included in gray color, and the crosses in the x axis indicate the kick magnitude of each of the injected signals.

However, if more precise spin measurements are possible in the presence of a large kick, then the decrease in the uncertainty of the spin measurements should lead to more informative kick posteriors.

Figure 14 includes the kick posteriors of the face-on injections we have performed with IMRPhenomXO4a . We observe that the posterior distribution of the large-kick injection A (with $v \sim 4000$ km/s) is informative and has a distinctive shape different from the prior distribution. Even though its median value is not centered at the injected value, its value is only consistent with a precessing binary. In the case of low-kick injection, B, the kick prior has a dominant effect on the posterior distributions. As expected, the ability to recover the injected value improves as we increase the signal SNR. As shown in Fig. 15, the increase

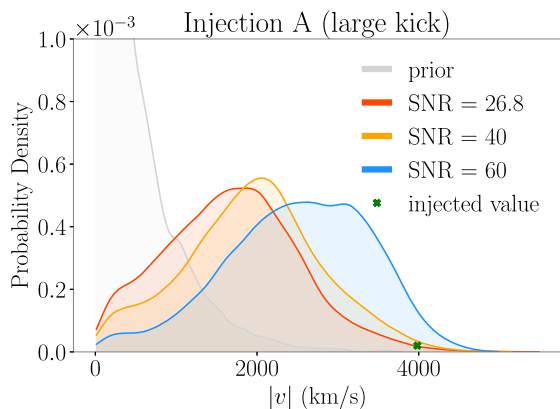


FIG. 15. Influence of the signal SNR on the kick posteriors of injection A estimated with IMRPhenomXO4a . The green cross indicates the injected kick value. The plot shows that the increase in SNR helps in reducing the support for zero kicks on the inferred kick posterior and leads to more accurate constraints of the true value.

in SNR leads to more accurate kick posteriors with a reduced support for zero kicks. On the other hand, IMRPhenomXPHM cannot predict large precessing kicks and recovers, in all cases, a low kick velocity close to the injected value.

We further investigate what leads to an accurate kick posterior, whether it is the parameter estimation samples and/or the mapping from intrinsic properties to the kick velocity. First, we test the influence of the posterior samples. We use samples estimated with and without including mode asymmetries in IMRPhenomXO4a , and map them to kick velocities using the complete IMRPhenomXO4a model, which includes mode asymmetries. Figure 16 shows the comparison of these two kick posteriors for the large-kick injection A. We can see that including mode asymmetries on the inference of the source parameters plays an important role and impacts the kick posterior.

Second, we test the impact of including mode asymmetries on the model used to infer the kick velocity. Since mode asymmetries are responsible for the out-of-plane component of the kick velocity, we find that without asymmetries one can only obtain kick magnitudes up to 500 km/s. Hence, in cases where the injected kick value is a large precessing kick, the model will not be able to recover it. This states the importance of including mode asymmetries in the estimation of the kick posterior.

Besides, as mentioned before, the same binary configuration might have two different estimates depending on the waveform model that is used. This means that using two different models, one for the parameter estimation and a different one for the kick inference, can introduce large

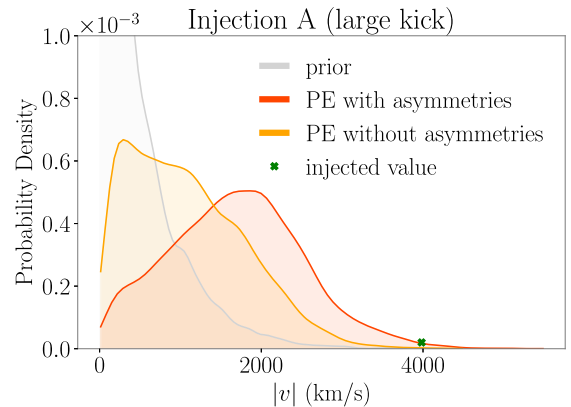


FIG. 16. Kick posterior distributions of injection A displaying the impact of excluding mode asymmetries on the recovery model of the parameter estimation analysis. To obtain the kick posterior in orange we used posterior samples obtained excluding mode asymmetries in IMRPhenomXO4a , and estimated the kick posterior using the complete model, which includes mode asymmetries. The posterior in red represents the kick posterior obtained using the complete IMRPhenomXO4a model for both parameter estimation and the kick estimate. The green cross indicates the injected kick value.

systematic errors, as the kick estimate of the posterior sample obtained with model 1 might not agree with the kick estimate of model 2. However, it is common practice to use posterior samples obtained with PHENOM and SEOBNR waveform models and map them to remnant kicks with either NRSurrogate fits or NR fitting formulas (see, e.g., [18,77,78]). We would like to emphasize the importance of using the same waveform model both for parameter estimation and the kick inference, to avoid introducing systematic errors and make more meaningful statements about the kick velocity.

V. CONCLUSIONS

We have investigated whether the GW imprint of the kick can help to extract more information from the signal. To exclude the impact of higher harmonics in parameter estimation, we have focused on face-on, equal-mass binaries. This is also motivated by the fact that the largest kick velocities are found in equal-mass binaries. Measuring spin precession in these orientations and mass ratios has been shown to be challenging. Here, we have explored whether the presence of a kick in the GW signal can improve our ability to infer precession in these cases. Our findings are summarized in the following bullet points:

- (i) In Sec. II D, we have presented the relation between the dominant mode asymmetry and the kick magnitude. We explore the two-spin parameter space and find that large mode asymmetries do not necessarily induce large kicks. However, for a given mass ratio and spin misalignment, large kicks are only generated by signals with large asymmetries.
- (ii) Based on our injection and recovery study, we observe that we can make more accurate measurements of the spins and mass ratio when the GW signal includes a large kick. This applies to equal-mass, face-on binaries, for which the merger phase of the signal is clearly visible by the detectors. Since the kick leaves an imprint on the merger phase of the GW signal, the impact of the kick is the largest when the merger phase is observable by the detectors.
- (iii) We find that one can distinguish between precessing and nonprecessing binaries in signals from equal-mass, face-on binaries, only when the signal includes a kick. In Sec. III F, we have discussed the problem in the context of the two-harmonic approximation. This is a framework that quantifies the measurability of precession and it states that to unambiguously determine precession, two different GW modes need to be observable. Signals from equal-mass, face-on binaries only include the dominant mode, which makes precession difficult to be measured. However, if these signals include large kicks, they necessarily include large asymmetries. The dominant mode can be decomposed into the two

coprocessing dominant modes, meaning that, if mode asymmetries are included in the signal, as in IMRPhenomXO4a, the dominant mode asymmetry can make the signal more informative. The presence of mode asymmetries in the signal can help to observe two harmonics and to identify precession. If we exclude mode asymmetries in the description of the large-kick signal, as with IMRPhenomXPHM, then the two coprocessing dominant modes will be symmetric, and the signal will only contain one mode, making precession hard to measure. In the case of a small kick where the asymmetries are small, the dominant coprocessing modes are close to being symmetric, for which identifying precession will again be challenging.

- (iv) We find that the formulation of the two-harmonic approximation is not complete for the case of face-on, equal-mass binaries, as it does not consider the asymmetries between the $(\ell, m) = (2, 2)$ and $(\ell, m) = (2, -2)$ GW harmonics. As many observed GW candidates are expected to be close to this specific configuration, we find it is important to consider the asymmetries in the dominant mode to estimate the observability of precession in current GW events.
- (v) Regarding kick measurements, we find that the waveform model used in the Bayesian analysis is equally important as the model used for the estimation of the kick posterior. We observe that mixing different waveform models can introduce systematic errors into the kick posterior estimate. In addition, we find that including mode asymmetries is essential to infer an accurate kick posterior.

ACKNOWLEDGMENTS

We are grateful to Mark Hannam, N. V. Krishnendu, Maite Mateu-Lucena, and Vijay Varma for useful discussions. We also thank the anonymous referee for the valuable comments on this paper. This work was supported by the Max Planck Society's Independent Research Group Grant. Computations were carried out on the Holodeck cluster of the Max Planck Independent Research Group "Binary Merger Observations and Numerical Relativity."

APPENDIX

For completeness, we include corner plots with the posteriors of injections A (large kick) and B (small kick) using IMRPhenomXO4a and IMRPhenomXPHM. In Figs. 17–20, we show the posteriors of the injections with $\text{SNR} = 26.8$, while Figs. 21 and 22 show posteriors of the IMRPhenomXO4a injections with $\text{SNR} = 60$. The corner plots include posteriors of the chirp mass, the mass ratio, the component spin magnitudes, the spin tilts, the spin azimuthal angle φ_{12} , the

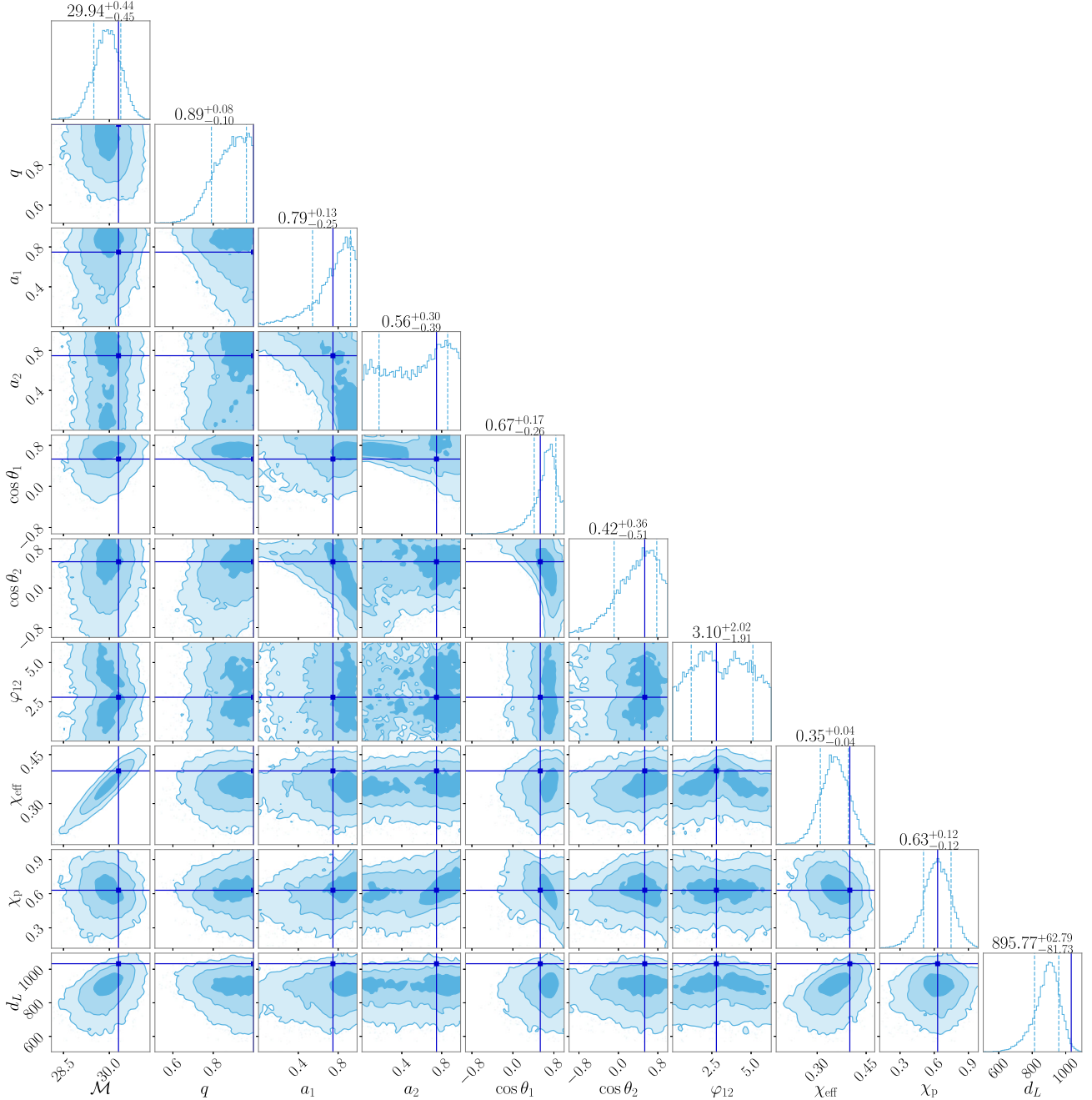


FIG. 17. Corner plot of the posteriors of injection A using IMRPhenomXO4a with $\text{SNR} = 26.8$. The plot includes the posteriors of the chirp mass, the mass ratio, the component spin magnitudes, the spin tilts, the spin azimuthal angle φ_{12} , χ_{eff} , χ_p , and the luminosity distance. The true parameter values are indicated by the vertical lines in dark blue.

effective spin χ_{eff} , the effective precession parameter χ_p , and the luminosity distance. The vertical lines in dark blue indicate the true parameter values.

When comparing the two IMRPhenomXO4a injections in Figs. 17 and 18, we observe that the posteriors of the chirp mass \mathcal{M} and the luminosity distance d_L are slightly biased in the large kick injection (A). This is because signals with

significant kicks have amplitude modulations in the merger phase caused by the anisotropic emission of GWs. In the case of a binary with the parameters of injection A, the remnant moves towards the observer nearly in the line of sight. This means that the signal has a slightly smaller amplitude than if the remnant moved away from the observer, or if the binary had no remnant kick. A smaller

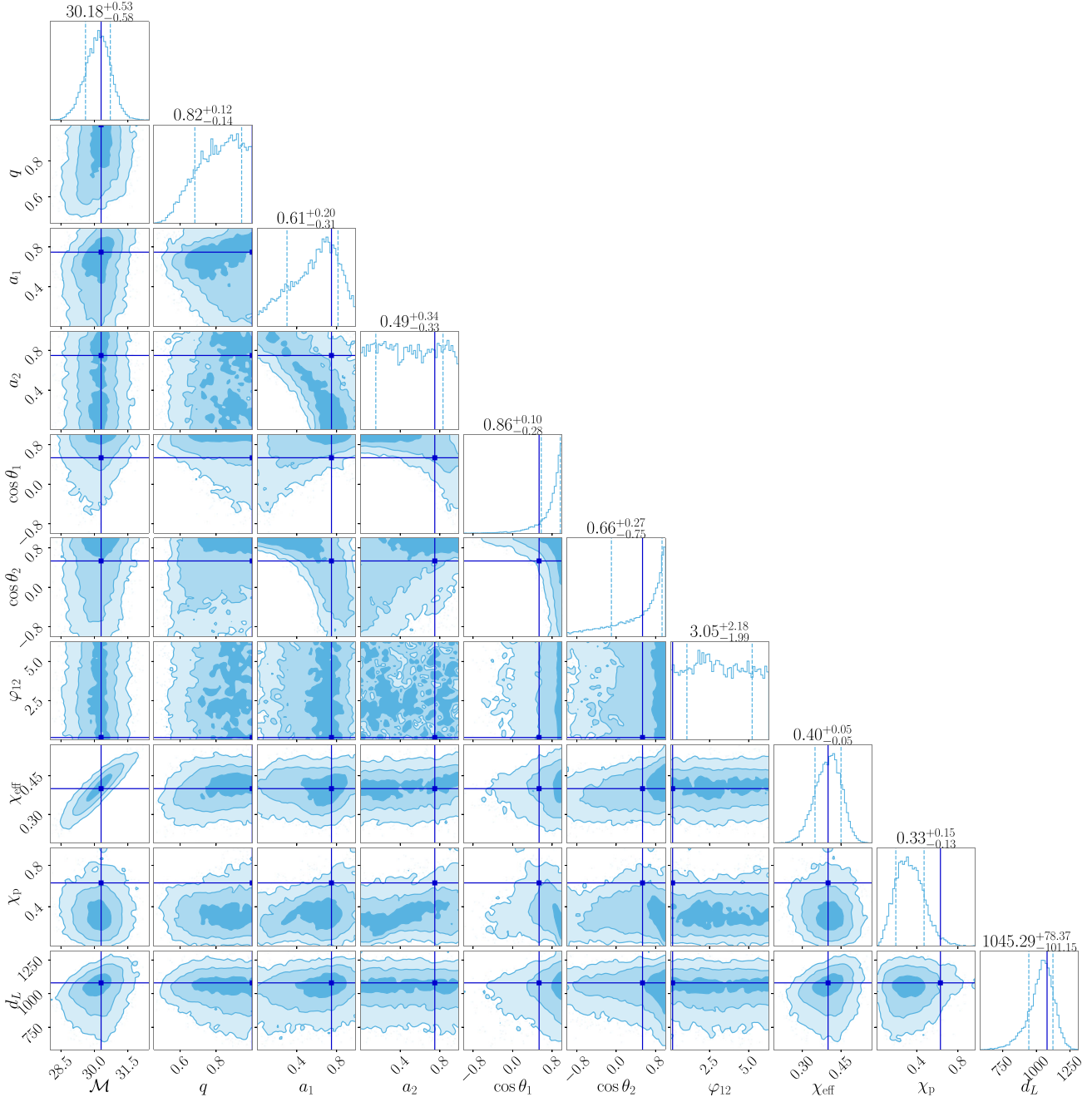


FIG. 18. Corner plot of the posteriors of injection B using IMRPhenomXO4a with $\text{SNR} = 26.8$. The plot includes the posteriors of the chirp mass, the mass ratio, the component spin magnitudes, the spin tilts, the spin azimuthal angle φ_{12} , χ_{eff} , χ_p , and the luminosity distance. The true parameter values are indicated by the vertical lines in dark blue.

GW amplitude can be mimicked by a less massive binary, hence the bias in chirp mass. To compensate the amplitude in the inspiral corresponding to a lower-mass binary, the luminosity distance needs to be modified such that it is closer to the observer. The bias reduces as we increase the SNR (see Fig. 21). On the other hand, we observe that the spin posteriors of the small-kick injection (B) remain

biased even when increasing the SNR to 60, while those of the large-kick injection become more accurate with the increase in SNR.

As discussed in Sec. III F, we generally observe larger biases in IMRPhenomXPHM than in IMRPhenomXO4a posteriors. These differences are visible in Figs. 17–20 for a number of source parameters, including χ_p .

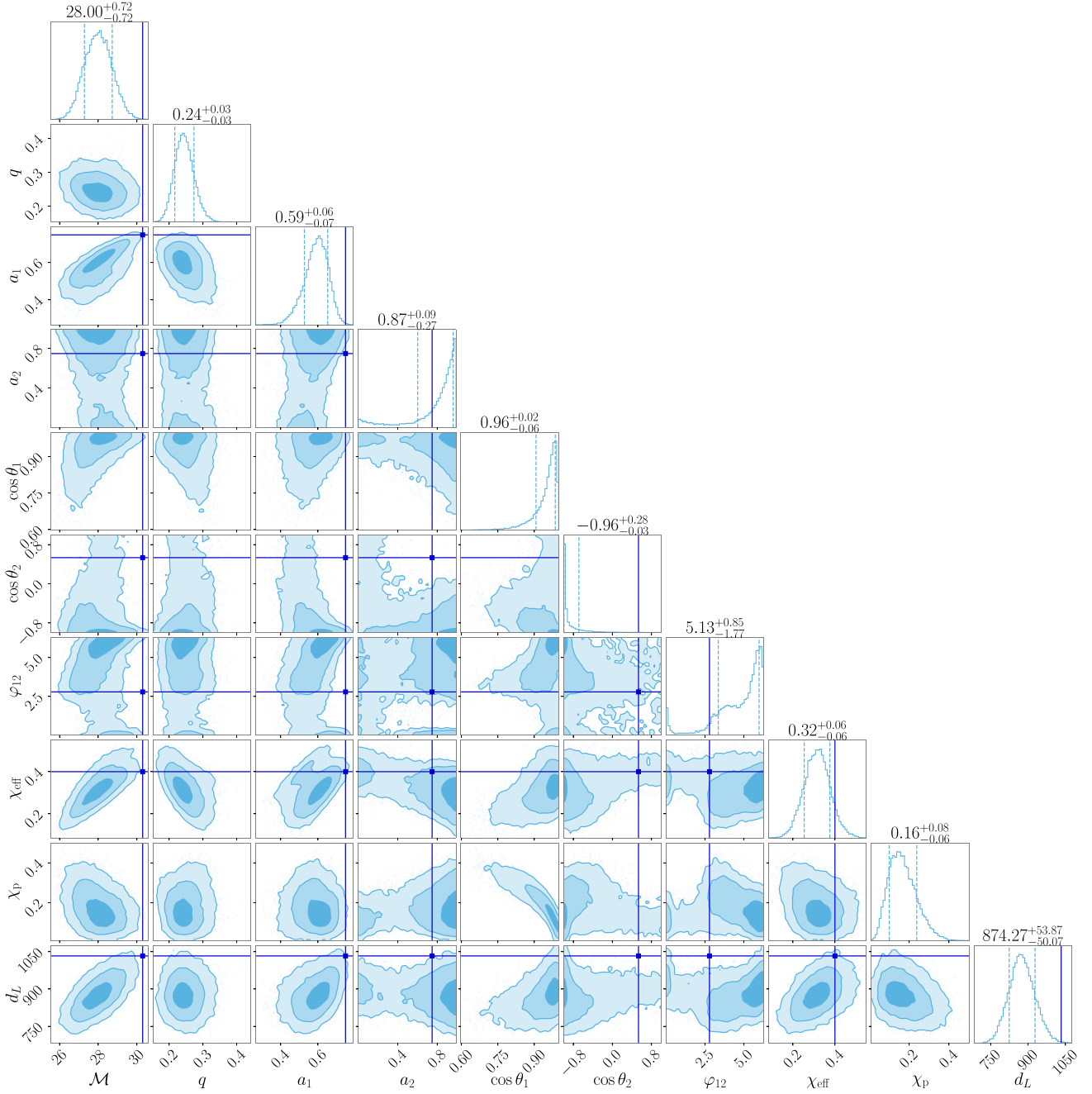


FIG. 19. Corner plot of the posteriors of injection A using IMRPhenomXPHM with $\text{SNR} = 26.8$. The plot includes the posteriors of the chirp mass, the mass ratio, the component spin magnitudes, the spin tilts, the spin azimuthal angle φ_{12} , χ_{eff} , χ_p , and the luminosity distance. The true parameter values are indicated by the vertical lines in dark blue.

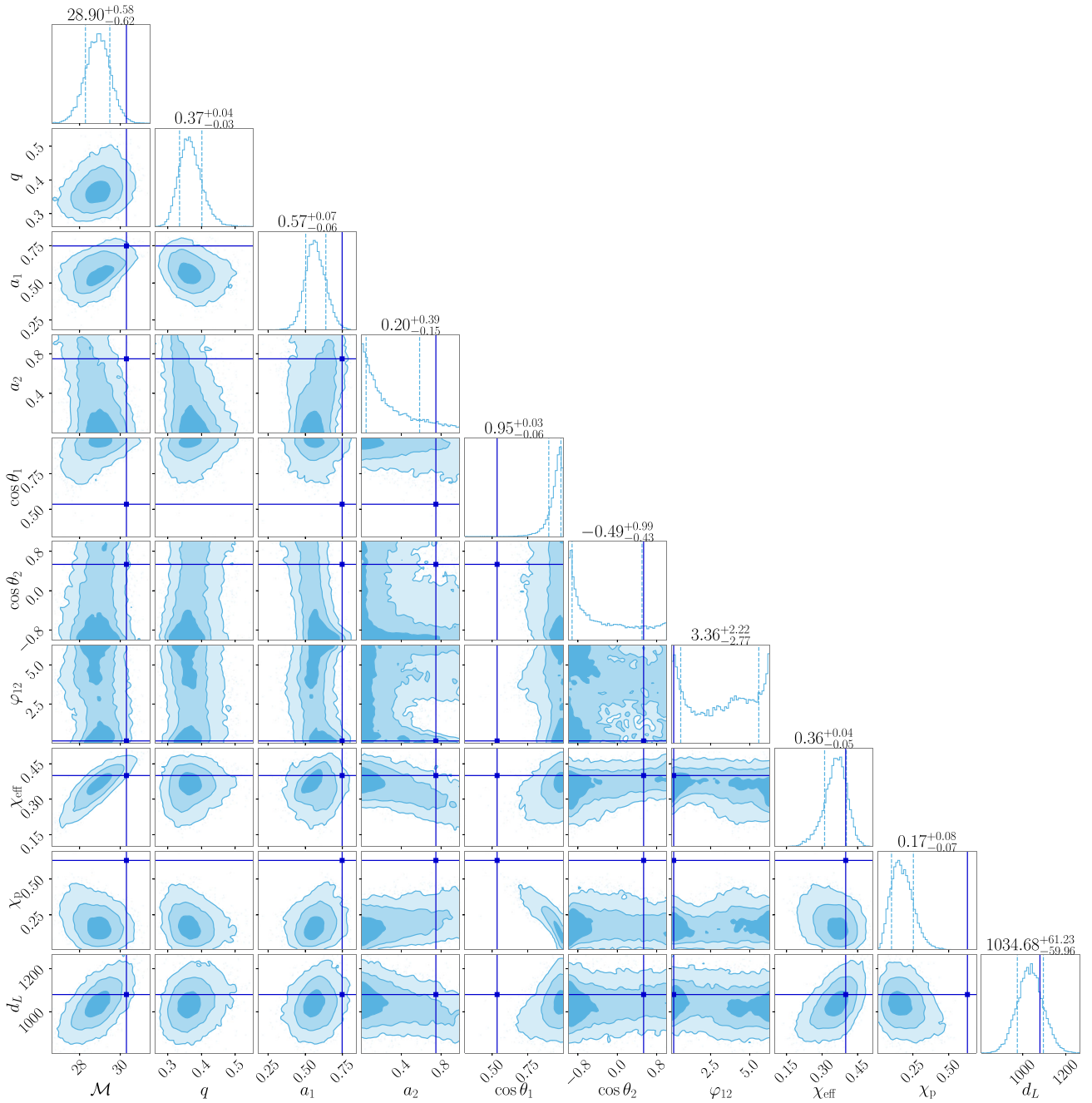


FIG. 20. Corner plot of the posteriors of injection B using IMRPhenomXPHM with SNR = 26.8. The plot includes the posteriors of the chirp mass, the mass ratio, the component spin magnitudes, the spin tilts, the spin azimuthal angle φ_{12} , χ_{eff} , χ_p , and the luminosity distance. The true parameter values are indicated by the vertical lines in dark blue.

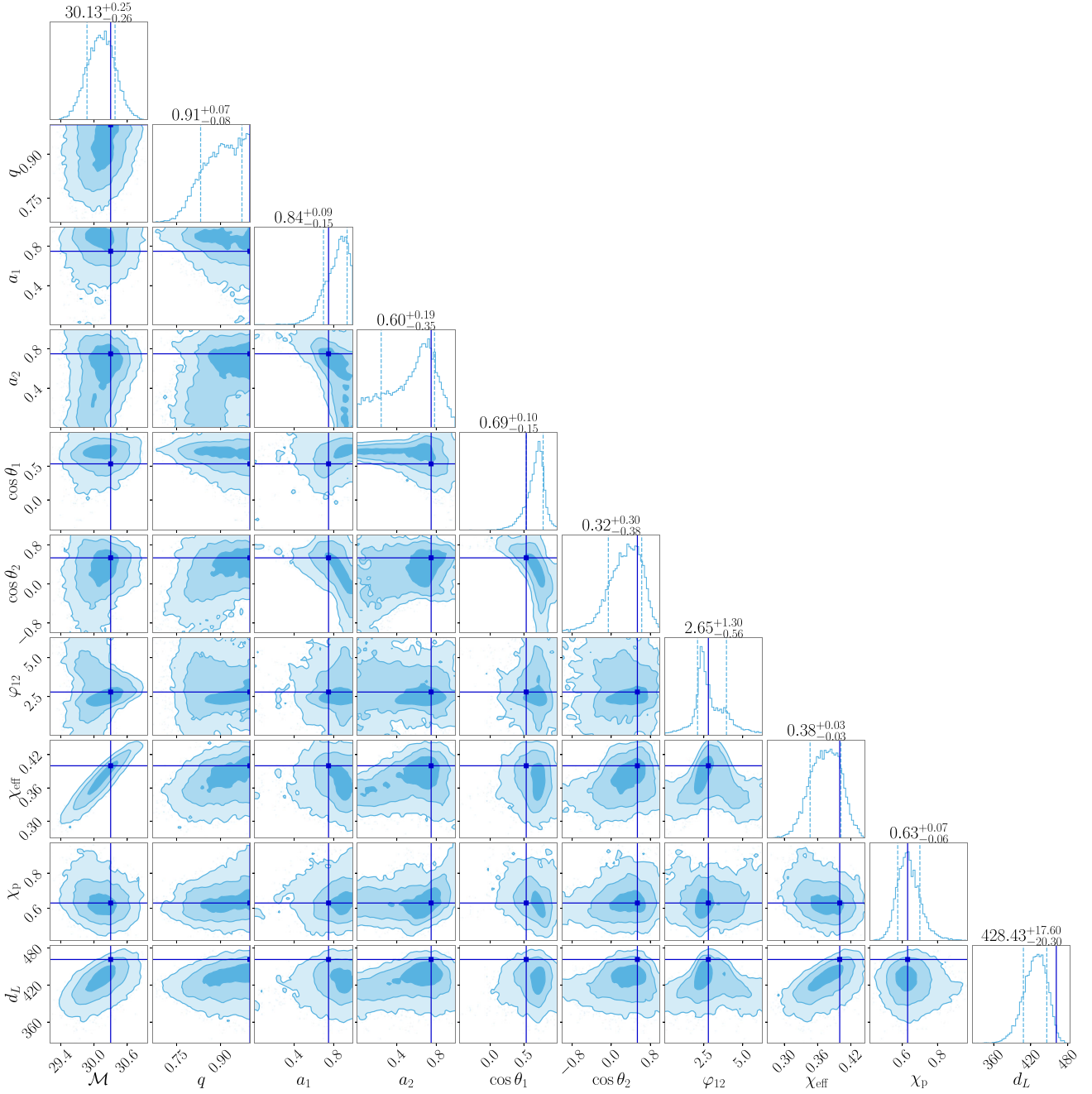


FIG. 21. Corner plot of the posteriors of injection A using IMRPhenomXO4a with SNR = 60. The plot includes the posteriors of the chirp mass, the mass ratio, the component spin magnitudes, the spin tilts, the spin azimuthal angle φ_{12} , χ_{eff} , χ_p , and the luminosity distance. The true parameter values are indicated by the vertical lines in dark blue.

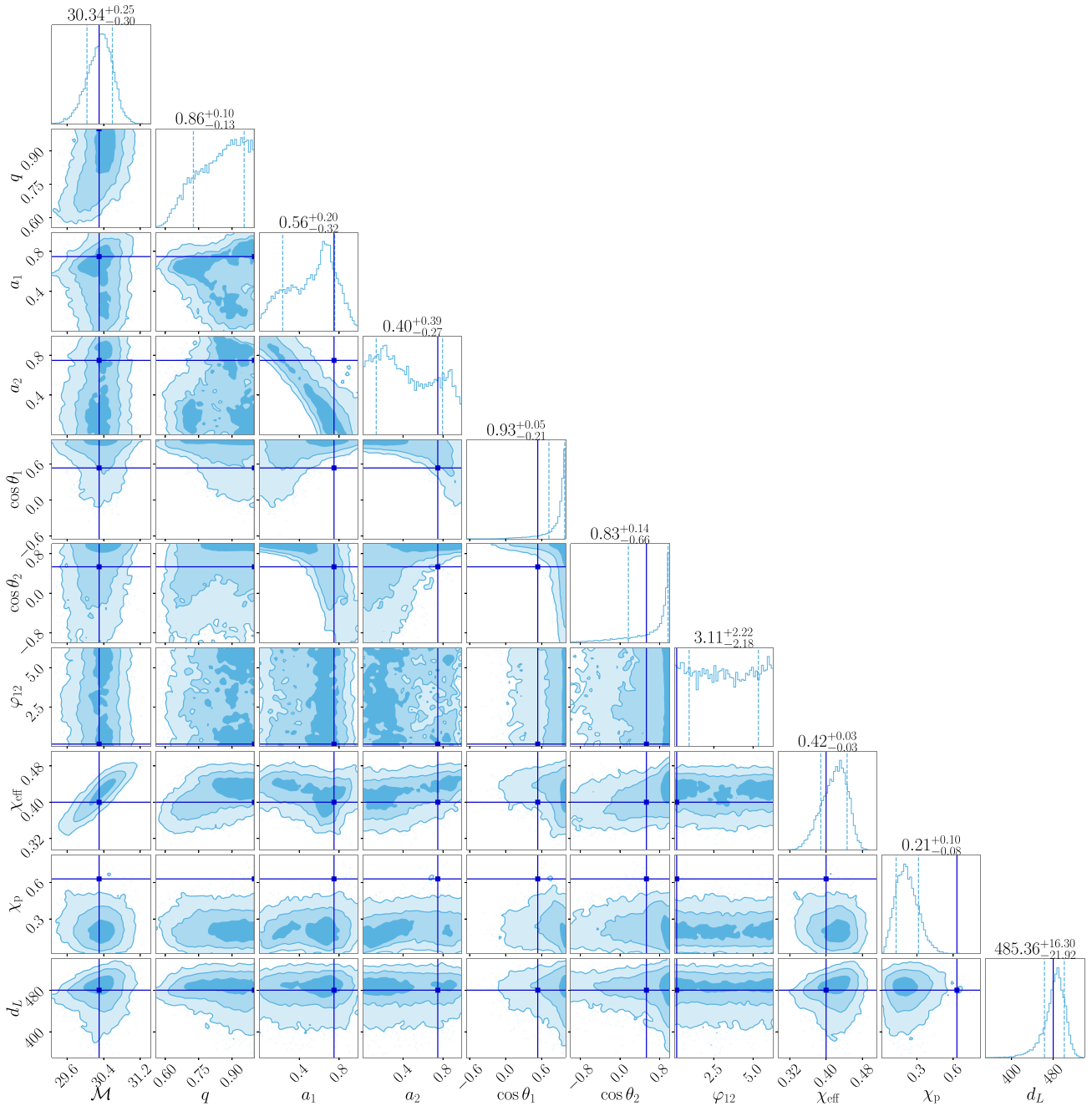


FIG. 22. Corner plot of the posteriors of injection B using IMRPhenomXO4a with SNR = 60. The plot includes the posteriors of the chirp mass, the mass ratio, the component spin magnitudes, the spin tilts, the spin azimuthal angle φ_{12} , χ_{eff} , χ_p , and the luminosity distance. The true parameter values are indicated by the vertical lines in dark blue.

- [1] W. B. Bonnor and M. A. Rotenberg, Transport of momentum by gravitational waves: The linear approximation, *Proc. R. Soc. A* **265**, 109 (1961).
- [2] Jacob D. Bekenstein, Gravitational-radiation recoil and runaway black holes, *Astrophys. J.* **183**, 657 (1973).
- [3] M. J. Fitchett, The influence of gravitational wave momentum losses on the centre of mass motion of a Newtonian binary system, *Mon. Not. R. Astron. Soc.* **203**, 1049 (1983).
- [4] J. A. Gonzalez, M. D. Hannam, U. Sperhake, Bernd Bruegmann, and S. Husa, Supermassive recoil velocities for binary black-hole mergers with antialigned spins, *Phys. Rev. Lett.* **98**, 231101 (2007).
- [5] Bernd Bruegmann, Jose A. Gonzalez, Mark Hannam, Sascha Husa, and Ulrich Sperhake, Exploring black hole superkicks, *Phys. Rev. D* **77**, 124047 (2008).
- [6] Manuela Campanelli, Carlos O. Lousto, Yosef Zlochower, and David Merritt, Maximum gravitational recoil, *Phys. Rev. Lett.* **98**, 231102 (2007).
- [7] Carlos O. Lousto and Yosef Zlochower, Hangup kicks: Still larger recoils by partial spin/orbit alignment of black-hole binaries, *Phys. Rev. Lett.* **107**, 231102 (2011).
- [8] James Healy, Carlos O. Lousto, Ian Ruchlin, and Yosef Zlochower, Evolutions of unequal mass, highly spinning black hole binaries, *Phys. Rev. D* **97**, 104026 (2018).
- [9] Carlos O. Lousto and James Healy, Kicking gravitational wave detectors with recoiling black holes, *Phys. Rev. D* **100**, 104039 (2019).
- [10] Frank Herrmann, Ian Hinder, Deirdre Shoemaker, Pablo Laguna, and Richard A. Matzner, Gravitational recoil from spinning binary black hole mergers, *Astrophys. J.* **661**, 430 (2007).
- [11] Michael Koppitz, Denis Pollney, Christian Reisswig, Luciano Rezzolla, Jonathan Thornburg, Peter Diener, and Erik Schnetter, Recoil velocities from equal-mass binary-black-hole mergers, *Phys. Rev. Lett.* **99**, 041102 (2007).
- [12] S. Komossa, Recoiling black holes: Electromagnetic signatures, candidates, and astrophysical implications, *Adv. Astron.* **2012**, 364973 (2012).
- [13] David Merritt, Milos Milosavljevic, Marc Favata, Scott A. Hughes, and Daniel E. Holz, Consequences of gravitational radiation recoil, *Astrophys. J. Lett.* **607**, L9 (2004).
- [14] Michela Mapelli, Formation channels of single and binary stellar-mass black holes, [arXiv:2106.00699](https://arxiv.org/abs/2106.00699).
- [15] Majda Smole and Miroslav Micić, Statistical analysis of kicked black holes from TNG300 simulation, *Publ. Astron. Soc. Aust.* **40**, e045 (2023).
- [16] Davide Gerosa and Emanuele Berti, Escape speed of stellar clusters from multiple-generation black-hole mergers in the upper mass gap, *Phys. Rev. D* **100**, 041301 (2019).
- [17] Davide Gerosa and Maya Fishbach, Hierarchical mergers of stellar-mass black holes and their gravitational-wave signatures, *Nat. Astron.* **5**, 749 (2021).
- [18] Parthapratim Mahapatra, Anuradha Gupta, Marc Favata, K. G. Arun, and B. S. Sathyaprakash, Remnant black hole kicks and implications for hierarchical mergers, *Astrophys. J. Lett.* **918**, L31 (2021).
- [19] Michael Zevin and Daniel E. Holz, Avoiding a cluster catastrophe: Retention efficiency and the binary black hole mass spectrum, *Astrophys. J. Lett.* **935**, L20 (2022).
- [20] Parthapratim Mahapatra, Debatri Chattopadhyay, Anuradha Gupta, Marc Favata, B. S. Sathyaprakash, and K. G. Arun, Predictions of a simple parametric model of hierarchical black hole mergers, [arXiv:2209.05766](https://arxiv.org/abs/2209.05766).
- [21] Juan Calderón Bustillo, James A. Clark, Pablo Laguna, and Deirdre Shoemaker, Tracking black hole kicks from gravitational wave observations, *Phys. Rev. Lett.* **121**, 191102 (2018).
- [22] Vijay Varma, Maximiliano Isi, and Sylvia Biscoveanu, Extracting the gravitational recoil from black hole merger signals, *Phys. Rev. Lett.* **124**, 101104 (2020).
- [23] B. P. Abbott *et al.*, Prospects for observing and localizing gravitational-wave transients with Advanced LIGO, Advanced Virgo and KAGRA, *Living Rev. Relativity* **21**, 3 (2018).
- [24] J. Aasi *et al.*, Advanced LIGO. *Classical Quantum Gravity* **32**, 074001 (2015).
- [25] F. Acernese *et al.*, Advanced Virgo: A second-generation interferometric gravitational wave detector, *Classical Quantum Gravity* **32**, 024001 (2015).
- [26] Yoichi Aso, Yuta Michimura, Kentaro Somiya, Masaki Ando, Osamu Miyakawa, Takanori Sekiguchi, Daisuke Tatsumi, and Hiroaki Yamamoto, Interferometer design of the KAGRA gravitational wave detector, *Phys. Rev. D* **88**, 043007 (2013).
- [27] R. Abbott *et al.*, GWTC-3: Compact binary coalescences observed by LIGO and Virgo during the second part of the third observing run, *Phys. Rev. X* **13**, 041039 (2023).
- [28] Michael Pürrer, Mark Hannam, and Frank Ohme, Can we measure individual black-hole spins from gravitational-wave observations?, *Phys. Rev. D* **93**, 084042 (2016).
- [29] Vijay Varma, Sylvia Biscoveanu, Tousif Islam, Feroz H. Shaik, Carl-Johan Haster, Maximiliano Isi, Will M. Farr, Scott E. Field, and Salvatore Vitale, Evidence of large recoil velocity from a black hole merger signal, *Phys. Rev. Lett.* **128**, 191102 (2022).
- [30] Mark Hannam *et al.*, General-relativistic precession in a black-hole binary, *Nature (London)* **610**, 652 (2022).
- [31] Ethan Payne, Sophie Hourihane, Jacob Golomb, Rhiannon Udall, Richard Udall, Derek Davis, and Katerina Chatziioannou, Curious case of GW200129: Interplay between spin-precession inference and data-quality issues, *Phys. Rev. D* **106**, 104017 (2022).
- [32] D. Davis, T. B. Littenberg, I. M. Romero-Shaw, M. Millhouse, J. McIver, F. Di Renzo, and G. Ashton, Subtracting glitches from gravitational-wave detector data during the third LIGO-Virgo observing run, *Classical Quantum Gravity* **39**, 245013 (2022).
- [33] Ronaldas Macas, Andrew Lundgren, and Gregory Ashton, Revisiting GW200129 with machine learning noise mitigation: It is (still) precessing, [arXiv:2311.09921](https://arxiv.org/abs/2311.09921).
- [34] Emily Baird, Stephen Fairhurst, Mark Hannam, and Patricia Murphy, Degeneracy between mass and spin in black-hole-binary waveforms, *Phys. Rev. D* **87**, 024035 (2013).
- [35] Stephen Fairhurst, Rhys Green, Charlie Hoy, Mark Hannam, and Alistair Muir, Two-harmonic approximation for gravitational waveforms from precessing binaries, *Phys. Rev. D* **102**, 024055 (2020).
- [36] Stephen Fairhurst, Rhys Green, Mark Hannam, and Charlie Hoy, When will we observe binary black holes precessing?, *Phys. Rev. D* **102**, 041302 (2020).

- [37] Rhys Green, Charlie Hoy, Stephen Fairhurst, Mark Hannam, Francesco Pannarale, and Cory Thomas, Identifying when precession can be measured in gravitational waveforms, *Phys. Rev. D* **103**, 124023 (2021).
- [38] Charlie Hoy, Stephen Fairhurst, Mark Hannam, and Vaibhav Tiwari, Understanding how fast black holes spin by analyzing data from the second gravitational-wave catalogue, *Astrophys. J.* **928**, 75 (2022).
- [39] Chinmay Kalaghatgi and Mark Hannam, Investigating the effect of in-plane spin directions for precessing binary black hole systems, *Phys. Rev. D* **103**, 024024 (2021).
- [40] Antoni Ramos-Buades, Patricia Schmidt, Geraint Pratten, and Sascha Husa, Validity of common modeling approximations for precessing binary black holes with higher-order modes, *Phys. Rev. D* **101**, 103014 (2020).
- [41] Panagiota Kolitsidou, Jonathan E. Thompson, and Mark Hannam, Impact of anti-symmetric contributions to signal multipoles in the measurement of black-hole spins, arXiv: 2402.00813.
- [42] N. V. Krishnendu and Frank Ohme, Interplay of spin-precession and higher harmonics in the parameter estimation of binary black holes, *Phys. Rev. D* **105**, 064012 (2022).
- [43] Maya Fishbach and Daniel E. Holz, Picky partners: The pairing of component masses in binary black hole mergers, *Astrophys. J. Lett.* **891**, L27 (2020).
- [44] Ilya Mandel and Alison Farmer, Merging stellar-mass binary black holes, *Phys. Rep.* **955**, 1 (2022).
- [45] Carl L. Rodriguez, Sourav Chatterjee, and Frederic A. Rasio, Binary black hole mergers from globular clusters: Masses, merger rates, and the impact of stellar evolution, *Phys. Rev. D* **93**, 084029 (2016).
- [46] Ryan M. O’Leary, Yohai Meiron, and Bence Kocsis, Dynamical formation signatures of black hole binaries in the first detected mergers by LIGO, *Astrophys. J. Lett.* **824**, L12 (2016).
- [47] Angela Borchers and Frank Ohme, Inconsistent black hole kick estimates from gravitational-wave models, *Classical Quantum Gravity* **40**, 095008 (2023).
- [48] Geraint Pratten, Sascha Husa, Cecilio Garcia-Quiros, Marta Colleoni, Antoni Ramos-Buades, Hector Estelles, and Rafel Jaume, Setting the cornerstone for a family of models for gravitational waves from compact binaries: The dominant harmonic for nonprecessing quasicircular black holes, *Phys. Rev. D* **102**, 064001 (2020).
- [49] Cecilio García-Quirós, Marta Colleoni, Sascha Husa, Héctor Estellés, Geraint Pratten, Antoni Ramos-Buades, Maite Mateu-Lucena, and Rafel Jaume, Multimode frequency-domain model for the gravitational wave signal from nonprecessing black-hole binaries, *Phys. Rev. D* **102**, 064002 (2020).
- [50] Cecilio García-Quirós, Sascha Husa, Maite Mateu-Lucena, and Angela Borchers, Accelerating the evaluation of inspiral-merger-ringdown waveforms with adapted grids, *Classical Quantum Gravity* **38**, 015006 (2021).
- [51] Geraint Pratten *et al.*, Computationally efficient models for the dominant and subdominant harmonic modes of precessing binary black holes, *Phys. Rev. D* **103**, 104056 (2021).
- [52] Jonathan E. Thompson, Eleanor Hamilton, Lionel London, Shrobona Ghosh, Panagiota Kolitsidou, Charlie Hoy, and Mark Hannam, Phenomenological gravitational-wave model for precessing black-hole binaries with higher multipoles and asymmetries, *Phys. Rev. D* **109**, 063012 (2024).
- [53] Shrobona Ghosh, Panagiota Kolitsidou, and Mark Hannam, First frequency-domain phenomenological model of the multipole asymmetry in gravitational-wave signals from binary-black-hole coalescence, *Phys. Rev. D* **109**, 024061 (2024).
- [54] Eleanor Hamilton, Lionel London, Jonathan E. Thompson, Edward Fauchon-Jones, Mark Hannam, Chinmay Kalaghatgi, Sebastian Khan, Francesco Pannarale, and Alex Vano-Vinuales, Model of gravitational waves from precessing black-hole binaries through merger and ringdown, *Phys. Rev. D* **104**, 124027 (2021).
- [55] Eleanor Hamilton, Lionel London, and Mark Hannam, Ringdown frequencies in black holes formed from precessing black-hole binaries, *Phys. Rev. D* **107**, 104035 (2023).
- [56] Vijay Varma, Scott E. Field, Mark A. Scheel, Jonathan Blackman, Davide Gerosa, Leo C. Stein, Lawrence E. Kidder, and Harald P. Pfeiffer, Surrogate models for precessing binary black hole simulations with unequal masses, *Phys. Rev. Res.* **1**, 033015 (2019).
- [57] Vijay Varma, Davide Gerosa, Leo C. Stein, François Hébert, and Hao Zhang, High-accuracy mass, spin, and recoil predictions of generic black-hole merger remnants, *Phys. Rev. Lett.* **122**, 011101 (2019).
- [58] Lee Samuel Finn and David F. Chernoff, Observing binary inspiral in gravitational radiation: One interferometer, *Phys. Rev. D* **47**, 2198 (1993).
- [59] Curt Cutler and Éanna E. Flanagan, Gravitational waves from merging compact binaries: How accurately can one extract the binary’s parameters from the inspiral waveform?, *Phys. Rev. D* **49**, 2658 (1994).
- [60] Thibault Damour, Coalescence of two spinning black holes: An effective one-body approach, *Phys. Rev. D* **64**, 124013 (2001).
- [61] Étienne Racine, Analysis of spin precession in binary black hole systems including quadrupole-monopole interaction, *Phys. Rev. D* **78**, 044021 (2008).
- [62] P. Ajith *et al.*, Inspiral-merger-ringdown waveforms for black-hole binaries with non-precessing spins, *Phys. Rev. Lett.* **106**, 241101 (2011).
- [63] Patricia Schmidt, Mark Hannam, and Sascha Husa, Towards models of gravitational waveforms from generic binaries: A simple approximate mapping between precessing and non-precessing inspiral signals, *Phys. Rev. D* **86**, 104063 (2012).
- [64] Patricia Schmidt, Frank Ohme, and Mark Hannam, Towards models of gravitational waveforms from generic binaries II: Modeling precession effects with a single effective precession parameter, *Phys. Rev. D* **91**, 024043 (2015).
- [65] Milton Ruiz, Ryoji Takahashi, Miguel Alcubierre, and Dario Nunez, Multipole expansions for energy and momenta carried by gravitational waves, *Gen. Relativ. Gravit.* **40**, 2467 (2008).
- [66] LIGO Scientific Collaboration, LIGO Algorithm Library—LALSuite, free software (GPL) (2018), 10.7935/GT1W-FZ16.

- [67] Karl Wette, SWIGLAL: Python and Octave interfaces to the LALSuite gravitational-wave data analysis libraries, *SoftwareX* **12**, 100634 (2020).
- [68] Mike Boyle, Dante Iozzo, and Leo C. Stein, MOBLE/SCRI: v1.2, Zenodo, [10.5281/zenodo.4041972](https://doi.org/10.5281/zenodo.4041972) (2020).
- [69] Michael Boyle, Angular velocity of gravitational radiation from precessing binaries and the corotating frame, *Phys. Rev. D* **87**, 104006 (2013).
- [70] Michael Boyle, Lawrence E. Kidder, Serguei Ossokine, and Harald P. Pfeiffer, Gravitational-wave modes from precessing black-hole binaries, [arXiv:1409.4431](https://arxiv.org/abs/1409.4431).
- [71] Michael Boyle, Transformations of asymptotic gravitational-wave data, *Phys. Rev. D* **93**, 084031 (2016).
- [72] Frans Pretorius, Binary black hole coalescence, [arXiv:0710.1338](https://arxiv.org/abs/0710.1338).
- [73] Gregory Ashton *et al.*, Bilby: A user-friendly Bayesian inference library for gravitational-wave astronomy, *Astrophys. J. Suppl. Ser.* **241**, 27 (2019).
- [74] Joshua S. Speagle, DYNesty: A dynamic nested sampling package for estimating Bayesian posteriors and evidences, *Mon. Not. R. Astron. Soc.* **493**, 3132 (2020).
- [75] Charlie Hoy and Vivien Raymond, PESummary: The code agnostic parameter estimation summary page builder, *SoftwareX* **15**, 100765 (2021).
- [76] Theocharis A. Apostolatos, Curt Cutler, Gerald J. Sussman, and Kip S. Thorne, Spin induced orbital precession and its modulation of the gravitational wave forms from merging binaries, *Phys. Rev. D* **49**, 6274 (1994).
- [77] Giacomo Fragione and Abraham Loeb, Implications of recoil kicks for black hole mergers from LIGO/Virgo catalogs, *Mon. Not. R. Astron. Soc.* **502**, 3879 (2021).
- [78] Zoheyr Doctor, Ben Farr, and Daniel E. Holz, Black hole leftovers: The remnant population from binary black hole mergers, *Astrophys. J. Lett.* **914**, L18 (2021).

Chapter 7




Gravitational-wave kicks impact the spins of black holes from hierarchical mergers

In this chapter, we include a reprint of the following article:

[32] Angela Borchers, Claire S. Ye, and Maya Fishbach. Gravitational-wave kicks impact the spins of black holes from hierarchical mergers. *The Astrophysical Journal* 987, 146 (2025)



Gravitational-wave Kicks Impact the Spins of Black Holes from Hierarchical Mergers

Angela Borchers^{1,2} , Claire S. Ye³ , and Maya Fishbach^{3,4,5} ¹ Max-Planck-Institut für Gravitationsphysik, Albert-Einstein-Institut, Callinstr. 38, D-30167 Hannover, Germany² Leibniz Universität Hannover, D-30167 Hannover, Germany³ Canadian Institute for Theoretical Astrophysics, 60 St. George St., University of Toronto, Toronto, ON M5S 3H8, Canada⁴ David A. Dunlap Department of Astronomy and Astrophysics, University of Toronto, 50 St. George St., Toronto, ON M5S 3H4, Canada⁵ Department of Physics, University of Toronto, 60 St. George St., Toronto, ON M5S 3H8, Canada

Received 2025 March 31; revised 2025 May 18; accepted 2025 May 28; published 2025 July 4

Abstract

One proposed black hole formation channel involves hierarchical mergers, where black holes form through repeated binary mergers. Previous studies have shown that such black holes follow a near-universal spin distribution centered around 0.7. However, gravitational-wave kicks can eject remnants from their host environments, meaning only retained black holes can participate in subsequent mergers. We calculate the spin distribution of retained black holes in typical globular clusters, accounting for remnant kick velocities. Since the kick magnitude depends on the binary's mass ratio and spin orientations, certain configurations are more likely to be retained than others. This preferentially selects certain remnant spin magnitudes, skewing the spin distribution of second-generation black holes away from the universal distribution. In low escape velocity environments, the distribution can become bimodal, as remnants with spins of 0.7 typically receive larger kicks than in other configurations. Regarding higher-generation black holes, their spin distribution does not converge to a unique form, and can span a broad range of spins, $a_f \in (0.4, 1)$, depending on their merger history, birth spins, and the escape velocity. Additionally, we find that the presence of a small fraction of binaries with near-aligned spins can produce a second, more dominant peak, whose position depends on the birth spin magnitude. Our findings identify observable features of hierarchical merger black holes, which is essential for understanding their contribution to the gravitational-wave population. Moreover, the dependence of the spin distribution on astrophysical parameters means that precise spin measurements could provide insights into their formation environments.

Unified Astronomy Thesaurus concepts: [Gravitational waves \(678\)](#); [Black holes \(162\)](#); [Gravitational wave astronomy \(675\)](#)

1. Introduction

Black holes formed through hierarchical mergers of lighter black holes are expected to have a unique spin distribution, peaking around $a_f \sim 0.7$ (E. Berti & M. Volonteri 2008; M. Fishbach et al. 2017). Such mergers typically occur in dense environments where black holes are dynamically assembled into binaries, leading to isotropic-spin orientations (S. F. Portegies Zwart & S. McMillan 2000; C. L. Rodriguez et al. 2016; D. Gerosa & M. Fishbach 2021). These distinctive features are often used to characterize binary black hole mergers from dynamical origins and differentiate them from other formation channels, such as isolated field formation, where black holes are expected to have small, aligned spins (V. Kalogera 2000; S. S. Bavera et al. 2020; D. Gerosa et al. 2018a; T. A. Callister et al. 2021).

Because black hole spins leave a specific imprint in the gravitational-wave (GW) signal, it is possible to estimate them from GW observations (see, e.g., K. Chatziioannou et al. 2024). Current GW observations generally provide poor constraints on black hole spins for individual events (R. O'Shaughnessy et al. 2014; K. Chatziioannou et al. 2015; M. Pürrer et al. 2016; R. Abbott et al. 2023a), as these measurements are limited by a partial degeneracy between the mass ratio and a combination of the spin parameters (C. Cutler & E. E. Flanagan 1994; E. Poisson

& C. M. Will 1995; E. Baird et al. 2013; M. Hannam et al. 2013; F. Ohme et al. 2013). However, improved detector sensitivity will enable more precise spin measurements in the future.

Despite the uncertainties in the spin estimates of individual events, after three observing runs of the GW detector network (R. Abbott et al. 2023a) formed by Advanced LIGO (J. Aasi et al. 2015), Advanced Virgo (F. Acernese et al. 2015), and KAGRA (T. Akutsu et al. 2021), it is possible to analyze the spin distribution of the binary black hole population (R. Abbott et al. 2023b). The spin and mass distributions can be used to infer the formation origin of the population of black holes (e.g., S. Stevenson et al. 2015; C. L. Rodriguez et al. 2016; W. M. Farr et al. 2017; M. Fishbach et al. 2017; D. Gerosa & E. Berti 2017; B. Farr et al. 2018; M. Fishbach et al. 2018; M. Fishbach et al. 2021; D. Gerosa et al. 2021; R. Abbott et al. 2023b; A. M. Farah et al. 2023; T. A. Callister & W. M. Farr 2024; S. Banagiri et al. 2025). To do so, it is crucial to have accurate models of the expected parameter distributions in different formation channels. While early works by W. Tichy & P. Marronetti (2008) and C. O. Lousto et al. (2010) derived statistical distributions of spin magnitudes for generic binary configurations, M. Fishbach et al. (2017) investigated the spin distribution specific to hierarchical mergers. In the hierarchical-merger scenario, the spin distribution has been shown to be unique, approximately independent of the mass distribution (assuming only a preference for major mergers with near-unity mass ratios), the black hole birth spins, and the merger generation (M. Fishbach et al. 2017).

In this paper, we revisit the problem of determining the spin distribution of black holes from hierarchical mergers,



Original content from this work may be used under the terms of the [Creative Commons Attribution 4.0 licence](#). Any further distribution of this work must maintain attribution to the author(s) and the title of the work, journal citation and DOI.

incorporating a key consideration: the GW remnant kick velocities produced in binary black hole mergers. Remnant kicks occur due to the anisotropic emission of linear momentum through GWs during a merger. Because of momentum conservation, any loss of linear momentum is balanced by a recoil kick imparted to the merger remnant (W. B. Bonnor & M. A. Rotenberg 1961; J. D. Bekenstein 1973; M. J. Fitchett 1983). The magnitude of this kick depends on the properties of the parent black holes, and it can be as large as 5000 km s^{-1} for certain binary configurations (J. A. Gonzalez et al. 2007a; B. Bruegmann et al. 2008; M. Campanelli et al. 2007; C. O. Lousto & Y. Zlochower 2011; C. O. Lousto & J. Healy 2019). These velocities often exceed the escape velocities of dense star clusters, potentially ejecting merger remnants from their host environments. If a black hole is ejected, it is unlikely it will find a companion and merge again in the galactic field. Thus, for a GW signal to originate from a binary involving a black hole formed in a previous merger, that black hole must have remained within its environment before acquiring a new companion. Therefore, in this study, we compute the kick velocities of binary mergers and determine the spin distribution of retained remnants, particularly in dense star clusters.

Although several studies have highlighted the role of kicks in hierarchical mergers (e.g., D. Merritt et al. 2004; D. Gerosa & E. Berti 2019; Z. Doctor et al. 2021; P. Mahapatra et al. 2021, 2025; C. A. Álvarez et al. 2024), the spin distribution of retained black holes remains largely unexplored. C. A. Álvarez et al. (2024) and P. Mahapatra et al. (2024) have proposed methods to assess whether black holes from individual GW events originate from hierarchical mergers by calculating both the final spin and the kick velocity. In particular, C. A. Álvarez et al. (2024) explore how the relation between these two quantities changes with different initial spin configurations. Yet, none of these studies have explicitly derived the spin distribution of retained black holes.

For some time, many studies have argued that the birth spin of black holes resulting from stellar collapse is highly uncertain (see, e.g., M. C. Miller & J. M. Miller 2014; D. Kushnir et al. 2016). While some recent studies suggest that black hole birth spins are generally small (J. Fuller & L. Ma 2019; S. S. Bavera et al. 2020), GW observations indicate that black holes can have nonzero spins, reaching values of up to 0.4 (T. A. Callister et al. 2022). In this work, we do not restrict ourselves to considering only zero birth spins; instead, we explore how the magnitude of the birth spin impacts the spin distribution of retained black holes across multiple generations of mergers. Furthermore, it has traditionally been argued that black holes in dense star clusters have isotropic-spin orientations (e.g., C. L. Rodriguez et al. 2016), but there may be alternative mechanisms that cause some binary spins to be aligned (e.g., F. Kiroğlu et al. 2025). We investigate whether a small fraction of binaries with nearly aligned spins can influence the spin distribution of black holes resulting from hierarchical mergers.

2. Methods

We calculate the spin distribution of black holes formed through hierarchical mergers, focusing specifically on those that are retained by their host environments. This retention depends on the kick velocities of the merger remnants. This kick velocity is determined by general relativity, in particular, by the initial properties of the binary.

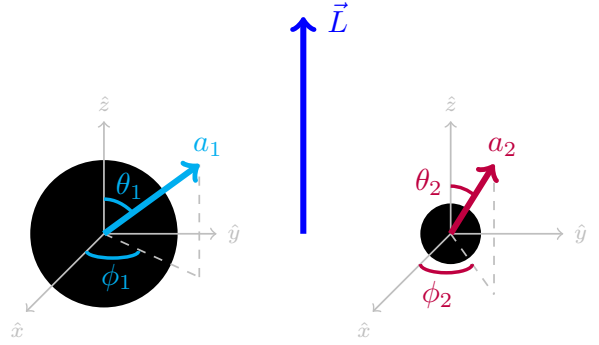


Figure 1. The spin parameters of the primary and secondary black holes. It is common to describe the spins by their magnitudes a_1 and a_2 , their tilt angles θ_1 and θ_2 , and their azimuthal angles ϕ_1 and ϕ_2 , in a reference frame where the z -axis is aligned with the orbital angular momentum of the system, \vec{L} .

Approximately 10% of binaries in dense star clusters are expected to have nonzero orbital eccentricities (C. L. Rodriguez et al. 2018). While post-Newtonian estimates suggest that the kick scales as $1 + e$ (C. F. Sopuerta et al. 2007), recent studies indicate that eccentricity can amplify the kick magnitude by up to 25%. This amplification makes it more challenging for eccentric binaries to remain in such environments (U. Sperhake et al. 2020; M. Radia et al. 2021). Despite these findings, the phenomenology of kicks in eccentric binaries remains insufficiently explored, and no fitting formula currently exists to estimate the kicks from generic binaries. Therefore, in our study, we assume that binaries have quasi-circular orbits. Given the small fraction of eccentric binaries in clusters and their high likelihood of being ejected, this assumption is unlikely to significantly affect our results.

Given that the kick is determined by the mass ratio and the initial spins, only certain combinations of masses and spins will result in retained remnants. On the other hand, the spin of the remnant black hole is determined by the same initial properties. Intuitively, the final spin can be understood as the sum of the initial spins and the angular momentum of a test particle at the last stable orbit around a Kerr black hole (A. Buonanno et al. 2008). Therefore, the parameter combinations that allow for the retention of a particular black hole will also determine its final spin value.

2.1. Predicting the Black Hole Spin Distribution

We consider a large ensemble of black holes, with $N = 10^6$, and randomly select pairs for mergers. First-generation (1G) black holes are assumed to have the same spin magnitude, denoted as a_i , while higher-generation black holes inherit their spins from previous mergers. The spin orientations of all binary black holes are random and isotropic. Figure 1 illustrates the corresponding spin parameters. For each pair, we compute the final spin and the kick velocity using the state-of-the-art fitting formula for black hole remnant properties, `NRSur7dq4Remnant` (V. Varma et al. 2019a). In our model, only black holes with kick velocities smaller than the escape velocity of typical globular clusters can undergo subsequent mergers; those with higher kicks are removed from the ensemble.

We refer to black holes born from stellar collapse as first-generation (1G) black holes, while we refer to those black holes that are remnants from a black hole binary merger as

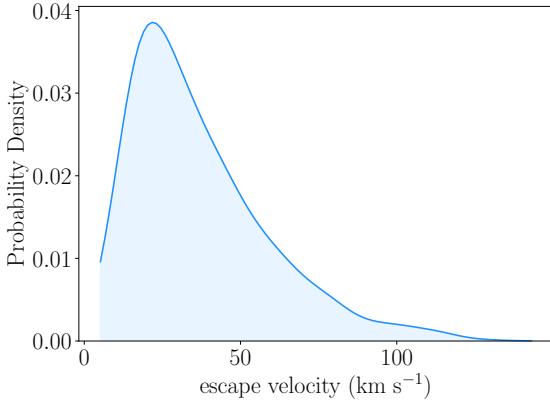


Figure 2. Escape velocity distribution of all 1G + 1G mergers in all CMC simulations weighted by the host cluster’s initial mass ($\propto M_0^{-2}$). This distribution does not represent the escape velocity distribution of a single cluster but rather that of all CMC simulated clusters. As the plot shows, the distribution peaks at approximately 22 km s^{-1} and decreases to zero around 5 km s^{-1} and 140 km s^{-1} , respectively.

second-generation (2G) black holes or, in a more general case, n th generation black holes.

Since hierarchical mergers typically occur in dense star clusters, we also consider the characteristic escape velocities and mass ratio distributions found in these environments. Specifically, we use data from the Cluster Monte Carlo (CMC) cluster catalog, which includes simulations of globular clusters with different initial properties (K. Kremer et al. 2020). Our analysis incorporates data from all 144 CMC simulations currently available.

To determine the spin distribution of the remnants from 1G + 1G mergers, we use the escape velocities provided by the CMC simulations. For each 1G + 1G merger that occurs within these simulations, CMC provides the escape velocity by calculating the gravitational potential at the time and location of the merger. With one escape velocity value per merger, we can construct a distribution representing the escape velocities of host clusters of all 1G + 1G mergers across all simulations. We weight each velocity by the host cluster’s initial mass M_0 , following a $\propto M_0^{-2}$ scaling, which corresponds to a power-law mass distribution expected in young massive clusters (see, e.g., M. Gieles et al. 2006; S. S. Larsen 2009). As shown by Figure 2, the weighted escape velocity distribution peaks at approximately 22 km s^{-1} and decreases to zero around 5 km s^{-1} and 140 km s^{-1} , respectively.

It is important to note that this profile does not represent the escape velocity distribution of a single globular cluster, but rather a combination of multiple clusters with varying masses and radii. For each black hole pair in our model, we randomly sample from this escape velocity distribution. We then compare the binary’s kick velocity to the sampled escape velocity to decide whether the remnant is retained or ejected. When analyzing the convergence of the spin distribution across multiple merger generations, we assume a fixed escape velocity and test a range of values, $v_{\text{esc}} \in (50, 100, 200) \text{ km s}^{-1}$.

We extract the mass ratio distributions of 1G + 1G and 1G + 2G black hole mergers from the CMC simulations, weighting all mergers by the initial mass of the host cluster, according to $\propto M_0^{-2}$. Figure 3 presents these distributions. Mass ratios are reported as the ratio of the primary (more massive) black hole to the secondary (less massive) black hole, so that

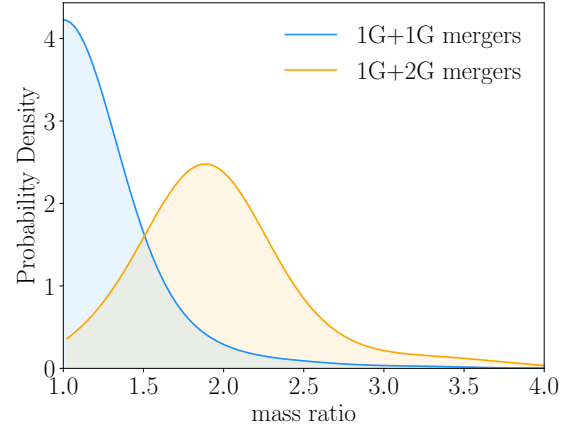


Figure 3. Mass ratio distributions of 1G + 1G (blue) and 1G + 2G (orange) mergers obtained from CMC simulation data, weighted by the host cluster’s initial mass ($\propto M_0^{-2}$).

mass ratios are greater than one. For the rest of the higher-generation mergers (i.e., 2G + 2G and above), the CMC data lack sufficient samples to produce a reliable distribution. In these cases, we adopt a fixed mass ratio value. Motivated by the values at which the mass ratio distributions of the 1G + 1G and 1G + 2G mergers peak, we define the mass ratio as m/n , where m and n denote the generations of the primary and secondary black holes, respectively.

2.2. The Kick Velocity across the Binary Black Hole Parameter Space

Even though we consider isotropically oriented spins, the remnant kick velocity is sensitive to the masses and, especially, to the spin orientations of black hole binaries (see, e.g., J. A. Gonzalez et al. 2007b; F. Herrmann et al. 2007; M. Koppitz et al. 2007). This parameter dependency implies that certain binary configurations are more likely to be retained than others.

In binaries where both black holes are spinning, isotropic spins produce significantly larger kicks than aligned spins. This is illustrated in Figure 4. For instance, for a mass ratio of $q = 1$, isotropic spins yield an average kick magnitude of $570 \pm 443 \text{ km s}^{-1}$, whereas aligned spins produce an average kick of $47 \pm 34 \text{ km s}^{-1}$, with the error bars representing 1σ deviations from the mean values. Figure 5 shows how different spin orientations influence the resulting kick velocity, assuming different values of the binary’s mass ratio. The position of each colored dot indicates the spin magnitude and spin tilt of the primary black hole, while the color indicates the kick velocity averaged over 50 different binaries with a random, isotropic secondary spin direction and magnitude, and a random primary spin azimuthal angle. As we increase the spin magnitudes, the plot shows that binaries where the primary spin is aligned have smaller kicks than binaries with an in-plane or antialigned primary spin. The difference between the kick estimates of these configurations becomes more pronounced as we increase the mass ratio to $q = 4$. These results already suggest that retained remnants have higher chances of having parents with aligned spins.

Regarding the mass ratio dependency of the kick, equal-mass systems have, on average, larger kick magnitudes than unequal-mass systems when assuming isotropic spins, as illustrated by Figure 4. Therefore, their remnants have higher

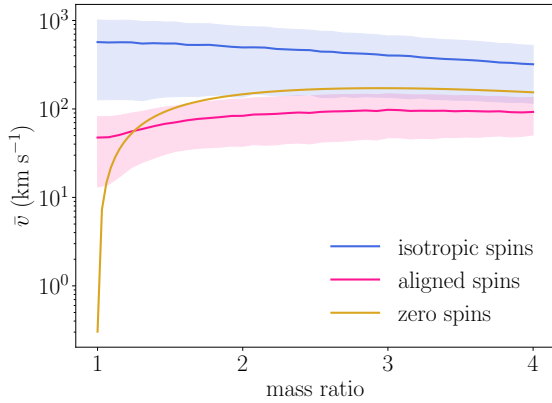


Figure 4. The mass ratio dependence of the kick velocity for three cases: binaries with random isotropic spins (blue), with aligned spins (pink), and with zero spins (brown). For isotropic and aligned spins, we have generated 10^4 binary configurations for each mass ratio value, with spins sampled in the following way. In the isotropic case, for each black hole, the spin magnitude a_i is drawn uniformly from $[0, 0.8]$, the spin tilt angle from $\cos \theta_i \in [-1, 1]$, and the spin azimuthal angle ϕ_i from $[0, 2\pi]$. For aligned spins, we sample the spin magnitude of each black hole uniformly from $[0, 0.8]$. The solid line represents the mean kick velocity, while the shaded region indicates one standard deviation. The kick estimates were computed using the `NRSur7dq4Remnant` fitting formula.

chances of being ejected than those from unequal-mass binaries. On the other hand, the kick velocities from aligned-spin binaries do not depend on the mass ratio so strongly. For unequal mass ratios, aligned-spin binaries produce on average smaller kicks than nonspinning binaries. We investigate this feature in more detail in the [Appendix](#).

Similar to the approach in C. A. Álvarez et al. (2024), Figure 6 illustrates the relationship between the kick velocity and the final spin for an ensemble of 10^6 1G black holes, assuming isotropic-spin orientations and initial spin magnitudes of $a_i = 0.0$ (yellow), $a_i = 0.1$ (pink), and $a_i = 0.6$ (blue). Panel (b) presents the same relation as panel (a), but restricts the y-axis to the range of velocities of the escape velocity distribution we consider in our study (see Figure 2). Since black holes with a kick velocity larger than 150 km s^{-1} are ejected from their host environment in our model, panel (b) provides a more relevant view for our analysis. The figure highlights that 2G black holes formed in typical globular clusters can attain spins greater than 0.7 only if their progenitors had nonzero initial spins. Conversely, as previously noted by D. Gerosa & M. Fishbach (2021) and C. A. Álvarez et al. (2024), 2G black holes cannot have spins below 0.3.

2.3. Impact of Black Hole Spins on the Retention Rate

As the kick velocity is sensitive to the spin magnitudes and orientations, we investigate how the retention rate of 1G + 1G mergers depends on the black hole spin parameters. We consider an ensemble of 10^6 black holes and explore five cases: (i) both black holes have random isotropic spins (representing a 1G + 1G or 2G + 2G merger); (ii) the primary black hole has a random isotropic spin and the secondary is nonspinning (representing a 1G + 2G merger); (iii) the primary black hole has an aligned spin, and the secondary is nonspinning; (iv) the primary is antialigned and the secondary is aligned; and (v) both black holes have aligned spins. In the case where both black holes have spin, we assume both black

holes have the same spin magnitude. For this calculation, we use the mass ratio distribution and escape velocity profile of 1G + 1G mergers from CMC data.

Figure 7 shows the retention rate as a function of the initial spin magnitude for the five cases we mentioned. We observe that the retention rate decreases with increasing spin magnitude in most of the cases, except for the aligned–nonspinning case, where the retention rate increases up to initial spins of $a_i = 0.2$ before decreasing to zero, and for the aligned–aligned case, where the retention rate increases with the initial spin magnitude. This is because the kick magnitude decreases with the increase in spin magnitudes (see the [Appendix](#) for more details). On the other hand, the retention rate of isotropic-spin binaries decreases faster than for other spin configurations, as these binaries produce larger kicks than aligned-spin binaries (see Figure 4).

Many codes used for simulating dense star clusters, including the CMC code, rely on the fitting formula from D. Gerosa & M. Kesden (2016) to estimate final spins and kick velocities. This prescription is available through the Python package `PRECESSION`. Since the development of this model, the catalog of numerical relativity simulations has increased in size and accuracy (see, e.g., M. Boyle et al. 2019; J. Healy & C. O. Lousto 2022; E. Hamilton et al. 2024), allowing the development of more accurate remnant models in recent years (X. Jiménez-Forteza et al. 2017; V. Varma et al. 2019a, 2019b; M. Boschini et al. 2023; M. d. L. Planas et al. 2024). As we mentioned earlier, in our study, we use the state-of-the-art model `NRSur7dq4Remnant` from V. Varma et al. (2019a).

As demonstrated by V. Varma et al. (2019a), the kick estimates of this model are nearly 2 orders of magnitude more accurate than those from `PRECESSION` (see the top right panel of Figure 7 in V. Varma et al. 2019a). Furthermore, `NRSur7dq4Remnant` shows greater accuracy than the improved version of `PRECESSION`, as noted in D. Gerosa et al. (2023). To understand whether modeling differences can impact retention rates, we compare the estimates from `PRECESSION` (v1.0.3) with those from `NRSur7dq4Remnant`.

We find that systematic errors can indeed impact the retention rate estimates, particularly when 1G black holes have nonzero spins. The estimates differ even for small initial spins of $a_i = 0.1$. As observed by D. Gerosa & M. Kesden (2016), `PRECESSION` tends to lose accuracy in the equal-mass limit and when dealing with nonspinning or single-spin binaries. Figure 8 shows the differences in the kick estimates between `NRSur7dq4Remnant` and `PRECESSION` for 2×10^6 binary configurations with random spin magnitudes and orientations, plotted as a function of the mass ratio. We have sampled the spin magnitude uniformly over $a_i \in [0, 0.8]$, the spin tilt angle uniformly in $\cos \theta_i \in [-1, 1]$, and the spin azimuthal angle over $\phi_i \in [0, 2\pi]$. As shown in Figure 8, on average, `NRSur7dq4Remnant` predicts kick magnitudes that are an order of magnitude smaller than those from `PRECESSION` and has a significantly smaller spread in the kick estimates.

Finding disagreements between different models is not uncommon, as kick estimates are particularly sensitive to waveform systematic errors happening during the merger phase (A. Borchers & F. Ohme 2023). Figure 8 explains why the retention rates in Figure 7 are slightly larger when using `NRSur7dq4Remnant`. Having smaller kick velocities means a higher chance of black holes being retained.

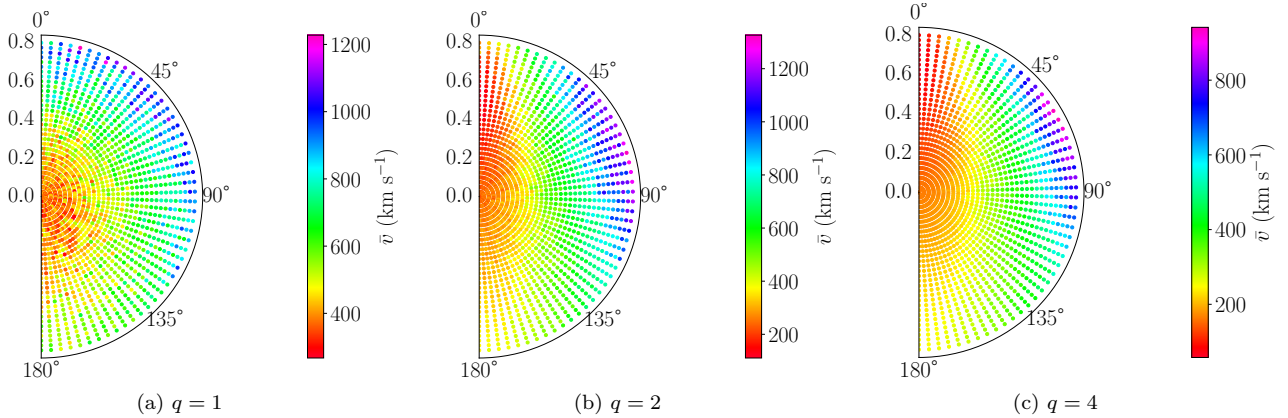


Figure 5. Kick velocities of double-spin binaries with mass ratios $q = 1$, $q = 2$, and $q = 4$, from left to right, respectively. In each polar plot, every dot represents a different spin configuration. The radial distance indicates the primary spin magnitude a_1 , while the tilt angle of the polar plot represents the primary spin tilt angle θ_1 . For every primary spin configuration, we compute the kick velocity, choosing a random secondary spin magnitude and orientation. The points in the polar plots are colored according to the kick velocity. The kick magnitude shown is averaged over 50 different configurations, where the primary spin magnitude and tilt are fixed (specified by the position of the dot in the plot), and the primary spin azimuthal angle and the secondary spin are randomly chosen. Kick velocities have been computed using the `NRSur7dq4Remnant` fit.

In codes that employ `PRECESSION`, the retention rate of 1G + 1G mergers will not be strongly affected by kick biases, as the black holes in these systems are assumed to have negligible spin, and their kick estimates are not expected to be strongly biased. However, for binaries involving 2G or higher-generation black holes (e.g., 1G + 2G or 2G + 2G), where black holes have nonzero spins, the kick estimates will likely be biased (see Figure 8), leading to corresponding biases in the retention rates (as shown by Figure 7) and therefore, the spin distribution of the retained black holes. For these reasons, we adopt a more accurate fitting formula, `NRSur7dq4Remnant`, for our study.

3. Spin Distribution in Hierarchical Mergers

3.1. 1G + 1G mergers

As previously mentioned, the final spin is determined by the initial binary properties. When restricting to retained black holes, we only consider binaries with a kick velocity that is lower than the escape velocity. The kick velocity, which is determined by the same parameters as the final spin, selects which combinations of mass ratios and initial spins contribute to the overall spin distribution.

In Figure 9, we show the spin distribution of 1G + 1G merger remnants, assuming various initial spin magnitudes. We use the mass ratio distribution of 1G + 1G mergers and the escape velocity distribution from the CMC catalog data. The solid lines in the figure represent the spin distribution of the retained black holes, while the dashed lines show the distribution of all remnants.

As anticipated, the spin distribution of all remnants, including the ejected ones, is centered around $a = 0.69$. This finding is consistent with earlier studies (e.g., M. Fishbach et al. 2017). However, when examining the spins of retained black holes, we observe that the distribution peaks at slightly higher values compared to the distribution of all remnants. This difference becomes more pronounced as we increase the initial spin magnitude, especially for values of $a_i \gtrsim 0.3$. For instance, with an initial spin of $a_i = 0.6$ the distribution peaks at $a_f \sim 0.8$. In addition, as we increase the initial spin magnitude, the distribution broadens, showing greater support

for larger spins. As we increase the initial spin magnitude, the mergers of these black holes produce larger kick velocities, and therefore, fewer remnants are retained in the cluster (as shown in Figure 7).

These results show that if birth spins are nonzero, the retained black holes may have spins larger than $a_f = 0.69$. The exact value of the spin depends on the magnitude of the birth spin and other parameters, which will be discussed later in this section. To understand why the spin distribution peaks at values higher than 0.69, we investigate the common properties of the binaries that produce retained remnants.

First, we examine the initial spin orientations of these binaries. Figure 10 displays the initial spin tilts for cases where the initial spin magnitudes are $a_i = 0.6$, as this is the case where the difference between the spin distributions of all remnants and that of the retained remnants is the largest among the cases considered (see Figure 9). In this plot, each dot represents one binary merger. The blank region in the upper left corner indicates that binaries with a primary spin that is antialigned with the orbital angular momentum and a secondary spin that is aligned produce black holes that are generally ejected. We find that 48% of the retained remnants have both parent spins above the orbital plane, supporting final spins greater than $a_f > 0.75$. Twenty-six percent of the retained remnants come from parents with opposite spin tilts that are close to the orbital plane, resulting in final spins between $a_f \in (0.65, 0.75)$. Meanwhile, 25% of the retained remnants have both parent spins below the orbital plane, producing final spins of $a_f < 0.65$. As mentioned earlier, spin-aligned binaries have significantly lower kick velocities compared to binaries with misaligned spins (see Figure 5). This explains the preference of clusters to retain binaries with spins that are close to aligned.

Since the spins are closely aligned with the orbital angular momentum of the system, these orientations lead to larger final spin values than 0.69. This further explains why the spin distribution peaks at final spin values greater than 0.69.

Another important parameter that influences the kick velocity is the mass ratio. As shown in Figure 3, the mass ratio distribution of 1G + 1G mergers peaks at $q = 1$ and tails off to zero around $q \sim 3.5$. In binaries with equal masses,

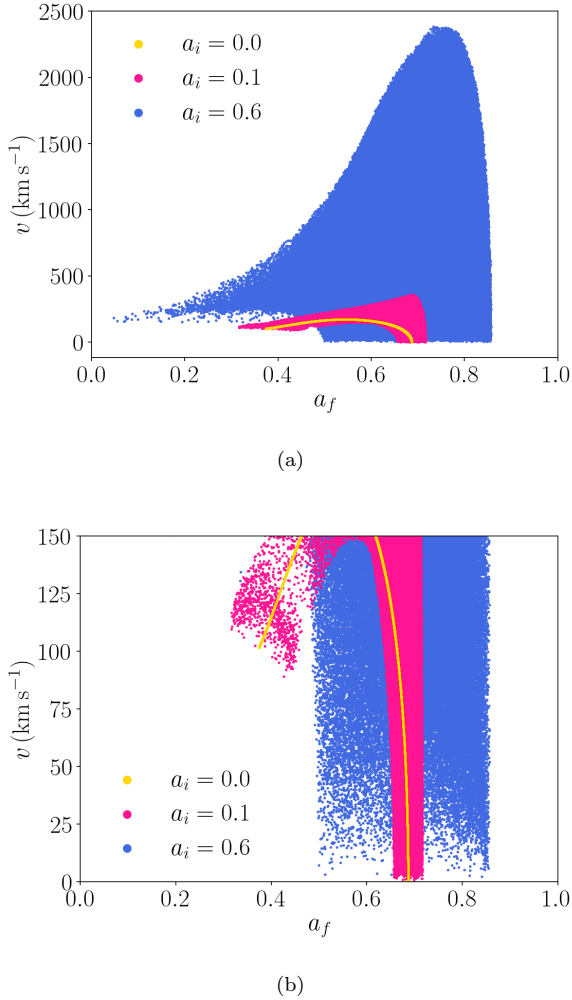


Figure 6. Relation between the kick velocity and the final spin for an ensemble of 10^6 1G black holes with random isotropic-spin orientations and spin magnitudes of $a_i = 0.0$ (yellow), $a_i = 0.1$ (pink), and $a_i = 0.6$ (blue). Remnant properties were computed using the mass ratio distribution of 1G + 1G mergers shown in Figure 3. Panel (b) presents the same relation as panel (a), but with the y-axis restricted to the range of velocities of the escape velocity distribution depicted in Figure 2.

aligned and antialigned spin configurations lead to similar kick velocities (see Figure 5). However, in binaries with $q > 1$, aligned-spin systems have smaller kicks than those with antialigned spins. Therefore, for unequal-mass 1G + 1G mergers, we expect to find a stronger preference to retain remnants from aligned-spin binaries than any other spin configuration.

To further illustrate the impact of the initial properties of the binary on the final spin distribution, we repeat the calculation by assuming that all 1G + 1G mergers have a fixed mass ratio. First, we test the case where $q = 1$, and then we test $q = 2$. Figure 11 presents the spin distribution for these two scenarios, assuming initial spins of $a_i = 0.3$ and $a_i = 0.6$. When assuming that all 1G + 1G mergers have a mass ratio of $q = 1$, the spin distribution of the retained remnants is centered at $a_f \sim 0.7$ independent of the initial spin magnitude. However, when we assume that the binaries have a mass ratio value of $q = 2$, the spin distribution of the retained remnants peaks at values slightly higher than $a_f = 0.7$ for initial spins of $a_i = 0.3$, and

around $a_f = 0.8$ for initial spins of $a_i = 0.6$. It is important to note that the distributions in Figure 11 do not represent the expected spin distribution, as the mass ratios used do not correspond to the expected mass ratio distribution of 1G + 1G mergers in globular clusters. The purpose of including these results is to show that the final spin distribution of retained black holes is highly sensitive to both the mass ratio and the initial spins of the binaries.

3.2. Impact of a Cluster’s Escape Velocity

The question of whether a black hole is retained depends on both the kick velocity and the escape velocity. So far, we have considered the escape velocity distribution typically found in globular clusters. More massive clusters, such as nuclear star clusters, have higher escape velocities, which enables them to retain more black holes. As we increase the escape velocity of a cluster, the spin distribution of retained black holes begins to resemble that of all remnants more closely. Figure 12 illustrates this effect, assuming initial spins of $a_i = 0.3$ and a fixed escape velocity. In this plot, different colors indicate different escape velocities. When the escape velocity decreases, the peak of the spin distribution shifts toward larger spin values.

A notable feature of the spin distribution is the bimodality that emerges, particularly in the case where $v_{\text{esc}} = 20 \text{ km s}^{-1}$. Binaries that result in final spins of $a_f \sim 0.7$ are suppressed in the distribution because they generally have in-plane spins and consequently produce larger kicks than those with aligned or antialigned spins (see Figure 5). In contrast, binaries with aligned and antialigned spins, which are more likely to be retained, lead to slightly higher and lower final spins, respectively. Given the dependence of the spin distribution on the escape velocity, we can expect clusters with different properties to exhibit slightly different spin distributions.

As we lower the escape velocity to $v_{\text{esc}} = 20 \text{ km s}^{-1}$, we must carefully account for the systematic errors in NRSur7dq4-Remnant. The uncertainty in the kick estimate may prevent us from conclusively determining whether the kick is greater or less than the escape velocity, raising the question of whether the observed bimodality is physical. For generic spin configurations, the kick estimate has an average 1σ error of approximately 15 km s^{-1} . However, for configurations where the kicks are smaller than $v_{\text{esc}} = 20 \text{ km s}^{-1}$, the average error is reduced to about 10 km s^{-1} .

To assess the uncertainty in the distribution, we compute the spin distribution considering a subset of retained remnants for which the kick velocity is well resolved and below the escape velocity. Specifically, we include only those cases where the kick plus its 1σ error remains below the escape velocity. This distribution only includes 15% of the retained remnants. Figure 13 compares our original distribution (in red), which includes remnants for which the kick may not be well resolved and could exceed the escape velocity within its uncertainty, with our new distribution (in blue), which includes only remnants for which the kick estimate confidently remains below the escape velocity. The differences between the two distributions reflect the uncertainty in the relative heights of the two peaks, yet the bimodality remains present.

Given the kick uncertainties, the precise escape velocities at which the bimodality emerges cannot be well constrained. This may be resolved in the future once a more accurate fitting formula becomes available.

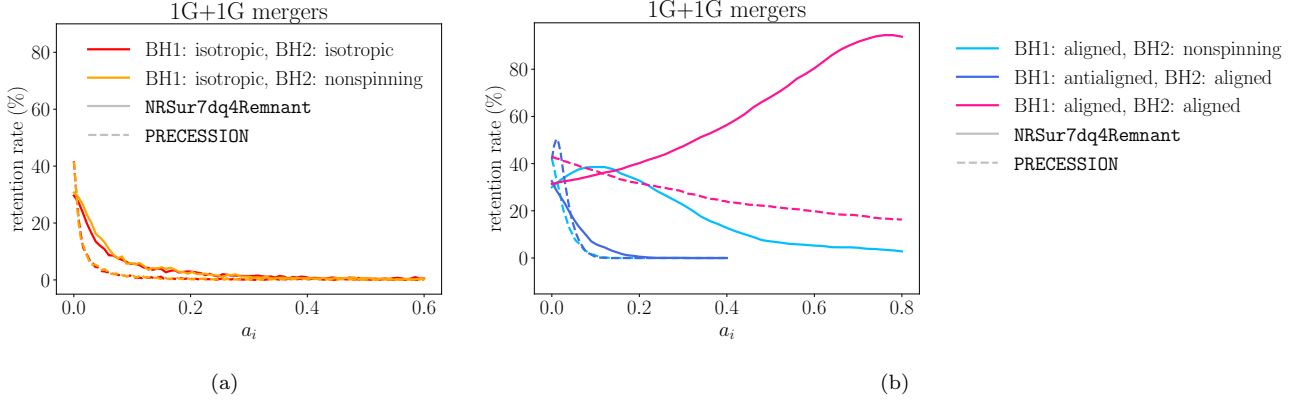


Figure 7. Retention rate of 1G + 1G mergers as a function of the initial spin magnitude assuming an escape velocity distribution of the CMC data. Both plots show how the retention rate changes depending on the spin orientations considered for the components of the binary: in red, assuming both black holes have random isotropic spins (left panel); in orange, assuming the primary has a random isotropic spin, and the secondary is nonspinning (left panel); in light blue, assuming the primary has an aligned spin and the secondary is nonspinning (right panel); in dark blue, assuming the primary has an antialigned spin and the secondary an aligned spin (right panel); and in pink, assuming both black holes have aligned spins (right panel). Solid lines show the estimates using NRSur7dq4Remnant, while dashed lines show the estimates using PRECESSION. In the legend, we use the acronym “BH” to refer to black hole.

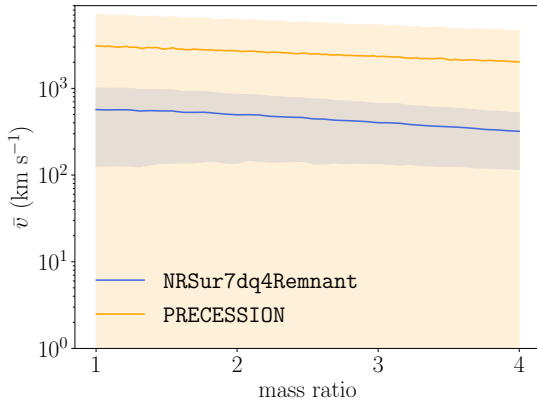


Figure 8. Kick estimates of NRSur7dq4Remnant (blue) and PRECESSION (orange) for 2×10^6 binary configurations with random spin magnitudes and spin orientations as a function of the mass ratio. Solid lines indicate the mean value, while the shaded region indicates one standard deviation from the mean value. Given the improved numerical relativity calibration of the model, NRSur7dq4Remnant is more accurate than PRECESSION. As indicated by the solid lines, on average, NRSur7dq4Remnant predicts kick values that are an order of magnitude smaller than those from PRECESSION, and its estimates have a significantly smaller spread.

Open clusters are examples of dense star clusters with lower escape velocities than globular clusters. In these environments, black holes are also expected to be dynamically assembled into binaries (see, e.g., S. Banerjee 2017, 2021). Because of the low escape velocities, most remnants of binary black hole mergers are ejected from the cluster, limiting the number of merger generations to one. Nevertheless, since the mass ratio distribution of 1G + 1G mergers in these lower-mass clusters is expected to resemble that in globular clusters, the results presented in this section remain applicable to these systems. The low escape velocities also imply that the spin distribution of black holes retained after mergers is likely skewed toward higher values, as shown in Figure 12. Determining the precise shape of this distribution, however, requires knowledge of both the cluster’s escape velocity at the time of the merger and the spin magnitudes of the 1G black holes.

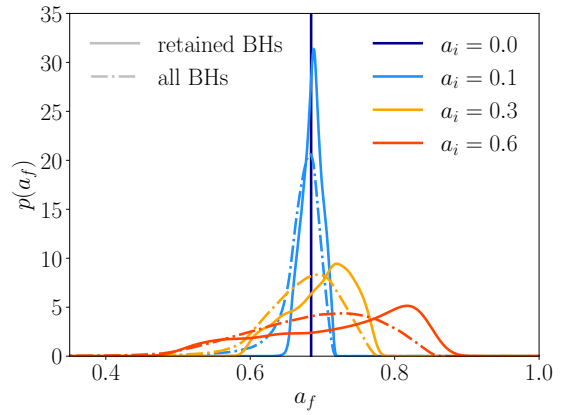


Figure 9. Spin distribution of 1G + 1G merger remnants considering different initial spin magnitudes. We assume isotropic-spin orientations, and consider the escape velocity profile and the mass ratio distribution of 1G + 1G mergers from the CMC data. The dashed lines indicate the spin distributions of all remnants, while the solid lines indicate the spin distributions of the retained ones. For the $a_i = 0.0$ case, the vertical line is centered at $a_f = 0.69$. The plot shows that the spin distribution of the retained black holes shifts toward values larger than $a_f = 0.69$ as we increase the spin magnitude of the 1G black holes.

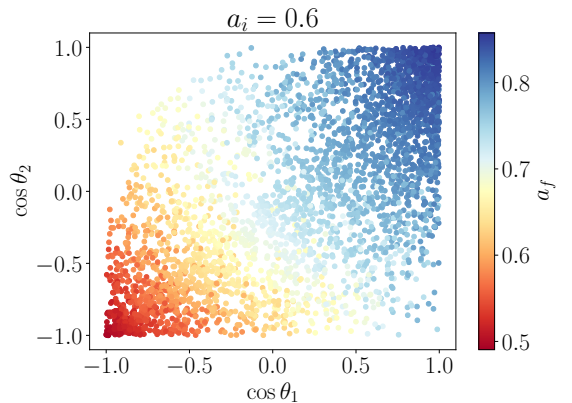


Figure 10. Spin tilts of the retained remnants’ parents, considering that the initial spin magnitudes are $a_i = 0.6$. The points are colored according to the final spin value, as indicated by the color map.

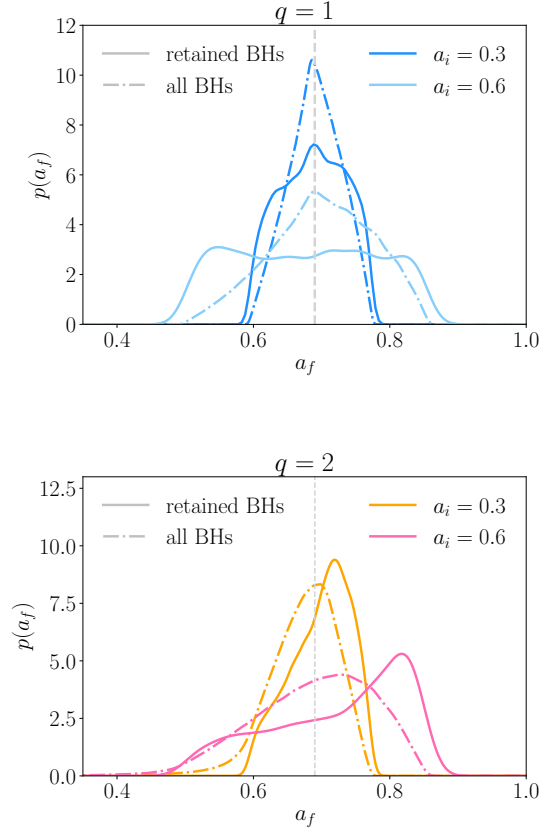


Figure 11. Spin distribution of 1G + 1G mergers, assuming that the mass ratio has a fixed value and nonzero initial spin magnitudes. The top plot shows the spin distribution considering binaries with $q = 1$, while the bottom plot shows the spin distributions assuming $q = 2$. Solid lines indicate the spin distribution of retained remnants, while dashed curves indicate the distribution of all remnants, including the ejected ones. The gray vertical line is centered at $a_f = 0.69$ and is included as a reference. We assume initial spins have random isotropic orientations.

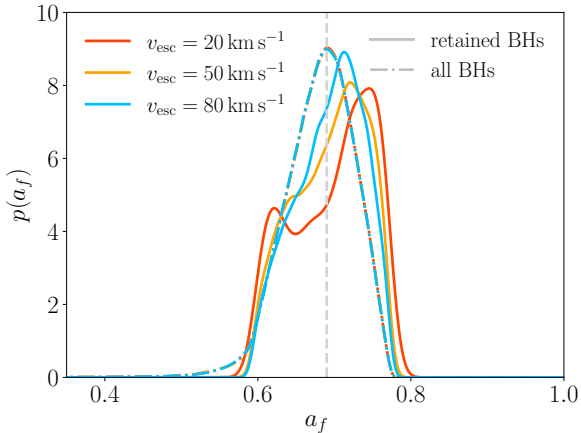


Figure 12. Spin distribution of 1G + 1G merger remnants, assuming birth spins of $a_i = 0.3$ and a fixed value of the escape velocity indicated by the colors in the legend. Solid lines show the distribution of retained black holes, while dashed lines show that of all black holes. The dashed vertical line indicates $a_f = 0.69$ as a reference.

In contrast, clusters with large escape velocities, such as nuclear star clusters, can retain black holes more efficiently and therefore, they are able to host multiple generations of

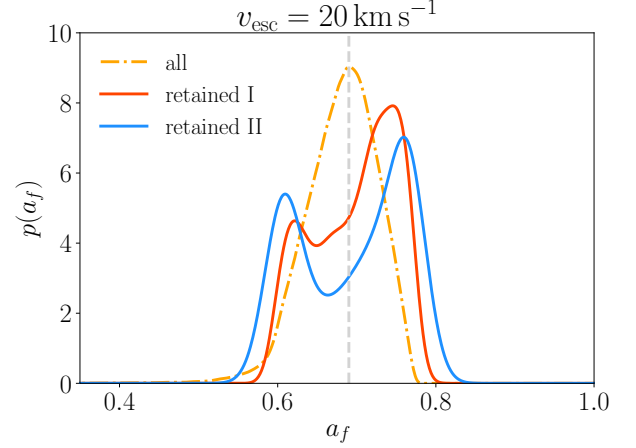


Figure 13. Spin distribution of 1G + 1G merger remnants, assuming birth spins of $a_i = 0.3$ and an escape velocity of $v_{\text{esc}} = 20 \text{ km s}^{-1}$. The orange curve shows the spin distribution of all remnants, the red curve represents the distribution of retained remnants, and the blue curve represents the spin distribution of a subset of the retained remnants for which the kick estimate, including its 1σ error, remains below the escape velocity. The dashed vertical line indicates $a_f = 0.69$ as a reference.

mergers more easily. In the following, we will investigate the spin distribution after several generations of mergers.

3.3. Does the Spin Distribution Converge after Several Mergers?

As discussed in the previous section, 1G black hole binaries produce remnants with a distinct spin distribution, influenced by factors such as mass ratio, initial spins, and escape velocity. We now investigate whether the spin distribution of retained black holes converges after several generations. Figure 14 summarizes our findings.

We find that the spin distribution of retained remnants varies across different black hole generations and does not converge to a unique distribution. Different initial conditions lead to significantly different distributions of the highest-generation mergers retained, namely, 2G + 2G or third-generation (3G) + 3G binaries. In some cases, the distribution flattens out after several mergers, as shown by the panels in the second column of Figure 14, supporting a wide range of spin values, while in other cases, it peaks around $a_f \sim 0.8$, as shown by the panels in the bottom left. Our results show that a n th generation black hole that is retained does not necessarily have a spin of $a_f \sim 0.7$, but its value will range between $a_f \in (0.4, 1)$ depending on the spin magnitudes and orientations of the 1G black holes, the escape velocity of its environment, and the merger generations of its parent black holes.

At the same time, the retention rate of these mergers decreases as we consider higher-generation black holes. Since these black holes have larger spins than 1G black holes, they tend to produce larger kick velocities, which leads to more remnants being ejected from the cluster. Consequently, the likelihood of observing a binary that includes a black hole from a higher-generation merger is lower than for 1G + 1G mergers. Only highly massive star clusters, such as nuclear star clusters, have sufficiently high escape speeds to retain black hole remnants with large kicks, allowing multiple generations of mergers. In these dense clusters, hierarchical mergers may produce intermediate-mass black holes. In particular,

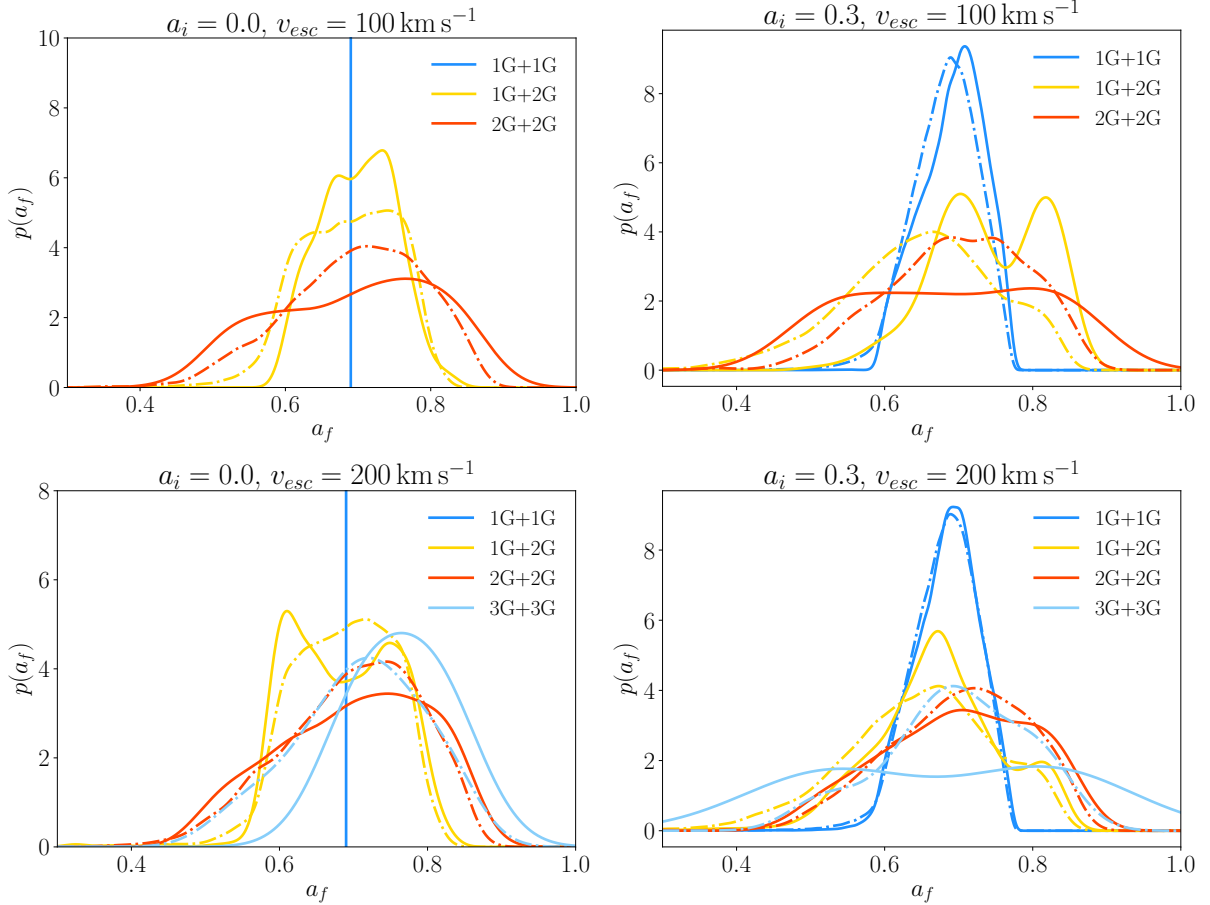


Figure 14. Panels show the spin distribution of different merger generations assuming different initial spins and escape velocities. The panels in the first column assume an initial spin of $a_i = 0.0$, while the panels in the second column assume $a_i = 0.3$. The panels in the first row assume an escape velocity of $v_{esc} = 100 \text{ km s}^{-1}$, while the panels in the second row assume $v_{esc} = 200 \text{ km s}^{-1}$. The spin distribution of retained remnants is shown in solid lines, while the spin distribution of all remnants is shown in dashed lines. In the case of 1G + 1G mergers with $a_i = 0.0$, all remnants are retained and have spins of $a_f = 0.69$, which we indicate with a vertical line.

D. Chattopadhyay et al. (2023) demonstrate that while stellar-mass binaries typically produce spins clustered around $a_f \sim 0.7$, after tens of generations, higher-generation mergers can have mass ratios of up to $q = 100$ and produce a spin distribution that peaks around $a_f \sim 0.2$.

In contrast, the spin distribution of all remnants converges to a near-universal distribution after two merger generations, regardless of the initial spin magnitude, the escape velocity and the black hole generations. Figure 14 shows how the spin distributions of 2G + 2G (red) and 3G + 3G mergers (light blue) are almost identical in the two lower panels. These distributions are consistent with the findings of M. Fishbach et al. (2017).

4. What if Some 1G+ 1G Binaries Have Near-aligned Spins?

Although spin alignment mechanisms are usually associated with isolated binary evolution channels, about 10% of the black holes produced in dense star clusters may also exhibit aligned spins (F. Kiroğlu et al. 2025). Aligned spins may also arise from a cluster’s population of primordial black hole binaries in some less dense young massive star clusters (S. Banerjee et al. 2023). In this section, we allow some fraction of the 1G + 1G binaries to have near-aligned spins

and investigate whether this can impact the distribution of the final spin. As aligned-spin binaries have significantly smaller kicks than isotropic-spin binaries, we can expect the majority of the near-aligned-spin binaries to be retained and contribute to the spin distribution of black holes in a cluster.

To investigate this question, we built a new toy model in which we randomly pair black holes. In this model, the majority of 1G + 1G binaries have random, isotropic spins, except for a fraction that have near-aligned spins. We test three different fraction values: 25%, 50%, and 75%. In the case of the near-aligned-spin binaries, the spin tilt of each black hole is drawn from a Gaussian distribution in the cosine of the tilt angle, $\cos \theta_i$, centered at $\cos(0^\circ)$ and with a standard deviation of $\sigma = \cos(10^\circ)$, while the spin azimuthal angle is drawn from a uniform distribution in $\phi \in [0, 2\pi]$. Regarding the spin magnitude, we test two different values: $a_i = 0.1$ and $a_i = 0.3$. In the same way as in previous sections, we use the mass ratio distribution of 1G + 1G and 1G + 2G mergers from the CMC data, while for higher-generation mergers, we use the fixed value m/n , where m is the generation of the primary black hole and n the generation of the secondary. We use a fixed value of the escape velocity $v_{esc} = 50 \text{ km s}^{-1}$, which is in the range of the typical escape velocities in globular clusters.

Figure 15 shows the spin distribution of 1G + 1G mergers assuming different fractions of near-aligned-spin binaries for

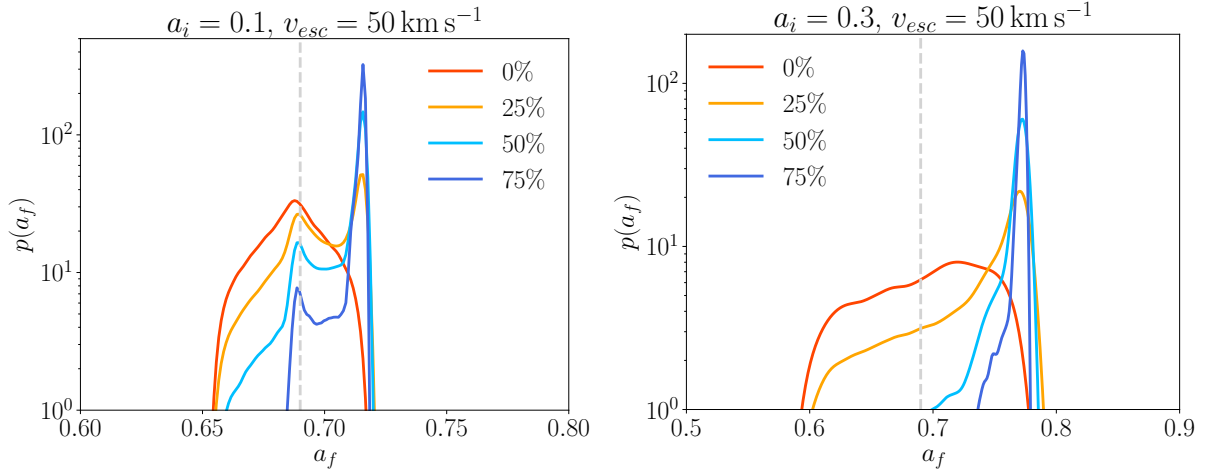


Figure 15. Spin distribution of 1G + 1G mergers, assuming different fractions of near-aligned-spin binaries: 0% (red), 25% (orange), 50% (light blue), and 75% (dark blue). The left panel considers an initial spin magnitude of $a_i = 0.1$, while the right panel considers spins of $a_i = 0.3$. The escape velocity is fixed to $v_{\text{esc}} = 50 \text{ km s}^{-1}$. For reference, the dashed vertical line indicates the final spin value at $a_f = 0.69$.

an escape velocity of $v_{\text{esc}} = 50 \text{ km s}^{-1}$. The left panel assumes a spin magnitude of $a_i = 0.1$, while the right panel assumes $a_i = 0.3$. As shown by the left panel, when the fraction of binaries with near-aligned spins is 25%, the final spin distribution has two peaks. The first peak is centered at $a_f = 0.69$, while the second one peaks at $a_f = 0.72$. Binaries with aligned spins lead to larger final spin values than other initial spin orientations. In our case, the presence of aligned-spin binaries produces a second peak in the spin distribution. As we increase the fraction of near-aligned-spin binaries, the first peak loses support, while the second peak becomes more dominant.

As expected, larger initial spin magnitudes lead to larger final spin values. When we increase the initial spin magnitude to $a_i = 0.3$ (see right panel), the second peak is centered at higher final spin values, specifically at $a_f = 0.77$. Larger initial spins generally lead to higher kick velocities, which in turn results in fewer binaries being retained. Between the aligned-spin binaries and the isotropic-spin binaries, the latter are more prone to ejection, as they typically produce larger kicks (see Figure 4). This explains why, in the right panel, the spin distribution has less support around $a_f = 0.69$ compared to the case with initial spins of $a_i = 0.1$ in the left panel. Increasing the escape velocity allows the cluster to retain more binaries, increasing the support of spins around $a_f = 0.69$.

As discussed in S. Banerjee et al. (2023), dynamical encounters occurring prior to binary mergers can cause initially aligned spins to become misaligned with a peak at approximately 15° in some star clusters. As a result, the support for a secondary peak in the spin distribution would be diminished. The extend of this effect depends primarily on the black holes' birth spins and the escape velocity of the host cluster. For instance, equal-mass binaries with spins misaligned by 15° experience average kick velocities of approximately $v \approx 39 \pm 28 \text{ km s}^{-1}$ for $a_i = 0.1$ and $v \approx 138 \pm 100 \text{ km s}^{-1}$ for $a_i = 0.3$, where the error bars represent a 1σ deviation from the mean value. Therefore, in star clusters with a large fraction of primordial binary black hole mergers and an escape velocity of 50 km s^{-1} , the secondary peak would still be visible for black holes with $a_i = 0.1$, but would likely disappear for those with $a_i = 0.3$.

Regarding the spins of higher-generation merger remnants, similar to our findings in Section 3.3, the distribution depends on several parameters: the initial spin magnitudes and orientations, the escape velocity of the cluster, and additionally, in this case, the fraction of aligned-spin 1G + 1G binaries.

The presence of spin-aligning mechanisms in a cluster can therefore lead to black holes with spins larger than $a_f = 0.69$. As shown in this section, the magnitude of the black hole birth spin, the fraction of binaries affected by spin-aligning mechanisms in a cluster, and the black hole generations will determine the spin magnitude distribution of the retained black holes.

5. Conclusions

One of the open questions in GW astronomy is whether black holes formed via hierarchical mergers can be identified in GW data. Previous studies have indicated that the spin distribution of black holes from hierarchical mergers is centered at $a_f \sim 0.7$, and is approximately independent of the black hole's initial spin, the binary's mass ratio, and the merger generation (M. Fishbach et al. 2017; E. Berti & M. Volonteri 2008). However, the anisotropic emission of GWs imparts a kick velocity to merger remnants, which may exceed the escape velocities of many star clusters. As a result, not all merger remnants are retained within their host environments. Only those that remain bound can later form binaries, undergo mergers, and produce next-generation black holes.

To identify black holes from hierarchical mergers in GW observations, we must focus on those that were retained in their clusters, and successfully formed binaries, which eventually merged. In contrast, ejected merger remnants are unlikely to form new binaries in the galactic field. In this paper, we have investigated the spins of retained black holes by considering the kick velocities produced in every binary merger.

Since the kick velocity depends on the mass ratio and the initial spins of the component black holes, not every binary configuration is equally likely to be retained. In particular, binaries with both spins aligned have significantly smaller kick velocities than binaries with random, isotropic spins. For this

reason, clusters are more effective in retaining binaries with spins that are closely aligned with the angular momentum of the system. We demonstrate how the mass ratio and the initial spins impact the kick velocity and, consequently, the retention of black hole merger remnants. Because the spins of these merger remnants are determined by the same parameters as the kick, we find that remnant kicks influence and shape the spin distribution of black holes from hierarchical mergers. We have provided a detailed analysis of how the spin distribution depends on the binary’s mass ratio, the birth spins of the black holes, the escape velocity, and the generations of the black holes.

In the case of 1G+1G mergers, we find that the spin distribution of retained black holes is skewed toward slightly larger spin values than 0.7 as we increase the magnitude of the black hole birth spins (or decrease the escape speed of the environment). For small birth spins of $a_i = 0.1$, the distribution peaks at $a_f \sim 0.7$, as previously expected, but for moderate birth spins of $a_i = 0.6$, the spin distribution peaks around $a_f \sim 0.8$.

Unlike the spin distribution of all remnants, we find that the spins of retained black holes do not converge to a unique distribution after several generations of mergers. Each generation exhibits its own distinct spin distribution, which varies based on the initial conditions. Specifically, the spins depend on the magnitudes of the birth spins, the mass ratio distribution, the escape velocity of the host environment, and the generations of the black holes. We observe that higher-generation black holes can have spins between $a_f \in (0.4, 1)$, and not necessarily $a_f = 0.7$. This is because the binary configurations that lead to $a_f = 0.7$ are more likely to get ejected from the cluster. In environments with low escape velocities, this leads to a bimodal spin distribution, with two peaks around $a_f \sim 0.6$ and $a_f \sim 0.8$, though their exact positions depend on the birth spins. These peaks arise from antialigned and aligned-spin configurations, which, on average, produce significantly smaller kicks than other binary configurations.

In addition, we have investigated whether the presence of spin-aligning mechanisms in dense star clusters can impact black hole spins. We find that aligned-spin binaries disproportionately produce retained merger remnants, meaning that even a small fraction of nearly aligned binaries leads to a second peak in the spin distribution centered at higher values. The precise location of this second peak depends on the birth spins. For instance, when the black hole birth spins are $a_i = 0.3$, the second and most dominant peak occurs near $a_f \sim 0.8$. In the case of higher-generation mergers, the spin distribution is determined by the fraction of binaries affected by spin-aligning mechanisms in a cluster, together with the birth spin magnitudes and the black hole generations. Once again, we find that higher-generation black holes can have a wide range of spin values, $a_f \in (0.4, 1)$. While spin alignment mechanisms might be present in certain environments such as active galactic nuclei (see, e.g., T. Bogdanovic et al. 2007; B. McKernan et al. 2018), our results do not directly apply to these, as the properties of black hole binaries may differ from those in dense star clusters (Y. Yang et al. 2019).

We have also examined whether systematic errors in models of remnant properties could influence these predictions. Specifically, we compared PRECESSION, the model commonly used in simulations of dense star clusters, with

NRSur7dq4Remnant, a state-of-the-art model. Our analysis shows that, on average, PRECESSION predicts kick velocities that are an order of magnitude higher than those of NRSur7dq4Remnant, resulting in biased retention rates.

With this study, we complement previous work on characterizing the spins of black holes from hierarchical mergers, which can be useful for distinguishing hierarchical-merger black holes in GW observations. For example, we showed that in many scenarios, higher-generation black holes are more likely to have dimensional spin magnitudes $a \approx 0.5$ or $a \approx 0.8$, rather than the canonical value of $a = 0.7$. This is because the binaries that produce remnant black holes with $a_f = 0.7$ receive the largest kicks and are most likely to be ejected from the cluster (and thus unable to participate in future mergers). Given current measurement uncertainty on black hole component spins, we do not expect current GW observations to be sensitive to these differences in the spin distributions, as they will have a minor effect on well-measured parameters like the effective inspiral spin χ_{eff} (P. Ajith et al. 2011). For a population of binaries from hierarchical mergers, where spins are generally expected to be isotropically distributed, the χ_{eff} distribution is symmetric around zero, with spin magnitudes slightly affecting the width of the distribution (W. M. Farr et al. 2017). We expect that the features of the spin distributions described here will become observable once spin parameters can be measured with sufficient precision. Upcoming improvements in the sensitivity of current detectors are expected to yield thousands of GW observations during the O5 observing run (e.g., B. P. Abbott et al. 2020; R. W. Kiendrebeogo et al. 2023), including many high signal-to-noise ratio events. These high signal-to-noise ratio events will enable more accurate measurements of black hole spins, including their magnitudes. As spin measurements become more precise, it will be important to take into account the precise spin distributions of retained black holes, rather than the canonical “universal” approximation, to accurately measure the contribution of higher-generation black holes to the GW population. While the spin distribution from retained hierarchical mergers may be less universal than previously thought, the additional features in the spin distribution encode astrophysical properties such as the escape speed of the environment and black hole birth spins. Therefore, precise measurements of the black hole spin distribution with future catalogs will reveal detailed insights into their formation environments.

Acknowledgments

We are grateful to Aditya Vijaykumar, who first suggested looking at the kick estimates of CMC simulations. The authors are also grateful to Amanda Farah, Davide Gerosa, Shrobana Ghosh, Jannik Mielke, Lavinia Paiella, Frank Ohme, and the CITA GW group for useful discussions. We thank Sharan Banagiri for valuable suggestions during the LVK internal review. We also thank the anonymous referee for their insightful comments. A.B. thanks the CITA GW group for hospitality while part of this work was carried out and acknowledges support from the Deutscher Akademischer Austauschdienst (DAAD) “Forschungsstipendien für Doktorandinnen und Doktoranden” Scholarship 57694189 and the Max Planck Society’s Independent Research Group Grant. C. S.Y. acknowledges support from the Natural Sciences and Engineering Research Council of Canada (NSERC) DIS-2022-

568580. M.F. acknowledges support from the Natural Sciences and Engineering Research Council of Canada (NSERC) under grant RGPIN-2023-05511, the University of Toronto Connaught Fund, and the Alfred P. Sloan Foundation. Computations were performed on the Holodeck cluster of the Max Planck Independent Research Group “Binary Merger Observations and Numerical Relativity.”

Appendix

A Closer Look into the Kick Velocities of Aligned-spin Binaries

In this appendix, we examine the peculiarities of kicks in binaries with aligned spins and unequal mass ratios. Contrary to our intuition, we find that increasing the spin magnitude produces smaller kicks in these binaries. To understand the kick velocities of these systems, we investigate how the kick velocity is built up during the binary evolution.

We calculate the velocity of the binary’s center of mass as a function of time using the waveform model IMRPhenomXO4a (J. E. Thompson et al. 2024). Figure 16 shows the kick profile of aligned-spin binaries with mass ratios $q = 1.5$ (left panel) and $q = 4$ (right panel). In these plots, $t = 0$ s corresponds to the maximum peak of the signal amplitude, which happens at the merger. As we can see, the kick builds up in the merger, decreases drastically after $t = 0$ s, and stabilizes at a value that is much smaller than the maximum peak. The

decrease in velocity has traditionally been denoted as an “antikick” and is thought to be related to the emission of quasi-normal modes, as the newly formed remnant is highly perturbed and radiates GWs to stabilize into a Kerr black hole. This additional emission of GWs and linear momentum flux instantaneously changes the velocity of the remnant (A. Le Tiec et al. 2010; L. Rezzolla et al. 2010; R. H. Price et al. 2011; J. L. Jaramillo et al. 2012). This behavior is particularly strong for aligned–aligned binaries and has previously been pointed out in the literature (J. Healy et al. 2014; D. Gerosa et al. 2018b).

As shown in Figure 16, the largest spin magnitudes have indeed the largest maximum peaks of the velocity. However, as we increase the spin magnitude, the antikick is stronger and the velocity of the remnant becomes smaller. This behavior is unexpected, as one would typically expect higher spin magnitudes to produce larger kick velocities. We verified this effect with numerical relativity waveforms from the Simulating eXtreme Spacetimes (SXS) Catalog (M. Boyle et al. 2019) and found the same phenomenon.

From an astrophysical point of view, this effect implies that if aligned-spin binaries are formed in a certain environment, their retention rate would increase with the initial spin magnitude, which would allow hosting several generations of hierarchical mergers. The impact of aligned-spin binaries on the spin distribution of hierarchical-merger black holes is described in detail in Section 4.

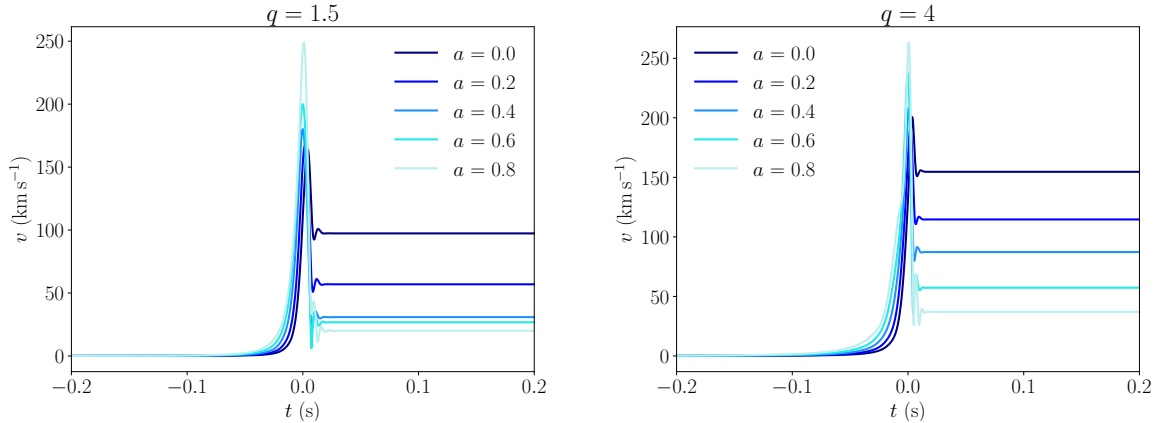




Figure 16. Kick profile of aligned-spin binaries with spin magnitudes $a \in (0.0, 0.2, 0.4, 0.6, 0.8)$, and fixing the mass ratio to $q = 1.5$ (left) and $q = 4$ (right). We assume both black holes have the same spin magnitude. The plot shows that the maximum peak of the velocity increases with the spin magnitude. After the merger, the drop in velocity also becomes more pronounced as the spin magnitude increases. The kick profile has been computed using the waveform model IMRPhenomXO4a.

ORCID iDs

Angela Borchers  <https://orcid.org/0000-0002-2184-7388>
 Claire S. Ye  <https://orcid.org/0000-0001-9582-881X>
 Maya Fishbach  <https://orcid.org/0000-0002-1980-5293>

References

- Aasi, J., Abbott, B. P., Abbott, R., et al. 2015, *CQGra*, **32**, 074001
 Abbott, B. P., Abbott, R., Abbott, T. D., et al. 2020, *LRR*, **23**, 3
 Abbott, R., Abbott, T. D., Acernese, F., et al. 2023a, *PhRvX*, **13**, 041039
 Abbott, R., Abbott, T. D., Acernese, F., et al. 2023b, *PhRvX*, **13**, 011048
 Acernese, F., Agathos, M., Agatsuma, K., et al. 2015, *CQGra*, **32**, 024001
 Ajith, P., Hannam, M., Husa, S., et al. 2011, *PhRvL*, **106**, 241101
 Akutsu, T., Ando, M., Arai, K., et al. 2021, *PTEP*, **2021**, 05A101
 Álvarez, C. A., Wong, H. W. Y., Liu, A., & Calderón Bustillo, J. 2024, *ApJ*, **977**, 220
 Baird, E., Fairhurst, S., Hannam, M., & Murphy, P. 2013, *PhRvD*, **87**, 024035
 Banagiri, S., Callister, T. A., Doctor, Z., & Kalogera, V. 2025, arXiv:2501.06712
 Banerjee, S. 2017, *MNRAS*, **467**, 524
 Banerjee, S. 2021, *MNRAS*, **503**, 3371
 Banerjee, S., Olejak, A., & Belczynski, K. 2023, *ApJ*, **953**, 80
 Bavera, S. S., Fragos, T., Qin, Y., et al. 2020, *AA&A*, **635**, A97
 Bekenstein, J. D. 1973, *ApJ*, **183**, 657
 Berti, E., & Volonteri, M. 2008, *ApJ*, **684**, 822
 Bogdanovic, T., Reynolds, C. S., & Miller, M. C. 2007, *ApJL*, **661**, L147
 Bonnor, W. B., & Rotenberg, M. A. 1961, *RSPSA*, **265**, 109
 Borchers, A., & Ohme, F. 2023, *CQGra*, **40**, 095008
 Boschini, M., Gerosa, D., Varma, V., et al. 2023, *PhRvD*, **108**, 084015
 Boyle, M., Hemberger, D., Iozzo, D. A. B., et al. 2019, *CQGra*, **36**, 195006
 Bruegmann, B., Gonzalez, J. A., Hannam, M., Husa, S., & Sperhake, U. 2008, *PhRvD*, **77**, 124047
 Buonanno, A., Kidder, L. E., & Lehner, L. 2008, *PhRvD*, **77**, 026004
 Callister, T. A., & Farr, W. M. 2024, *PhRvX*, **14**, 021005
 Callister, T. A., Farr, W. M., & Renzo, M. 2021, *ApJ*, **920**, 157
 Callister, T. A., Miller, S. J., Chatziioannou, K., & Farr, W. M. 2022, *ApJL*, **937**, L13
 Campanelli, M., Lousto, C. O., Zlochower, Y., & Merritt, D. 2007, *PhRvL*, **98**, 231102
 Chattopadhyay, D., Stegmann, J., Antonini, F., Barber, J., & Romero-Shaw, I. M. 2023, *MNRAS*, **526**, 4908
 Chatziioannou, K., Cornish, N., Klein, A., & Yunes, N. 2015, *ApJL*, **798**, L17
 Chatziioannou, K., Dent, T., Fishbach, M., et al. 2024, arXiv:2409.02037
 Cutler, C., & Flanagan, E. E. 1994, *PhRvD*, **49**, 2658
 Doctor, Z., Farr, B., & Holz, D. E. 2021, *ApJL*, **914**, L18
 Farah, A. M., Edelman, B., Zevin, M., et al. 2023, *ApJ*, **955**, 107
 Farr, B., Holz, D. E., & Farr, W. M. 2018, *ApJL*, **854**, L9
 Farr, W. M., Stevenson, S., Coleman Miller, M., et al. 2017, *Natur*, **548**, 426
 Fishbach, M., Holz, D. E., & Farr, B. 2017, *ApJL*, **840**, L24
 Fishbach, M., Holz, D. E., & Farr, W. M. 2018, *ApJL*, **863**, L41
 Fishbach, M., Doctor, Z., Callister, T., et al. 2021, *ApJ*, **912**, 98
 Fitchett, M. J. 1983, *MNRAS*, **203**, 1049
 Fuller, J., & Ma, L. 2019, *ApJL*, **881**, L1
 Gerosa, D., & Berti, E. 2017, *PhRvD*, **95**, 124046
 Gerosa, D., & Berti, E. 2019, *PhRvD*, **100**, 041301
 Gerosa, D., Berti, E., O’Shaughnessy, R., et al. 2018a, *PhRvD*, **98**, 084036
 Gerosa, D., & Fishbach, M. 2021, *NatAs*, **5**, 749
 Gerosa, D., Fumagalli, G., Mould, M., et al. 2023, *PhRvD*, **108**, 024042
 Gerosa, D., Giacobbo, N., & Vecchio, A. 2021, *ApJ*, **915**, 56
 Gerosa, D., Hébert, F., & Stein, L. C. 2018b, *PhRvD*, **97**, 104049
 Gerosa, D., & Kesden, M. 2016, *PhRvD*, **93**, 124066
 Gieles, M., Larsen, S., Bastian, N., & Stein, I. 2006, *A&A*, **450**, 129
 Gonzalez, J. A., Hannam, M. D., Sperhake, U., Bruegmann, B., & Husa, S. 2007a, *PhRvL*, **98**, 231101
 Gonzalez, J. A., Sperhake, U., Bruegmann, B., Hannam, M., & Husa, S. 2007b, *PhRvL*, **98**, 091101
 Hamilton, E., Fauchon-Jones, E., Hannam, M., et al. 2024, *PhRvD*, **109**, 044032
 Hannam, M., Brown, D. A., Fairhurst, S., Fryer, C. L., & Harry, I. W. 2013, *ApJL*, **766**, L14
 Healy, J., & Lousto, C. O. 2022, *PhRvD*, **105**, 124010
 Healy, J., Lousto, C. O., & Zlochower, Y. 2014, *PhRvD*, **90**, 104004
 Herrmann, F., Hinder, I., Shoemaker, D., Laguna, P., & Matzner, R. A. 2007, *ApJ*, **661**, 430
 Jaramillo, J. L., Panosso Macedo, R., Moesta, P., & Rezzolla, L. 2012, *PhRvD*, **85**, 084030
 Jiménez-Forteza, X., Keitel, D., Husa, S., et al. 2017, *PhRvD*, **95**, 064024
 Kalogera, V. 2000, *ApJ*, **541**, 319
 Kiendrebeogo, R. W., Farah, A. M., Foley, E. M., et al. 2023, *ApJ*, **958**, 158
 Kiroğlu, F., Lombardi, J. C., Kremer, K., Vanderzyden, H. D., & Rasio, F. A. 2025, *ApJ*, **983**, 9
 Koppitz, M., Pollney, D., Reisswig, C., et al. 2007, *PhRvL*, **99**, 041102
 Kremer, K., Ye, C. S., Rui, N. Z., et al. 2020, *ApJS*, **247**, 48
 Kushnir, D., Zaldarriaga, M., Kollmeier, J. A., & Waldman, R. 2016, *MNRAS*, **462**, 844
 Larsen, S. S. 2009, *A&A*, **494**, 539
 Le Tiec, A., Blanchet, L., & Will, C. M. 2010, *CQGra*, **27**, 012001
 Lousto, C. O., & Healy, J. 2019, *PhRvD*, **100**, 104039
 Lousto, C. O., Nakano, H., Zlochower, Y., & Campanelli, M. 2010, *PhRvD*, **81**, 084023
 Lousto, C. O., & Zlochower, Y. 2011, *PhRvL*, **107**, 231102
 Mahapatra, P., Chattopadhyay, D., Gupta, A., et al. 2024, *ApJ*, **975**, 117
 Mahapatra, P., Chattopadhyay, D., Gupta, A., et al. 2025, *PhRvD*, **111**, 023013
 Mahapatra, P., Gupta, A., Favata, M., Arun, K. G., & Sathyaprakash, B. S. 2021, *ApJL*, **918**, L31
 Mckernan, B., Ford, K. E. S., Bellovary, J., et al. 2018, *ApJ*, **866**, 66
 Merritt, D., Milosavljevic, M., Favata, M., Hughes, S. A., & Holz, D. E. 2004, *ApJL*, **607**, L9
 Miller, M. C., & Miller, J. M. 2014, *PhR*, **548**, 1
 Ohme, F., Nielsen, A. B., Keppel, D., & Lundgren, A. 2013, *PhRvD*, **88**, 042002
 O’Shaughnessy, R., Farr, B., Ochsner, E., et al. 2014, *PhRvD*, **89**, 064048
 Planas, M. d. L., Llobera-Querol, J., & Husa, S. 2024, *PhRvD*, **109**, 124028
 Poisson, E., & Will, C. M. 1995, *PhRvD*, **52**, 848
 Portegies Zwart, S. F., & McMillan, S. 2000, *ApJL*, **528**, L17
 Price, R. H., Khanna, G., & Hughes, S. A. 2011, *PhRvD*, **83**, 124002
 Pürrer, M., Hannam, M., & Ohme, F. 2016, *PhRvD*, **93**, 084042
 Radia, M., Sperhake, U., Berti, E., & Croft, R. 2021, *PhRvD*, **103**, 104006
 Rezzolla, L., Macedo, R. P., & Jaramillo, J. L. 2010, *PhRvL*, **104**, 221101
 Rodriguez, C. L., Amaro-Seoane, P., Chatterjee, S., & Rasio, F. A. 2018, *PhRvL*, **120**, 151101
 Rodriguez, C. L., Zevin, M., Pankow, C., Kalogera, V., & Rasio, F. A. 2016, *ApJL*, **832**, L2
 Sopuerta, C. F., Yunes, N., & Laguna, P. 2007, *ApJL*, **656**, L9
 Sperhake, U., Rosca-Mead, R., Gerosa, D., & Berti, E. 2020, *PhRvD*, **101**, 024044
 Stevenson, S., Ohme, F., & Fairhurst, S. 2015, *ApJ*, **810**, 58
 Thompson, J. E., Hamilton, E., London, L., et al. 2024, *PhRvD*, **109**, 063012
 Tichy, W., & Marronetti, P. 2008, *PhRvD*, **78**, 081501
 Varma, V., Field, S. E., Scheel, M. A., et al. 2019a, *PhRvR*, **1**, 033015
 Varma, V., Gerosa, D., Stein, L. C., Hébert, F., & Zhang, H. 2019b, *PhRvL*, **122**, 011101
 Yang, Y., Bartos, I., Gayathri, V., et al. 2019, *PhRvL*, **123**, 181101

Chapter 8

Conclusions

8.1 Summary of results

At the beginning of this thesis, we presented three existing challenges in gravitational-wave astronomy that we have addressed throughout this thesis:

- Are waveform models accurate enough in all relevant regions of the parameter space? How do we assess waveform systematic errors?
- With the limited signal strength of current detections, how can we extract the most information out of these signals? Can we make more meaningful measurements of the source parameters?
- How did the black holes we observe through gravitational waves form? Can we distinguish black holes from different formation channels?

Together, our three investigations have demonstrated the valuable role of remnant kicks in tackling these challenges: from evaluating waveform accuracy, to enabling more precise parameter measurements, and refining the prediction of black hole spins in hierarchical merger scenarios. These are crucial steps towards better understanding the black holes we observe. We now summarise the key findings of each study.

Our first study demonstrated that kick velocity estimates can serve as a valuable diagnostic for assessing the accuracy of waveform models across the parameter space. As mentioned earlier, waveform accuracy is essential not only for detecting gravitational-wave signals, but also for making reliable inferences about the properties of the individual black holes.

We tested the performance of three nonprecessing waveform models, PhenomHM, PhenomXHM, and SEOBNRv4HM_ROM, by comparing their kick estimates to those of NRHybSur3dq8, which is generally the most faithful to NR estimates. We illustrated the sensitivity of the kick to waveform inaccuracies by examining nonspinning binaries with varying mass ratios, which are systems for which waveform models are generally well calibrated to NR and considered accurate enough for data analysis purposes. Even in these well-understood cases, we observed discrepancies in the kick estimates of up to $\Delta v \sim 40 \text{ km s}^{-1}$ compared to NRHybSur3dq8, corresponding to a relative kick error of about 27% when using NRHybSur3dq8 as the reference or "true" value.

Since the kick uncertainty of NRHybSur3dq8 is comparable to that of NR simulations from the SXS catalog, we quantified the errors in the kick magnitude and direction of the SXS waveforms. Specifically, we considered all SXS waveforms that included at least two resolution levels. On average, we found that the uncertainty in the kick magnitude is approximately $\Delta v \sim 10 \text{ km s}^{-1}$. In contrast, the kick direction is not as well constrained, with uncertainties extending up to the maximum possible angular deviation. This limitation likely arises from the difficulty of tracking the black hole spin orientations at merger, as it is a highly relativistic and non-linear regime. Since the kick direction depends sensitively on these spin orientations, the inability to resolve them accurately may explain the large uncertainties in the kick direction.

We compared the kick estimates across the parameter space, by sampling the symmetric mass ratio over $\eta \in [0.10, 0.25]$ and the spin magnitudes over $a \in [-0.8, 0.8]$, which is the region where NRHybSur3dq8 is calibrated to NR. Our results show that PhenomHM exhibits the largest discrepancies with NRHybSur3dq8 in both kick magnitude and direction. The distribution of kick differences has a mean value of approximately $\Delta v \sim 42 \text{ km s}^{-1}$ for the kick magnitude, and $\Delta\theta \sim \pi/8$ for the kick direction. In contrast, PhenomXHM, which is an improved version of PhenomHM with enhanced NR calibration, produces kick estimates much closer to NRHybSur3dq8, with a mean difference of $\Delta v \sim 9 \text{ km s}^{-1}$. SEOBNRv4HM_ROM yields the closest agreement, with a mean difference of $\Delta v \sim -0.4 \text{ km s}^{-1}$. Both PhenomXHM and SEOBNRv4HM_ROM show similar values to NRHybSur3dq8 in estimating the kick direction. When analysing the dependence of the kick differences on the mass ratio and the individual black hole spins, we found that the largest deviations occur in regions where one or both black holes have high spins, a region that is known to be challenging to model accurately.

The total kick velocity arises from the sum of contributions from various gravitational-wave harmonics. Decomposing the kick into these individual contributions allowed us to assess the accuracy of each component separately. Our results reveal a significant improvement from PhenomHM to PhenomXHM, particularly in the contributions from the $(2, \pm 1)(2, \pm 2)$ and $(3, \pm 2)(3, \pm 3)$ modes, which reflects the improvement in NR calibration of PhenomXHM.

We note that these waveform models were not designed to produce accurate kick estimates, as they were not calibrated to NR kick values. The differences we observed in their kick estimates are therefore not surprising. However, we emphasise that the kick prediction is a novel accuracy estimator. This is important because waveform accuracy directly affects our ability to extract reliable information from gravitational-wave signals and, ultimately, our understanding of the properties of the black hole population.

Finally, we proposed a method to improve waveform models and their kick estimates using accurate NR-based kick predictions. This approach involves tuning the phases of individual gravitational-wave harmonics to match NR kick orientations by applying specific phase shifts. Current NR waveforms may not be well suited for this approach given the large uncertainties in the estimate of the kick direction, but our method may become useful once more accurate NR waveforms are available.

In our second study, we switched our focus from waveform accuracy to the estimation of source parameters in signals with significant kicks. One of the main goals of

gravitational-wave astronomy is to maximize the information extracted from each event, in particular, measuring the spins magnitudes and orientations of the source components, as they can help to distinguish different formation channels.

We demonstrated that the presence of a large kick in a gravitational-wave signal can improve our ability to extract more information about the source properties, in particular, about the spins. Our results are particularly relevant for equal-mass binaries that are oriented face-on or face-away to the detectors, where the signal only includes the dominant mode. This is likely the case of many gravitational-wave events observed so far [7]. As the higher harmonics are negligible in the observed signal radiated by these configurations, previous studies have suggested that measuring spin precession is nearly impossible [200]. We demonstrated that if the signal includes a kick, it is indeed possible, even at SNRs as low as ~ 25 , a level already achievable in the current LVK observing run (O4) [201].

We found that signals with large kicks necessarily involve significant asymmetries in the emitted gravitational waves. However, the opposite is not true. Strong mode asymmetries can exist without producing a net kick. Through our analysis of signals from binaries with varying degrees of kick and mode asymmetries, we concluded that asymmetry alone is insufficient for achieving the most precise measurements. Instead, it is the combination of strong mode asymmetries *and* a significant kick what yields the most informative constraints on source properties.

Our results can be partially interpreted within the theoretical framework of the two-harmonic approximation [123, 202], which states that detecting spin precession requires the presence of at least two distinct harmonics in the signal, either in the inertial or co-precessing frame. While the original two-harmonic approximation does not account for mode asymmetries, such asymmetries play a crucial role in our analysis. If a signal contains a measurable kick, it necessarily involves significant mode asymmetries. For the waveform model we used to simulate the signal, it means the signal includes the asymmetries between the $(\ell, m) = (2, 2)$ and $(\ell, m) = (2, -2)$ harmonics in the co-precessing frame. In such cases, the observed inertial-frame $(\ell, m) = (2, 2)$ mode is effectively a combination of both co-precessing harmonics, $(2, 2)$ and $(2, -2)$. Therefore, according to the two-harmonic approximation, a signal with a large kick should enable measurements of spin precession, since it inherently contains two distinct harmonic components. In turn, a signal with a small kick and small asymmetries will not contain two distinct harmonics, and therefore, will lead to uncertain measurements of precession. Hence, the presence of mode asymmetries enriches the structure of the signal, making it more informative for parameter estimation.

The finding that the most precise measurements arise from the *combination* of large mode asymmetries and large kicks cannot be fully explained by the two-harmonic approximation, and is simply an observation of our results.

One of the primary goals of gravitational-wave science is to learn as much as possible from individual detections to build a complete picture of the black hole population. Our study contributes to this effort by showing a pathway for spin measurements in scenarios previously thought to be uninformative.

In our third study, we shifted our focus from individual gravitational-wave events to

black hole population studies, a rapidly growing area of research driven by the increasing number of detections. As we mentioned earlier, a central goal of this field is to use the observed distributions of source properties to infer the astrophysical origins of the detected black holes.

We investigated the role of gravitational-wave kicks in shaping the spin distributions of black holes formed through hierarchical mergers in dense star clusters, particularly for globular clusters. Our results show that when accounting for kick velocities, the spin distribution of second-generation black holes may not be centered at around 0.7, as suggested by previous studies [19, 20]. Instead, we found that the distribution becomes skewed toward higher spin values, depending on two key factors: the initial spin magnitudes of first-generation black holes and the escape velocity of the host cluster at the time of merger. For very low escape velocities, the distribution can even become bimodal. For example, when the birth spins are $a_i = 0.3$, a bimodal distribution emerges at escape velocities around 20 km s^{-1} , with minimal support for spins of 0.7.

The reason is the following. Although spin orientations in binaries are initially assigned randomly and isotropically, not all configurations are equally likely to be retained after merger. We found that binaries with nearly aligned spins produce kick velocities that are, on average, an order of magnitude smaller than those with random orientations. This means that these binaries are significantly more likely to remain gravitationally bound to the host cluster. As a result, most retained merger remnants originate from binaries with spins close to alignment, which naturally leads to higher remnant spin values. Interestingly, antialigned spin configurations also produce relatively small kicks and contribute to the second peak in the bimodal spin distribution. This secondary mode is centered at lower spin values.

We found that higher-generation black holes can acquire a broad range of spin values, typically in the range $a \in (0.4, 1)$. The final spin distribution depends not only on the birth spin of first-generation black holes and the escape velocity of the cluster, but also on the generation number of the merging black holes.

In addition, recent studies suggested that spin orientations in dense clusters may not always be isotropic. Up to 10% of binaries may form with nearly aligned spins [203]. We found that such a subpopulation can give rise to a second, more dominant peak in the overall spin distribution of retained black holes, further highlighting the impact of spin alignment and gravitational-wave kicks in shaping black hole populations. The location of this secondary peak is determined by the spin magnitude of the first-generation black holes, while its significance depends on the fraction of binaries with nearly aligned spins.

Our study refines previous predictions for the characteristic spins of black holes formed through hierarchical mergers, providing a valuable tool for determining whether the black holes detected via gravitational waves originate from such processes and distinguish them from other formation channels. Hierarchical mergers may explain the origin of certain events, such as GW190521 [204] or the recent detection GW231123 [205], where the component black hole masses exceed the expected limits from stellar collapse constrained by pair-instability supernova models. Our results are also crucial for understanding the contribution of hierarchical mergers to the overall population of gravitational-wave sources.

8.2 Future work and outlook on key questions

Our first study introduced a novel diagnostic to assess waveform accuracy. This work can be extended by examining kick predictions from waveform models for precessing binaries. At the time of our first project, the only available model that included mode asymmetries for precessing systems was the NR surrogate NRSur7dq4. Neither EOB nor phenomenological models accounted for this effect, leading to significantly biased kick estimates, limited to a maximum of about 500 km s^{-1} , which is the upper bound for non-precessing binaries. Since then, waveform modeling has advanced considerably, with new precessing models in both the EOB and phenomenological families now incorporating mode asymmetries [117, 131]. A natural and relevant extension of our earlier work is to compare kick predictions from these improved models with those from the NR surrogate, or directly against NR simulations.

A complementary test to the kick velocity estimates is to compute the four-momentum (or supermomentum) using balance laws derived from Einstein's equations [206], rather than focusing solely on the three-dimensional linear momentum. While previous studies have already tested the angular momentum balance law to evaluate state-of-the-art waveform models [207], a similar analysis using the linear momentum balance law offers a promising approach to further assess model accuracy.

Beyond kick velocity estimates, waveform accuracy across the parameter space can of course be evaluated through mismatches with NR simulations and injection-recovery studies, which remain essential tools. Another promising direction is to explicitly incorporate waveform systematics into models, as proposed by [208], and to account for these uncertainties during parameter estimation, which is a strategy increasingly suggested in recent works [209–213].

Accurate and complete waveform models are of course necessary for extracting meaningful information from gravitational-wave signals. We have mentioned that certain favorable configurations, such as inclined orientations, high spin magnitudes, high SNRs, can significantly enhance parameter estimation precision. In our second study, we have shown that large kick velocities can also contribute to improved parameter constraints. A limitation of that study is that the kick leaves only a subtle imprint on the merger phase of the waveform. As a result, improved precision due to the kick is achievable only when the merger is within the observable frequency band, which typically occurs for binaries with relatively large total masses.

The improvement in parameter estimation due to the kick is most pronounced for binaries observed face-on or face-away. For inclined systems, our results show that higher-order gravitational-wave modes have a greater impact on measurement precision than the kick itself. Since the signals that were simulated with PhenomXO4a included only the dominant mode asymmetry, it remains an open question whether subdominant mode asymmetries could significantly enhance parameter estimation for inclined configurations. A natural extension of this work is therefore to investigate the influence of subdominant mode asymmetries on parameter estimation and to further explore their relationship with the kick velocity.

In our last study, a key finding is the non-universality of the spin distribution for black

holes formed through hierarchical mergers. Since the kick velocity depends sensitively on the black holes' spins, the resulting spin distribution is influenced by three main factors: the black hole's birth spin, the escape velocity of its host environment, and the number of merger generations. This finding suggests that, if these factors can be disentangled, the spin distribution could serve as a valuable probe of the astrophysical environments and formation histories of black holes.

A first step is to investigate whether one can one-to-one map a change on the birth spin, escape velocity, and merger generation to the spin distribution, and find out whether these effects can be distinguished from one another. Then, one could simulate a population of black holes formed exclusively through hierarchical mergers and test whether these underlying parameters can be reliably recovered from the resulting spin distribution. A natural extension would then be to model more realistic populations that combine multiple formation channels, such as isolated binary evolution and dynamical formation including hierarchical mergers, and investigate whether subpopulations can still be identified through their distinct spin signatures.

Our original study can also benefit from using more realistic escape velocity distribution. In our work, the escape velocity of first-generation (1G+1G) mergers was drawn from the CMC cluster simulations, which serves as a good representation of the escape velocities of globular clusters. However, for higher-generation black holes, we adopted a fixed escape velocity due to insufficient sampling in the CMC data. Improving the modelling of escape velocity distributions, particularly for higher-generation mergers, will enhance the accuracy of spin distribution predictions and strengthen the connection between observed spins and their astrophysical origins.

Several studies have suggested that eccentric orbits can significantly enhance kick velocities [179, 180]. However, the precise impact of eccentricity on kicks remains poorly understood, mainly due to limitations in the number NR simulations for eccentric binaries. With recent expansions of NR catalogs, it is now more feasible to explore this aspect in detail. Such investigations are timely and important, as a small but non-negligible fraction of binaries in dense stellar environments are expected to have significant eccentricity. Accurately predicting the kicks in these systems will help refine even more our understanding of the black hole properties in these environments.

A direct application of our results is to assess whether individual gravitational-wave events, such as the recent black hole binary GW231123, could be of hierarchical origin. In the case of GW231123, the inferred spin magnitudes are $0.9^{+0.10}_{-0.19}$ and $0.8^{+0.20}_{-0.51}$ [205]. Our findings show that, contrary to the common assumption that hierarchical mergers typically yield spins near 0.7, these systems can produce spin magnitudes up to 1. Based on this, the observed spins of GW231123 are consistent with a hierarchical origin. Conversely, our analysis suggests that spin magnitudes significantly below 0.4 are unlikely to result from hierarchical mergers, providing a useful diagnostic for ruling out such origins in low-spin systems.

More broadly, distinguishing black holes formed through different evolutionary channels will become possible once a few conditions are met. First, we need accurate theoretical predictions for black hole properties across various formation scenarios. This remains a challenge in some cases. For instance, binary population synthesis models must in-

corporate complex physical processes, many of which are still poorly understood (see e.g. [16]). Consequently, several model parameters can only be constrained through observations (see e.g. [214]). In this context, both electromagnetic observations and maybe even gravitational-wave data can help to refine these models. Equally important are precise measurements of black hole properties across the gravitational-wave black hole population, not just for a few exceptional events, as has been the case so far [7, 28]. As detector sensitivity improves in the coming years, and especially with the arrival of third-generation gravitational-wave observatories, we expect to detect many more signals with significantly higher SNRs. Together with continued advances in waveform modelling, these developments will enable more accurate and informative parameter estimates. The combination of improved waveform models, enhanced observational capabilities, and better astrophysical models will ultimately allow us to gain deeper insight into the formation and evolution of the black hole population. This thesis provided an example of how the combination of waveform modelling, astrophysics and population studies will shape the future of gravitational-wave astronomy.

Acknowledgements

This PhD has given me so much more than knowledge and research experience. When I started this journey, I never imagined everything else I would gain along the way. I had the chance to meet people from many different parts of the world, to be part of a big scientific collaboration, to travel to new places, to live in two different countries... I'm truly grateful for all of it. But above all, I've met so many friendly, kind and open-minded people over these years, some of whom have become lifelong friends. Before ending this thesis, I want to thank everyone I had the chance to cross paths with. In one way or another, each of you helped me get to this point.

First and foremost, I want to thank my incredible supervisor, Frank. I can't thank you enough for giving me the chance to stay in the group. I'm really glad I did. I especially appreciate the trust you placed in me, giving me the freedom to explore my own research path and to work at my own pace, without a rush. I've felt very lucky to have that space. I'm also thankful for the many hours we spent discussing ideas, addressing issues or just chatting about life outside of science, even when you were halfway around the world or busy refereeing at the Olympics! Your optimism and positive energy have really brightened my years here. I often stressed about things not working out and our conversations always lifted me up. And in the more difficult moments, your support and kindness made all the difference. Thank you so much for everything!

I'm grateful to all past and present members of the group for creating such a friendly and welcoming atmosphere: Jannik, Julian, Krishnendu, Marius, Max, Sebastián, Shrobana, Sumit, Wolfgang and our visitors Juan, Maite and Verónica. I will always remember our little jokes, the funny German expressions, our coffee breaks, the tipping games and of course, our dear banana tree. To all my officemates: Sebastián, Jannik and Shrobana, it was great sharing the office with you. Thank you for your company, and for listening to me when I most needed it. I'm deeply sorry for the times I interrupted you from your work for being too expressive and thinking too loud!

To my colleagues, fellow students, postdocs, secretaries, administrative staff and lovely pets of the AEI, thank you for creating such a warm, familiar and supportive environment at the institute. I always felt a sense of belonging here.

During this PhD, I had the chance to visit several research groups. I would like to thank Maya Fishbach and the entire GWs group at CITA for hosting me during my visit and for giving me the opportunity to collaborate with them. I'm also grateful to Thomas Dent, Ofek Birnholtz and Davide Gerosa for inviting me to their institutions, and allowing me to present my work there. These visits were very enriching. I took valuable scientific insights, and they also gave me a glimpse into how the life of a scientist can vary across

countries and cultures.

I would also like to acknowledge my previous mentors, Raúl Vera, who gave me the opportunity to explore General Relativity during my undergraduate studies, and Sascha Husa, who first introduced me to the world of gravitational waves. Both experiences played a major role in guiding me to the AEI and I'm grateful to you both.

I would like to express my sincere gratitude to Mark Hannam and Guido Müller for kindly agreeing to review this thesis. I'm also deeply thankful to Benno Willke and Domenico Giulini for their willingness to serve on my defense committee.

I thank the Max Planck Society for the support, the valuable resources and the incredible opportunities I had during my time here. I also want to thank the DAAD for granting me the "Forschungsstipendien für Doktorandinnen und Doktoranden" scholarship that allowed me to visit CITA for a research stay.

A sincere thank you to Jannik Mielke, Krishnendu NV, Nina Bode, and Rahul Dhurkunde for their careful proofreading of various parts of this thesis. And a big Danke schön to Max Melching and Jannik Mielke for their help in writing the summary in German.

To my dear friend Serena, I'm so happy that our PhDs overlapped and that we got to share so much of this journey together. We are even submitting our theses at the same time! I'm grateful for all the plans we made to make life in Hannover more joyful and memorable. From our cozy baking sessions on those gloomy autumn days, to our refreshing Monday swims, pizza nights at Bestia, and spring bike rides around the Ricklinger Kiesteiche. But most importantly, I'm especially glad I got to introduce you to "croquetas". Sharing life in Hannover with you has been such a joy. I will miss you deeply in the coming months.

A very special thank you to my dear friend, tandem and music partner, Steffi, especially for all our music sessions, which brightened my days every single time. I'm so proud of our two little performances at Café Lohengrin. I'm also super grateful for all the afternoons and the wonderful "pizza parties" you hosted at your place with your beautiful family. Eine herzliche Danke schön! And to Johnny, thank you so much for letting me join the jam sessions in Nelkenstraße during my first years in Hannover. Those evenings really lifted my mood.

To Alvis, Luis and Stefano, I'm so happy that we accidentally met while you were organising your first trip to Norway. Takk takk for allowing me to join! I keep so many memorable moments from our adventures in Scandinavia. From the Reinebringen hike, to aurora nights in Iceland and of course, our jacuzzi night during midsummer. Those trips brought me immense joy and gave me the chance to recharge and reset.

I'm grateful to Alicia, Alvis, Anjana, Carolina, Gabriella, Giada, Gianluca, Graziano, Johnny, Jordina, Luis, Marina, Matteo, Medea, Qazal, Rahul, Reshma, Roberta, Sari, Sariga, Sergio and Stefano for making life in Hannover more social and beautiful. And to Helene and Hans-Peter Daub, thank you for your generosity, for your patience with my German, and all the support I received from you throughout my time here.

A big thank you to Sofía and Chris for the great times we had together in Canada! My visits to Kingston truly became the best part of my experience there. I appreciated so much all the fun plans you organised, from hiking in the national parks, to the food choices (which were always fantastic!) and the bike trip during Easter.

To the people that are close to me, but unfortunately far from Hannover. To Sara and Verónica, thank you for being there when I needed you. To my parents and siblings, you have shaped so much of who I am as a person. Thank you for everything you have done for me since I was little. I'm also grateful for the times you visited me in Hannover. It meant so much! And I'm happy for the moments we spent together during holidays, at the sea, in the mountains or eating a delicious meal at home. A very special mention to my Spanish-Chilean family in Berlin, my "Universung" of Kreuzberg. Thank you for the fantastic music sessions, the most wonderful meals I ever had and especially the Hula dancing that reduced my stress in the last week of thesis writing. To Albertín and Leo, thank you for all the happiness you've brought into my life. I loved having you by my side while I finished this thesis.

This PhD also brought me moments of uncomfortable emotions, insecurities and self-doubt. I would like to thank the coaches of the EMAP and my personal psychologist, Ana, for helping me manage those emotions. To you, Ana, thanks for helping me understand all my emotions, and in particular my critical and demanding sides, which often appear in me more than I would like them to. With you, I learned to enjoy the moments that made me feel the most uncomfortable, when the word "to enjoy" was not even a possibility for me. I'm deeply grateful for your help in this process.

Finally, I'd like to take a moment to acknowledge myself, for showing up every day and for staying committed even when things felt overwhelming. I'm grateful for the strength and perseverance I found in myself and the growth I've experienced in this process.

Being part of the AEI has been a true privilege, and I'm incredibly grateful for the life I had during these years in Hannover. I will always remember this time with gratitude and nostalgia.

Bibliography

- [1] B. P. Abbott et al. Observation of Gravitational Waves from a Binary Black Hole Merger. *Phys. Rev. Lett.*, 116(6):061102, 2016.
- [2] B. P. Abbott et al. Properties of the Binary Black Hole Merger GW150914. *Phys. Rev. Lett.*, 116(24):241102, 2016.
- [3] J. Aasi et al. Advanced LIGO. *Class. Quant. Grav.*, 32:074001, 2015.
- [4] F. Acernese et al. Advanced Virgo: a second-generation interferometric gravitational wave detector. *Class. Quant. Grav.*, 32(2):024001, 2015.
- [5] T. Akutsu et al. Overview of KAGRA: Detector design and construction history. *PTEP*, 2021(5):05A101, 2021.
- [6] R. Abbott et al. GWTC-2.1: Deep extended catalog of compact binary coalescences observed by LIGO and Virgo during the first half of the third observing run. *Phys. Rev. D*, 109(2):022001, 2024.
- [7] R. Abbott et al. GWTC-3: Compact Binary Coalescences Observed by LIGO and Virgo during the Second Part of the Third Observing Run. *Phys. Rev. X*, 13(4):041039, 2023.
- [8] B. P. Abbott et al. Binary Black Hole Mergers in the first Advanced LIGO Observing Run. *Phys. Rev. X*, 6(4):041015, 2016. [Erratum: *Phys. Rev. X* 8, 039903 (2018)].
- [9] Michael Pürrer, Mark Hannam, and Frank Ohme. Can we measure individual black-hole spins from gravitational-wave observations? *Phys. Rev. D*, 93(8):084042, 2016.
- [10] Curt Cutler and Eanna E. Flanagan. Gravitational waves from merging compact binaries: How accurately can one extract the binary's parameters from the inspiral wave form? *Phys. Rev. D*, 49:2658–2697, 1994.
- [11] Eric Poisson and Clifford M. Will. Gravitational waves from inspiraling compact binaries: Parameter estimation using second postNewtonian wave forms. *Phys. Rev. D*, 52:848–855, 1995.
- [12] Emily Baird, Stephen Fairhurst, Mark Hannam, and Patricia Murphy. Degeneracy between mass and spin in black-hole-binary waveforms. *Phys. Rev. D*, 87(2):024035, 2013.

- [13] R. Abbott et al. Tests of General Relativity with GWTC-3. 12 2021.
- [14] R. Abbott et al. Constraints on the Cosmic Expansion History from GWTC-3. *Astrophys. J.*, 949(2):76, 2023.
- [15] R. Abbott et al. Population of Merging Compact Binaries Inferred Using Gravitational Waves through GWTC-3. *Phys. Rev. X*, 13(1):011048, 2023.
- [16] Simone S. Bavera, Tassos Fragos, Ying Qin, Emmanouil Zapartas, Coenraad J. Neijssel, Ilya Mandel, Aldo Batta, Sebastian M. Gaebel, Chase Kimball, and Simon Stevenson. The origin of spin in binary black holes: Predicting the distributions of the main observables of Advanced LIGO. *Astron. Astrophys.*, 635:A97, 2020.
- [17] Carl L. Rodriguez, Michael Zevin, Pau Amaro-Seoane, Sourav Chatterjee, Kyle Kremer, Frederic A. Rasio, and Claire S. Ye. Black holes: The next generation—repeated mergers in dense star clusters and their gravitational-wave properties. *Phys. Rev. D*, 100(4):043027, 2019.
- [18] Davide Gerosa, Emanuele Berti, Richard O’Shaughnessy, Krzysztof Belczynski, Michael Kesden, Daniel Wysocki, and Wojciech Gladysz. Spin orientations of merging black holes formed from the evolution of stellar binaries. *Phys. Rev. D*, 98(8):084036, 2018.
- [19] Maya Fishbach, Daniel E. Holz, and Ben Farr. Are LIGO’s Black Holes Made From Smaller Black Holes? *Astrophys. J. Lett.*, 840(2):L24, 2017.
- [20] Emanuele Berti and Marta Volonteri. Cosmological black hole spin evolution by mergers and accretion. *Astrophys. J.*, 684:822–828, 2008.
- [21] Arnab Dhani, Sebastian Völkel, Alessandra Buonanno, Hector Estelles, Jonathan Gair, Harald P. Pfeiffer, Lorenzo Pompili, and Alexandre Toubiana. Systematic Biases in Estimating the Properties of Black Holes Due to Inaccurate Gravitational-Wave Models. 4 2024.
- [22] J. A. Gonzalez, M. D. Hannam, U. Sperhake, Bernd Bruegmann, and S. Husa. Supermassive recoil velocities for binary black-hole mergers with antialigned spins. *Phys. Rev. Lett.*, 98:231101, 2007.
- [23] Bernd Bruegmann, Jose A. Gonzalez, Mark Hannam, Sascha Husa, and Ulrich Sperhake. Exploring black hole superkicks. *Phys. Rev. D*, 77:124047, 2008.
- [24] Manuela Campanelli, Carlos O. Lousto, Yosef Zlochower, and David Merritt. Maximum gravitational recoil. *Phys. Rev. Lett.*, 98:231102, 2007.
- [25] Carlos O. Lousto and Yosef Zlochower. Hangup Kicks: Still Larger Recoils by Partial Spin/Orbit Alignment of Black-Hole Binaries. *Phys. Rev. Lett.*, 107:231102, 2011.
- [26] Carlos O. Lousto and James Healy. Kicking gravitational wave detectors with recoiling black holes. *Phys. Rev. D*, 100(10):104039, 2019.

- [27] Theocharis A. Apostolatos, Curt Cutler, Gerald J. Sussman, and Kip S. Thorne. Spin induced orbital precession and its modulation of the gravitational wave forms from merging binaries. *Phys. Rev. D*, 49:6274–6297, 1994.
- [28] Mark Hannam et al. General-relativistic precession in a black-hole binary. *Nature*, 610(7933):652–655, 2022.
- [29] Vijay Varma, Sylvia Biscoveanu, Tousif Islam, Feroz H. Shaik, Carl-Johan Haster, Maximiliano Isi, Will M. Farr, Scott E. Field, and Salvatore Vitale. Evidence of Large Recoil Velocity from a Black Hole Merger Signal. *Phys. Rev. Lett.*, 128(19):191102, 2022.
- [30] Angela Borchers and Frank Ohme. Inconsistent black hole kick estimates from gravitational-wave models. *Class. Quant. Grav.*, 40(9):095008, 2023.
- [31] Angela Borchers, Frank Ohme, Jannik Mielke, and Shrobona Ghosh. Observability of spin precession in the presence of a black-hole remnant kick. *Phys. Rev. D*, 110(2):024037, 2024.
- [32] Angela Borchers, Claire S. Ye, and Maya Fishbach. Gravitational-wave kicks impact the spins of black holes from hierarchical mergers. *The Astrophysical Journal*, 987(2):146, jul 2025.
- [33] Jannik Mielke, Shrobona Ghosh, Angela Borchers, and Frank Ohme. Revisiting the relationship of black-hole kicks and multipole asymmetries. *Phys. Rev. D*, 111(6):064009, 2025.
- [34] Jonathan E. Thompson, Eleanor Hamilton, Lionel London, Shrobona Ghosh, Panagiota Kolitsidou, Charlie Hoy, and Mark Hannam. PhenomXO4a: a phenomenological gravitational-wave model for precessing black-hole binaries with higher multipoles and asymmetries. *Phys. Rev. D*, 109(6):063012, 2024.
- [35] Vijay Varma, Scott E. Field, Mark A. Scheel, Jonathan Blackman, Davide Gerosa, Leo C. Stein, Lawrence E. Kidder, and Harald P. Pfeiffer. Surrogate models for precessing binary black hole simulations with unequal masses. *Phys. Rev. Research.*, 1:033015, 2019.
- [36] Eleanor Hamilton et al. PhenomXPNR: An improved gravitational wave model linking precessing inspirals and NR-calibrated merger-ringdown. 7 2025.
- [37] Albert Einstein. Zur Allgemeinen Relativitätstheorie. *Sitzungsber. Preuss. Akad. Wiss. Berlin (Math. Phys.)*, 1915:778–786, 1915. [Addendum: *Sitzungsber. Preuss. Akad. Wiss. Berlin (Math. Phys.)* 1915, 799–801 (1915)].
- [38] Albert Einstein. The foundation of the general theory of relativity. *Annalen Phys.*, 49(7):769–822, 1916.
- [39] Karl Schwarzschild. On the gravitational field of a mass point according to Einstein’s theory. *Sitzungsber. Preuss. Akad. Wiss. Berlin (Math. Phys.)*, 1916:189–196, 1916.

- [40] Roger Penrose. Gravitational collapse and space-time singularities. *Phys. Rev. Lett.*, 14:57–59, 1965.
- [41] R. Penrose. Gravitational collapse: The role of general relativity. *Riv. Nuovo Cim.*, 1:252–276, 1969.
- [42] S. W. Hawking and R. Penrose. The Singularities of gravitational collapse and cosmology. *Proc. Roy. Soc. Lond. A*, 314:529–548, 1970.
- [43] Roy P. Kerr. Gravitational field of a spinning mass as an example of algebraically special metrics. *Phys. Rev. Lett.*, 11:237–238, 1963.
- [44] Kazunori Akiyama et al. First M87 Event Horizon Telescope Results. I. The Shadow of the Supermassive Black Hole. *Astrophys. J. Lett.*, 875:L1, 2019.
- [45] 59 Productions. <https://59.studio/>.
- [46] Tycho Brahe Planetarium in Copenhagen, Denmark. <https://www.planetarium.dk/>.
- [47] Frans Pretorius. Evolution of binary black hole spacetimes. *Phys. Rev. Lett.*, 95:121101, 2005.
- [48] J. B. Hartle. *Gravity: An introduction to Einstein's general relativity*. 2003.
- [49] R. Abbott et al. All-sky search for continuous gravitational waves from isolated neutron stars using Advanced LIGO and Advanced Virgo O3 data. *Phys. Rev. D*, 106(10):102008, 2022.
- [50] B. Steltner, M. A. Papa, H. B. Eggenstein, R. Prix, M. Bensch, B. Allen, and B. Machenschalk. Deep Einstein@Home All-sky Search for Continuous Gravitational Waves in LIGO O3 Public Data. *Astrophys. J.*, 952(1):55, 2023.
- [51] A. G. Abac et al. Search for continuous gravitational waves from known pulsars in the first part of the fourth LIGO-Virgo-KAGRA observing run. 1 2025.
- [52] Gianluca Pagliaro, Maria Alessandra Papa, Jing Ming, Jianhui Lian, Daichi Tsuna, Claudia Maraston, and Daniel Thomas. Continuous Gravitational Waves from Galactic Neutron Stars: Demography, Detectability, and Prospects. *Astrophys. J.*, 952(2):123, 2023.
- [53] Ish Gupta et al. Characterizing gravitational wave detector networks: from A[#] to cosmic explorer. *Class. Quant. Grav.*, 41(24):245001, 2024.
- [54] A. G. Abac et al. Search for gravitational waves emitted from SN 2023ixf. 10 2024.
- [55] A. G. Abac et al. A Search Using GEO600 for Gravitational Waves Coincident with Fast Radio Bursts from SGR 1935+2154. *Astrophys. J.*, 977(2):255, 2024.
- [56] R. Abbott et al. Search for Gravitational-wave Transients Associated with Magnetar Bursts in Advanced LIGO and Advanced Virgo Data from the Third Observing Run. *Astrophys. J.*, 966(1):137, 2024.

- [57] Bruce Allen and Adrian C. Ottewill. Detection of anisotropies in the gravitational wave stochastic background. *Phys. Rev. D*, 56:545–563, 1997.
- [58] Joseph D. Romano and Neil J. Cornish. Detection methods for stochastic gravitational-wave backgrounds: a unified treatment. *Living Rev. Rel.*, 20(1):2, 2017.
- [59] Heng Xu et al. Searching for the Nano-Hertz Stochastic Gravitational Wave Background with the Chinese Pulsar Timing Array Data Release I. *Res. Astron. Astrophys.*, 23(7):075024, 2023.
- [60] J. Antoniadis et al. The second data release from the European Pulsar Timing Array - III. Search for gravitational wave signals. *Astron. Astrophys.*, 678:A50, 2023.
- [61] Gabriella Agazie et al. The NANOGrav 15 yr Data Set: Evidence for a Gravitational-wave Background. *Astrophys. J. Lett.*, 951(1):L8, 2023.
- [62] Daniel J. Reardon et al. Search for an Isotropic Gravitational-wave Background with the Parkes Pulsar Timing Array. *Astrophys. J. Lett.*, 951(1):L6, 2023.
- [63] R. Abbott et al. All-sky, all-frequency directional search for persistent gravitational waves from Advanced LIGO’s and Advanced Virgo’s first three observing runs. *Phys. Rev. D*, 105(12):122001, 2022.
- [64] K. L. Dooley et al. GEO 600 and the GEO-HF upgrade program: successes and challenges. *Class. Quant. Grav.*, 33:075009, 2016.
- [65] B. P. Abbott et al. GW150914: First results from the search for binary black hole coalescence with Advanced LIGO. *Phys. Rev. D*, 93(12):122003, 2016.
- [66] B. P. Abbott et al. GW150914: The Advanced LIGO Detectors in the Era of First Discoveries. *Phys. Rev. Lett.*, 116(13):131103, 2016.
- [67] Monica Colpi et al. LISA Definition Study Report. 2 2024.
- [68] Seiji Kawamura et al. Current status of space gravitational wave antenna DECIGO and B-DECIGO. *PTEP*, 2021(5):05A105, 2021.
- [69] R. w. Hellings and G. s. Downs. UPPER LIMITS ON THE ISOTROPIC GRAVITATIONAL RADIATION BACKGROUND FROM PULSAR TIMING ANALYSIS. *Astrophys. J. Lett.*, 265:L39–L42, 1983.
- [70] Jolien D. E. Creighton and Warren G. Anderson. *Gravitational-wave physics and astronomy: An introduction to theory, experiment and data analysis*. 2011.
- [71] Alexandre Le Tiec and Jérôme Novak. *Theory of Gravitational Waves*, pages 1–41. 2017.
- [72] <https://www.ligo.caltech.edu/page/ligos-ifo>.
- [73] Gravitational Wave Interferometer Noise Calculator (GWINC). <https://git.ligo.org/gwinc/pygwinc>.

- [74] M. Heurs. Gravitational wave detection using laser interferometry beyond the standard quantum limit. *Phil. Trans. Roy. Soc. Lond. A*, 376(2120):20170289, 2018.
- [75] David Reitze et al. Cosmic Explorer: The U.S. Contribution to Gravitational-Wave Astronomy beyond LIGO. *Bull. Am. Astron. Soc.*, 51(7):035, 2019.
- [76] Michele Maggiore et al. Science Case for the Einstein Telescope. *JCAP*, 03:050, 2020.
- [77] S. S. Y. Chua, B. J. J. Slagmolen, D. A. Shaddock, and D. E. McClelland. Quantum squeezed light in gravitational-wave detectors. *Class. Quant. Grav.*, 31:183001, 2014.
- [78] A gravitational wave observatory operating beyond the quantum shot-noise limit. *Nature Physics*, 7(12):962–965, sep 2011.
- [79] Simon Chelkowski, Henning Vahlbruch, Boris Hage, Alexander Franzen, Nico Lastzka, Karsten Danzmann, and Roman Schnabel. Experimental characterization of frequency-dependent squeezed light. *Phys. Rev. A*, 71:013806, 2005.
- [80] Eric Oelker, Tomoki Isogai, John Miller, Maggie Tse, Lisa Barsotti, Nergis Mavalvala, and Matthew Evans. Audio-Band Frequency-Dependent Squeezing for Gravitational-Wave Detectors. *Phys. Rev. Lett.*, 116(4):041102, 2016.
- [81] D. Ganapathy et al. Broadband Quantum Enhancement of the LIGO Detectors with Frequency-Dependent Squeezing. *Phys. Rev. X*, 13(4):041021, 2023.
- [82] F. Acernese et al. Frequency-Dependent Squeezed Vacuum Source for the Advanced Virgo Gravitational-Wave Detector. *Phys. Rev. Lett.*, 131(4):041403, 2023.
- [83] B. P. Abbott et al. Multi-messenger Observations of a Binary Neutron Star Merger. *Astrophys. J. Lett.*, 848(2):L12, 2017.
- [84] Thomas Bayes, Rev. An essay toward solving a problem in the doctrine of chances. *Phil. Trans. Roy. Soc. Lond.*, 53:370–418, 1764.
- [85] E. T. Jaynes. *Probability Theory: The Logic of Science*. Cambridge University Press, 2003.
- [86] Carl W Helstrom. Statistical theory of signal detection. (*No Title*), 1960.
- [87] Bruce Allen, Warren G. Anderson, Patrick R. Brady, Duncan A. Brown, and Jolien D. E. Creighton. FINDCHIRP: An Algorithm for detection of gravitational waves from inspiraling compact binaries. *Phys. Rev. D*, 85:122006, 2012.
- [88] J. Veitch et al. Parameter estimation for compact binaries with ground-based gravitational-wave observations using the LALInference software library. *Phys. Rev. D*, 91(4):042003, 2015.
- [89] N. Metropolis, A. W. Rosenbluth, M. N. Rosenbluth, A. H. Teller, and E. Teller. Equation of state calculations by fast computing machines. *J. Chem. Phys.*, 21:1087–1092, 1953.

- [90] W. K. Hastings. Monte Carlo Sampling Methods Using Markov Chains and Their Applications. *Biometrika*, 57:97–109, 1970.
- [91] John Skilling. Nested Sampling. *AIP Conf. Proc.*, 735(1):395, 2004.
- [92] Eric Thrane and Colm Talbot. An introduction to Bayesian inference in gravitational-wave astronomy: parameter estimation, model selection, and hierarchical models. *Publ. Astron. Soc. Austral.*, 36:e010, 2019. [Erratum: *Publ.Astron.Soc.Austral.* 37, e036 (2020)].
- [93] Gregory Ashton et al. BILBY: A user-friendly Bayesian inference library for gravitational-wave astronomy. *Astrophys. J. Suppl.*, 241(2):27, 2019.
- [94] K. Chatziioannou, T. Dent, M. Fishbach, F. Ohme, M. Pürrer, V. Raymond, and J. Veitch. Compact binary coalescences: gravitational-wave astronomy with ground-based detectors. 9 2024.
- [95] Luc Blanchet. Gravitational radiation from post-Newtonian sources and inspiralling compact binaries. *Living Rev. Rel.*, 9:4, 2006.
- [96] Luc Blanchet. Analyzing Gravitational Waves with General Relativity. *Comptes Rendus Physique*, 20:507–520, 2019.
- [97] Alessandra Buonanno, Bala Iyer, Evan Ochsner, Yi Pan, and B. S. Sathyaprakash. Comparison of post-Newtonian templates for compact binary inspiral signals in gravitational-wave detectors. *Phys. Rev. D*, 80:084043, 2009.
- [98] Thibault Damour, Bala R. Iyer, and B. S. Sathyaprakash. Improved filters for gravitational waves from inspiralling compact binaries. *Phys. Rev. D*, 57:885–907, 1998.
- [99] A. Buonanno and T. Damour. Effective one-body approach to general relativistic two-body dynamics. *Phys. Rev. D*, 59:084006, 1999.
- [100] Alessandra Buonanno and Thibault Damour. Transition from inspiral to plunge in binary black hole coalescences. *Phys. Rev. D*, 62:064015, 2000.
- [101] Manuela Campanelli, C. O. Lousto, P. Marronetti, and Y. Zlochower. Accurate evolutions of orbiting black-hole binaries without excision. *Phys. Rev. Lett.*, 96:111101, 2006.
- [102] John G. Baker, Joan Centrella, Dae-Il Choi, Michael Koppitz, and James van Meter. Gravitational wave extraction from an inspiraling configuration of merging black holes. *Phys. Rev. Lett.*, 96:111102, 2006.
- [103] Mark A. Scheel et al. The SXS Collaboration’s third catalog of binary black hole simulations. 5 2025.
- [104] James Healy and Carlos O. Lousto. Fourth RIT binary black hole simulations catalog: Extension to eccentric orbits. *Phys. Rev. D*, 105(12):124010, 2022.

- [105] Eleanor Hamilton et al. Catalog of precessing black-hole-binary numerical-relativity simulations. *Phys. Rev. D*, 109(4):044032, 2024.
- [106] William H. Press. Long Wave Trains of Gravitational Waves from a Vibrating Black Hole. *Astrophys. J. Lett.*, 170:L105–L108, 1971.
- [107] S. A. Teukolsky. Rotating black holes - separable wave equations for gravitational and electromagnetic perturbations. *Phys. Rev. Lett.*, 29:1114–1118, 1972.
- [108] Saul A. Teukolsky. Perturbations of a rotating black hole. 1. Fundamental equations for gravitational electromagnetic and neutrino field perturbations. *Astrophys. J.*, 185:635–647, 1973.
- [109] P. Ajith, M. Hannam, S. Husa, Y. Chen, B. Brügmann, N. Dorband, D. Müller, F. Ohme, D. Pollney, C. Reisswig, L. Santamaría, and J. Seiler. Inspiral-merger-ringdown waveforms for black-hole binaries with nonprecessing spins. *Phys. Rev. Lett.*, 106:241101, Jun 2011.
- [110] L. Santamaría, F. Ohme, P. Ajith, B. Brügmann, N. Dorband, M. Hannam, S. Husa, P. Mösta, D. Pollney, C. Reisswig, E. L. Robinson, J. Seiler, and B. Krishnan. Matching post-newtonian and numerical relativity waveforms: Systematic errors and a new phenomenological model for nonprecessing black hole binaries. *Phys. Rev. D*, 82:064016, Sep 2010.
- [111] Lawrence E. Kidder. Coalescing binary systems of compact objects to postNewtonian 5/2 order. 5. Spin effects. *Phys. Rev. D*, 52:821–847, 1995.
- [112] Patricia Schmidt, Frank Ohme, and Mark Hannam. Towards models of gravitational waveforms from generic binaries: II. modelling precession effects with a single effective precession parameter. *Phys. Rev. D*, 91:024043, Jan 2015.
- [113] Davide Gerosa, Matthew Mould, Daria Gangardt, Patricia Schmidt, Geraint Pratten, and Lucy M. Thomas. A generalized precession parameter χ_p to interpret gravitational-wave data. *Phys. Rev. D*, 103(6):064067, 2021.
- [114] Lucy M. Thomas, Patricia Schmidt, and Geraint Pratten. New effective precession spin for modeling multimodal gravitational waveforms in the strong-field regime. *Phys. Rev. D*, 103(8):083022, 2021.
- [115] Carl L. Rodriguez, Pau Amaro-Seoane, Sourav Chatterjee, and Frederic A. Rasio. Post-newtonian dynamics in dense star clusters: Highly eccentric, highly spinning, and repeated binary black hole mergers. *Phys. Rev. Lett.*, 120:151101, Apr 2018.
- [116] J. N. Goldberg, A. J. MacFarlane, E. T. Newman, F. Rohrlich, and E. C. G. Sudarshan. Spin s spherical harmonics and edth. *J. Math. Phys.*, 8:2155, 1967.
- [117] Shrobana Ghosh, Panagiota Kolitsidou, and Mark Hannam. First frequency-domain phenomenological model of the multipole asymmetry in gravitational-wave signals from binary-black-hole coalescence. *Phys. Rev. D*, 109(2):024061, 2024.

- [118] Michael Boyle, Lawrence E. Kidder, Serguei Ossokine, and Harald P. Pfeiffer. Gravitational-wave modes from precessing black-hole binaries. 9 2014.
- [119] Patricia Schmidt, Mark Hannam, and Sascha Husa. Towards models of gravitational waveforms from generic binaries: A simple approximate mapping between precessing and non-precessing inspiral signals. *Phys. Rev. D*, 86:104063, 2012.
- [120] Michael Boyle. Angular velocity of gravitational radiation from precessing binaries and the corotating frame. *Phys. Rev. D*, 87(10):104006, 2013.
- [121] Cecilio García-Quirós, Marta Colleoni, Sascha Husa, Héctor Estellés, Geraint Pratten, Antoni Ramos-Buades, Maite Mateu-Lucena, and Rafel Jaume. Multimode frequency-domain model for the gravitational wave signal from nonprecessing black-hole binaries. *Phys. Rev. D*, 102(6):064002, 2020.
- [122] Manuela Campanelli, C. O. Lousto, and Y. Zlochower. Spinning-black-hole binaries: The orbital hang up. *Phys. Rev. D*, 74:041501, 2006.
- [123] Stephen Fairhurst, Rhys Green, Mark Hannam, and Charlie Hoy. When will we observe binary black holes precessing? *Phys. Rev. D*, 102(4):041302, 2020.
- [124] Geraint Pratten et al. Computationally efficient models for the dominant and subdominant harmonic modes of precessing binary black holes. *Phys. Rev. D*, 103(10):104056, 2021.
- [125] Andrea Taracchini, Yi Pan, Alessandra Buonanno, Enrico Barausse, Michael Boyle, Tony Chu, Geoffrey Lovelace, Harald P. Pfeiffer, and Mark A. Scheel. Prototype effective-one-body model for nonprecessing spinning inspiral-merger-ringdown waveforms. *Phys. Rev. D*, 86:024011, 2012.
- [126] Lorenzo Pompili et al. Laying the foundation of the effective-one-body waveform models SEOBNRv5: Improved accuracy and efficiency for spinning nonprecessing binary black holes. *Phys. Rev. D*, 108(12):124035, 2023.
- [127] Andrea Taracchini et al. Effective-one-body model for black-hole binaries with generic mass ratios and spins. *Phys. Rev. D*, 89(6):061502, 2014.
- [128] Alejandro Bohé et al. Improved effective-one-body model of spinning, nonprecessing binary black holes for the era of gravitational-wave astrophysics with advanced detectors. *Phys. Rev. D*, 95(4):044028, 2017.
- [129] Antoni Ramos-Buades, Alessandra Buonanno, Héctor Estellés, Mohammed Khalil, Deyan P. Mihaylov, Serguei Ossokine, Lorenzo Pompili, and Mahlet Shiferaw. Next generation of accurate and efficient multipolar precessing-spin effective-one-body waveforms for binary black holes. *Phys. Rev. D*, 108(12):124037, 2023.
- [130] Mohammed Khalil, Alessandra Buonanno, Hector Estelles, Deyan P. Mihaylov, Serguei Ossokine, Lorenzo Pompili, and Antoni Ramos-Buades. Theoretical groundwork supporting the precessing-spin two-body dynamics of the effective-one-body waveform models SEOBNRv5. *Phys. Rev. D*, 108(12):124036, 2023.

- [131] Héctor Estellés, Alessandra Buonanno, Raffi Enficiaud, Cheng Foo, and Lorenzo Pompili. Adding equatorial-asymmetric effects for spin-precessing binaries into the SEOBNRv5PHM waveform model. 6 2025.
- [132] Antoni Ramos-Buades, Alessandra Buonanno, Mohammed Khalil, and Serguei Ossokine. Effective-one-body multipolar waveforms for eccentric binary black holes with nonprecessing spins. *Phys. Rev. D*, 105(4):044035, 2022.
- [133] Aldo Gamboa et al. Accurate waveforms for eccentric, aligned-spin binary black holes: The multipolar effective-one-body model SEOBNRv5EHM. 12 2024.
- [134] Jan Steinhoff, Tanja Hinderer, Alessandra Buonanno, and Andrea Taracchini. Dynamical Tides in General Relativity: Effective Action and Effective-One-Body Hamiltonian. *Phys. Rev. D*, 94(10):104028, 2016.
- [135] Andrew Matas et al. Aligned-spin neutron-star-black-hole waveform model based on the effective-one-body approach and numerical-relativity simulations. *Phys. Rev. D*, 102(4):043023, 2020.
- [136] Michael Pürrer. Frequency domain reduced order models for gravitational waves from aligned-spin compact binaries. *Class. Quant. Grav.*, 31(19):195010, 2014.
- [137] Sarp Akcay, Rossella Gamba, and Sebastiano Bernuzzi. Hybrid post-Newtonian effective-one-body scheme for spin-precessing compact-binary waveforms up to merger. *Phys. Rev. D*, 103(2):024014, 2021.
- [138] Simone Albanesi, Rossella Gamba, Sebastiano Bernuzzi, Joan Fontbuté, Alejandra Gonzalez, and Alessandro Nagar. Effective-one-body modeling for generic compact binaries with arbitrary orbits. 3 2025.
- [139] Rossella Gamba, Danilo Chiaramello, and Sayan Neogi. Toward efficient effective-one-body models for generic, nonplanar orbits. *Phys. Rev. D*, 110(2):024031, 2024.
- [140] Alessandro Nagar et al. Time-domain effective-one-body gravitational waveforms for coalescing compact binaries with nonprecessing spins, tides and self-spin effects. *Phys. Rev. D*, 98(10):104052, 2018.
- [141] Frank Ohme. Analytical meets numerical relativity - status of complete gravitational waveform models for binary black holes. *Class. Quant. Grav.*, 29:124002, 2012.
- [142] Parameswaran Ajith et al. Phenomenological template family for black-hole coalescence waveforms. *Class. Quant. Grav.*, 24:S689–S700, 2007.
- [143] P. Ajith et al. A Template bank for gravitational waveforms from coalescing binary black holes. I. Non-spinning binaries. *Phys. Rev. D*, 77:104017, 2008. [Erratum: *Phys.Rev.D* 79, 129901 (2009)].
- [144] P. Ajith et al. Inspiral-merger-ringdown waveforms for black-hole binaries with non-precessing spins. *Phys. Rev. Lett.*, 106:241101, 2011.

- [145] L. Santamaria et al. Matching post-Newtonian and numerical relativity waveforms: systematic errors and a new phenomenological model for non-precessing black hole binaries. *Phys. Rev. D*, 82:064016, 2010.
- [146] Sebastian Khan, Sascha Husa, Mark Hannam, Frank Ohme, Michael Pürrer, Xisco Jiménez Forteza, and Alejandro Bohé. Frequency-domain gravitational waves from nonprecessing black-hole binaries. II. A phenomenological model for the advanced detector era. *Phys. Rev. D*, 93(4):044007, 2016.
- [147] Sascha Husa, Sebastian Khan, Mark Hannam, Michael Pürrer, Frank Ohme, Xisco Jiménez Forteza, and Alejandro Bohé. Frequency-domain gravitational waves from nonprecessing black-hole binaries. I. New numerical waveforms and anatomy of the signal. *Phys. Rev. D*, 93(4):044006, 2016.
- [148] Lionel London, Sebastian Khan, Edward Fauchon-Jones, Cecilio García, Mark Hannam, Sascha Husa, Xisco Jiménez-Forteza, Chinmay Kalaghatgi, Frank Ohme, and Francesco Pannarale. First higher-multipole model of gravitational waves from spinning and coalescing black-hole binaries. *Phys. Rev. Lett.*, 120(16):161102, 2018.
- [149] Mark Hannam, Patricia Schmidt, Alejandro Bohé, Leïla Haegel, Sascha Husa, Frank Ohme, Geraint Pratten, and Michael Pürrer. Simple Model of Complete Precessing Black-Hole-Binary Gravitational Waveforms. *Phys. Rev. Lett.*, 113(15):151101, 2014.
- [150] Sebastian Khan, Katerina Chatziioannou, Mark Hannam, and Frank Ohme. Phenomenological model for the gravitational-wave signal from precessing binary black holes with two-spin effects. *Phys. Rev. D*, 100(2):024059, 2019.
- [151] Sebastian Khan, Frank Ohme, Katerina Chatziioannou, and Mark Hannam. Including higher order multipoles in gravitational-wave models for precessing binary black holes. *Phys. Rev. D*, 101(2):024056, 2020.
- [152] Geraint Pratten, Sascha Husa, Cecilio Garcia-Quiros, Marta Colleoni, Antoni Ramos-Buades, Hector Estelles, and Rafel Jaume. Setting the cornerstone for a family of models for gravitational waves from compact binaries: The dominant harmonic for nonprecessing quasicircular black holes. *Phys. Rev. D*, 102(6):064001, 2020.
- [153] Marta Colleoni, Felip A. Ramis Vidal, Cecilio García-Quirós, Sarp Akçay, and Sayantani Bera. Fast frequency-domain gravitational waveforms for precessing binaries with a new twist. *Phys. Rev. D*, 111(10):104019, 2025.
- [154] Héctor Estellés, Antoni Ramos-Buades, Sascha Husa, Cecilio García-Quirós, Marta Colleoni, Leïla Haegel, and Rafel Jaume. Phenomenological time domain model for dominant quadrupole gravitational wave signal of coalescing binary black holes. *Phys. Rev. D*, 103(12):124060, 2021.
- [155] Héctor Estellés, Marta Colleoni, Cecilio García-Quirós, Sascha Husa, David Keitel, Maite Mateu-Lucena, Maria de Lluç Planas, and Antoni Ramos-Buades. New twists

- in compact binary waveform modeling: A fast time-domain model for precession. *Phys. Rev. D*, 105(8):084040, 2022.
- [156] Héctor Estellés, Sascha Husa, Marta Colleoni, David Keitel, Maite Mateu-Lucena, Cecilio García-Quirós, Antoni Ramos-Buades, and Angela Borchers. Time-domain phenomenological model of gravitational-wave subdominant harmonics for quasi-circular nonprecessing binary black hole coalescences. *Phys. Rev. D*, 105(8):084039, 2022.
- [157] Maria de Lluc Planas, Antoni Ramos-Buades, Cecilio García-Quirós, Héctor Estellés, Sascha Husa, and Maria Haney. Time-domain phenomenological multipolar waveforms for aligned-spin binary black holes in elliptical orbits. 3 2025.
- [158] Cecilio García-Quirós, Sascha Husa, Maite Mateu-Lucena, and Angela Borchers. Accelerating the evaluation of inspiral–merger–ringdown waveforms with adapted grids. *Class. Quant. Grav.*, 38(1):015006, 2021.
- [159] Jonathan Blackman, Scott E. Field, Mark A. Scheel, Chad R. Galley, Christian D. Ott, Michael Boyle, Lawrence E. Kidder, Harald P. Pfeiffer, and Béla Szilágyi. Numerical relativity waveform surrogate model for generically precessing binary black hole mergers. *Phys. Rev. D*, 96(2):024058, 2017.
- [160] Gene H Golub and Charles F Van Loan. Matrix computations, Johns Hopkins U. *Math. Sci., Johns Hopkins University Press, Baltimore, MD*, 1996.
- [161] Vijay Varma, Scott E. Field, Mark A. Scheel, Jonathan Blackman, Lawrence E. Kidder, and Harald P. Pfeiffer. Surrogate model of hybridized numerical relativity binary black hole waveforms. *Phys. Rev. D*, 99(6):064045, 2019.
- [162] Nur E. M. Rifat, Scott E. Field, Gaurav Khanna, and Vijay Varma. Surrogate model for gravitational wave signals from comparable and large-mass-ratio black hole binaries. *Phys. Rev. D*, 101(8):081502, 2020.
- [163] Tousif Islam, Scott E. Field, Scott A. Hughes, Gaurav Khanna, Vijay Varma, Matthew Giesler, Mark A. Scheel, Lawrence E. Kidder, and Harald P. Pfeiffer. Surrogate model for gravitational wave signals from nonspinning, comparable-to large-mass-ratio black hole binaries built on black hole perturbation theory waveforms calibrated to numerical relativity. *Phys. Rev. D*, 106(10):104025, 2022.
- [164] Tousif Islam, Vijay Varma, Jackie Lodman, Scott E. Field, Gaurav Khanna, Mark A. Scheel, Harald P. Pfeiffer, Davide Gerosa, and Lawrence E. Kidder. Eccentric binary black hole surrogate models for the gravitational waveform and remnant properties: comparable mass, nonspinning case. *Phys. Rev. D*, 103(6):064022, 2021.
- [165] Lee Lindblom, Benjamin J. Owen, and Duncan A. Brown. Model Waveform Accuracy Standards for Gravitational Wave Data Analysis. *Phys. Rev. D*, 78:124020, 2008.

- [166] B. P. Abbott et al. Search for Gravitational Waves from Low Mass Binary Coalescences in the First Year of LIGO's S5 Data. *Phys. Rev. D*, 79:122001, 2009.
- [167] S. Babak, R. Biswas, P. R. Brady, D. A. Brown, K. Cannon, C. D. Capano, J. H. Clayton, T. Cokelaer, J. D. E. Creighton, T. Dent, A. Dietz, S. Fairhurst, N. Fotopoulos, G. González, C. Hanna, I. W. Harry, G. Jones, D. Keppel, D. J. A. McKechn, L. Pekowsky, S. Privitera, C. Robinson, A. C. Rodriguez, B. S. Sathyaprakash, A. S. Sengupta, M. Vallisneri, R. Vaulin, and A. J. Weinstein. Searching for gravitational waves from binary coalescence. *Phys. Rev. D*, 87:024033, Jan 2013.
- [168] WB Bonnor and MA Rotenberg. Transport of momentum by gravitational waves: the linear approximation. *Proceedings of the Royal Society of London. Series A. Mathematical and Physical Sciences*, 265(1320):109–116, 1961.
- [169] Jacob D. Bekenstein. Gravitational-Radiation Recoil and Runaway Black Holes. *Astrophys. J.*, 183:657–664, 1973.
- [170] M. J. Fitchett. The influence of gravitational wave momentum losses on the centre of mass motion of a Newtonian binary system. *Mon. Not. Roy. Astron. Soc.*, 203(4):1049–1062, 1983.
- [171] Jose A. Gonzalez, Ulrich Sperhake, Bernd Bruegmann, Mark Hannam, and Sascha Husa. Total recoil: The Maximum kick from nonspinning black-hole binary inspiral. *Phys. Rev. Lett.*, 98:091101, 2007.
- [172] Alexandre Le Tiec, Luc Blanchet, and Clifford M. Will. Gravitational-Wave Recoil from the Ringdown Phase of Coalescing Black Hole Binaries. *Class. Quant. Grav.*, 27:012001, 2010.
- [173] Luciano Rezzolla, Rodrigo P. Macedo, and Jose Luis Jaramillo. Understanding the 'anti-kick' in the merger of binary black holes. *Phys. Rev. Lett.*, 104:221101, 2010.
- [174] Richard H. Price, Gaurav Khanna, and Scott A. Hughes. Systematics of black hole binary inspiral kicks and the slowness approximation. *Phys. Rev. D*, 83:124002, 2011.
- [175] Jose Luis Jaramillo, Rodrigo Panosso Macedo, Philipp Moesta, and Luciano Rezzolla. Black-hole horizons as probes of black-hole dynamics I: post-merger recoil in head-on collisions. *Phys. Rev. D*, 85:084030, 2012.
- [176] Michael Boyle et al. The SXS Collaboration catalog of binary black hole simulations. *Class. Quant. Grav.*, 36(19):195006, 2019.
- [177] Frank Herrmann, Ian Hinder, Deirdre Shoemaker, Pablo Laguna, and Richard A. Matzner. Gravitational recoil from spinning binary black hole mergers. *Astrophys. J.*, 661:430–436, 2007.
- [178] Michael Koppitz, Denis Pollney, Christian Reisswig, Luciano Rezzolla, Jonathan Thornburg, Peter Diener, and Erik Schnetter. Recoil Velocities from Equal-Mass Binary-Black-Hole Mergers. *Phys. Rev. Lett.*, 99:041102, 2007.

- [179] U. Sperhake, R. Rosca-Mead, D. Gerosa, and E. Berti. Amplification of superkicks in black-hole binaries through orbital eccentricity. *Phys. Rev. D*, 101(2):024044, 2020.
- [180] Miren Radia, Ulrich Sperhake, Emanuele Berti, and Robin Croft. Anomalies in the gravitational recoil of eccentric black-hole mergers with unequal mass ratios. *Phys. Rev. D*, 103(10):104006, 2021.
- [181] Luc Blanchet, Moh'd S. S. Qusailah, and Clifford M. Will. Gravitational recoil of inspiralling black-hole binaries to second post-Newtonian order. *Astrophys. J.*, 635:508, 2005.
- [182] David Merritt, Milos Milosavljevic, Marc Favata, Scott A. Hughes, and Daniel E. Holz. Consequences of gravitational radiation recoil. *Astrophys. J. Lett.*, 607:L9–L12, 2004.
- [183] S. Komossa. Recoiling black holes: electromagnetic signatures, candidates, and astrophysical implications. *Adv. Astron.*, 2012:364973, 2012.
- [184] A. sesana. Extreme recoils: impact on the detection of gravitational waves from massive black hole binaries. *Mon. Not. Roy. Astron. Soc.*, 382:6, 2007.
- [185] Marco Chiaberge et al. A recoiling supermassive black hole in a powerful quasar. 1 2025.
- [186] S. Komossa, H. Zhou, and H. Lu. A recoiling supermassive black hole in the quasar SDSSJ092712.65+294344.0? *Astrophys. J. Lett.*, 678:L81–L84, 2008.
- [187] Andrew Robinson, Stuart Young, David J. Axon, Preeti Kharb, and James E. Smith. Spectropolarimetric evidence for a kicked supermassive black hole in the Quasar E1821+643. *Astrophys. J. Lett.*, 717:L122, 2010.
- [188] F. Civano et al. A Runaway Black Hole in COSMOS: Gravitational Wave or Slingshot Recoil? *Astrophys. J.*, 717:209–222, 2010.
- [189] Davide Gerosa and Emanuele Berti. Escape speed of stellar clusters from multiple-generation black-hole mergers in the upper mass gap. *Phys. Rev. D*, 100(4):041301, 2019.
- [190] Davide Gerosa and Maya Fishbach. Hierarchical mergers of stellar-mass black holes and their gravitational-wave signatures. *Nature Astron.*, 5(8):749–760, 2021.
- [191] Michela Mapelli et al. Hierarchical black hole mergers in young, globular and nuclear star clusters: the effect of metallicity, spin and cluster properties. *Mon. Not. Roy. Astron. Soc.*, 505(1):339–358, 2021.
- [192] Parthapratim Mahapatra, Anuradha Gupta, Marc Favata, K. G. Arun, and B. S. Sathyaprakash. Remnant Black Hole Kicks and Implications for Hierarchical Mergers. *Astrophys. J. Lett.*, 918(2):L31, 2021.
- [193] Davide Gerosa and Christopher J. Moore. Black hole kicks as new gravitational wave observables. *Phys. Rev. Lett.*, 117(1):011101, 2016.

- [194] Juan Calderón Bustillo, James A. Clark, Pablo Laguna, and Deirdre Shoemaker. Tracking black hole kicks from gravitational wave observations. *Phys. Rev. Lett.*, 121(19):191102, 2018.
- [195] Vijay Varma, Maximiliano Isi, and Sylvia Biscoveanu. Extracting the Gravitational Recoil from Black Hole Merger Signals. *Phys. Rev. Lett.*, 124(10):101104, 2020.
- [196] Milton Ruiz, Ryoji Takahashi, Miguel Alcubierre, and Dario Nunez. Multipole expansions for energy and momenta carried by gravitational waves. *Gen. Rel. Grav.*, 40:2467, 2008.
- [197] Davide Gerosa and Michael Kesden. PRECESSION: Dynamics of spinning black-hole binaries with python. *Phys. Rev. D*, 93(12):124066, 2016.
- [198] Davide Gerosa, François Hébert, and Leo C. Stein. Black-hole kicks from numerical-relativity surrogate models. *Phys. Rev. D*, 97(10):104049, 2018.
- [199] Vijay Varma, Davide Gerosa, Leo C. Stein, François Hébert, and Hao Zhang. High-accuracy mass, spin, and recoil predictions of generic black-hole merger remnants. *Phys. Rev. Lett.*, 122(1):011101, 2019.
- [200] N. V. Krishnendu and Frank Ohme. Interplay of spin-precession and higher harmonics in the parameter estimation of binary black holes. *Phys. Rev. D*, 105(6):064012, 2022.
- [201] B. P. Abbott et al. Prospects for observing and localizing gravitational-wave transients with Advanced LIGO, Advanced Virgo and KAGRA. *Living Rev. Rel.*, 19:1, 2016.
- [202] Stephen Fairhurst, Rhys Green, Charlie Hoy, Mark Hannam, and Alistair Muir. Two-harmonic approximation for gravitational waveforms from precessing binaries. *Phys. Rev. D*, 102(2):024055, 2020.
- [203] Fulya Kiroğlu, James C. Lombardi, Kyle Kremer, Hans D. Vanderzanden, and Fred-eric A. Rasio. Spin–Orbit Alignment in Merging Binary Black Holes Following Collisions with Massive Stars. *Astrophys. J. Lett.*, 983(1):L9, 2025.
- [204] R. Abbott et al. GW190521: A Binary Black Hole Merger with a Total Mass of $150M_{\odot}$. *Phys. Rev. Lett.*, 125(10):101102, 2020.
- [205] GW231123: a Binary Black Hole Merger with Total Mass 190-265 M_{\odot} . 7 2025.
- [206] Abhay Ashtekar, Tommaso De Lorenzo, and Neev Khera. Compact binary coalescences: Constraints on waveforms. *Gen. Rel. Grav.*, 52(11):107, 2020.
- [207] Neev Khera, Abhay Ashtekar, and Badri Krishnan. Testing gravitational waveform models using angular momentum. *Phys. Rev. D*, 104(12):124071, 2021.
- [208] Sebastian Khan. Probabilistic model for the gravitational wave signal from merging black holes. *Phys. Rev. D*, 109(10):104045, 2024.

- [209] Charlie Hoy, Sarp Akcay, Jake Mac Uilliam, and Jonathan E. Thompson. Incorporating model accuracy into gravitational-wave Bayesian inference. 9 2024.
- [210] Christopher J. Moore and Jonathan R. Gair. Novel Method for Incorporating Model Uncertainties into Gravitational Wave Parameter Estimates. *Phys. Rev. Lett.*, 113:251101, 2014.
- [211] Lorenzo Pompili, Alessandra Buonanno, and Michael Pürrer. Accounting for Numerical-Relativity Calibration Uncertainty in Gravitational-Wave Modeling and Inference. 10 2024.
- [212] Ritesh Bachhar, Michael Pürrer, and Stephen R. Green. Incorporating waveform calibration error in gravitational-wave modeling and inference for SEOBNRv4. *Phys. Rev. D*, 111(8):084050, 2025.
- [213] Sumit Kumar, Max Melching, and Frank Ohme. Accounting for the Known Unknown: A Parametric Framework to Incorporate Systematic Waveform Errors in Gravitational-Wave Parameter Estimation. 2 2025.
- [214] Ines Brott, Selma E. de Mink, Matteo Cantiello, Norbert Langer, Alex de Koter, Chris J. Evans, Ian Hunter, Carrie Trundle, and Jorick S. Vink. Rotating Massive Main-Sequence Stars I: Grids of Evolutionary Models and Isochrones. *Astron. Astrophys.*, 530:A115, 2011.

Curriculum Vitae

PERSONAL DETAILS

Angela Borchers Pascual

Born on December 7th, 1997, in Gautegiz Arteaga, Spain

EDUCATION

- 2025 **Max Planck Institute for Gravitational Physics**
Leibniz Universität Hannover, Hannover, Germany
PhD in Natural Sciences
- 2021 **Leibniz Universität Hannover**, Hannover, Germany
Master's Degree in Physics
- 2019 **University of the Basque Country**, Leioa, Spain
Bachelor's Degree in Physics

RESEARCH EXPERIENCE

- Dec 2021 - Jul 2025 **PhD Thesis Research**
Max Planck Institute for Gravitational Physics
Hannover, Germany
Advisor: *Frank Ohme*
- Jan 2024 - Apr 2024 **PhD Research Stay**
Canadian Institute for Theoretical Astrophysics
Toronto, Canada
Advisor: *Maya Fishbach*
- Oct 2020 - Oct 2021 **Master's Thesis Research**
Max Planck Institute for Gravitational Physics
Hannover, Germany
Title: *"The imprint of black-hole kicks on the gravitational-wave signal"*
Advisor: *Frank Ohme*
- Sep 2020 - Oct 2020 **Summer Research Student**
University of the Balearic Islands, Palma, Spain
Advisor: *Sascha Husa*

- Jun 2019 - Jul 2019 **Summer Research Student**
University of the Balearic Islands, Palma, Spain
Advisor: *Sascha Husa*
- Jan 2019 - Jul 2019 **Bachelor's Thesis Research**
University of the Basque Country, Leioa, Spain
Title: "*Global properties of charged black holes with cosmological constant*"
Advisor: *Raül Vera*

PUBLICATIONS

7. [Angela Borchers](#), Claire S. Ye, Maya Fishbach, "Gravitational-wave kicks impact the spins of black holes from hierarchical mergers", *Astrophys. J.* 987, 146 (2025)
6. Jannik Mielke, Shrobana Ghosh, [Angela Borchers](#) and Frank Ohme, "Revisiting the relationship of black-hole kicks and multipole asymmetries", *Phys. Rev. D* 111, 064009 (2025)
5. [Angela Borchers](#), Frank Ohme, Jannik Mielke and Shrobana Ghosh, "Observability of spin precession in the presence of a black-hole remnant kick", *Phys. Rev. D* 110, 024037 (2024)
4. [Angela Borchers](#) and Frank Ohme, "Inconsistent black hole kick estimates from gravitational-wave models", *Class. Quant. Grav.* 40, 095008 (2023)
3. Héctor Estellés, Sascha Husa, Marta Colleoni, David Keitel, Maite Mateu-Lucena, Cecilio García-Quirós, Antoni Ramos-Buades, [Angela Borchers](#), "Time domain phenomenological model of gravitational wave subdominant harmonics for quasi-circular non-precessing binary black hole coalescences", *Phys. Rev. D* 105, 084039 (2022)
2. [Angela Borchers](#) and Frank Ohme, "Black-hole kicks: a tool to measure the accuracy of gravitational-wave models", Contribution to: 55th Rencontres de Moriond on Gravitation (2021)
1. Cecilio García-Quirós, Sascha Husa, Maite Mateu-Lucena and [Angela Borchers](#), "Accelerating the evaluation of inspiral-merger-ringdown waveforms with adapted grids", *Class. Quant. Grav.* 38, 015006 (2021)

I am also a co-author in the following LVK Collaborations' papers:

9. The LIGO Scientific Collaboration, the Virgo Collaboration, the KAGRA Collaboration, "All-sky search for long-duration gravitational-wave transients in the first part of the fourth LIGO-Virgo-KAGRA Observing run", arXiv:2507.12282 (2025)

8. The LIGO Scientific Collaboration, the Virgo Collaboration, the KAGRA Collaboration, "All-sky search for short gravitational-wave bursts in the first part of the fourth LIGO-Virgo-KAGRA observing run", arXiv:2507.12374 (2025)

7. The LIGO Scientific Collaboration, the Virgo Collaboration, the KAGRA Collaboration, "GW231123: a Binary Black Hole Merger with Total Mass $190\text{-}265 M_{\odot}$ ", arXiv:2507.08219 (2025)

6. The LIGO Scientific Collaboration, the Virgo Collaboration, the KAGRA Collaboration, "Search for continuous gravitational waves from known pulsars in the first part of the fourth LIGO-Virgo-KAGRA observing run", *Astrophys. J.* 983, 99 (2025)

5. The LIGO Scientific Collaboration, the Virgo Collaboration, the KAGRA Collaboration, "Search for gravitational waves emitted from SN 2023ixf", *Astrophys. J.* 985, 183 (2025)

4. The LIGO Scientific, Virgo, KAGRA and Swift-BAT/GUANO Collaborations, "Swift-BAT GUANO Follow-up of Gravitational-wave Triggers in the Third LIGO–Virgo–KAGRA Observing Run", *Astrophys. J.* 980, 207 (2025)

3. The LIGO Scientific Collaboration, the Virgo Collaboration, the KAGRA Collaboration, "A Search Using GEO600 for Gravitational Waves Coincident with Fast Radio Bursts from SGR 1935+2154", *Astrophys. J.* 977, 255 (2024)

2. The LIGO Scientific Collaboration, the Virgo Collaboration, the KAGRA Collaboration, "Observation of Gravitational Waves from the Coalescence of a $2.5\text{-}4.5 M_{\odot}$ Compact Object and a Neutron Star", *Astrophys. J. Lett.* 970, L34 (2024)

1. The LIGO Scientific Collaboration, the Virgo Collaboration, the KAGRA Collaboration, "Ultralight vector dark matter search using data from the KAGRA O3GK run", *Phys. Rev. D* 110 042001 (2024)

SCHOLARSHIPS

2. "Forschungsstipendien für Doktorandinnen und Doktoranden", DAAD 2023 Scholarship obtained to support a four-month research stay at the Canadian Institute for Theoretical Astrophysics in Toronto, Canada.

1. Erasmus Scholarship, European Union 2018
Scholarship obtained to spend a semester at the University of Oulu, Finland.